THE CONSTITUTION AND KINETICS OF THE SYSTEM Fe-Mn-S

THE CONSTITUTION AND KINETICS OF THE SYSTEM Fe-Mn-S BETWEEN 1200° AND 1600°C

By

PETER NISBET SMITH, B.Eng., M.Eng.

A Thesis

Submitted to the School of Graduate Studies

in Partial Fulfilment of the Requirements

for the Degree

Doctor of Philosophy

McMaster University

October 1970

DOCTOR OF PHILOSOPHY (1970)
(Metallurgy)

McMASTER UNIVERSITY
Hamilton, Ontario

TITLE: The Constitution and Kinetics of the System Fe-Mn-S Between 1200° and 1600°C.

AUTHOR: Peter Nisbet Smith, B.Eng. (McMaster University)
M.Eng. (McMaster University)

SUPERVISOR: Professor J.S. Kirkaldy

NUMBER OF PAGES: (xv); 322

SCOPE AND CONTENTS:

This thesis is concerned with the determination of the constitution of the ternary system Fe-Mn-S in the temperature range 1200° to 1600°C and the establishment of the kinetics of phase transformation (in the form of diffusion coefficients) within the system. Using the results of equilibration experiments and diffusion couple experiments, together with free energy-composition diagrams, a solubility theory based on the Gibbs-Duhem equation, and data from the literature, the Fe-Mn-S phase diagram is constructed and presented as a compendium of isotherms. The significance of the phase diagram, as related to commercial steels, is discussed by investigating both quantitatively and qualitatively the quaternary effect of carbon on the ternary constitution in the region of the melting point of iron. Also discussed is sulfide inclusion formation and transformation during and after solidification.

ACKNOWLEDGMENTS

The author would like to thank his supervisor, Dr. J.S. Kirkaldy, for suggesting the topic of research and for his continuing guidance, encouragement, help, and friendship throughout the many phases of the study. The author is also indebted to many of the faculty, graduate students, and technical staff in the Department of Metallurgy for their helpful discussions and aid, and to his wife for her continuing moral support.

Finally, the author gratefully acknowledges the following groups for their financial support: the National Research Council of Canada, the Ontario Graduate Fellowship Foundation, the Department of Metallurgy and Materials Science (each in the form of graduate fellowships), and the American Iron and Steel Institute (in the form of research grants to Dr. Kirkaldy).

TABLE OF CONTENTS

LIST OF FIGURES

LIST OF TABLES

CHAPTER 1

INTRODUCTION

The purpose of this thesis is to examine the kinetics of transformation between Fe-Mn alloys and the sulphides of Fe and Mn and to establish the boundary conditions for phase transformation through the ternary constitution. Of particular interest is the shape of the liquidus eutectic trough which has a temperature maximum in the iron rich corner of the Fe-Mn-S phase diagram. The location of this maximum controls the path of sulphide segregation during solidification.

During the past few years there has been a noticeable increase of interest in the Fe-Mn-S system. Most of this interest has been centered around studies of the morphology of manganese sulphide (MnS) inclusions in steels and the conditions which affect changes in this morphology.

Interest in the Fe-Mn-S system at McMaster University arose from a problem investigated by Kirkaldy et al[1] in 1963. It concerned the existence of ferrite banding and associated transverse cracking around sulphide stringers in the butt-weld region of steel pipes. A qualitative explanation of banding was offered. Sulphide stringers, presumably rich in iron sulphide (FeS), were supposed to have transformed to Mn rich sulphides by a solid state diffusion process in which the Fe in the sulphides was replaced by Mn from the surrounding austenite. Since Mn decreases the activity of carbon[2], the carbon in the Mn depleted zone diffuses from this zone to regions of higher Mn content. Subsequently upon cooling below the A_3 line the solute depleted austenite zone is the first to transform to

ferrite, while the richer neighboring austenite upon absorbing the rejected carbon transforms into the usual pearlitic structure. The result is alternating bands of ferrite (with MnS stringers) and pearlite. This banding leads to non-uniform mechanical properties which is averred to cause the observed cracking.

Unfortunately, this investigation and others like it have been carried out without an adequate knowledge of the equilibrium constitution of the system. To date, information concerning the constitution of the Fe-Mn-S system has been for the most part derived from work performed by researchers during the 1930's, and is very incomplete. The equilibrium phase relationships as a function of temperature, and the kinetics of approach to equilibrium between phases are not at all well-established. Quantitative analysis of technological processes like those described above is difficult, if not impossible, in the absence of this basic information.

With a view to providing such information this thesis concerns itself with a critical analysis of earlier data, extension of the earlier work to a wider range of temperatures and compositions in the Fe-Mn-S system, and the accumulation of data relative to a discussion of transformation kinetics.

CHAPTER II

REVIEW OF THE LITERATURE ON THE Fe-Mn-S SYSTEM

A. THE IRON-MANGANESE BINARY SYSTEM

The equilibrium diagram for Fe-Mn as reported in Smithells[3] and Hansen[4] has recently been redetermined by Hume-Rothery[5,6]. This recent result is illustrated in Figure 2.1. The experimental method involved a carefully controlled thermal analysis using 99.9% purity Fe and Mn alloys in a cooling-curve furnace with an argon and hydrogen atmosphere. Under these experimental conditions the loss of manganese due to evaporation was negligible.

The phase system is of the open γ-field type with a continuous series of solid solutions extending from γ-Fe to γ-Mn. The δ-γ reaction on the Fe-rich side is a peritectic reaction which occurs at 1472°C and is quantitatively described as

$$\delta\text{-Fe (9.6 at \% Mn)} + \text{Liquid (13 at \% Mn)} \rightleftarrows \delta\text{-Fe (10.2 at \% Mn)}$$

The earlier reaction temperature given in Hansen is 1504°C and has a δ-Fe solubility limit of only 1.0 at % Mn. The L + γ phase field is now a narrower field which extends across to the Mn-rich side.

On the Mn-rich side of the diagram Hansen reports that the solidification reaction is a peritectic reaction occurring at about 1240°C. However the more recent data of Hume-Rothery indicates that the reaction is a eutectic reaction occurring at 1232°C. Quantitatively the reaction is

$$\delta\text{-Mn (12 at \% Fe)} + \gamma\text{-Mn (13 at \% Fe)} \rightleftarrows \text{Liquid } (\sim 13 \text{ at \% Fe})$$

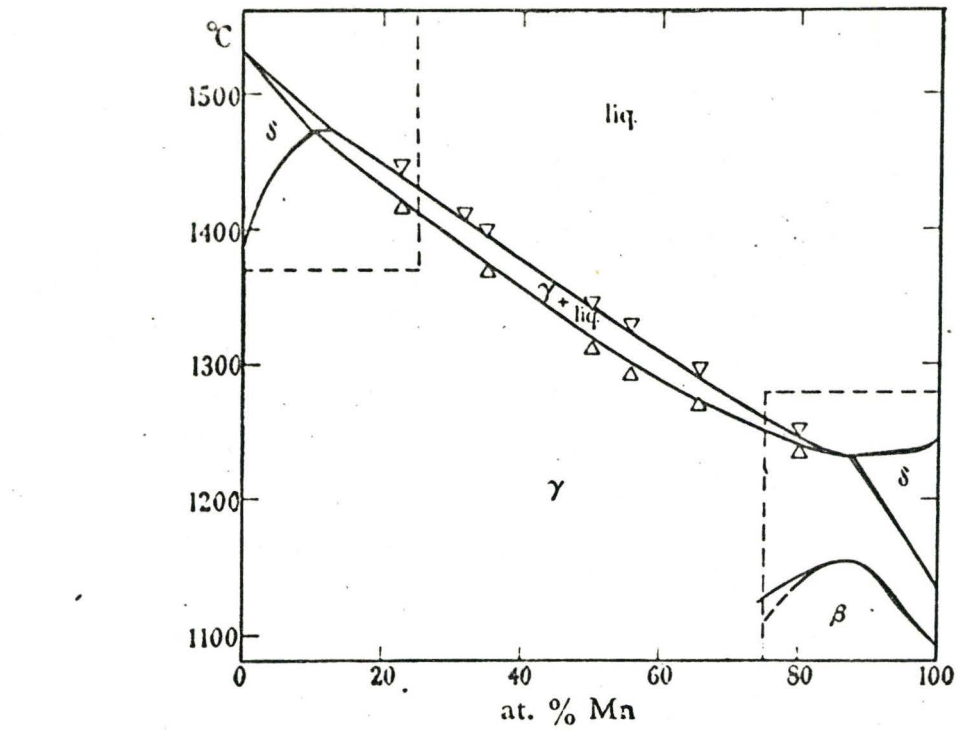

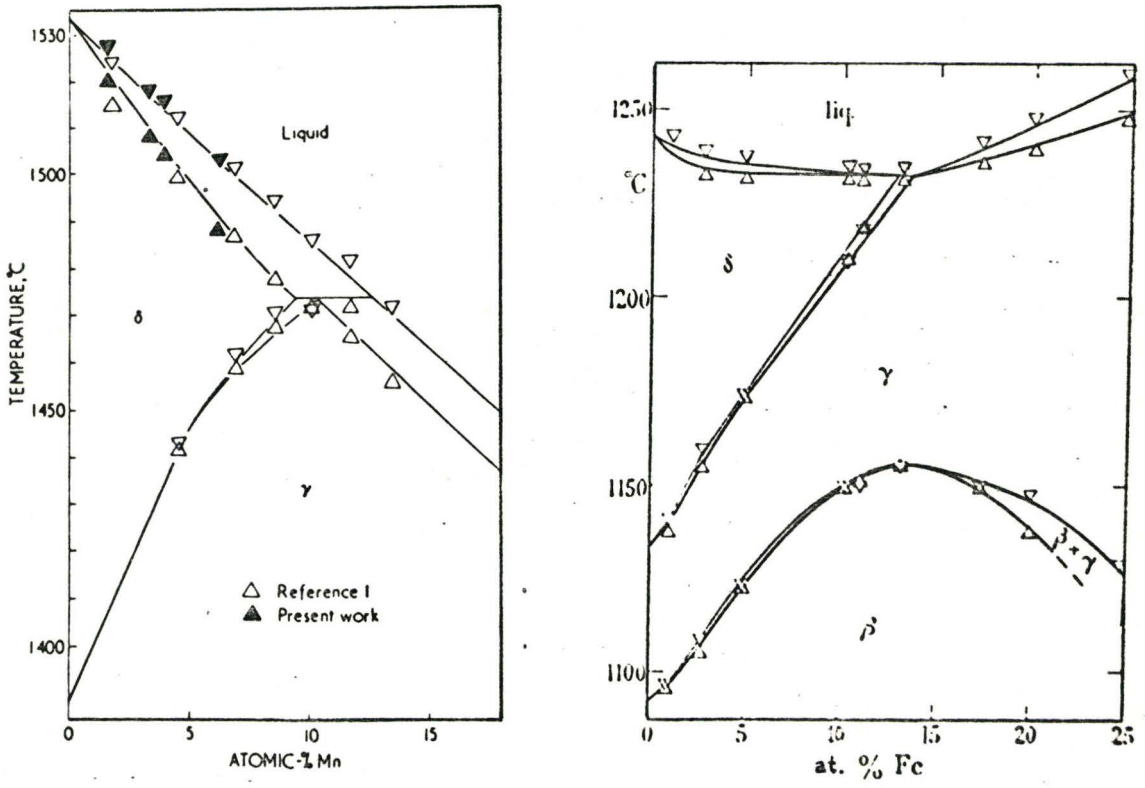

Figure 2.1 The Fe-Mn binary phase diagram after Hume-Rothery[5,6]

The near equality of the solubility limits, the consequent narrowness of the phase regions, and the experimental error involved in determining the diagram encouraged Hume-Rothery to remark that

> "It seems probable that the minimum at 1232°C is a eutectic point at which the solid phases are the δMn solid solution and the γ-phase whose composition is almost exactly the same as that of the liquid, but the possibility of a peritectic horizontal with a minimum in the freezing point curve on the iron-rich side cannot be entirely disproved."

This text will accordingly assume that this reaction is a eutectic reaction in subsequent discussions.

B. THE IRON-SULPHUR BINARY SYSTEM

The recent literature indicates that the iron-sulphur (Fe-S) phase diagram has not changed substantially from that reported earlier by Hansen[4]. This diagram is reproduced in Figure 2.2a for the composition range 0 to 55 at % S. The most important characteristic of this system in the high S region is the existence of a eutectic at 44 at % S (31 wt % S) at 988°C. This gives an indication of the large effect that a small amount of S can have on ferrous alloys, since at any temperature above 988°C only traces of S introduce a liquid phase into the alloy.

At 50 at % S, iron and sulphur exist as the compound FeS. However, FeS is not stoichiometric but exists over a range of S compositions. Recently, Burgman et al[7] presented a comprehensive study on FeS. They found that FeS_X (where $X = N_S/N_{Fe}$) has a maximum melting point at 1188°C for X = 1.09, and that the composition range exists from X = 1 to a maximum of X = 1.27 (56 at % S) at 1070°C. This latter data point is extrapolated from their Fe-S phase diagram reproduced in Figure 2.3.

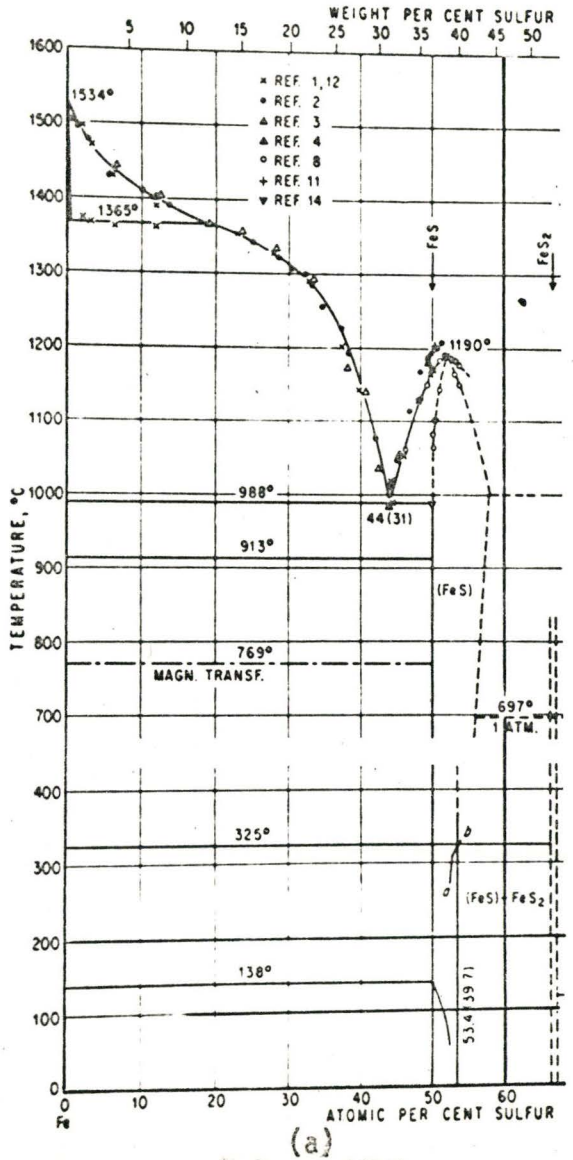

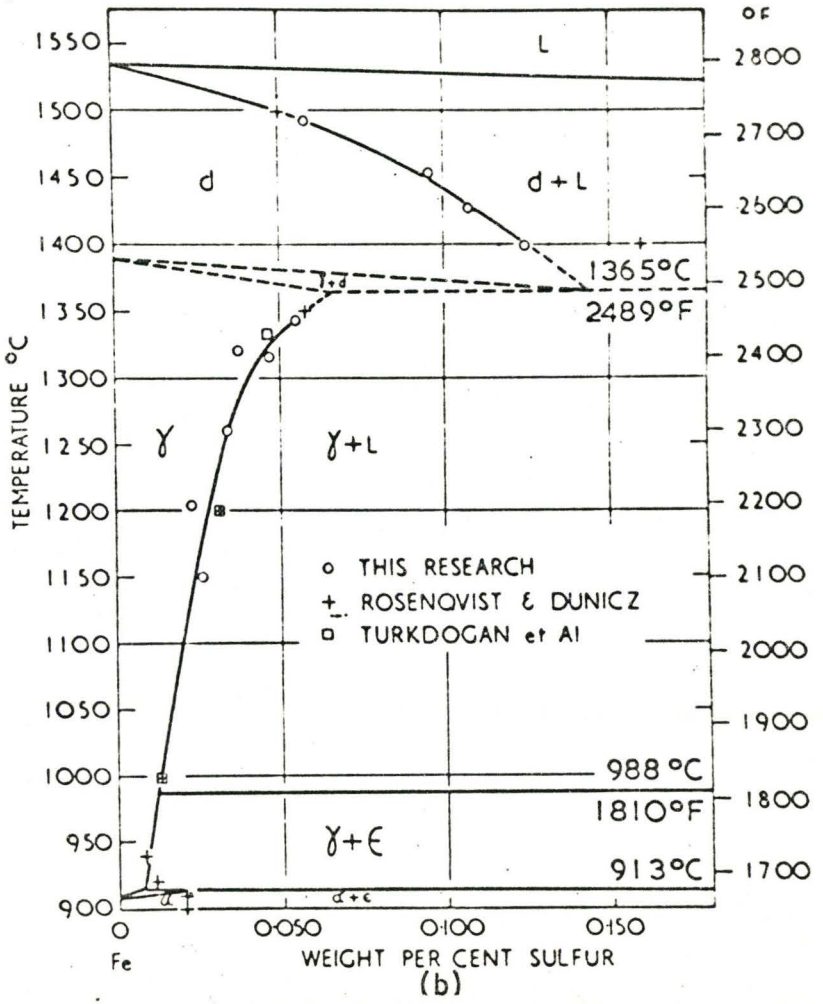

Figure 2.2 The Fe-S binary phase diagram, (a) after Hansen[4], (b) after Barloga et al[10].

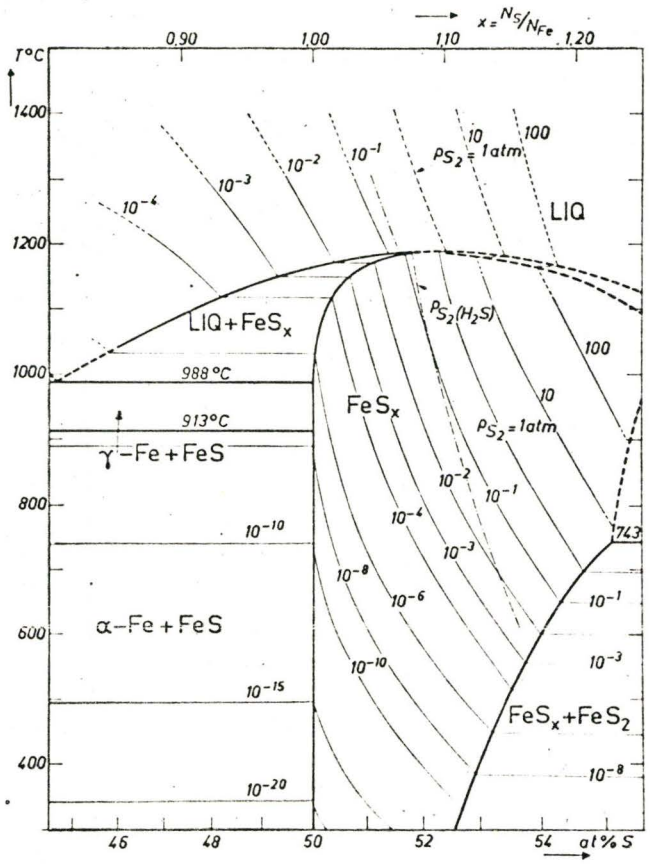

Figure 2.3 The solubility of S in iron sulphide after Burgman et al[7].

The Fe-FeS phase diagram shown in Figure 2.2a does not adequately illustrate the phase relations for sulphur contents less than 0.4 at % S. This latter region of the phase diagram is shown in Figure 2.2b. It is in this region that recent data has led to slight changes in the earlier phase diagram reported by Hansen.

Rosenqvist and Dunicz[8] carried out the early work on the solubility of S in α, γ, and δ-Fe by equilibrating Fe in H_2/H_2S atmospheres. Turdogan et al[9] more recently presented their results based on similar methods and are in good agreement with Rosenqvist and Dunicz for the solubility of S in γ-Fe. It was these results which Hansen used to compile the phase diagram in the low S region. The later work of Barloga et al[10] leads to only slight changes in the phase diagram. Rosenqvist and Dunicz first reported the position of the 'extectic' point at 1365°C and 0.18 wt % S (0.31 at % S)*. Barloga et al found that the solubility of S in δ-Fe is not as great as previously reported. They suggest that the 'extectic' point is closer to 0.14 wt % S (0.24 at % S) at 1365°C. The extectic reaction may be described as

$$\delta\text{-Fe (0.24 at \% S)} \rightleftarrows \gamma\text{-Fe (0.047 at \% S)} + \text{Liquid (19 at \% S)}$$

In this the data of Barloga et al is assumed to be the most reliable. Using a technique involving the equilibration of S and Fe in evacuated silica tubes, they were able to determine several solubility values at one temperature and use the average. This was carried out at four temperatures in the δ-Fe range. In contradistinction, the points of

* It should be pointed out that the phase relations shown in Figure 2.2b are very rare in metallic systems and as yet have not been officially named. The term 'extectic' has been coined by Barloga et al for this unusual reaction.

Rosenqvist and Dunicz represent only one determination per temperature setting.

Both Rosenqvist and Dunicz, and Barloga et al determined the position of the 'extectic'horizontal by applying the van't Hoff equation

$$\Delta T = \frac{RT_{tr}^2 \, \Delta[S]}{\Delta H_{tr} \quad 100} \qquad (2\text{-}1)$$

to the γ-δ transformation. In this ΔT is the depression of the γ-δ transformation temperature. This equation is valid for dilute solutions and relatively small values of ΔT. The heat of transformation, ΔH_{tr}, according to Olander[11] is 280 cal. The temperature of transformation, T_{tr}, is 1400°C. $\Delta[S]$ is the difference in S content of the two co-existing phases in at % S. Both Rosenqvist and Dunicz and Barloga et al determined ΔT to be close to 35°C. Because the value of $\Delta[S]$ incorporates a significant error, the quoted 'extectic' value of 1365°C must be regarded as accurate only to within $\pm$ 10°C, and according to Barloga et al

> "the exact position of the extectic cannot be regarded as fixed."

C. THE MANGANESE-SULPHUR BINARY SYSTEM

Of the binary systems to be discussed, the Mn-S system is the least well-defined quantitatively. The only systematic study was done by Vogel and Hotop[12] in 1937. They performed thermal arrest experiments on manganese-sulphur mixtures from 0 to 50 at % S in alumina and graphite crucibles. The phase diagram they determined is reproduced in Figure 2.4. The significant aspect of this system is the existence of a large liquid-liquid immiscibility region which is part of a monotectic reaction occurring

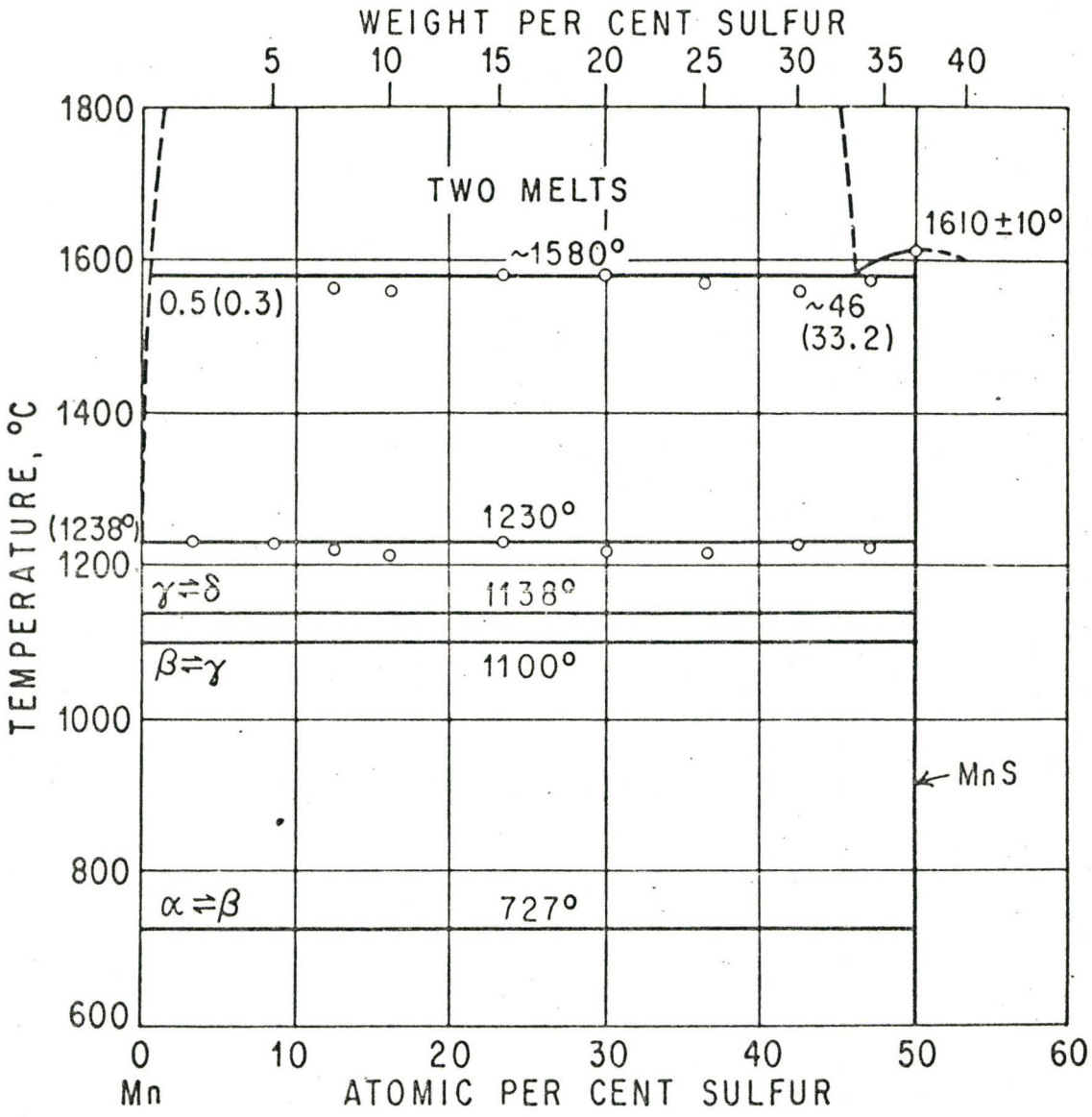

Figure 2.4 The Mn-S binary phase diagram after Vogel and Hotop[12].

at 1580°C. The reaction is described by

Liquid II (33.5 wt % S) $\rightleftarrows$ Liquid I (0.3 wt % S) + MnS (36.85 wt % S)

Though as yet undetermined, the miscibility gap appears to extend to a critical point at temperatures as high as 1900 to 2000°C. The effect of this miscibility gap on the ternary Fe-Mn-S system will be seen to be very significant.

Another important reaction in this system is the eutectic reaction at 1230°C. This is described by

Liquid I $\rightleftarrows$ γ-Mn + MnS (36.85 wt % S)

The S solubilities of the liquid and γ-Mn phases in this reaction are not known. From Figure 2.4 we can infer, however, that the S content in both Liquid I and γ-Mn is defined by the following inequality

$$S_{\gamma\text{-Mn}} < S_{\text{Liquid-I}} < 0.3 \text{ wt \% S}$$

From Figure 2.4 it is to be noted that MnS has been specified as stoichiometric. Of course a phase field must exist in which the MnS has a formula of the form MnS_X where $X = N_S/N_{Mn}$. However, there is no data on the variation of X; it is not even known whether X is greater or less than unity. Nakao[13] suggests that MnS, like FeS, is a metal deficit sulphide and may exist up to 52 at % S (X = 1.08), but his result is not reliable. On the other hand Le Pot and Quan[14] found that MnS might be sulphur deficit, in which case X may be less than unity.

There is considerable disagreement in the literature concerning the melting point of stoichiometric MnS. Several authors locate it in the region of 1600°C. Shibata[15] determined a value of 1610 $\pm$ 3°C whereas Rohl[16] in 1923 determined a value of 1620°C. Oelsen, in private communication with Vogel and Hotop, reported a value of 1600°C. Vogel

and Hotop also determined it to be 1600 ± 10°C. In each case the melting point was determined by thermal arrest experiments using calibrated thermocouples. On the other hand Silverman et al[17] in 1943 reported the melting point to be 1530°C, and this was verified by Coughlin[18] in 1950 while determining the heat content of MnS up to the melting point. The reference of Silverman et al is a tabulation of some physical data published in a bulletin from the U.S. National Research Council. Their reference for the melting point of MnS dates back to a report by Glaser[19] in 1926.

The discrepancy of between 70 and 90°C appears at first sight to be unaccountable. Vogel states that his thermocouple was calibrated before each run although he does not state how it was calibrated or what type of thermocouple was used. However the consistency of his results, plus his agreement with three other investigators is hard to refute. He at the same time determined the melting point of manganese to be 1238°C which is close to, but lower than, the present day value of 1244°C. Also the seven points he has reported for his monotectic reaction temperature vary within only 10°C of his stated average value of 1580°C, which indicates good reproducibility of his temperature measurements.

We are therefore strongly inclined to accept a melting temperature, ca. 1600°C, and this is so indicated in Figure 2.4.

D. THE IRON SULPHIDE-MANGANESE SULPHIDE PSEUDO-BINARY SYSTEM

S contents higher than 50 at % S are not particularly important in the Fe-Mn-S system since such compositions are rarely encountered in practice. It has therefore been considered sufficient to choose the upper

limit for the studies of the ternary system as 50 at % S where the compound FeS is formed on the Fe-S binary and the compound MnS is formed on the Mn-S binary. This termination is represented by a plane in the Fe-Mn-S system parallel to the temperature axis between stoichiometric FeS and stoichiometric MnS. It was hoped that the resultant boundary could be described by a pseudo-binary FeS-MnS section.

The equilibrium phase diagram of this supposed pseudo-binary system was first investigated by Shibata[15] in 1928 using thermal analytic and micrographic methods. His results (fig.2.5) indicated that the FeS-MnS System could in fact be described as a simple binary eutectic reaction, the eutectic occurring at 1164^{o}C and described by

Liquid (6.5 wt % MnS) $\rightleftarrows$ FeS (2 wt % MnS) + MnS (25 wt % MnS)

He determined FeS to have a melting point of 1173 $\pm$ 2^{o}C and MnS to have a melting point of 1610 $\pm$ 3^{o}C.

In a more recent study by Van Vlack et al[20] some sections of the diagram were redetermined using micrographic and microhardness methods. He found the eutectic reaction to occur at 1181^{o}C and to be represented by

Liquid (6 wt % MnS) $\rightleftarrows$ FeS (2 wt % MnS) + MnS (28 wt % MnS)

One notes particularly that the eutectic temperature found by Van Vlack is 8^{o}C higher than the melting point of FeS accepted by Shibata. This could indicate that the equilibrium reaction is peritectic rather than eutectic. Shibata pointed out that different authors have given different values of the melting point of FeS. Nornemann[21], Priltz[22], and Rohl[16] gave 1194^{o}, 1197 $\pm$ 2^{o}, and 1188^{o}C, respectively, whereas Friendlich[23] and Allen et al[24] gave 1171^{o} and 1170 $\pm$ 5^{o}C, respectively. The latter group agrees with Shibata's measurement while the former group

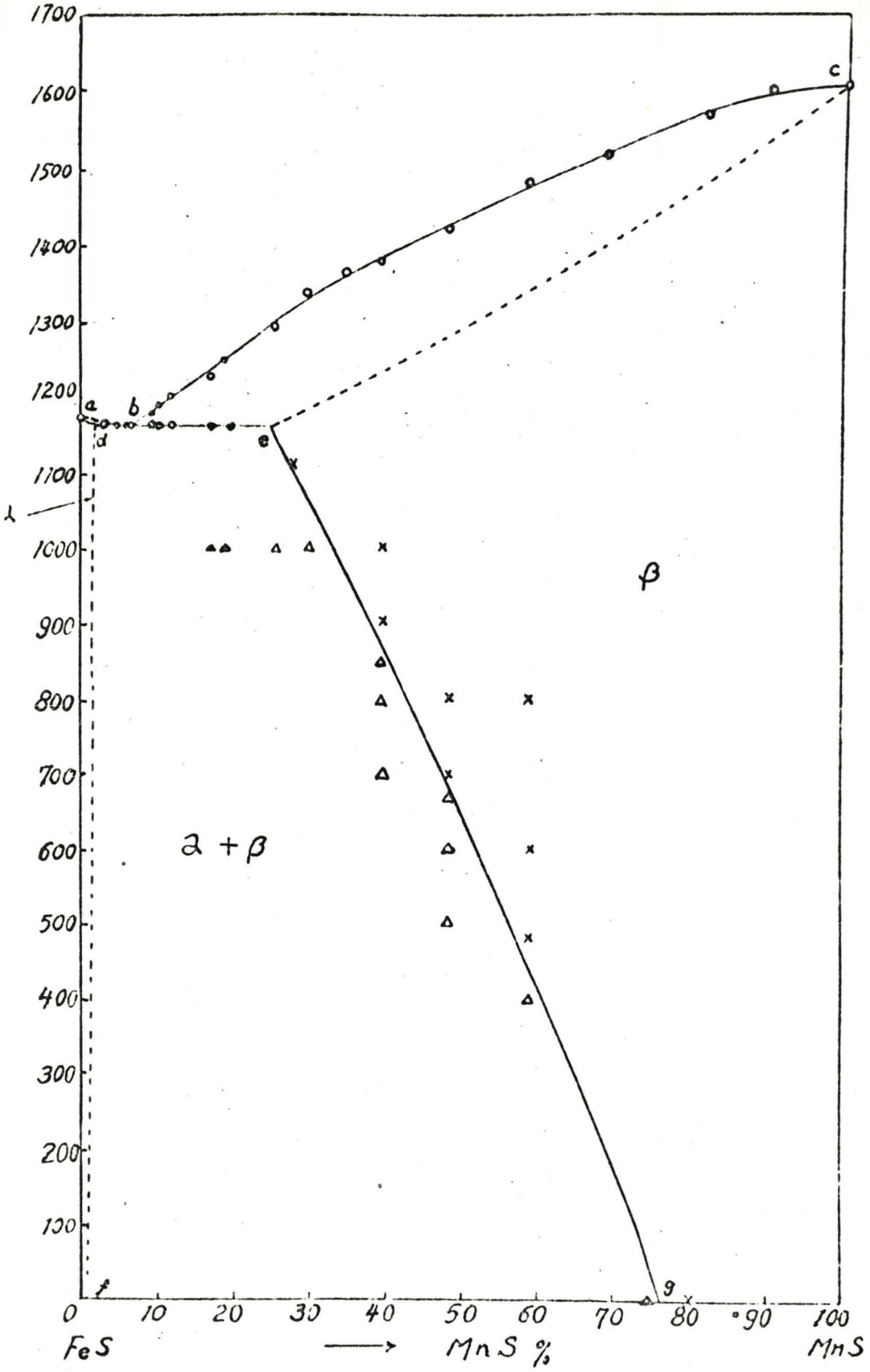

Figure 2.5 The FeS-MnS pseudo-binary phase diagram after Shibata[15].

supports a value of 1190°C, accepted by Van Vlack and apparently quoted from Hansen. This latter value is close to the most recent and precise value of 1188°C given by Burgman et al which was previously quoted.

Alternatively, this difference might imply that Shibata's thermocouple read low by 17°C. However he cites that it had been "certified at the Deutsche-Physikalische-Technische Reichsanstat", and one cannot overlook the fact that two other investigators agree with Shibata. As we shall see the explanation of the discrepancy lies in the incorrect concept of an FeS-MnS pseudo-binary.

In the Fe-S diagram, Figure 2.2a, one can see that the compound FeS exists over a range of sulphur contents. Thus the formula for iron sulphide should be written as FeS_X where $1 \leq X \leq 1.27$. The highest melting point of iron sulphide occurs at 1188°C at a composition of 52.2 at % S ($FeS_{1.09}$). This temperature agrees well with that proposed by Van Vlack and others. However the melting point of FeS (X = 1) begins near 1100° and ends near 1170°C which agrees with the Shibata value. Thus the observed discrepancies in the melting point of iron sulphide and the eutectic temperature can be attributed to small differences in the composition of FeS used in the experiments of Shibata and Van Vlack, respectively. From this it would appear likely that an equilibrium diagram of the eutectic type can rationalize the observed transitions at two different temperatures.

This discussion raises the question as to whether or not the FeS-MnS system can be regarded as a pseudo-binary according to the usual definition. This can best be answered by examining a qualitative ternary isotherm at a temperature just below the FeS-MnS eutectic, say at 1170°C,

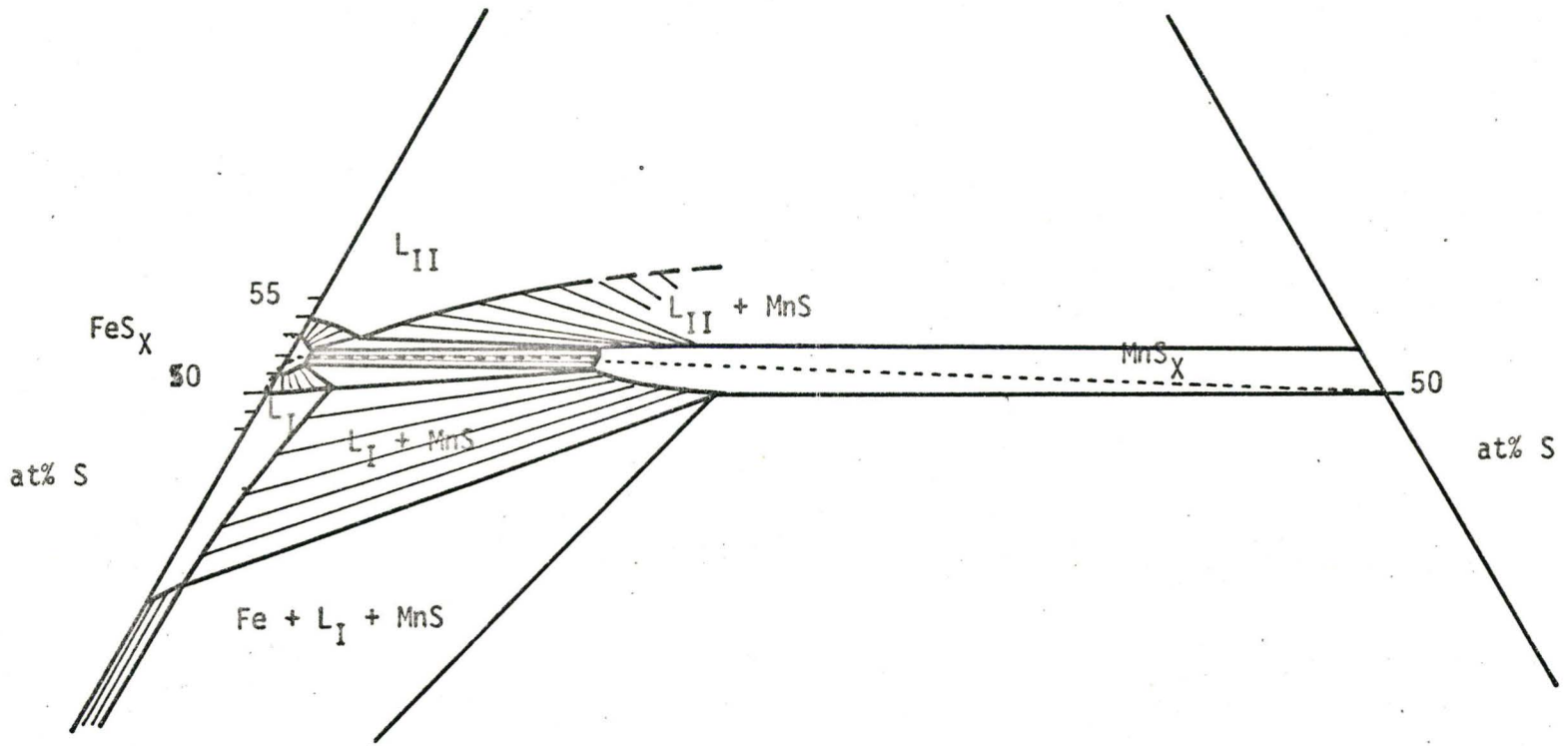

Figure 2.6 The pseudo-binary region of the 1170°C isotherm in the Fe-Mn-S system.

where the liquidus of the Fe-S binary system intersects the stoichiometric composition (50 at % S). Such an isotherm is constructed in Figure 2.6 from binary data and some pre-knowledge of our own work. From this one can see that a pseudo-binary drawn as a plane perpendicular to the isotherm at 50 at % S is incorrect. In fact, pseudo-binary planes, which must lie parallel to the tie-lines in the (FeS + MnS) field, can only be accommodated by a very special paired set of non-stoichiometric FeS_x-MnS_x compositions. A more detailed analysis of this situation can be found in Chapter VII.

Even though there is doubt as to the existence of a true pseudo-binary lying along the 50 at % S line, in the remainder of the text we will use the nominal figure 50 at % S to represent the set of true pseudo-binaries lying in the near vicinity of this composition, and it will be assumed in agreement with Van Vlack and Shibata that the section is of the eutectic type shown in Figure 2.6

E. IRON-MANGANESE-SULPHUR TERNARY SYSTEM

E.1. Early Studies of the Liquid State Constitution

The earliest constitution diagrams are very noticeably based on studies performed in Germany during the pre-war era. The resurgence of Germany industry during the 1930's prompted a parallel research effort, particularly as related to the iron and steel industry. Part of the research was aimed at finding methods of efficiently producing low sulphur-bearing steels, a task somewhat more difficult than in North America because of the higher sulphur contents found in European raw materials.

Qualitatively aware that manganese was of importance in desulphurization, significant effort was put into amassing a quantitative picture of its effect. A number of authors published lengthy papers devoted to the constitutional and thermodynamic analysis of the Fe-Mn-S system. Because the desulphurization process is carried out predominantly in the liquid state the research was focussed on the constitution and thermodynamics at temperatures around 1600°C. However some studies were also carried out at lower temperatures.

Subsequent to the war little work has been published, although in the past ten years a few researchers have become interested in this system.

E.1.1. The 1600°C Isotherm of Vogel and Baur

The first systematic study of the Fe-Mn-S system was carried out in 1933 by Vogel and Baur[25]. Their report says little about the experimental methods used, but it is inferred that their phase diagram was derived by differential thermal analytic methods in which liquid Fe alloys containing up to 35 wt % Mn and 30 wt % S were slowly cooled in 'pythagorus' (mullite) crucibles to temperatures below 300°C under a nitrogen atmosphere. The results of their experiments are a series of five plots of temperature versus wt % Fe, each plot at a different Fe/Mn ratio (isocomposition plots), and one plot of temperature versus wt % Fe at a constant Fe/S ratio. From these plots Vogel and Baur were able to reach some conclusions about the equilibrium of phases and to construct a model of the liquidus surface for the ternary system. This is illustrated in Figure 2.7.

Their results deviate significantly from the data published later. Because the experimental technique was not explained, it is impossible to adequately judge their results. Possibly the pythagorus crucibles reacted with their melts or perhaps the sampling and chemical analysis techniques were faulty. This study has been considered grossly incorrect by subsequent investigators.

E.1.2. The 1600°C Isotherm of Meyer and Schulte

In 1934 Meyer and Schulte[26] examined the equilibrium between the liquid metal and the sulphide slag phases in the Fe-Mn-S system. In their experiments the concentrations of the metal and slag phases were governed by equivalent weights according to equations 2-2 and 2-3, viz.,

$$[FeS] + [Mn] = [MnS] + [Fe] \qquad (2\text{-}2)$$

and

$$(FeS) + (Mn) = (MnS) + (Fe) \qquad (2\text{-}3)$$

The relationship for equilibrium between the metal and slag was obtained by substituting the distribution coefficients $L_{MnS} = (MnS)/[MnS]$ and $L_{FeS} = (FeS)/[FeS]$ into the expression for theequilibrium constant for reaction (2-2), viz.,

$$K_B^* = \frac{[FeS]\,[Mn]}{[MnS]\,[Fe]} = \frac{(FeS)\,L_{MnS}\,[Mn]}{(MnS)\,L_{FeS}\,[Fe]} \qquad (2\text{-}4)$$

Though Meyer and Schulte do not explicitly state that the L's are constant, they seem to have assumed this.

---

* The B in K_B stands for "Badreaktion", a German word for the metal bath reaction. The convention is used that [ ] stand for metal and ( ) for slag concentrations.

They rearranged equation 2-4, defining a new constant K_{MnS} as

$$K_{MnS} = K_B \frac{L_{FeS}}{L_{MnS}} = \frac{(FeS)\ [Mn]}{(MnS)\ [Fe]} \qquad (2\text{-}5)$$

They assume that all the Fe and Mn in the slag is tied up with the appropriate amount of S (equivalent weights), and then write (FeS) and (MnS) as (Fe) and (Mn), respectively, which they call the 'total iron' and 'total manganese'. Equation 2-5 then becomes

$$K_1 = \frac{(Fe)\ [Mn]}{(Mn)\ [Fe]} \qquad (2\text{-}6)$$

Meyer and Schulte also empirically identified a constant

$$K_2 = \frac{[S]\ \ [Mn]}{(S)\ \ [Fe]} \qquad (2\text{-}7)$$

where [S] and (S) represent the total sulphur in the metal and slag, respectively.

To determine K_1 and K_2 Meyer and Schulte performed carefully controlled experiments in which Fe-Mn-S alloys were equilibrated at 1600 $\pm$ 8°C in sintered alumina crucibles for 5 to 20 minutes in a nitrogen and hydrogen atmosphere. Each quenched sample was analysed for total Fe, Mn, and S in the slag and metal phases. The temperature was measured by an optical pyrometer (calibrated against a tungsten filament at the 'Physikalisch-Technischen Reichsanstalt'). The pyrometer was also compared with a calibrated thermocouple before each run. Their results fit very well to two curves defined by equations 2-6 and 2-7 in which (Fe)/(Mn) and [S]/(S) are plotted against [Mn] [Fe], and from which

$K_1 = 0.00425 \pm 0.00125$

$K_2 = 0.000725 \pm 0.000175$

Their results also showed that the solubility product [Mn] [S] has an average value of 2.6. They further examined the effect of adding carbon and silicon to the system and found that these additions in general, changed only K_2, and from their results they attributed this change to the fact that the product [Mn] [S] changed. In particular carbon lowered this constant, and silicon increased it. This product, of course, defines the solubility limits of the miscibility gap in the iron corner of the diagram. Lowering the constant has the effect of pushing the miscibility gap deeper into the iron corner, while raising the value of the constant pulls the gap out of the corner.

Meyer and Schulte did not report their data in the form of an isotherm at 1600°C. But from their data one is able to do so, and this is shown in Figures 2.7 and 2.8 with Vogel and Baur's data superimposed upon it for comparison. The striking difference between the two, other than the size of the miscibility gap, is the direction of the tie-lines within the gap. Practically this has great significance, for Meyer and Schulte's diagram implies that desulphurization towards the slag by phase separation is very efficient. In contradistinction, Vogel and Baur's diagram implies that the metal phase in equilibrium with a slag phase will be iron deficit, while the slag will have a high concentration of iron.

Meyer and Schulte's data for Mn and S solubilities in liquid Fe at 1600°C have also been plotted in Figure 2.14 as wt % Mn versus wt % S. It should be pointed out that of the 33 slag-metal equilibrium experiments

they performed, 17 showed a considerable amount of oxide in the slag phase (mostly as Al_2O_3 from the slag-crucible reaction). Also the $1600^o \pm 8^oC$ their report is misleading because their detailed data shows that the equilibrium temperatures varied from 1580^o to 1635^oC.

E.1.3. Wentrup's Analysis of Meyer and Schulte's Data

In 1935 H. Wentrup[27], while visiting at Carnegie Institute of Technology, wrote a review paper, "Desulphurization of Pig Iron and the General Laws of Desulphurization of Iron". His review discounted the work of Vogel and Baur for the reasons previously cited. His major contribution in this review was a re-analysis of the theory and data of Meyer and Schulte. Wentrup took exception to the latter's definition and use of the 'total iron, manganese, and sulphur contents' in the slag, and so using equations 2-2 and 2-3 and the equilibrium and distribution constants he developed his own semi-empirical relationships. His results, though written in terms of the total S, Fe, and Mn contents in the slag and metal, were derived by a procedure based on the metal tied up as a stoichiometric sulphide and the metal dissolved in the sulphide. His resultant empirical expression is

$$\frac{(S)}{[S]} = L_{FeS} + \frac{L_{FeS}\,[Mn]}{K_S\,[Fe]} = 3.6 + 1010\,\frac{[Mn]}{[Fe]} \qquad (2\text{-}8)$$

where L_{FeS} is a distribution coefficient for FeS in the slag and metal, and K_S is a special equilibrium constant defined within Wentrup's derivation. The numerical values are based on the data of Meyer and Schulte after appropriate corrections. Equation 2-8 may be compared with that developed

by Meyer and Schulte, viz.,

$$\frac{(S)}{[S]} = \frac{1}{K_2}\frac{[Mn]}{[Fe]} = 1400\ \frac{[Mn]}{[Fe]} \qquad (2\text{-}9)$$

The difference lies in the fact that the slope in Wentrup's equation 2-8 is about 30% less than Meyer and Schulte's thus producing a weaker variability between (S)/[S] and [Mn]/[Fe]. Also, Wentrup's equation contains a small intercept.

To show another interesting consequence of equation 2-8 we have multiplied both sides of equation 2-8 by [S]. After rearranging we get

$$[Mn]\,[S] = \{(S) - 3.6\ [S]\}\ \frac{[Fe]}{1010} \qquad (2\text{-}10)$$

Now if one considers concentrations of the metal where [S] is small, so that [S] << (S), and that [Fe] → 1, then

$$[Mn]\,[S] \simeq \frac{(S)}{1010} \qquad (2\text{-}11)$$

which states that the product [Mn] [S] is not a constant as assumed by Meyer and Schulte but depends upon the S content of the slag.

In conclusion, Wentrup comments that according to his equilibrium relations, desulphurization of Fe by Mn alone will not reduce the S contents to those generally found in steel and pig iron. This may be seen by assigning some typical values to equation 2-8. Let Mn = 0.01, Fe = 0.99 (assuming low S). Thus

$$\frac{(S)}{[S]} = 3.6 + 1.01 \times 10^3\ \frac{[0.01]}{[0.99]} = 13.6$$

If the sulphur content of the slag is 30 wt % S, then

$$[S] = 0.30/13.6 = 0.02 \text{ or } 2 \text{ wt \% S.}$$

He avers, however, that the presence of Mn ensures that when the Fe crystallizes and the S separates, it will do so not as liquid FeS but as a solid solution of iron and manganese sulphide. This transformation product, because of its high melting point, does not exercise the same deleterious effects as FeS.

Wentrup's analysis is subject to the usual criticism for having substituted weight percent concentration for the activity in the equilibrium equations. However, this thermodynamic approximation is not too bad since the bath solution does not deviate significantly from ideality. Similarly, though little is known quantitatively about the activities of the slags, it is fairly safe to assume Henrian behavior of small amounts of FeS dissolved in MnS.

E.1.4. The 1600°C Isotherm of Korber and Oelsen

The next study of the Fe-Mn-S system was by F. Korber[28] in 1936 and was directed to a study of the equilibrium between Fe melts and sulphide-silicate slags. He reports that experiments performed by he and Oelsen[29] in 1935 on the Fe-Mn-S system produced results which agreed completely with the 1600°C data of Meyer and Schulte. This data is shown in Figure 2.7 together with the data of Meyer and Schulte, and Vogel and Baur. He also corroborated Meyer and Schulte's result that the critical point, the point at which the ends of the tie-lines in the miscibility gap approach each other, is close to the Fe-FeS side of the

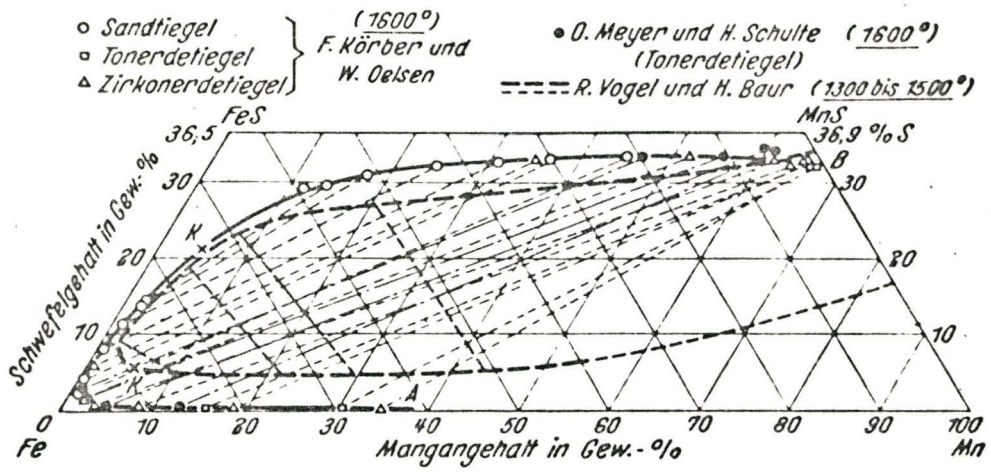

Figure 2.7

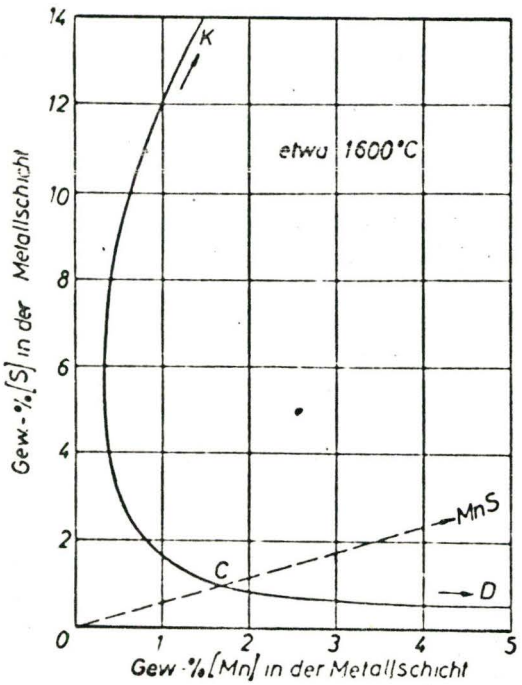

Figure 2.8

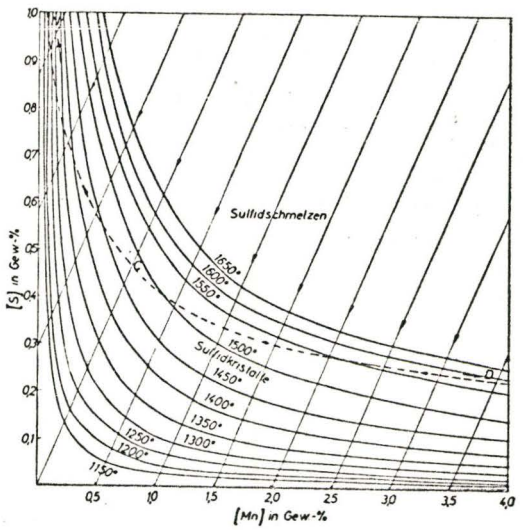

Figure 2.9

Figure 2.7 The 1600°C isotherm in the Fe-Mn-S system after Meyer and Schulte[26], Vogel and Baur[25], and Korber and Oelsen[29].

Figure 2.8 The solubility of Mn and S in liquid Fe at 1600°C drawn by Schurmann and Zellerfeld[31] using the data of Meyer and Schulte[26].

Figure 2.9 The temperature dependence of Mn and S solubility in carbon saturated liquid Fe after Korber and Oelsen[29]

isotherm (5 wt % Mn, 22 wt % S). The addition of Mn to an Fe-S melt results in an endothermic reaction (he noticed a temperature drop of nearly 100^{o}) whereby the liquid separates into two melts. He points out particularly that the direction of the tie-lines in the miscibility gap, when the Mn concentration of the liquid iron is only about 3%, indicates equilibration with a slag extremely rich in MnS.

His conclusions about the efficiency of desulphurization by a sulphide slag are the same as Wentrup's. Mn alone cannot produce a desulphurization typical of the contents desired in steels at $1600^{o}C$ unless an oxide slag of some form is present. However it is possible to reduce the S content to 0.04 to 0.1 wt % S in some cast irons and pig irons with 1 wt % Mn if the temperature is sufficiently low (1200^{o} to $1300^{o}C$). This can be seen in Figure 2.9 which reports Korber and Oelsen's determination of the S and Mn solubilities in carbon saturated liquid iron.

The use of silicon and manganese as a deoxidant produces a SiO_2-MnO slag. When sulphur is also present in the metal the MnO transforms to MnS-MnO and acts as a desulphurizer. However, Korber remarks that although a silicate-sulphide slag is better than a pure sulphide slag, it will not lower the sulphur content of the metal enough to meet steel-making standards.

E.1.5. Wentrup's Interpretation of the Liquidus Surface

H. Wentrup[30], in a second paper, reiterated his comments that manganese does not play a critical role in the desulphurization of industrial steels. He also described how Mn aids in transforming liquid FeS into a

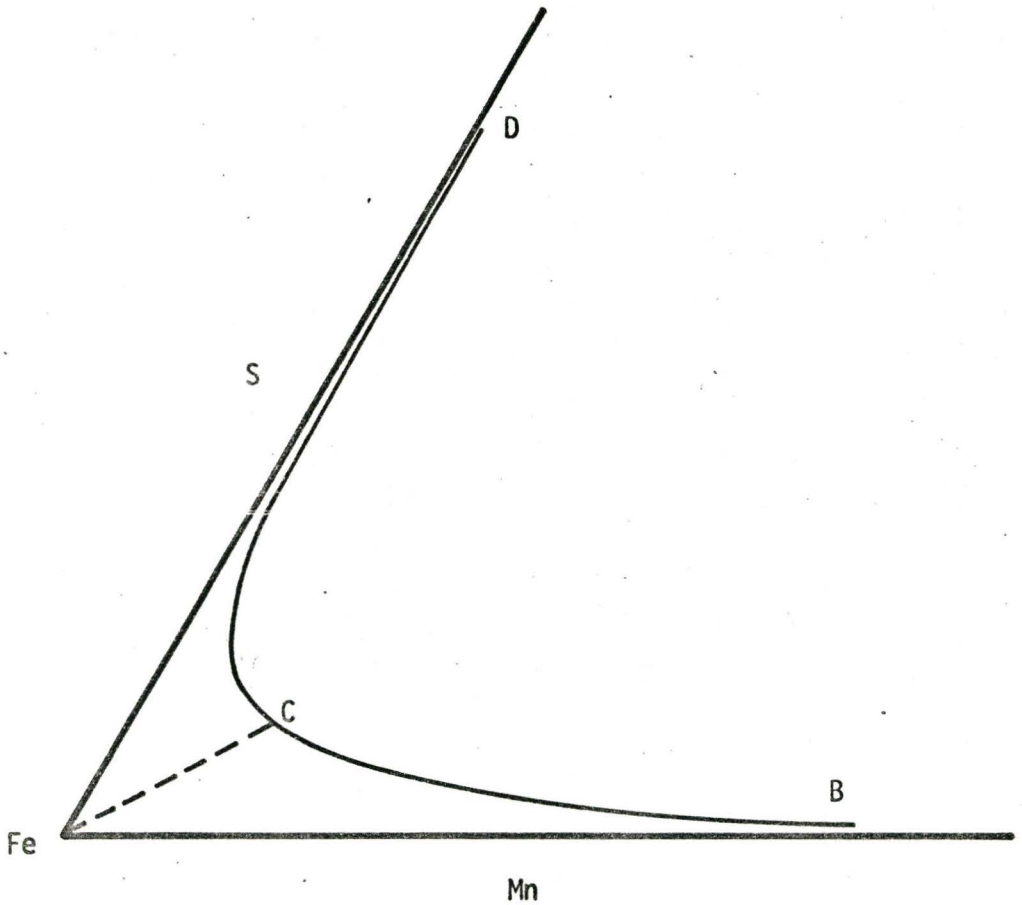

Figure 2.10 Schematic representation of the eutectic trough in the Fe corner of the Fe-Mn-S system.

more acceptable morphology. The following two paragraphs paraphrase a translation of his comments. To follow his discussion one must refer to Figure 2.10 which is a schematic representation of the liquidus surface in the Fe-rich corner of the Fe-Mn-S system.

In the Fe-Mn-S system the precipitation of sulphur as a sulphide will occur by one of two methods depending on which side of the line Fe-C the initial composition is found. Consider a liquid steel composition below and to the right of the line Fe-C. As solid Fe (with dissolved Mn and S) crystallizes, the remaining liquid shifts its composition down a curve representing the loci of end points of tie-lines until this composition reaches the curve CB. The curve CB is the eutectic trough which has a temperature maximum of point C. Once the composition reaches CB one gets a eutectic mixture of solid δ-Fe, solid MnS, and a liquid rich in Fe and Mn. This remaining liquid shifts its composition towards B as the temperature falls until it is spent in the freezing process. The result is an Fe-alloy which has the high melting point MnS phase in an intergranular eutectic structure.

Now consider a composition to the left of the line Fe-C. The initial solidification products are δFe and MnS as before, but the liquid phase in equilibrium with these products, upon reaching the line CD, shifts its composition down the eutectic trough towards D and towards higher sulphur contents. If this liquid persists down to the ternary eutectic point D, one can see that the solidification products will then contain a low melting poing compound rich in FeS. It is this product which produces the deleterious effects in steel manufacture.

From this one can see the technical importance of knowing exactly

where on the eutectic trough is the point of maximum temperature, T_c. For a steel of this simple ternary constitution one should strive to attain initial compositions to the right of the line Fe-C. According to the results of Meyer and Schulte, the addition of carbon to the Fe-Mn-S ternary shifts the miscibility gap, and thus the eutectic trough, deeper into the iron corner. Hence, for carbon steels, a desirable sulfide constitution should be attainable at lower Mn contents.

Also included in Wentrup's paper was a figure depicting his interpretation of the liquidus surface. This is reproduced in Figure 2.11.

E.1.6. The Liquidus Surface of Vogel and Hotop

In 1937 Vogel and Hotop[12] re-examined the Fe-Mn-S system. Their differential thermal analysis techniques were similar to those previously used. They slowly cooled four sets of 20 gm melts and produced cooling curves. The composition of each set of melts consisted of a constant Fe/Mn ratio and varying S content. From the cooling curves they constructed isocomposition plots (wt % S versus constant Fe/Mn). The cooling rate was $1.5^{o}C$/sec (i.e., $900^{o}C$ in 10 minutes). Frequent melt supercooling interfered with their earlier experiments but this difficulty was corrected by seeding the melt surface with iron filings. Chemical analysis of the melts were carried out mainly on the metal phase, but a few were carried out on the sulphide phase.

From their results and existing knowledge of the binary systems they were able to construct the liquidus surface of the Fe-Mn-S ternary system, and this is shown in Figure 2.12. Comparing Figures 2.11 and 2.12 we note

that their surface differs from Wentrup's construction. They argued that the curve representing the limits of the miscibility gap should contain two maxima with respect to temperature, one being in the iron corner, and the other near the MnS corner. Experimentally they were unable to determine the latter maximum temperature, but they supposed it to be close to 1600°C. They deduced from their results that the critical point of the miscibility gap, point K, occurred at 1370°C at a composition of 75% Fe, 4% Mn, and 21% S. Their results also confirmed the limits of the miscibility gap and the tie-line directions at 1600°C, as originally presented by Meyer and Schulte, and Korber and Oelsen and finally concluded that 'the exact extension of the miscibility gap in this system can be considered fixed'. The position of the maximum in the eutectic trough in the iron corner was stated to occur at 1510°C, but the composition was not determined.

From their cooling curve data and photo-micrographs they made some inferences about the phase relations at 1000°C. They found, for example, that the ternary eutectic point is extremely close to the Fe-FeS binary, and, at 1000°C, that the eutectic four-phase equilibrium occurs as

$$\text{S rich liquid} \rightleftarrows \gamma\text{-Fe} + \text{FeS}_{\text{solid}} + \text{MnS}_{\text{solid}}$$

This reaction can be readily predicted from the binary data with the further knowledge that γ-Fe and MnS equilibrate with each other at 1000°C.

Although their quantitative data, particularly for the solid state, is open to criticism because of the fast cooling rates used, their contribution is important because they were able to greatly clarify the shape of the liquidus surface.

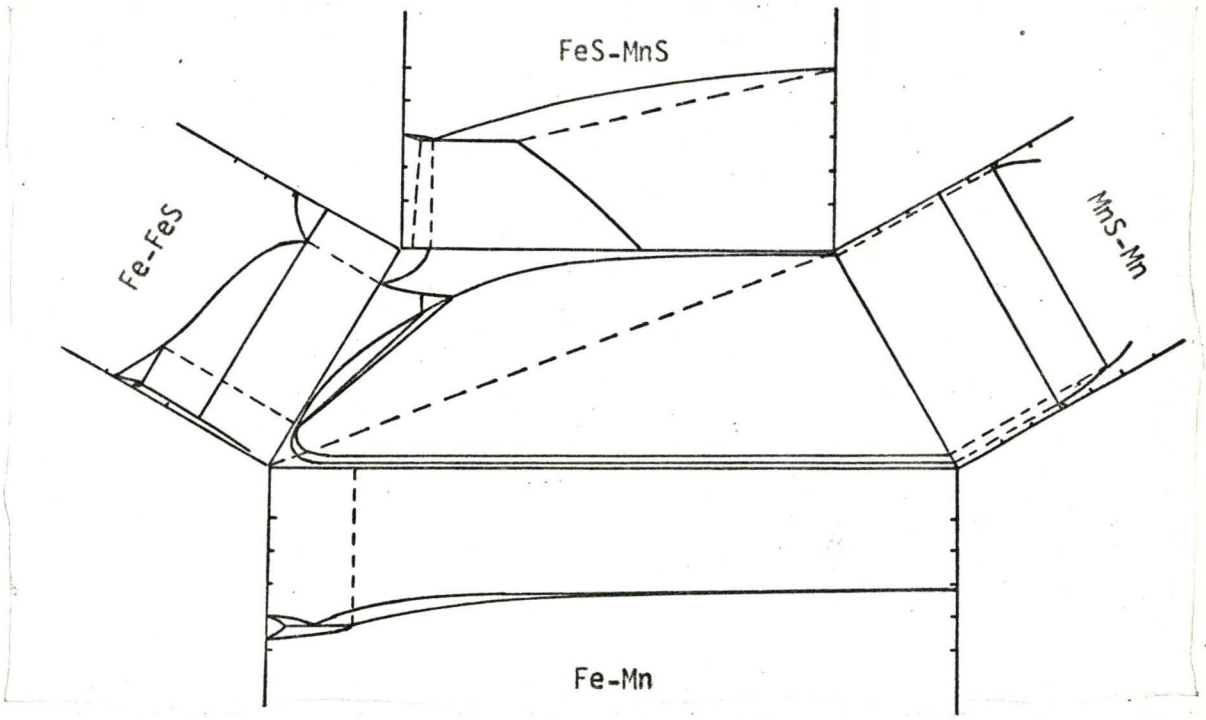

Figure 2.11 The Fe-Mn-S liquidus surface as constructed by Wentrup[30].

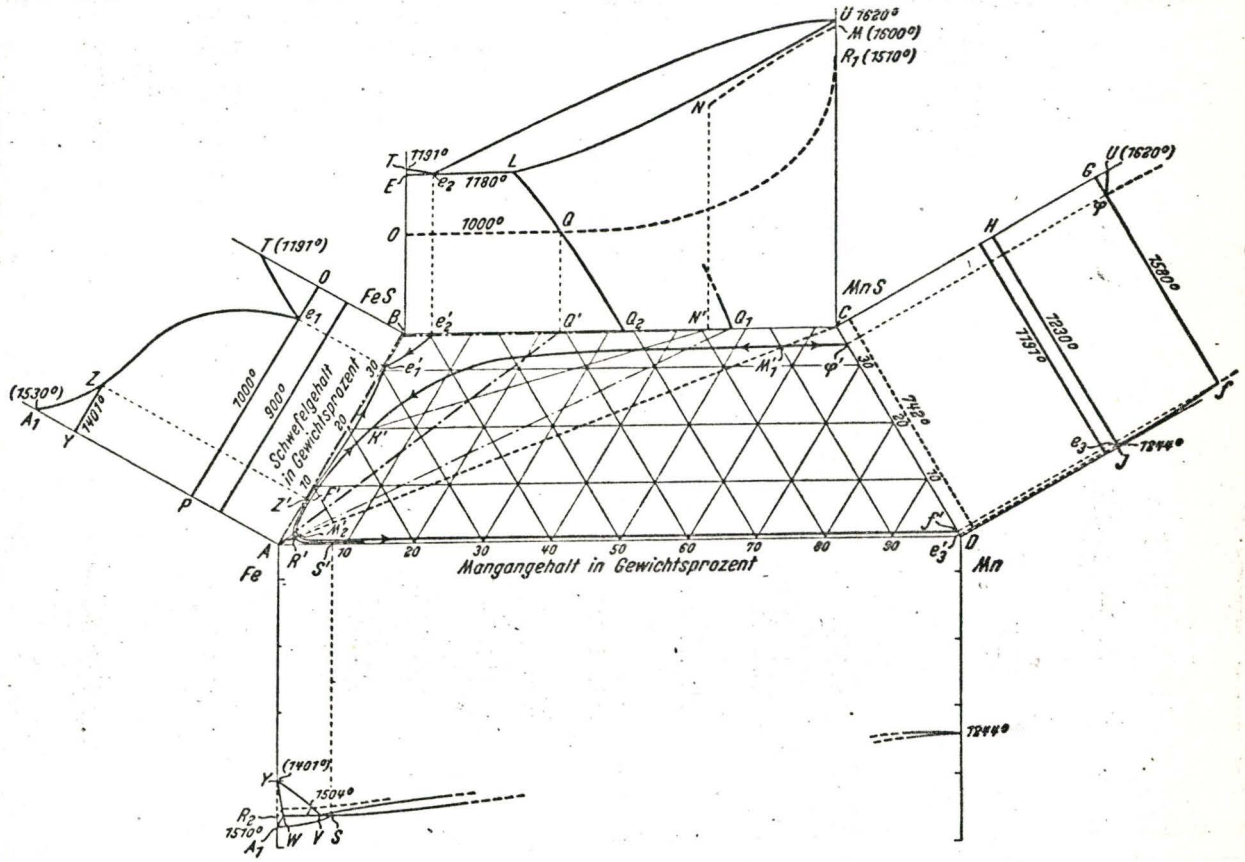

Figure 2.12 The Fe-Mn-S liquidus surface as constructed by Vogel and Hotop[12].

E.1.7. The Fe-MnS Pseudo-Binary Diagram

In 1955 V.E. Schurmann and C. Zellerfeld[31] published a descriptive paper on the 'Desulphurization of Pig Iron', utilizing the available knowledge of the Fe-Mn-S system. They stated that the conclusion of the preceding researchers, to the affect that Mn could not reduce the S contents of steels to industrial limits, applied only to the ternary system. They showed, with the aid of Figure 2.13, that if one can lower the melting point of iron, then a better desulphurization can be attained. Figure 2.13 is a pseudo-binary diagram between the termini of pure Fe and MnS. Upon cooling a melt of composition 'a'; the melt would separate into two liquids, one Fe rich and the other sulphide rich. At a temperature t_1, the sulphide product would become solid and the liquid Fe would become somewhat desulphurized as it progressed to a point (e) which, Schurmann and Zellerfeld agreed, was not low enough for industrial standards. However, if the melting point of iron was lowered from (A) to (A') by the addition of carbon, phosphorus, or silicon, then the transformation temperature t_2 would be lowered to t_3 and (ce) would be extended to (g).

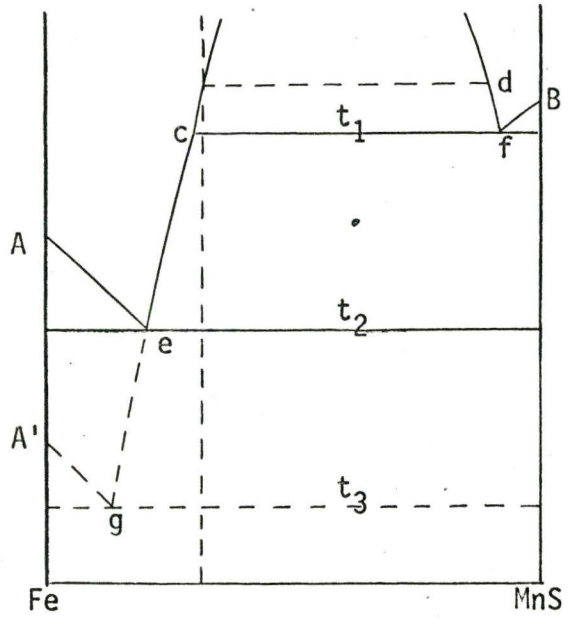

Figure 2.13

Schurmann and Zellerfeld pointed out, using the data of Korber and Oelsen (see Figure 2.9), that a carbon saturated iron melt could be desulphurized

by manganese to the limits typical of pig irons.

Of course Korber had previously pointed out that the addition of oxygen in the form of SiO_2 or MnO to the sulphide slag enhanced desulphurization, and that desulphurization could be improved if the melt temperature could be lowered significantly. Also Meyer and Schulte had stated that carbon had the effect of pushing the miscibility gap at 1600°C deeper into the iron corner, which would naturally result in greater desulphurization. Thus Schurmann and Zellerfeld's paper did not involve any new concepts but it did serve as a good summary and reference for the Fe-Mn-S system and desulphurization methods up to that time.

It is worth pointing out that Schurmann and Zellerfeld used an incorrect construction of the liquidus surface (Wentrup's construction) in their paper. More recent publications have made reference to Schurmann and Zellerfelds' paper and in one or two cases have republished the diagram without noticing or commenting upon this error. The liquidus surface proposed in this thesis is schematically illustrated in Figure 3.2. It can be seen that it is very similar to that of Vogel and Hotop. The only difference lies in the detailed form of the eutectic trough. We have identified two ternary eutectic points and two special transformation points along this line and the latter will be discussed in Chapter III.

E.2 Thermodynamics of Liquid Fe(Mn,S) Alloys

We conclude the review of the liquid state of the Fe-Mn-S system by presenting some of the more recent thermodynamic data relating to Mn and S in liquid Fe. In 1952 Sherman and Chipman[32] investigated the effect

of S on the activity coefficient of various alloying elements in liquid Fe at 1600°C. This was achieved by equilibrating the binary melts with H_2/H_2S atmospheres. Their results for Mn are plotted in Figure 2.14 as wt % Mn versus wt % S (they did not present their data in this form). The results are to be compared with Meyer and Schulte's data on the same figure. One notes that the two sets of data agree with each other except for a number of anomolous points in the Fe corner due to Sherman and Chipman. Presumably these experiments were not maintained for a sufficient time for the H_2/H_2S atmospheres to saturate the melts with S. From the data on Figure 2.14 we have calculated the solubility product, $K = [X_{Mn}]\,[X_S]$, (the X's are mole fractions) as,

$$K_{1600^oC} = 3.245 \times 10^{-4}$$

From their data Sherman and Chipman determined the liquid Fe cross-interaction coefficient

$$\varepsilon^{S}_{Mn} = \frac{\partial \ln \gamma_S}{\partial X_{Mn}} = -5.7$$

where γ_S is the activity coefficient of S in liquid Fe.

In 1965 Buzek[33] published a series of short papers on the effect of various solute elements on the solubility of S in liquid Fe at 1570°C. His solubility data for Mn is also plotted in Figure 2.14. In view of the fair agreement between the results of Meyer and Schulte, and Sherman and Chipman at 1600°C we are inclined to discount Buzek's results which, due to the known temperature dependence of the solubility product, should lie slightly below rather than above the 1600°C data.

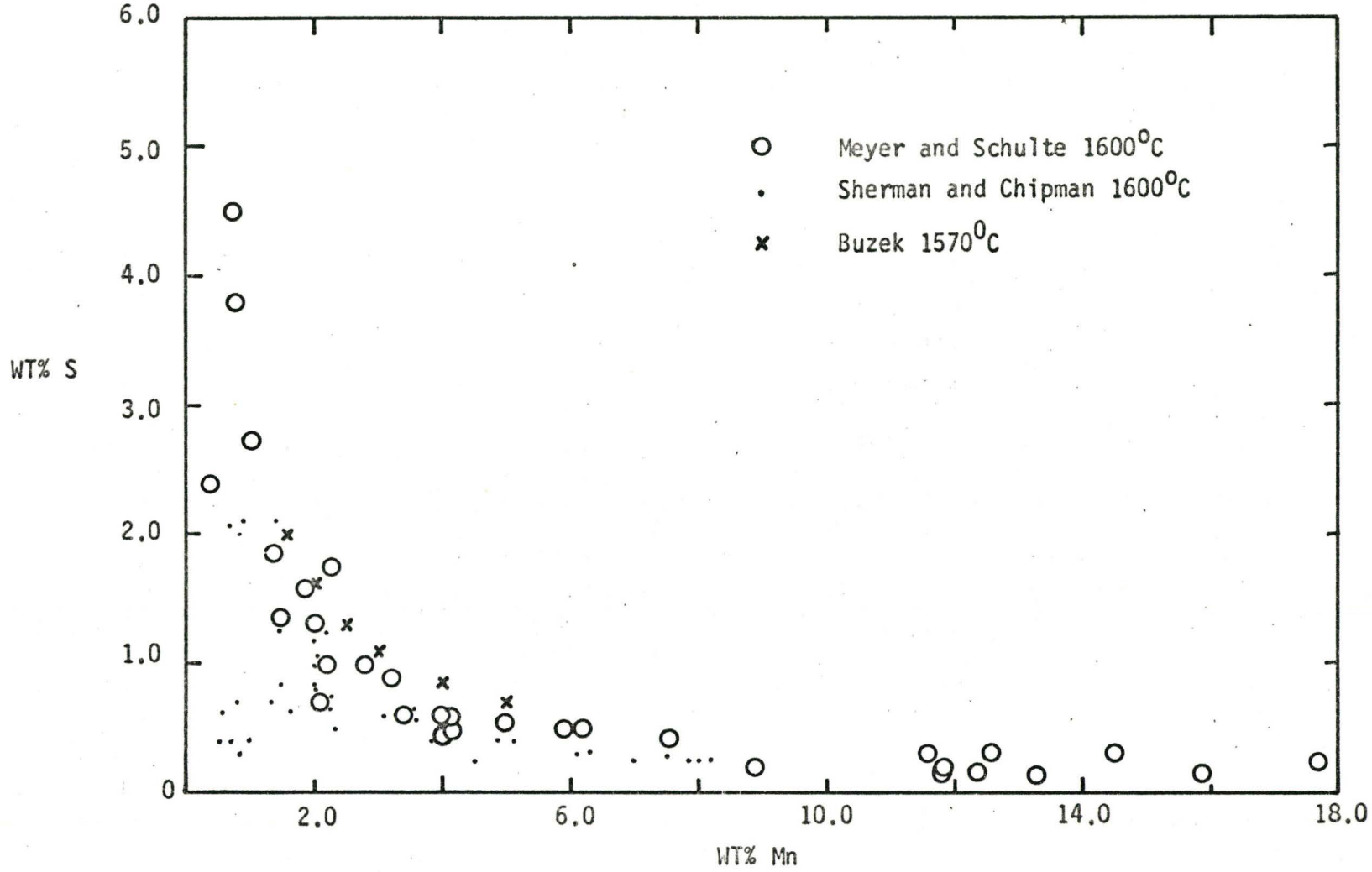

Figure 2.14 The Mn and S solubility in liquid Fe showing the experimental data of Meyer and Schulte[26], Sherman and Chipman[32], and Buzek[33].

We have extracted one further piece of information from the literature concerning the temperature dependence of the solubility product, K. In Figure 2.9 Korber and Oelsen have given the solubility of Mn and S as a function of temperature in carbon saturated liquid Fe. We can evaluate the solubility product, K_c, for carbon saturated Fe from this diagram at each temperature. In Figure 2.15 ln K_c so obtained is plotted versus 1/T leading to the equation

$$\ln K_c = 1.98 - \frac{40,100}{RT}$$

On the legitimate assumption that the enthalpy part of K_c in a carbon saturated Fe-Mn-S liquid is insignificantly different than in a carbon free Fe-Mn-S liquid, we can estimate the temperature dependence of the latter knowing K at 1600°C for carbon free Fe. The resulting calculation yields the temperature dependent expression for the ternary solubility product:

$$K = 14 \exp(-40,100/RT)$$

It is evident from the preceding that the energies of pre-war investigators were concentrated upon elucidating the capabilities of Mn as a desulphurization agent in iron and steelmaking. They were unanimous in the conclusion that Mn does not play a crucial role in desulphurization, especially in the Fe-Mn-S system. Their primary contribution to the knowledge of this ternary system, together with Sherman and Chipman, was the definition of the miscibility gap at 1600°C and the direction of the tie-lines in the gap, and a clarification of the liquidus surface of the ternary system.

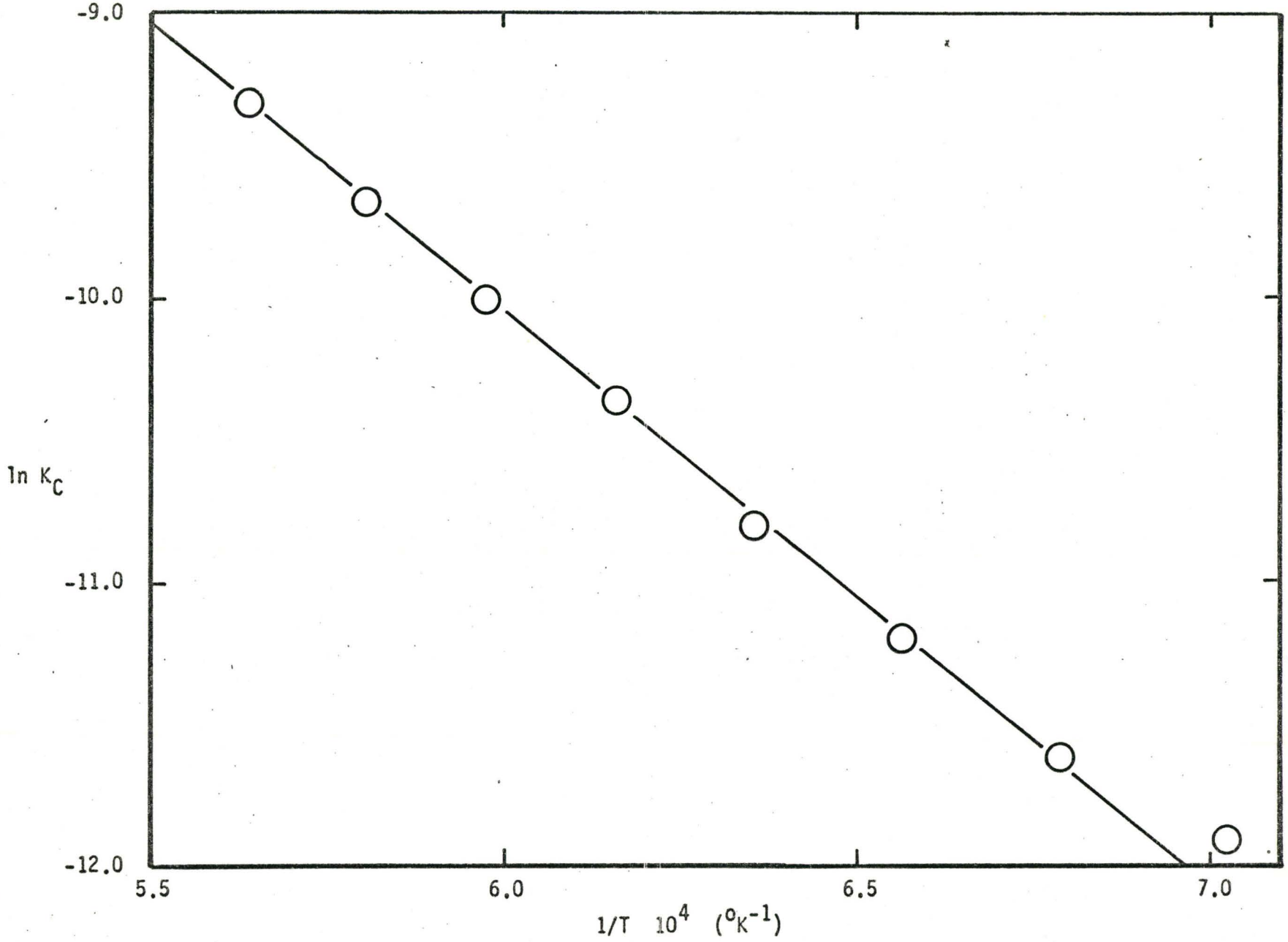

Figure 2.15 The variation of the solubility product, $K_C = X_{Mn}X_S$, in carbon saturated liquid Fe as a function of the absolute temperature.

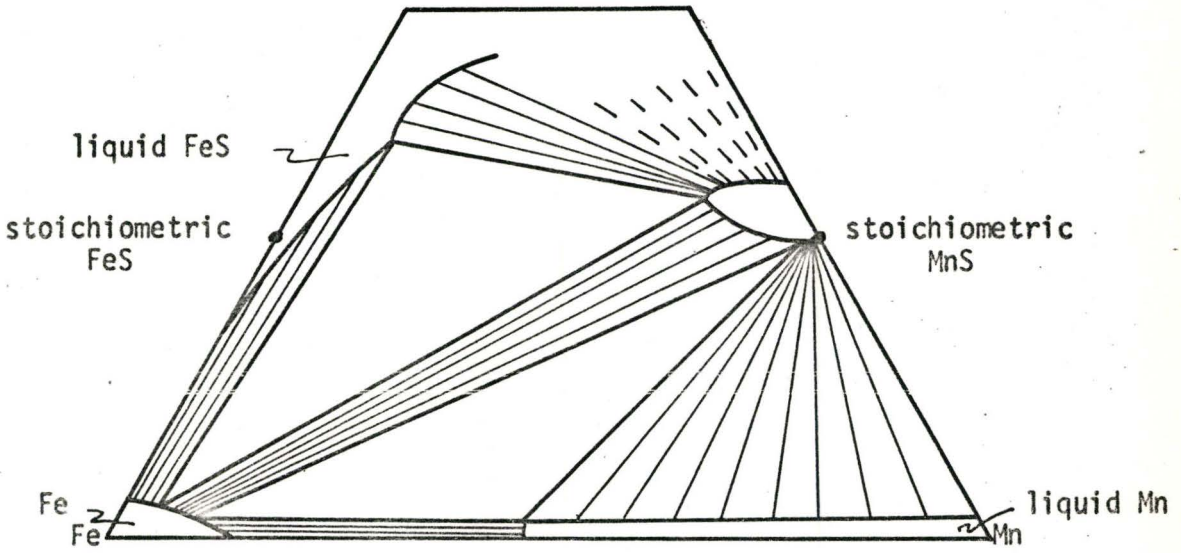

Figure 2.16 The 1300°C Fe-Mn-S isotherm after Clark[34].

Although some attempt was made to define the system below the liquidus temperatures, the efforts were generally unfruitful. As a result little quantitative constitutional information was available to permit the analysis of the effect of sulphur and/or sulphides on phase transformations in solid steels. It is indeed surprising that such information was not produced during this period, nor during the following few years.

E.3 Investigation of Solid State Reactions

In 1965, Clark[34] completed the initial study of solid-liquid state reactions in the Fe-Mn-S system at McMaster. His thesis presented a useful preliminary survey but it was apparent from his results that a more precise, quantitative investigation was required. His research was carried out at 1300°C with the hope of accurately defining this isotherm. With hindsight his techniques and methods of investigation clearly prevented him from doing this, but he was able to deduce from his results, a schematic picture of the 1300°C isotherm. This is reproduced in Figure 2.16.

In 1967 Nakao[13] reported in his M.Sc. thesis a more quantitative and realistic picture of this isotherm. This is reproduced in Figure 2.17. The key to the isotherm is the placement of the corners of the three phase field (γ-Fe + FeS + MnS). Nakao noted that the determination of the S and Mn contents of γ-Fe in equilibrium with MnS and FeS to any degree of accuracy is impossible using the electron probe microanalysis technique, and indeed the S content is inaccessible using this technique. Nakao estimated a value of 0.009 wt.% S and 0.15 wt.% Mn in γ-Fe by interpolating

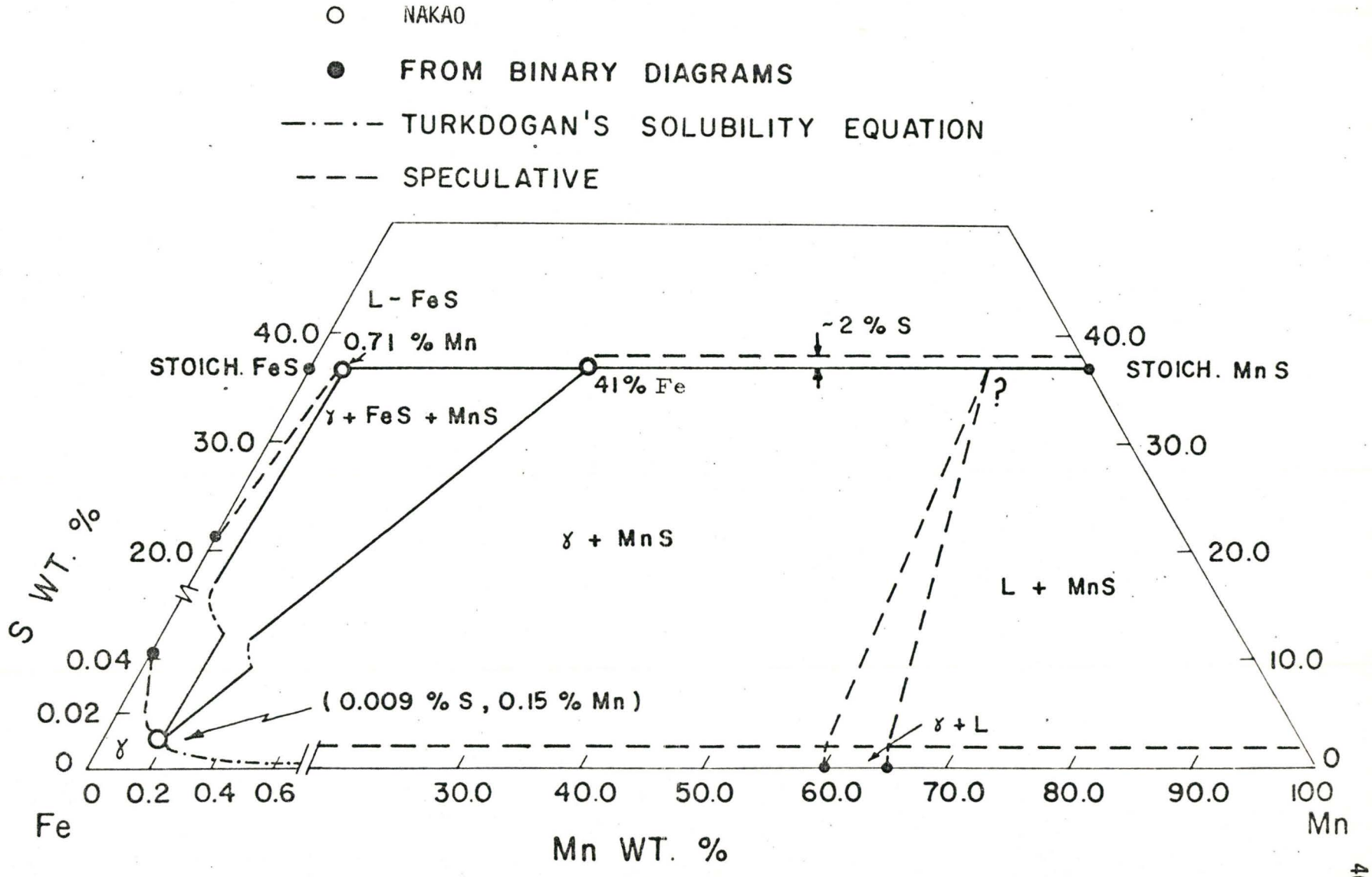

Figure 2.17 The 1300°C isotherm after Nakao[13].

the S content from Turkdogan's data on the basis of his own very approximate determination of the Mn content.

For the FeS in equilibrium with γ-Fe and MnS Nakao found the S content to be about 36 wt.% S, almost the stoichiometric amount found in pure FeS. As can be seen by comparing Figures 2.16 and 2.17, this value is appreciably lower than that found by Clark, and is closer in agreement with this author's conjecture that Clark's high sulfur contents would not satisfy a prediction of this isotherm when viewed from free energy considerations.

The main point of contention with Nakao's results concerns the Fe and Mn contents of the MnS phase in equilibrium with γ-Fe and liquid FeS. Nakao reported these contents as 39.4 wt.% Fe, 24.4 wt.% Mn, and 36.2 wt.% S. These values were a result of equilibrium experiments in which pure Fe, pure MnS, and pure FeS were isothermally equilibrated, quenched, and analysed. The results of these experiments produced a range of Fe contents in the MnS from 22.4 to 39.4 wt.% Fe. Another set of experiments designed to yield kinetic data was carried out by reacting FeS:MnS diffusion couples isothermally for varying times. In each case the interface concentrations of Fe in the MnS phase yielded a value of about 42 wt.% Fe. From this result Nakao concluded that the value of 39.4 wt.% Fe found in the equilibrium studies was close to the correct value, and that the other values were representative of systems which had not yet reached equilibrium, at least in the MnS phase. As we will later contend, Nakao actually observed a series of two-phase tie-lines and misinterpreted them as non-equibrated sides of the three-phase triangle.

E.4. Thermodynamics of Fe(Mn,S) Solid Solutions

Very little data is available on the solubility of Mn and S in solid Fe. The first reliable determination of the solubility limits of both of these elements in γ-Fe was carried out by Turkdogan, Ignatowicz, and Pearson[9] in 1955. Their experimental procedure involved the equilibrium of Fe-Mn alloys in controlled H_2/H_2S atmospheres. Table II-1 lists the Mn contents of the alloys and the S contents determined after equilibrating at various temperatures.

Table II-1

The solubility of Mn and S in γ-Fe, after Turkdogan et al[9].

wt% Mn	wt% S
at 1000°C	
0	0.013
at 1200°C	
0	0.031
0.37	0.0018
1.07	0.00066
1.30	0.00056
at 1335°C	
0	0.046
0.37	0.0058
1.07	0.0032
1.30	0.0018

From their solubility data they were able to show that for the reaction

$$H_2(g) + [S] = H_2S(g) \qquad (2\text{-}12)$$

in which the equilibrium constant is

$$K_1 = \frac{p_{H_2S}}{p_{H_2}} \quad \frac{1}{[\text{wt \% S}]\, f_s}, \qquad (2\text{-}13)$$

where f_s is the activity coefficient for S in the Fe-S binary system, that

$$\log_{10} K_1 = \frac{2157}{T} - 2.085 \qquad (2\text{-}14)$$

Also for the reaction

$$(MnS) = [Mn] + [S] \quad , \qquad (2\text{-}15)$$

in which the equilibrium constant is

$$K_2 = \frac{[\text{wt.\% Mn}]\,[\text{wt.\% S}]\, f_s^{Mn}}{a_{MnS}} \qquad (2\text{-}16)$$

where f_s^{Mn} is the activity coefficient for the Fe-Mn-S ternary system, they found that

$$\log_{10} f_s^{Mn} = \left[- \frac{215}{T} + 0.097 \right] [\text{wt.\% Mn}] \qquad (2\text{-}17)$$

and

$$\log_{10} K_2' = - \frac{9020}{T} + 2.929 \qquad (2\text{-}18)$$

It can be seen from Table II-1 that Mn strongly reduces the solubility of S in γ-Fe.

Data on the solubility of S and Mn in α- and δ-Fe is virtually non-existent. Brown[36], in 1967, published a sulphur potential diagram ($\Delta\bar{G}_S$ versus T) for predicting the sulphur contents in Fe-Mn alloys at temperatures from 0 to 1800°C. This diagram was constructed by combining the $\Delta\bar{G}_S$ versus T diagram for the Fe-S binary, and the $\Delta\bar{G}_{Mn}$ versus T diagram for the binary Fe-Mn system. The solubility and free energy information for these binaries was collected from the various studies cited previously and the standard reference texts. His diagram is useful for estimating

solubility values in the Fe-Mn-S system, but in explaining the possible errors in his diagram Brown wrote that

> 'Absolute reliance must not therefore be given to the predictions made from the diagram.'

For example at 1200°C Brown suggests an Fe-1 wt.% Mn alloy should have about 0.0012 wt.% S, whereas Turkdogan et al give 0.00066 wt.% S.

F. KINETICS OF PHASE TRANSFORMATIONS

F.1. Diffusion in the Fe-Mn-S System

The presently recorded kinetic data, in the form of diffusion coefficients for the Fe-Mn-S system, is tabulated in Table II-2. From our knowledge the values represent the most reliable experiments to date. It can be seen that the chemical diffusion coefficient of S and the self-diffusion coefficient of Fe in α-, γ-, and δ-Fe are fairly well established. However the chemical diffusion rate of Mn is not well established for all phases. There is in fact no data in the literature for Mn diffusion in α- and δ-Fe.

Diffusion coefficients for Mn, Fe, and S in MnS are non-existent with the exception of a single value reported by Nakao[13] at 1300°C, i.e., $D_{Fe} = D_{Mn} = 2 \times 10^{-7}$ cm^2/sec.

F.2. Kinetics at 1300°C

In section E.3 reference was made to the diffusion couples which Nakao utilized in his kinetic studies. Figures 2.18, 2.19 and 2.20 are reproductions of the concentration profiles obtained from the FeS:MnS,

Table II-2

Binary Diffusion Coefficients of the Elements for the Fe-Mn-S System

$D = D_o \exp(-Q/RT)$

	D_o cm^2/sec	Q cal.	Temp. Range ^oC	Ref.
S in α-Fe	1.68	42800	750-890	37
S in γ-Fe	0.018	38600	1150-1250	38
S in δ-Fe	-	-	-	
Mn in α-Fe	-	-	-	
Mn in γ-Fe	0.57 ± 0.11	66200	1150-1350	39
	0.486 ± 0.011 wt% Mn	66000	950-1450	39
Mn in δ-Fe	-	-	-	
Fe in para-magnetic α-Fe	5.4	60300	809-889	40
	2.01	57500	768-884	41
	1.6	57200		42
Fe in ferro-magnetic α-Fe	27.5	60700	683-726	41
	0.5	57200		42
Fe in γ-Fe	0.7	68200		42
Fe in δ-Fe	2.01	57500	1428-1492	41
Fe in MnS	$D = 2 \times 10^{-7}$ cm^2/sec		1300	13
Mn in MnS	$D = 2 \times 10^{-7}$ cm^2/sec		1300	13
S in MnS	-	-	-	
Fe in L-FeS	6.57	136000	1152-1238	43
Mn in L-FeS	-	-	-	
S in L-FeS	-	-	-	

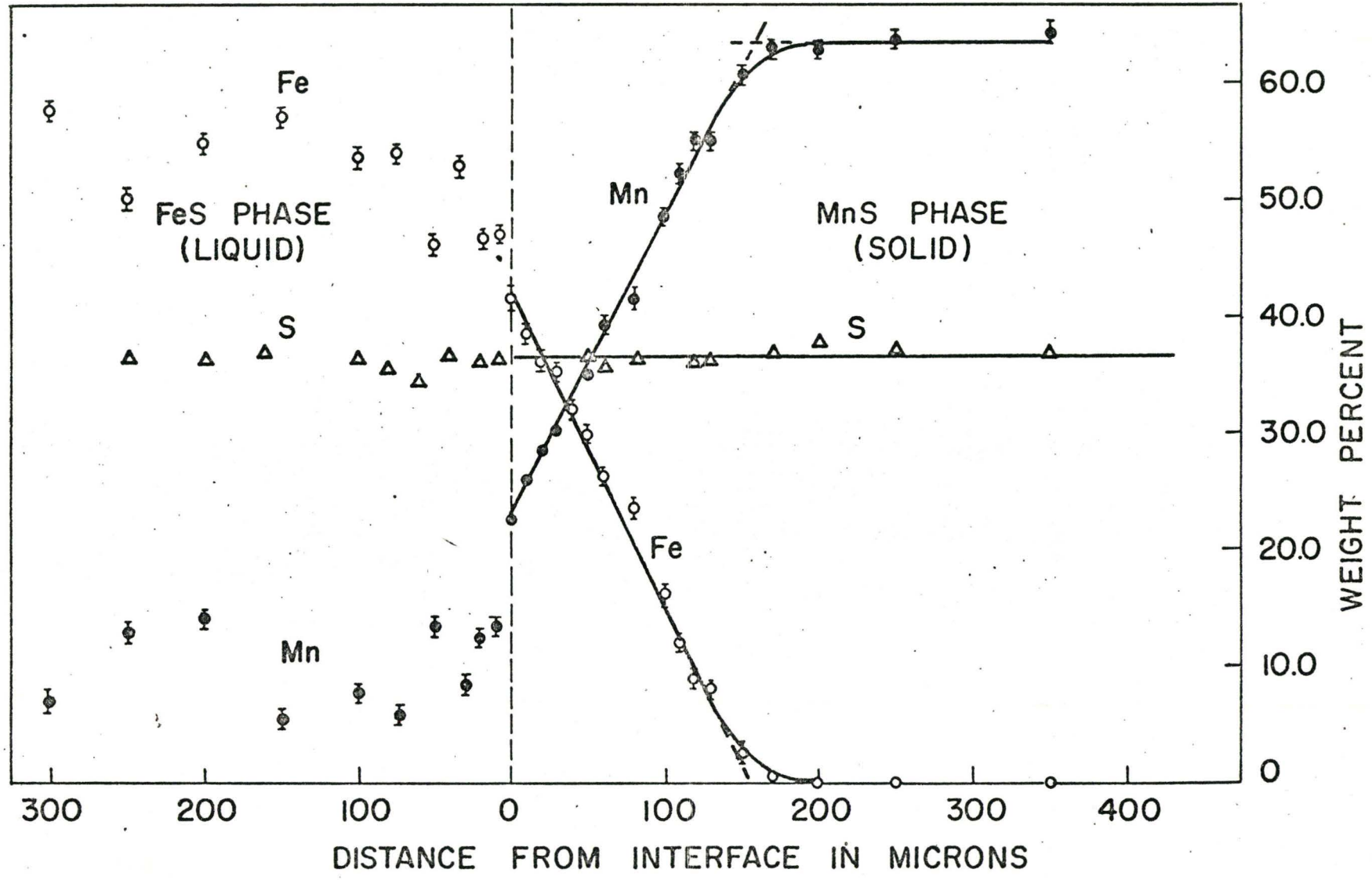

Fig. 2.18 Concentration-penetration curve for the FeS-MnS couple diffused for 6 min.

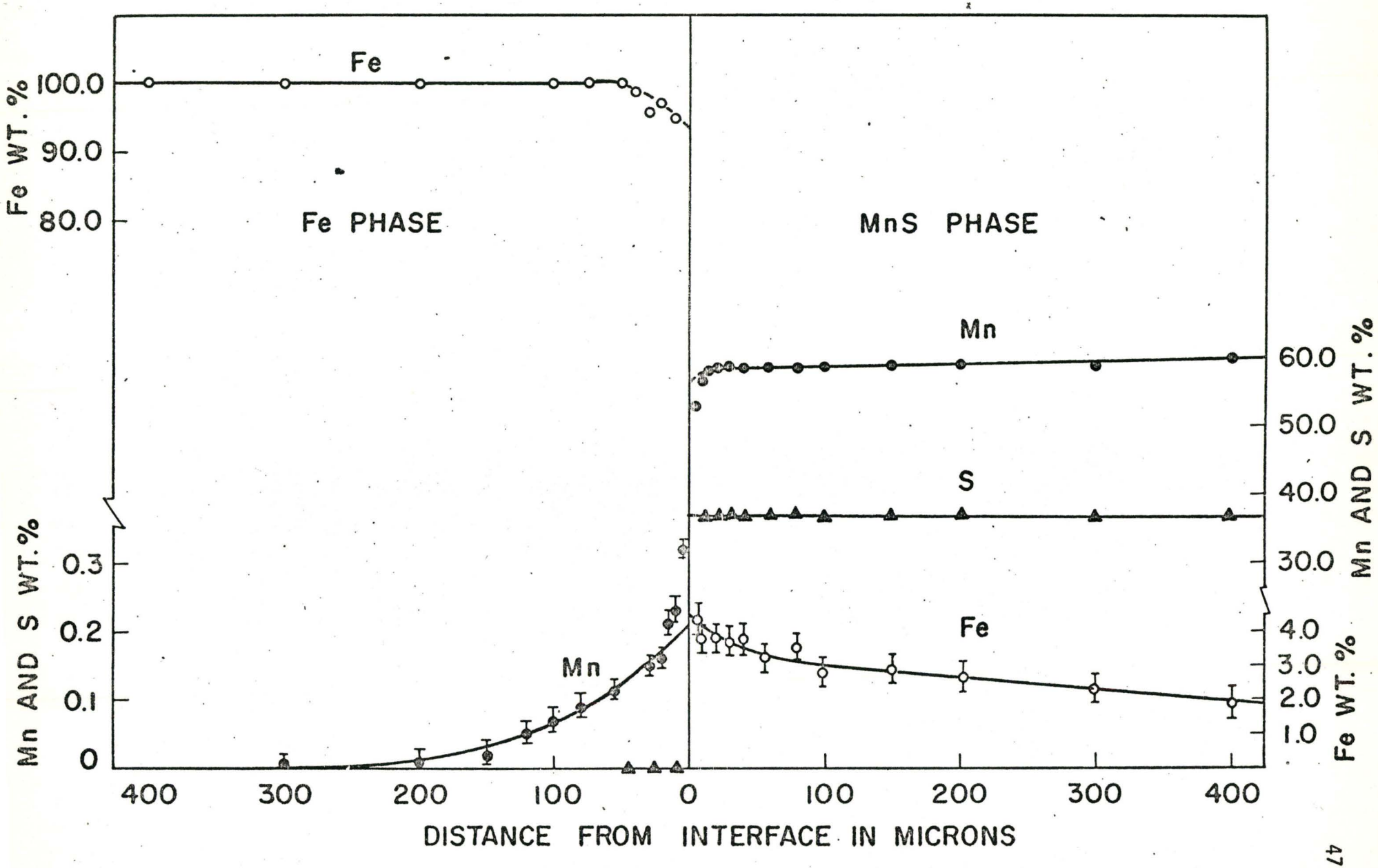

Fig. 2.19 Concentration-penetration curve for the Fe vs. MnS couple diffused for 35.33 hrs.

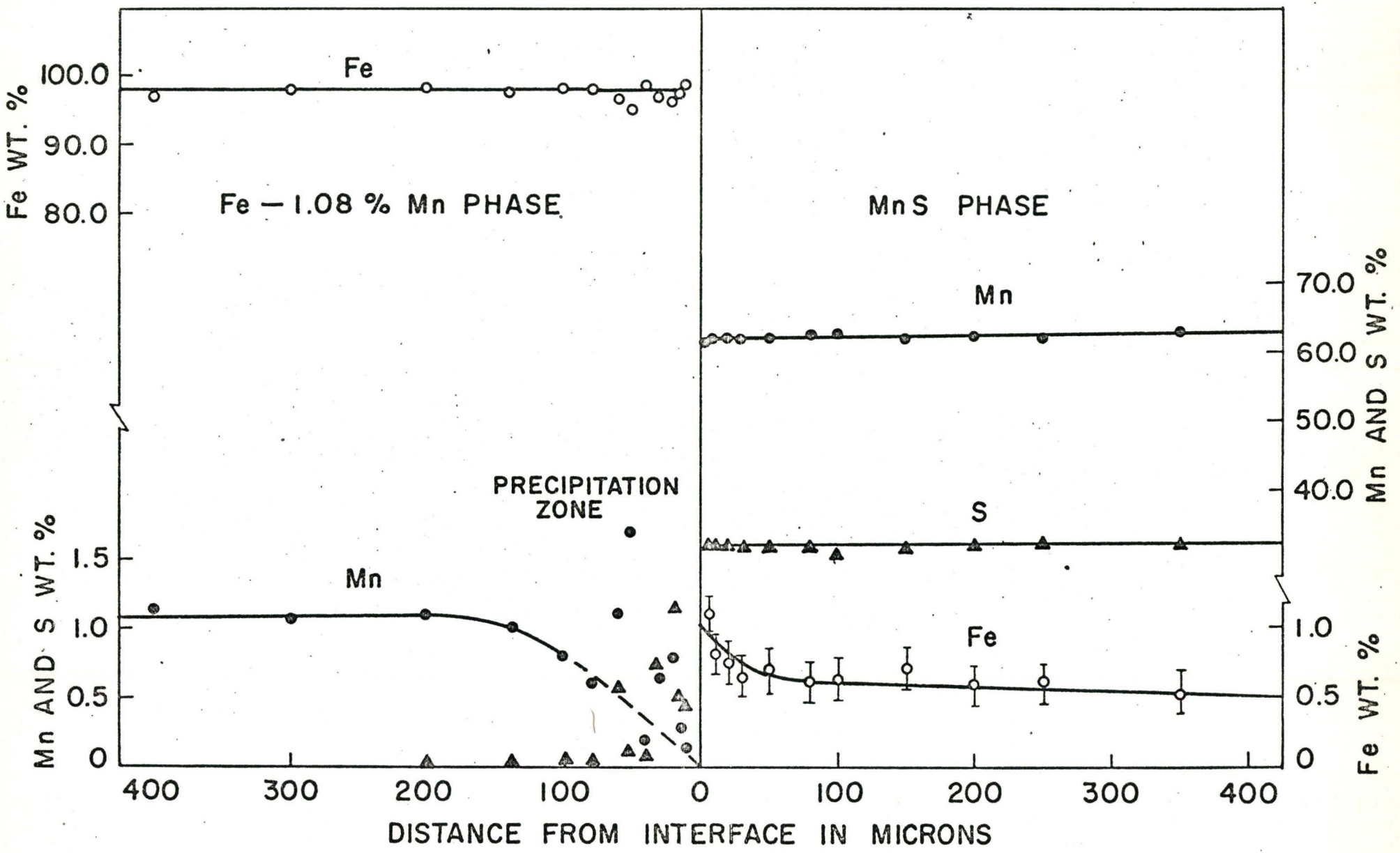

Fig. 2.20 Concentration-penetration curve for the Fe-1.08% Mn vs. MnS couple diffused for 6 hrs.

Fe:MnS and Fe-1% Mn:MnS couples, respectively. The diffusion coefficients for manganese and iron in MnS were obtained from this FeS:MnS data.

The interesting aspect of the iron profiles in MnS is the fact that they obviously are not the typical error function profiles one associates with solid state diffusion. In all cases the curve has a definite knee indicating that the rates are slow near the interface and fast in the interior of the MnS. Although it is possible to explain this behavior on structural grounds[13] the present investigation suggests that the apparent anomoly in Figure 2-18 is due to rapid penetration of the MnS by liquid FeS. The anomoly in Figure 2.19 describing a completely solid state reaction must be explained on structural grounds. This will be undertaken in the discussion of our results.

G. MnS INCLUSIONS IN STEELS

The following section is centered around inclusion studies, particularly of MnS in steels. During the 1950's and 60's studies of inclusion contents and control took precedence over fundamental thermodynamic and kinetic studies in the Fe-Mn-S system. This is a result of a demand for more stringent specifications and the introduction and production of specialty steels during this period. The results and conclusions of these investigations were aimed at explaining a myriad of complex observations by semi-quantitative and empirical methods. Only a sampling of the papers will be summarized here.

Excessive temperatures during hot working can cause permanent microstructural damage to a steel. 'Burnt' steels exhibit incipient

grain boundary melting and render the steel useless. An 'overheated' steel, hot worked at temperatures below that which causes 'burning' is also useless because the high temperatures have caused permanent microstructural weaknesses.

In 1950 Rollason and Roberts[44] addressed themselves to the phenomenon of overheating in a short note and concluded that the amount of MnS present in a steel (as inclusions) governed the minimum overheating temperature: the more MnS, the higher this temperature. Quenching from this temperature would retain the S and Mn in solution. Slow cooling would permit 'coagulation' of the precipitated particles into large inclusions. However an intermediate rate would produce a fine dispersion of MnS inclusions at the grain boundaries, which in turn affected cohesion of the grains, and caused mechanical failure. A plot of the sulphur content versus the Mn/S ratio at the minimum overheating temperature indicated that for Mn/S > 20, this temperature did not vary significantly.

In 1938 Sims and Dahle[45] had classified the shapes of inclusions found in as-cast steels into three types. Briggs[46] in his book 'The Metallurgy of Steel Casting' adopted this format and it has since become the standard method of describing the morphology of inclusions. The three types are schematically represented in Figure 2.21. The type I inclusion is a globular form with a wide range of size. Type II is a finer, eutectic chain-like dispersion of inclusions, and type III is a massive irregularly shaped type. Originally these shapes were thought to be associated with the aluminum content of the steel, type I being found in a steel with little or no aluminum and type III with an excess. More recently this specification has been debunked and the classification is

used in a straight morphological sense as shown in the diagram.

In 1965 Lichy, Duderstadt and Samways[47] presented a paper on the control of the shape of sulphide inclusions in low carbon, aluminum-killed rolled products. They observed that the type I MnS inclusions in the as-cast ingot were being transformed into long stringers during the rolling operation. These stringers resulted in surface defects causing a high percentage product rejection. Their investigation involved adding controlled amounts of aluminum, mischmetal, titanium, and zirconium to various sized ingots and observing the sulphide shape before and after rolling. They found that zirconium was the only additive that would retain a type I sulphide through the rolling operation. This was explained on the basis that the zirconium promotes the transformation of ductile manganese sulphides into non-ductile sulphides, the Mn and Fe, being replaced by Zr. It is interesting to note that their Al-killed steels contained type I sulphides which is contrary to what was originally thought to be the definition of a type I inclusion.

From the previous discussion it is evident that other elements may replace manganese in MnS. Keissling and Westman[48] carefully examined this characteristic by a study of the solubility of the transition metals Cr, V, Ti, Fe, Co, and Ni in synthetic MnS at 1150^{o}C. Their results are tabulated in Table II-3 and Figure 2.22. From Table II-3 one can see that the sulphides containing Ti, V, and Cr appear to be metal deficit sulphides. These elements have a valence of III and thus (Mn,Me)S phases with these metals would contain metal vacancies. Fe, Co, and Ni on the other hand have a valence of II and tend to be stoichiometric. Note that Fe can have a valence of III, and metal deficit (or S excess) (Mn Fe)S phases

Table II-3

The solubility of some transition metals in MnS at 1150°C.

Solid Solution System	Sulphide Formula	Sulphide Composition, (wt%) Mn	Me	S
(Mn,Ti)S	$Mn_{.96}Ti_{.03}S$	61.1	1.7	37.2
(Mn,V)S	$Mn_{.61}V_{.26}S$	42.5	16.8	40.7
(Mn,Cr)S	$Mn_{.26}Cr_{.49}S$	19.9	35.5	44.6
(MnS)	MnS	63.1	-	36.9
(Mn,Fe)S	$Mn_{.35}Fe_{.65}S$	22.0	41.5	36.5
(Mn,Co)S	$Mn_{.72}Co_{.28}S$	44.9	18.8	36.3
(Mn,Ni)S	$Mn_{.88}Ni_{.12}S$	55.3	8.0	36.7

have been observed with a formula $Mn_{.77}Fe_{.10}S$ (or $Mn_{.88}Fe_{.12}S_{1.15}$).

In 1966 Matsubara[49] recognized the need for a 'systematic fundamental survey of the behaviour of sulphur or sulphides in solid steel'. He undertook part of this survey by investigating the changes in morphology and composition of precipitated plate-like MnS inclusions when subjected to various cooling and heating rates and various soaking temperatures. The following few statements summarize his observations. A steel cooled at less than 60°C/min from above a temperature where all the Mn and S are in solution to below 1200°C resulted in the precipitation of plate-like (Widmanstatten) inclusions in the austenite, and fine globular inclusions in the austenite grain boundaries. The plate-like inclusions in steels, which were slowly cooled to the ferrite region and reheated to the austenite region rapidly decomposed into fine globular

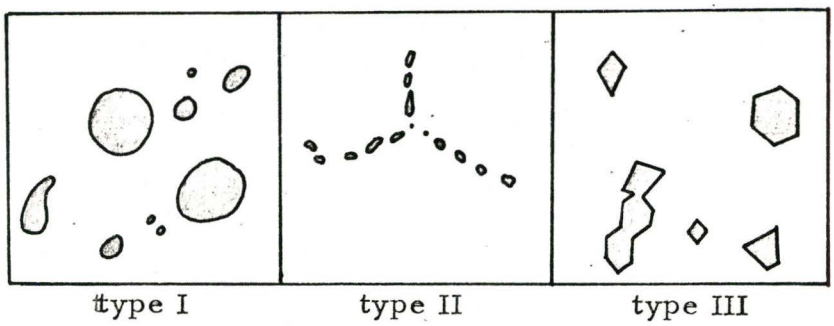

Figure 2.21 Morphological classification of inclusions in steels after Sims and Dahle[45].

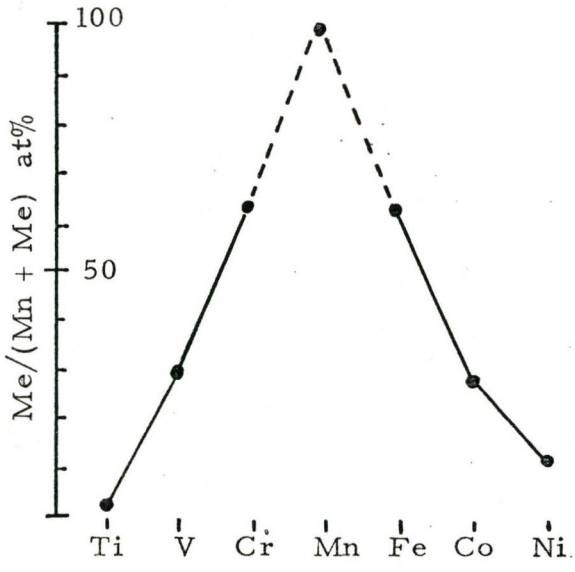

Figure 2.22 The solid solubility of neighboring transition metals (Me) in MnS after Keissling and Westman[48].

precipitates. Cooling and reheating completely in the austenite region did not cause the MnS plates to transform to globules. Steels with all the Mn and S in solid solution quenched to room temperature and then austenitized resulted in the precipitation of imperfect plates and fine globular precipitates. His conclusions do little more than reiterate his results, although he did indicate that the MnS plates could exist coherently with γ-Fe, and that cooling to α-Fe and reheating to γ-Fe would cause a breakdown of this coherency and favour spheroidization of the precipitates.

Matsubara missed an excellent opportunity to make a significant contribution to the constitutional and kinetic knowledge of the Fe-Mn-S system. He unfortunately chose to work with industrial steels containing Cr, Ni, Mo, Si, and V, all of which would have some affect on the constitution and therefore the precipitation phenomenon. He might also have put some emphasis on the nucleation rate of the various types of inclusions as a function of cooling rate.

These discussions on MnS inclusions and their effects in steels are typical of a great many papers on this subject. There is a common criticism in that the results and conclusions are derived without adequate knowledge of the solid-state constitution of the Fe-Mn-S system. There is no doubt that many of the problems investigated could be simplified if such information were available. The same can be said for the kinetics of phase transformation. If numerical data for the diffusion coefficients for the elements in the various phases was known then, together with the constitutional data, the observed morphological and composition changes during heat-treatment processes would be more easily explained.

CHAPTER III

A THEORETICAL ANALYSIS OF THE Fe-Mn-S PHASE DIAGRAM

The constitution of the Fe-Mn-S ternary system, or indeed any ternary system, can be determined experimentally with little or no prior knowledge of the system. This, however, would be a very tedious and laborious job. If by some means one can evolve a qualitative picture of the system to combine with the limited data available then subsequent experimental planning and procedures become much easier. The theoretical aid most frequently used is solution thermodynamics. Using free energy concepts and a derived solubility theory it will be shown in this chapter how one can qualitatively and quantitatively predict sections of the Fe-Mn-S ternary phase diagram.

A. QUALITATIVE PREDICTION OF THE Fe-Mn-S PHASE DIAGRAM

A reference to the prediction of the form of a ternary isotherm at 1000°C was made in Chapter II. Using binary data, this could be done if one knew in advance that the phases MnS and γ-Fe were able to equilibrate with each other. Because the binary systems at 1000°C do not exhibit complicated phase relationships, such predictions are possible. However at higher temperatures, particularly in the region of 1300° - 1600°C, the binaries become more complicated, exhibiting extectic, peritectic, and monotectic reactions. In order to deduce qualitative isotherms which are consistent with one another over a large range of temperatures, a method involving free energy surfaces as a function of composition was used.

This is by no means a new concept, but it is often overlooked in standard texts on the subject, and for this reason a simple example will follow. In this example the isotherm representing the phase relations between the melting point of iron (1535°C) and the Mn-MnS monotectic (1580°C) will be constructed.

In Figure 3.1 two free energy surfaces are shown (upside down for clarity). These surfaces are associated with the liquid phase and the MnS solid phase, the only stable phases at the present temperature of interest. This can be inferred from the binary phase diagrams. The shapes of the free energy surfaces can also be estimated from the inferred binary free energy curves and phase diagrams.

MnS is a compound with a very narrow solubility range for Mn, but according to the FeS-MnS pseudo-binary diagram, Figure 2.6, it can contain considerable Fe at lower temperatures. Thus its free energy surface must represent a vertical slab extending from pure MnS towards FeS, having a peak very close to MnS and projecting above the liquidus surface.

The shape of the liquidus surface is dictated by the Mn-S free energy curve which corresponds at higher temperatures to liquid-liquid immiscibility (see Figure 2.4). In the range of stable solid MnS this miscibility gap is metastable on the Mn-S binary, but we know from the literature that it remains stable near the Fe-S side of the ternary system so the liquid free energy surface must contain a depression as shown. Also, because the Fe-Mn and Fe-S binary diagrams, Figures 2.1 and 2.2, exhibit single phase liquids at this temperature, the miscibility gap, whether stable or metastable, must terminate at a critical point, K, within

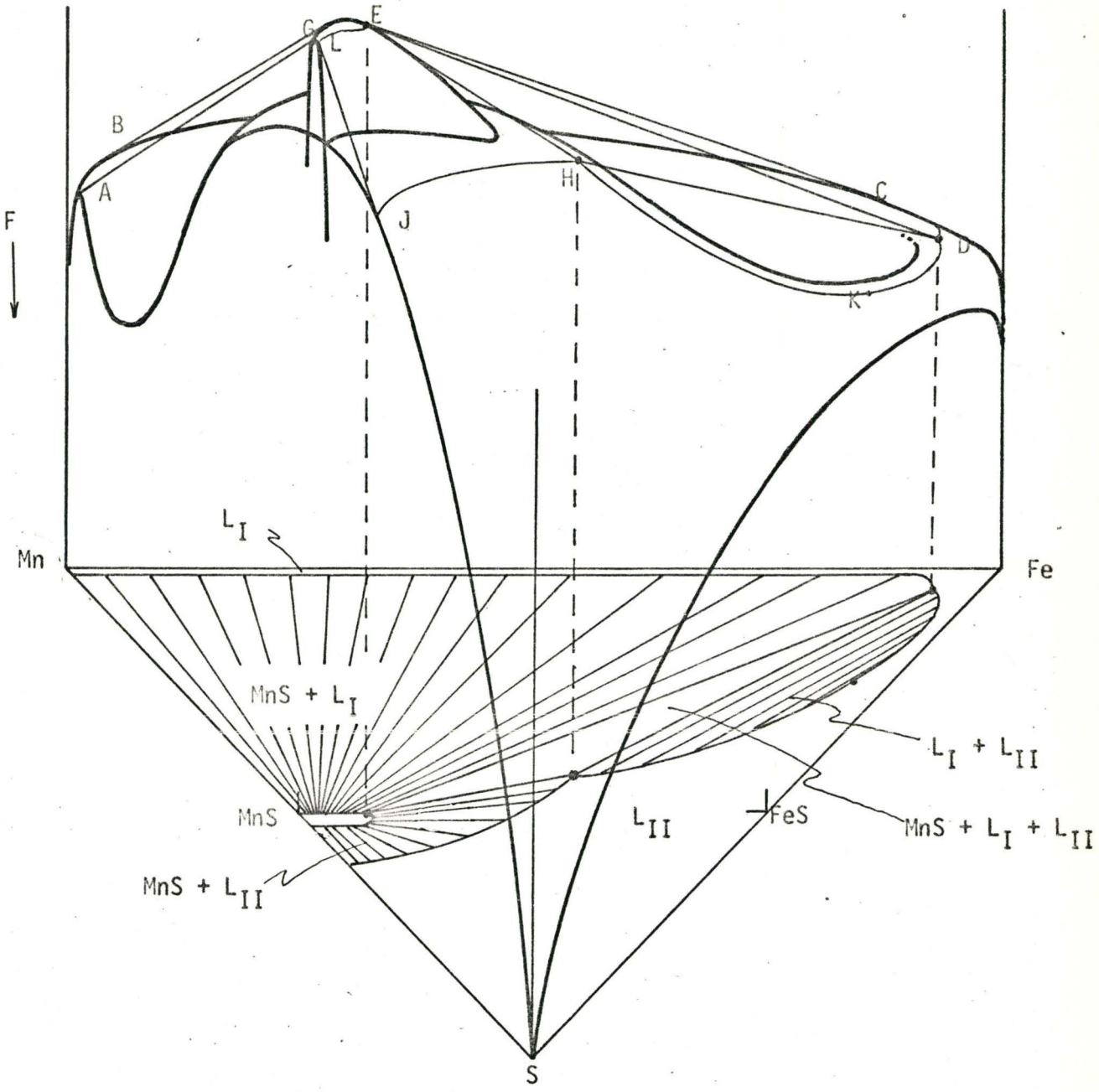

Figure 3.1 A schematic representation of the liquid and MnS free energy surfaces for the Fe-Mn-S system. The isotherm shows the relationship between the various phases predicted from the free energy surfaces.

the ternary system. As we shall discuss in Chapter VII, the Fe-S liquid free energy curve evolves to metastable liquid-liquid immiscibility at lower temperatures. That is, the critical point K finally emerges at the Fe-S binary. Because of this one can infer that the respective ridges on the FeS-MnS and Fe-Mn sides of the miscibility gap are roughly parallel to these binaries, and thus to each other.

To geometrically construct a ternary isotherm from complete free-energy information one slides an imaginary plane in contact with the free-energy surfaces. If this plane is tangent to the surface at one point only, then the alloy of composition at this point is composed of only one phase. If the plane is simultaneously tangent to two points only, then the region between the points is a two-phase region, and the two points describe the termini of this tie-line in the two-phase region. When the plane is rotated so that is is simultaneously tangent to three points on the surfaces, then the triangle joining these points (or compositions) describes the region of a three-phase field. If one projects this information from the free-energy surfaces to a horizontal plane (i.e. ternary isotherm) one finds that consistent phase regions in the isotherm are generated.

The method of construction of the isotherm can now be followed in Figure 3.1. If the imaginary plane is placed on top of the MnS free-energy surface and rotated downwards towards the Mn corner, the plane becomes tangential with both the MnS and liquid surface with the tie-line end points at G and A. If one rotates the plane across the liquidus surface, one finds that a series of tie-lines is described with the end points along GE and ABCD. The area under this region is the two-phase

field, ($MnS + L_I$). If one tries to rotate the plane further it is found that another point, point H, is now also tangential to the plane. The resultant triangle EDH describes the three-phase region ($MnS + L_I + L_{II}$). One can now rotate the plane about two directions. One is from HD to K. The two tangential points follow the ridges about the miscibility gap depression, and gradually move towards each other until they meet at K, the critical point. This region describes the liquid two-phase region, ($L_I + L_{II}$). The other rotation is about EH toward the Mn-S system to higher S contents. In this case the locus of the tie-line end points follow the lines EL and HJ, which describes another two phase region, ($MnS + L_{II}$).

These regions outlined on the free-energy surfaces have been projected down to a horizontal isotherm giving a clear, qualitative representation of the phase relations that exist at the temperature in question. Although this particular isotherm might be directly and safely inferred from the binary diagrams without the intermediary of free-energy surfaces, the free-energy method will be found to be a necessary aid to the avoidance of ambiguity when the combination of binary systems becomes very complicated. This procedure has proved extremely useful for the preliminary qualitative construction of the isotherms from 1000^{o} to >1600^{o}C and the testing for thermodynamic consistency of the quantitative diagrams finally evolved. These latter isotherms are presented in section A of Chapter VIII. They represent the combined information taken from the literature, from free energy-composition concepts, and from the present experimental data.

B. THE CHARACTER OF THE LIQUIDUS SURFACE

In Figure 3.2 the three binaries and the one pseudo-binary are shown surrounding the relevant part of the Fe-Mn-S ternary triangle. Knowing the extent of the miscibility gap, and projecting to compositions at which a liquid phase must react with another phase, either solid or liquid, permits one to sketch in the lines representing the intersection of the two-phase regions ($L_I + L_{II}$) and (L_I or L_{II} + MnS), where L_I and L_{II} are the two liquids present in the miscibility gap. The data of the preceding review indicates that the corner of the gap at N extends deep into the Fe corner and NM lies close to the Fe-Mn side of the ternary diagram. The line BSCTD, lying between the binaries and MNKL, represents an eutectic trough which borders the Fe-Mn and Fe-S binary limits.

The arrows on the lines are directed towards lower temperatures. We will show in the following sections that point K, the critical point at which the miscibility gap disappears, occurs at a temperature minimum on the line MNKL. The liquidus surface constructed by Vogel and Hotop contain two additional points of maximum temperature, M_1' and M_2' in Figure 2.12. The subsequent analysis will show that there is neither an experimental nor thermodynamic reason for seriously considering this complication.

There are two ternary eutectic points in the system. The eutectic point B occurs in the Mn corner at a temperature somewhat less than 1232°C. The ternary eutectic at point D is the most significant one because of its low temperature (less than 988°C) and because the liquid involved is close to pure FeS. The points S and T are not eutectic points. Their detailed character will be discussed in section B.3 of this chapter.

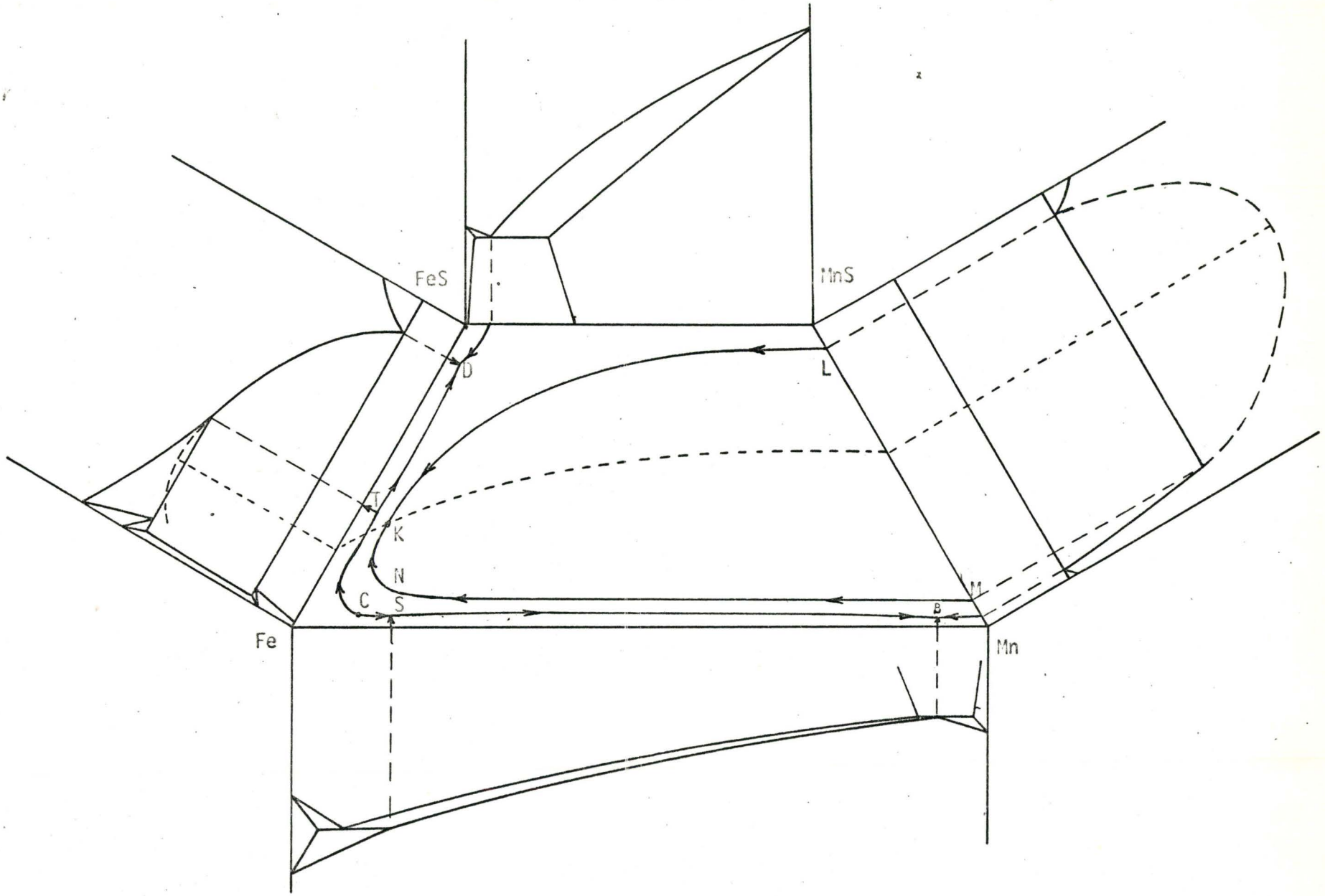

Figure 3.2 The liquidus surface of the Fe-Mn-S system up to 50 at% S.

B.1. The Boundaries of the Miscibility Gap

Figure 3.3A is a three dimensional schematic representation of the miscibility gap as viewed from the Mn corner, in which the line MNKL is the same as in Figure 3.2. Using the Gibbs-Duhem equations we will show that the line MNK must fall in temperature from point M as X_{Fe} increases, and that the line LK must fall with it in temperature from point L as X_{Fe} increases. We shall also show that in general, the critical point K must be either a maximum or minimum with respect to temperature, and therefore because MNK and LK fall, that K is a minimum with respect to temperature.

B.1.1. The Temperature Dependence of the Lines MN and LK

As previously indicated, the line MNK represents the mutual limits of the two-phase fields (L_I + L_{II}) and (L_I + MnS). On this line the three phases L_I, L_{II}, and MnS are in equilibrium. Experiments at 1600°C (see Figure 2.7) show the line MN to be parallel to the Fe-Mn binary system, and therefore the slope of the line MN as it enters the ternary triangle from the Mn-S monotectic at point M may be defined approximately as $(dT/dX_{Fe})_{X_S=\text{const}},\ X_{Fe}\to 0$. Also, since the three-phase triangle (L_I + L_{II} + MnS) is univariant, the line LK must have the same sign of temperature increment as MN.

Now depending upon the sign of the slope, two possible phase relationships can result. These are shown in Figure 3.3B. Vogel and Hotop[12] subscribe to case I in this figure. They claim that because the tie-line AB in Figure 2.7 is to the right of the tie-line Fe-MnS, the (L_I + L_{II} + MnS) three-phase triangle must evolve as case I when the MnS phase reacts with the miscibility gap. This requires that there be

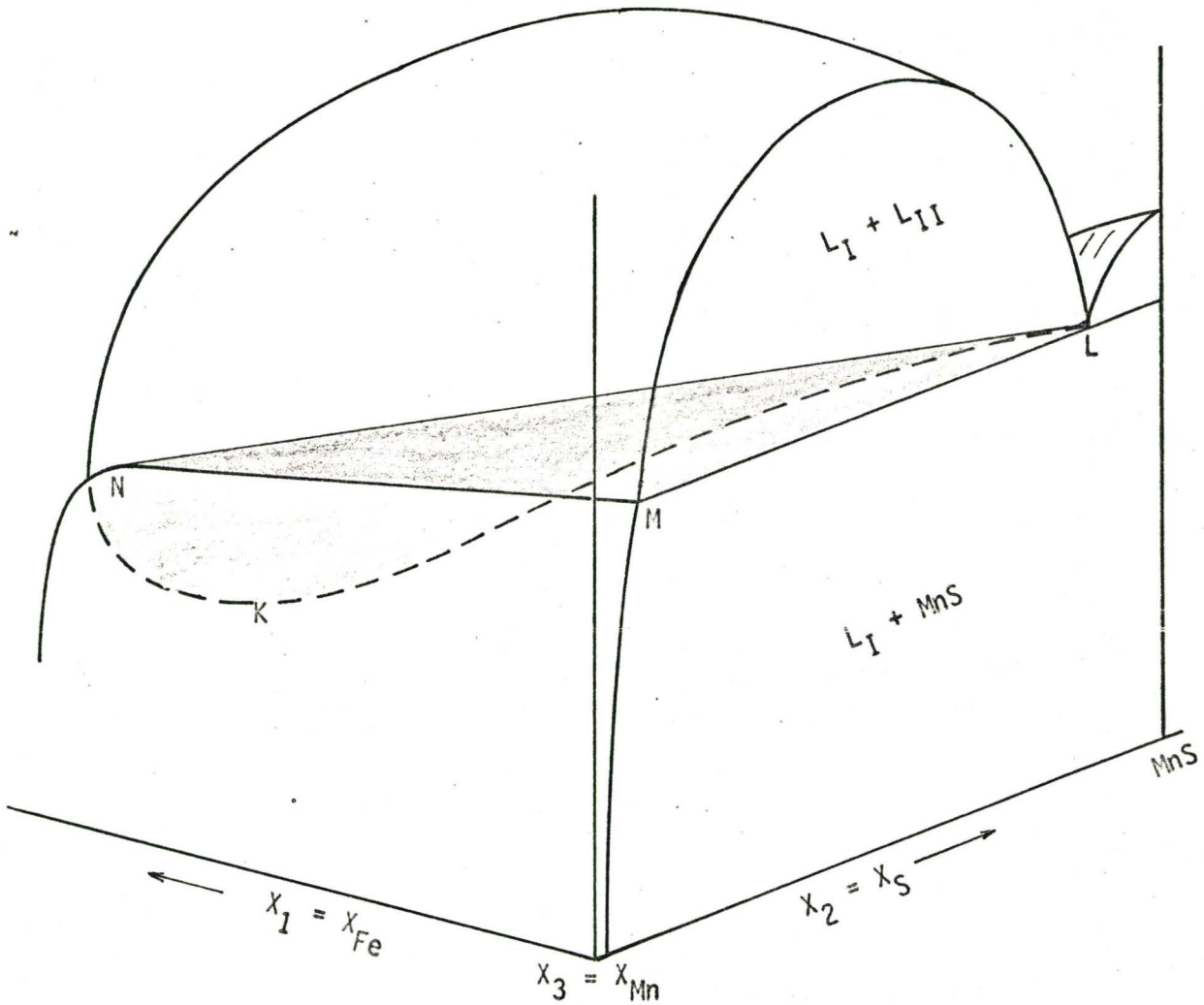

Figure 3.3A The Fe-Mn-S phase diagram showing the miscibility gap as viewed from the Mn corner of the diagram.

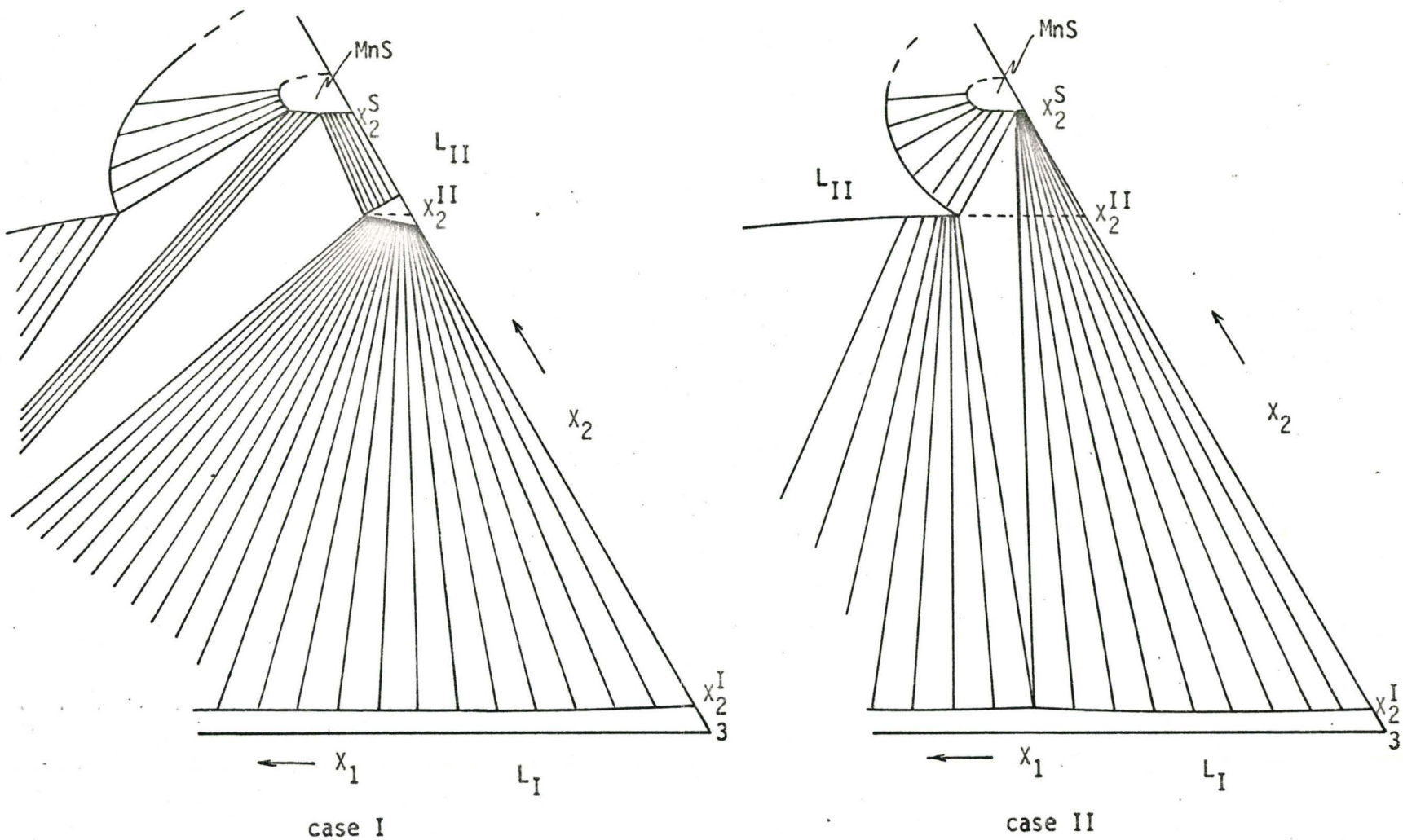

Figure 3.3B The possible phase relationships when the direct reaction between solid MnS and the miscibility gap occurs.

two points of temperature maximum on their miscibility gap limit curve as shown in Figure 2.12 (i.e., points M_1' and M_2'). The statement is by no means unequivocal, and while they predict that their maxima should be near 1600°C (and certainly above 1580°C) their experimental data, and the data of others, doesnot clearly indicate that the phase L_I has ever been in equilibrium with the MnS phase.

Case II is the more probable. We generally expect a binary eutectic temperature (and also a monotectic temperature) to be lowered by the addition of a third component, particularly when the third component has a lower melting point than the eutectic itself. This eutectic depression is almost certainly required by the freezing point depression which we observe in the FeS-MnS pseudo-binary when FeS is added to MnS and in the Mn-Fe binary when Fe is added to Mn. Case I also requires that the liquidus of the (MnS + L_{II}) two-phase field bow out to meet the (L_I + L_{II}) two-phase field at a point within the ternary system. This is inconsistent with out current conception of a highly singular solid MnS free energy surface in relation to a broad liquid MnS free energy surface and the fact that FeS depresses the melting point of MnS.

For case II where $(dT/dX_{Fe})_{X_S=\text{const}, X_{Fe}\to 0}$ is negative we can demonstrate thermodynamic consistency by writing the Gibbs-Duhem equations for three phases in equilibrium at constant pressure as

$$\Sigma\, X_i^I \, d\mu_i = -S^I \, dT \qquad (3\text{-}1)$$

$$\Sigma\, X_i^{II} \, d\mu_i = -S^{II} \, dT \qquad (3\text{-}2)$$

$$\Sigma\, X_i^S \, d\mu_i = -S^S \, dT \qquad (3\text{-}3)$$

where i = 1(Fe), 2(S), 3(Mn), and the superscripts I = L_I, II = L_{II}, and S = MnS. In determinant notation the chemical potential $d\mu_i$ for

component i is

$$d\mu_i = \frac{dT|A_i|}{|D|} \tag{3-4}$$

or

$$\frac{d\mu_i}{dT} = \frac{|A_i|}{|D|} \tag{3-5}$$

Using the Wagner formalism (see Appendix I) one can write that

$$d\mu_1 = RT \frac{dX_1^I}{X_1^I} \{ 1 + \varepsilon_{11} X_1^I + \varepsilon_{12} X_1^I \frac{dX_2^I}{dX_1^I} \} \tag{3-6}$$

and because X_1^I and $dX_2^I/dX_1^I \to 0$, the approach to the limit is accurately represented by

$$d\mu_1 = RT \frac{dX_1^I}{X_1^I} \tag{3-7}$$

Combining equations 3-5 and 3-7 gives

$$\left.\frac{dX_1^I}{dT}\right|_{X_1^I \to 0} = \frac{1}{RT} \frac{|A_1|}{|D|/X_1^I} \tag{3-8}$$

where

$$|A_1| = \begin{vmatrix} -S^I & X_2^I & X_3^I \\ -S^{II} & X_2^{II} & X_3^{II} \\ -S^S & X_2^S & X_3^S \end{vmatrix} \tag{3-9}$$

and

$$|D| = \begin{vmatrix} X_1^I & X_2^I & X_3^I \\ X_1^{II} & X_2^{II} & X_3^{II} \\ X_1^S & X_2^S & X_3^S \end{vmatrix} \tag{3-10}$$

Now since the entropy of a high temperature phase (liquid) is always greater than the entropy of a lower temperature phase (solid) we can write

$$S^I = S^S + \alpha = S + \alpha \tag{3-11}$$

and

$$S^{II} = S^S + \beta = S + \beta \tag{3-12}$$

where α and β are the respective positive entropies of fusion. (Empirical evidence indicates that for pure components one can use the approximation $\alpha = \beta = 1.1R$, which is known as Richard's Rule[50]).

Also, since the analysis is defined for $X_{Fe} = X_1 \to 0$ in all phases (i.e., approaching the Mn-S binary), then

$$X_3 = (1 - X_1 - X_2) \simeq (1 - X_2) \tag{3-13}$$

To determine the sign of $|A_1|$ we substitute equation 3-13 for X_3^I, X_3^{II} and X_3^S, and equations 3-11 and 3-12 into equation 3-9. This gives

$$|A_1| = - \begin{vmatrix} S + \alpha & X_2^I & 1 - X_2^I \\ S + \beta & X_2^{II} & 1 - X_2^{II} \\ S & X_2^S & 1 - X_2^S \end{vmatrix} \tag{3-14}$$

and thus

$$|A_1| = \alpha(X_2^S - X_2^{II}) - \beta(X_2^S - X_2^I) \tag{3-15}$$

Now if we note that α and β are of the same positive magnitude as $X_1 \to 0$, and from Figure 3.3A we see that $(X_2^S - X_2^I) \gg (X_2^S - X_2^{II})$, we can conclude that $|A_1|$ is negative.

To demonstrate that $|D|/X_1^I > 0$, so that $dT/dX_{Fe} < 0$, we substitute equation 3-13 for X_3^I, X_3^{II}, and X_3^S into equation 3-10 giving after rearrangement the non-zero quantity

$$|D|/X_1^I = -(X_2^S - X_2^{II}) + (X_2^S - X_2^I)X_1^{II}/X_1^I - (X_2^{II} - X_2^I)X_1^S/X_1^I \qquad (3\text{-}16)$$

Noting that for this system all tie-lines at the temperature of interest converge towards MnS we can say that $X_1^S << X_1^I$, X_1^{II}, and noting that $X_2^I << X_2^S$ (see Figure 2.4) we can approximate equation 3-16 by

$$|D|/X_1^I \simeq -(X_2^S - X_2^{II}) + X_2^S X_1^{II}/X_1^I \qquad (3\text{-}17)$$

Now the geometric requirement implied by case II in Figure 3.3B is

$$X_1^{II}/X_1^I > (X_2^S - X_2^{II})/X_2^S \qquad (3\text{-}18)$$

so

$$|D|/X_1^I > 0$$

from which

$$(dT/dX_{Fe})_{X_S=\text{const},X_{Fe}\to 0} > 0 \qquad (3\text{-}19)$$

B.1.2. The Optimum at Point K

We have been assuming with other workers that point K, the critical point of the miscibility gap on the line MNKL, is a minimum with respect to temperature but we have found no proof in the literature that this should be so. As we shall show in the following K must be an optimum, and because of the slopes of the line MNKL at points M and L it is indeed a minimum.

Since one characterization of the critical point is that $X_i^I = X_i^{II}$ and $S^I = S^{II}$, from relation 3-9 we see that $|A_1|=|A_2|=0$ and so $d\mu_1/dT=d\mu_2/dT=0$. Now since in general

$$\mu_1 = \mu_1 (X_1, X_2, T) \qquad (3\text{-}20)$$

$$\mu_2 = \mu_2 (X_1, X_2, T) \tag{3-21}$$

we can write the total derivatives as

$$\frac{d\mu_1}{dT} = \mu_{11} \frac{dX_1}{dT} + \mu_{12} \frac{dX_2}{dT} + \frac{\partial \mu_1}{\partial T} \tag{3-22}$$

and

$$\frac{d\mu_2}{dT} = \mu_{21} \frac{dX_1}{dT} + \mu_{22} \frac{dX_2}{dT} + \frac{\partial \mu_2}{\partial T} \tag{3-23}$$

where $\mu_{ij} = \partial \mu_i / \partial X_j$ for i,j = 1,2. The solutions are

$$\frac{dX_1}{dT} = \frac{|A_1'|}{|D'|} \quad \text{and} \quad \frac{dX_2}{dT} = \frac{|A_2'|}{|D'|} \tag{3-24}$$

where

$$D' = \mu_{11} \mu_{22} - \mu_{12} \mu_{21} \tag{3-25}$$

$$|A_1'| = - \mu_{22} \left(\frac{\partial \mu_1}{\partial T} - \frac{d\mu_1}{dT}\right) - \mu_{12} \left(\frac{\partial \mu_2}{\partial t} - \frac{d\mu_2}{dt}\right) \tag{3-26}$$

and

$$|A_2'| = - \mu_{11} \left(\frac{\partial \mu_2}{\partial T} - \frac{d\mu_2}{dt}\right) - \mu_{21} \left(\frac{\partial \mu_1}{\partial t} - \frac{d\mu_1}{dt}\right) \tag{3-27}$$

Since in general A_1' and A_2' are non-zero, and at a critical point $D' = 0$[51], it follows that

$$\frac{dX_1}{dT}, \frac{dX_2}{dT} \to \pm \infty \tag{3-28}$$

That is to say

$$dT/dX_i \to 0 \tag{3-29}$$

so the point is some kind of optimum in terms of temperature.

In section B.1.1 we have shown that the lines MN and LK fall towards the Fe-rich side of the phase diagram. Since these lines are part of the continuous curve MNKL, and since K is an optimum on this curve, we must conclude that point K is indeed a minimum with respect to temperature.

B.2. The Character of the Eutectic Trough Maximum*

The maximum at point C on the eutectic trough represents the composition and temperature at which the two-phase regions (L_I + MnS) and (L_I + δFe) first directly meet. From the fact that the tie-lines in the large (L_I + MnS) two-phase region tend to be oriented between the Fe and MnS corners and that δ-Fe and MnS are the only solids at this temperature, it appears reasonable that their first interaction should be deep in the iron corner.

In section A of this chapter the employment of free energy surfaces to qualitatively predict isotherms for a three-component system was outlined. In the following discussion use will be made of this method

---

* We have named point C the "eutectic trough maximum" for purposes of identification in subsequent discussions. Its composition in the Fe-Mn-S system is labelled (X^C_{Mn}, X^C_S) and the temperature at which it occurs, T_C.

to qualitatively examine the reaction between MnS and δ-Fe when these phases first react together. Knowing that MnS is a high melting point compound, knowing from our own research that MnS has a low solubility for iron when in equilibrium with iron and knowing the limits of the liquid-liquid miscibility gap near the melting point of iron, one can sensibly infer the shape of the free energy surfaces associated with MnS, δ-Fe, and the liquid phases. These surfaces are illustrated in Figure 3.4. One must remember throughout this analysis that the free energy surfaces are being viewed upside-down for ease of visualization.

Associated with the free energy versus composition diagram in Figure 3.4 is a Gibb's triangle with an arrow indicating the viewing direction, and the identification of the three component corners. The difference between this free energy diagram and that in Figure 3.1 is that the δ-Fe phase, having just crystallized, is present and is represented by a rather singular surface (inferred from the binaries) in the iron corner behind the liquidus surface.

As the temperature of the system decreases the liquid phase becomes less stable with respect to the δ-Fe and MnS phases. That is to say, the liquid free energy surface is lowered relative to the δ-Fe and MnS surfaces in Figure 3.4. Figure 3.5 illustrates the situation in which the temperature has decreased sufficiently to permit the direct interaction of δ-Fe and MnS, but is still high enough to maintain a liquid phase towards Mn and FeS. A tangent plane rotated about the surfaces then produces the 2-phase region, (δ-Fe + MnS), bounded by two 3-phase regions. The accompanying isotherm in Figure 3.5 shows the phase relations at this temperature T_2. The free energy surfaces and the isotherm indicate that the

liquid phase, L_I, of Figure 3.4 has split into two liquids, L_1 and L_{III}.

To show the precise character of the eutectic trough maximum we refer to Figure 3.6. A vertical plane is imagined to intersect the free energy surfaces such that this plane passes through points A and B. The inset in Figure 3.6 is the normal view of this vertical plane. The curve L on this plane represents the line of intersection between the liquid free energy surface and this plane, and it has the form associated with a binary miscibility gap (upside down). This suggests that if one could super cool a liquid having a composition between A and B on the vertical plane, then this liquid would eventually decompose into two metastable liquids, L_1 and L_{III}.

Also present on the vertical plane is the trace of the contact point of the tangent plane rotating between δ-Fe and MnS on the vertical plane (marked α and β). The combination of traces on the vertical plane permits one to predict the stable phases in this plane at temperature T_2 by treating the vertical plane as a pseudo-binary with the usual equilibrium tangent lines.

As we raise the temperature from T_2 the relatively flat liquid free energy surface in Figure 3.6 rises relative to the δ-Fe and MnS surfaces. As a result the two and three phase regions begin to collapse. This is illustrated in Figure 3.7, points A and B moving along the ridge towards each other. At the same time the other points of the three-phase region approach each other. The curves on the vertical plane through A and B also change character. This is shown in the inset of Figure 3.7. The δ-Fe and MnS trace remains relatively stationary as the L trace rises with respect to it, and loses its binary immiscibility character as the

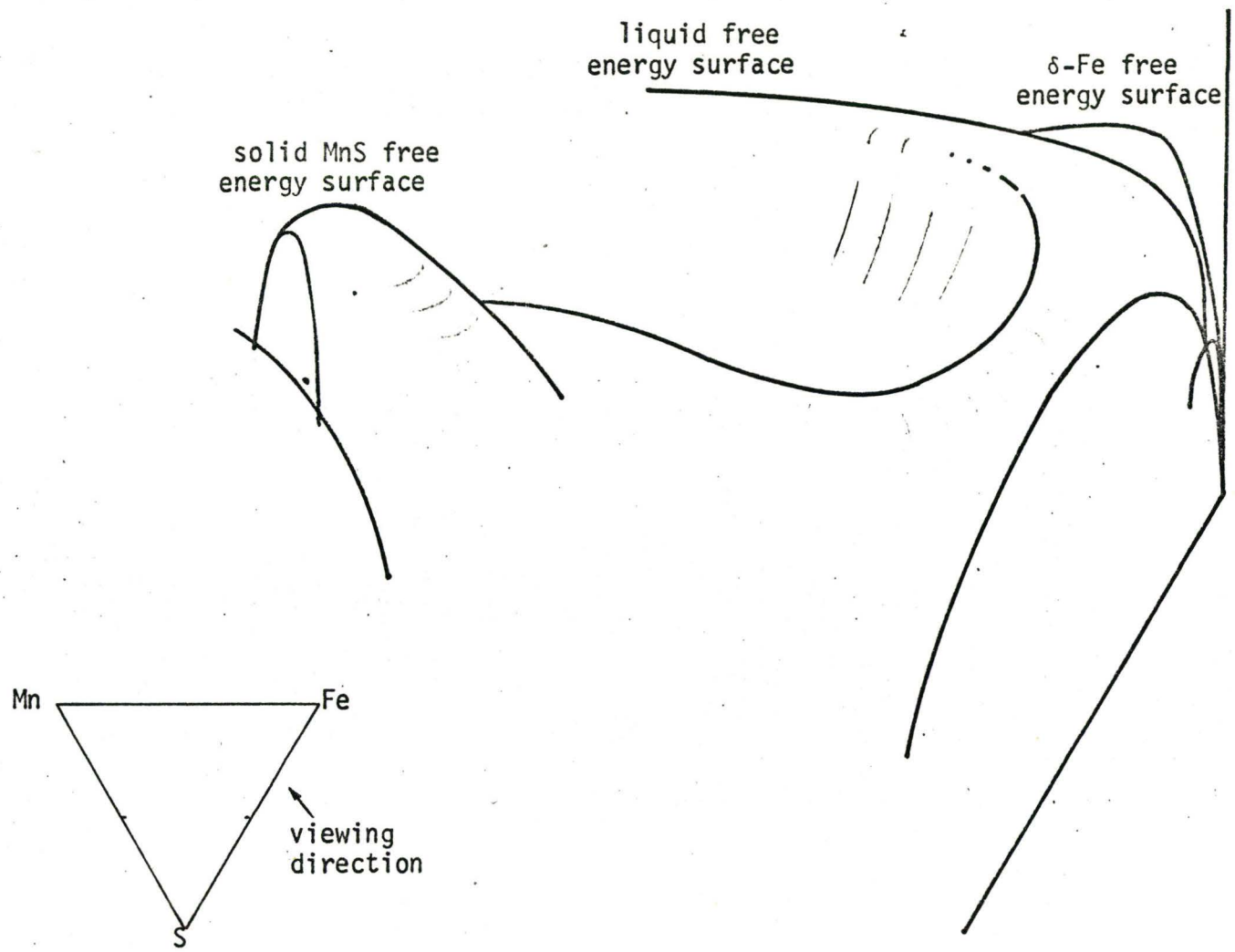

Figure 3.4 The schematic free energy-composition diagram for the Fe-Mn-S system at a temperature where δ-Fe has crystallized.

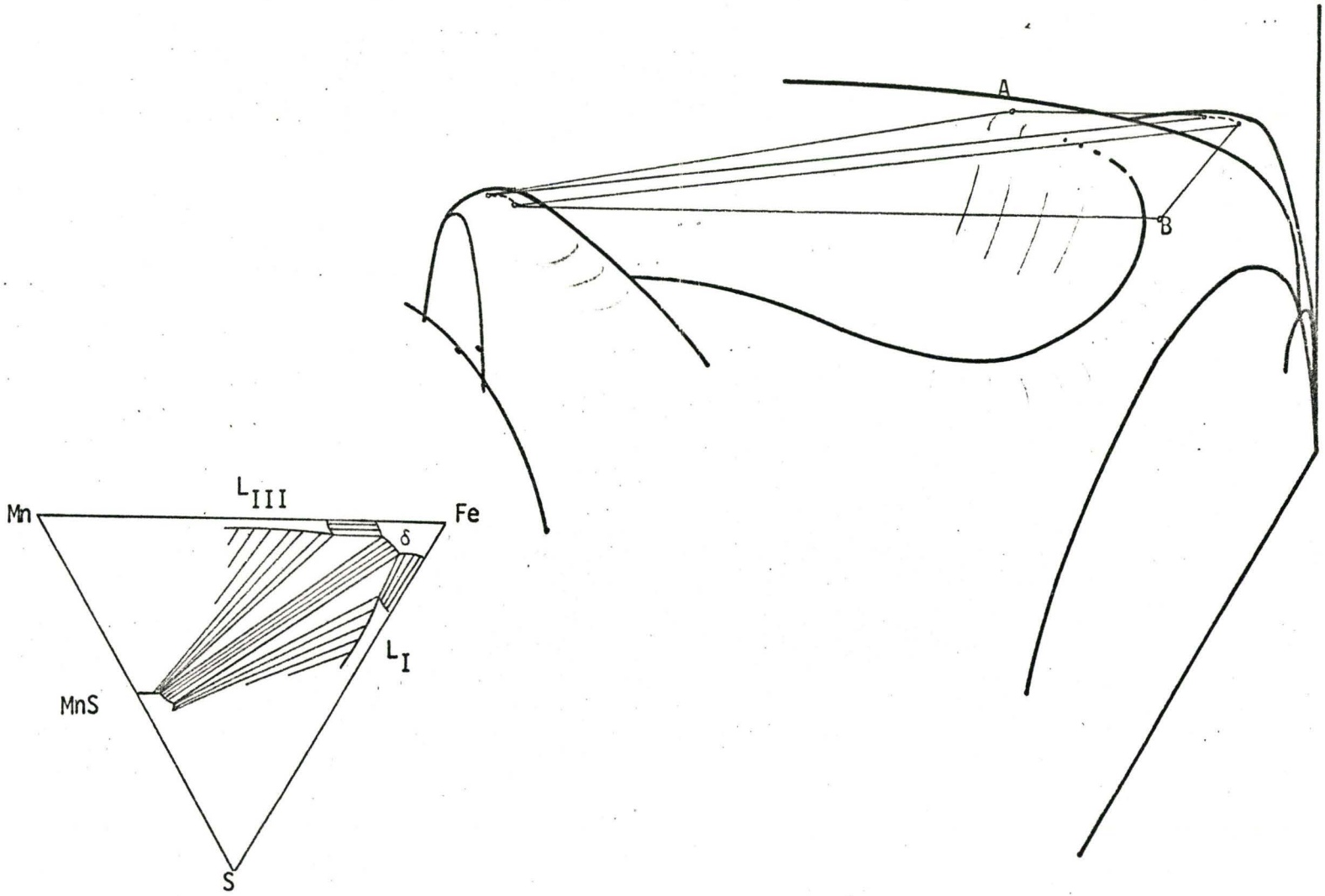

Figure 3.5 The schematic free energy-composition diagram for the Fe-Mn-S system at a temperature where δ-Fe and solid MnS can form a two-phase field.

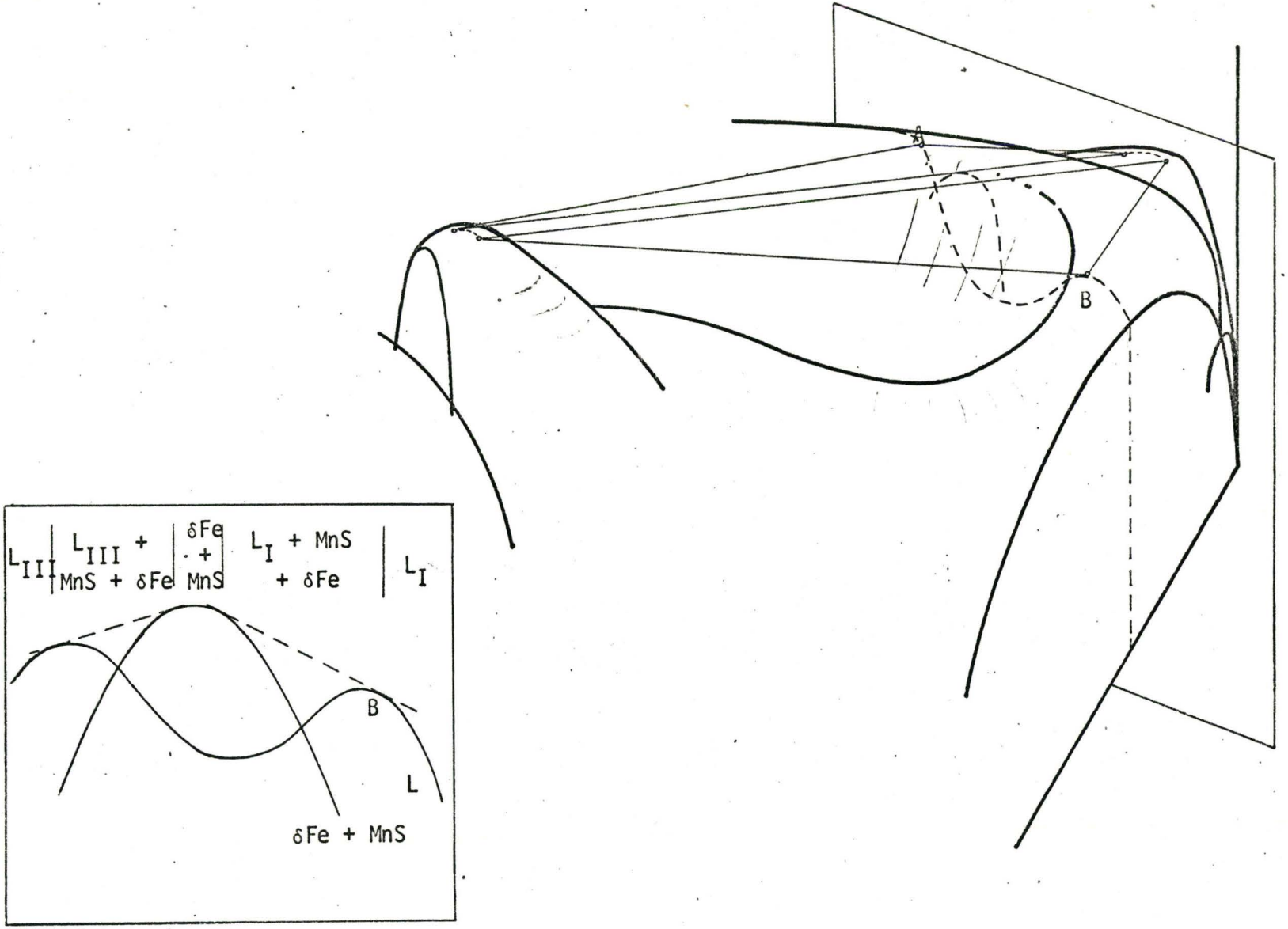

Figure 3.6 The schematic free energy-composition diagram for the Fe-Mn-S system showing a vertical plane cutting the surfaces at points A and B.

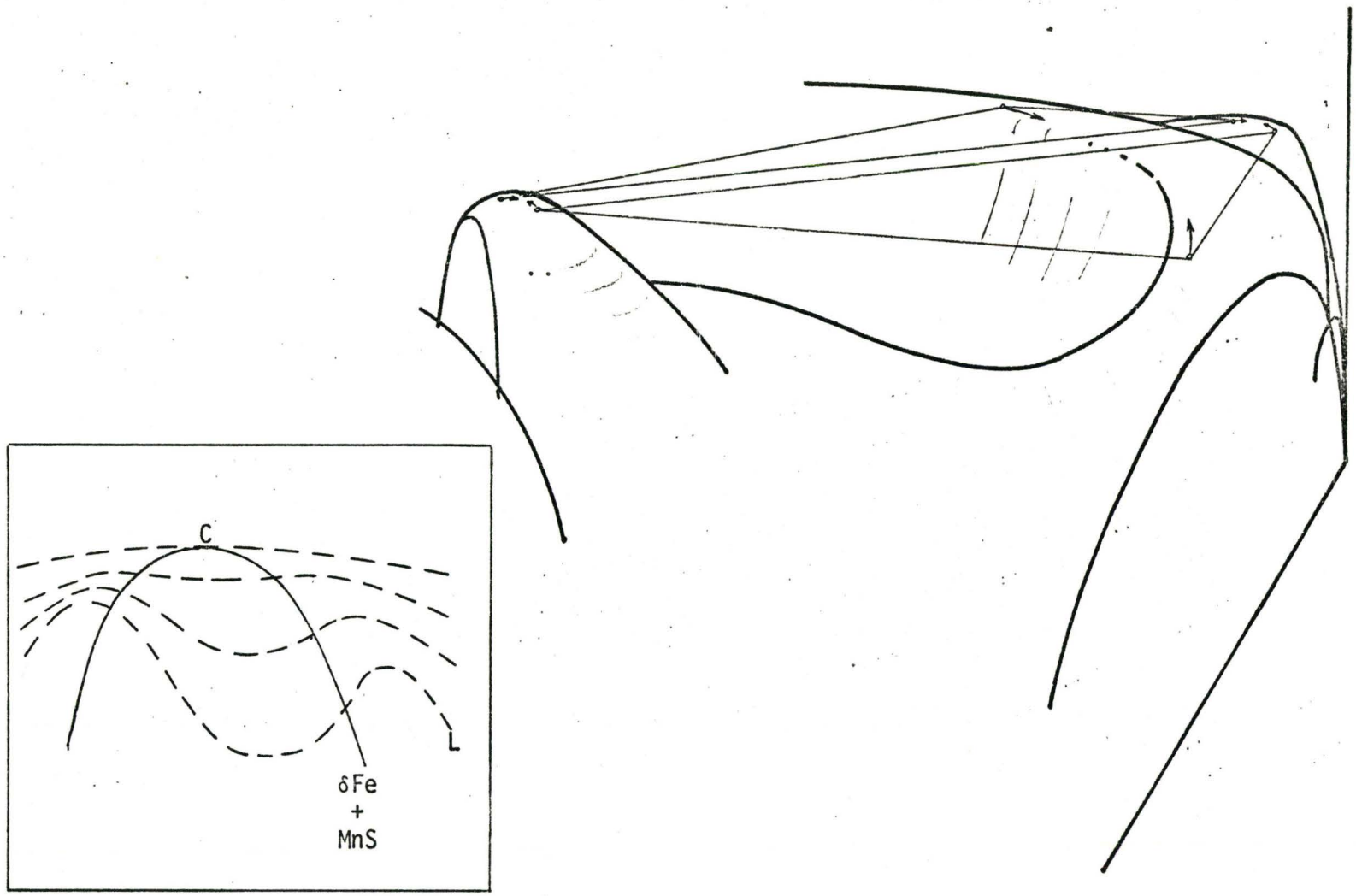

Figure 3.7 As the δ-Fe and Mns surfaces fall with respect to the liquid surface the corners of each three-phase tangent plane approach each other.

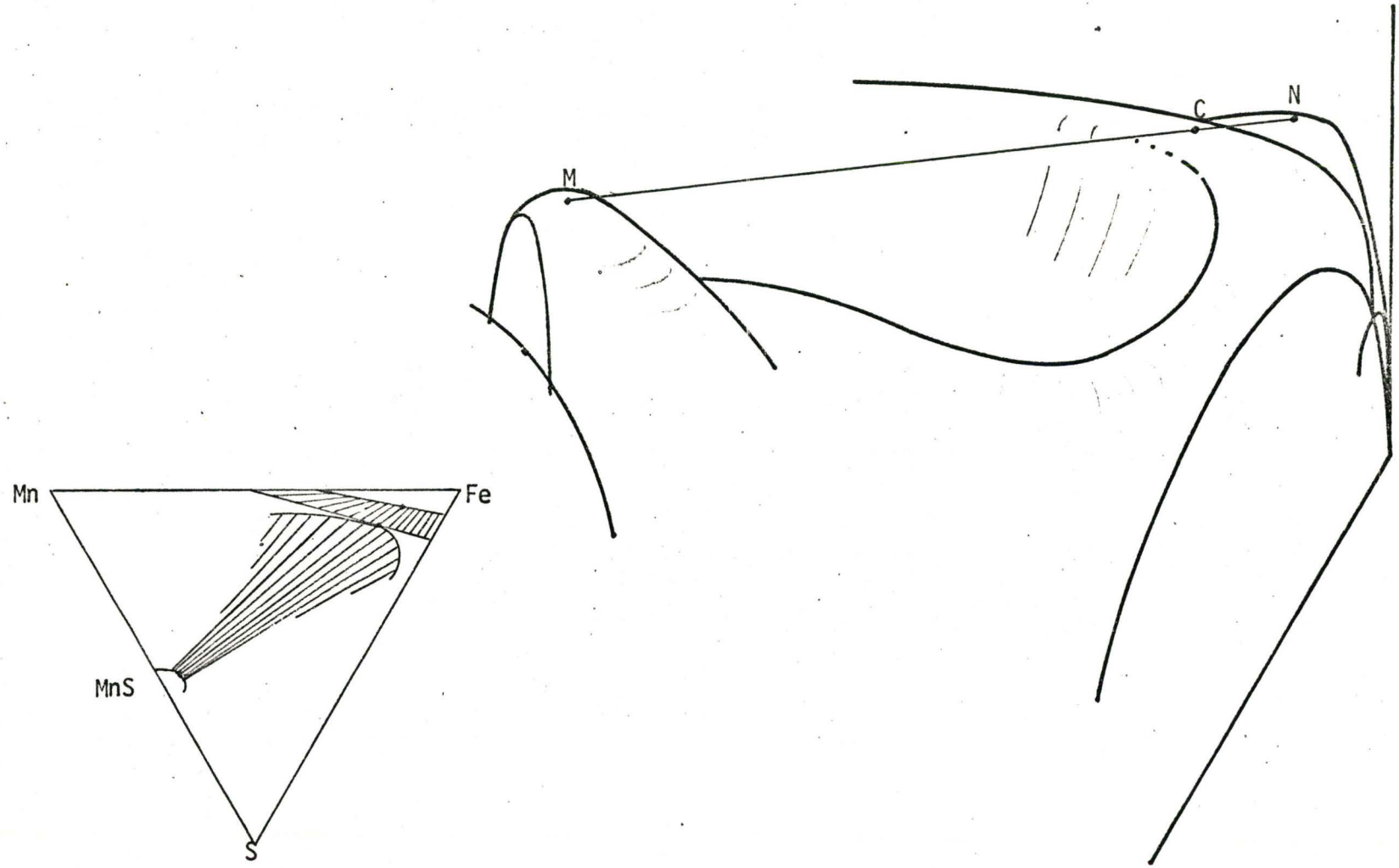

Figure 3.8 The two three-phase tangent planes have reduced to line MCN which is representative of a pseudo-binary reaction at the temperature $T = T_C$.

points A and B move closer together. At a temperature T_c the points A and B coincide with each other and with the δ-Fe and MnS trace at point C. The result is that the two liquids L_I and L_{III} merges as the single liquid L_I which in turn is in equilibrium with the δ-Fe and MnS phases. This is illustrated in Figure 3.8. The δ-Fe + MnS + L_I equilibrium is now represented by a straight line MCN, and not by the usual ternary triangle. This reaction is recognizeable as a true pseudo-binary eutectic. Accompanying Figure 3.8 is the isotherm to be associated with the free energy surfaces at the temperature T_c. We see that temperature T_c is the temperature at which the δ-Fe and MnS phases first react directly with each other. Since points A and B of Figure 3.5 also lie in the eutectic trough, T_c must be a maximum temperature in the trough. This maximum is a direct consequence of the strong singularity of the δ-Fe free energy surface relative to that of the liquid.

B.3. The Character of the γ-Fe-δ-Fe Equilibrium in the Eutectic Trough

In Figure 3.2 there are two points, S and T, on the eutectic trough, one on each side of point C, which have not as yet been described. Initially one might be inclined to regard these points as ternary eutectic points since they lie in the eutectic trough. This implies that, relative to the temperature of the surrounding liquidus surfaces, each point must be a temperature cusp of minimal character, and that each of the three troughs converging to each point is a eutectic trough. In general a ternary eutectic is represented by the four phase equilibrium

$$L \underset{\text{heating}}{\overset{\text{cooling}}{\rightleftarrows}} \alpha + \beta + \gamma$$

and geometrically on the Gibbs' triangle as

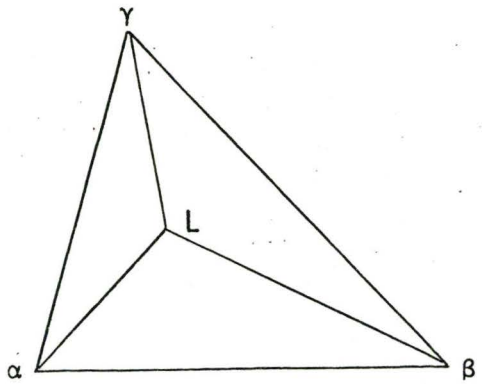

Referring to the Fe-Mn and Fe-S binary systems one notes that the troughs eminating from the Fe-Mn and Fe-S binaries are associated with peritectic and extectic reactions, respectively, and not with eutectic reactions so the points S and T can$_{not}$ be ternary eutectic points.

To describe the exact nature of these points a series of schematic isotherms have been presented in Figure 3.9, which represent the sequence of phase transformations that occur as the temperature is lowered through points S and T. The course of events is self-explanatory.

Figure 3.9c and Figure 3.9e are particularly significant. In each, one notes that a region of four phase equilibrium occurs, and recalling the Phase Rule, one realizes that each four phase region is invariant with respect to temperature and composition at a given pressure. At the temperature T_S (Figure 3.9c) the four phase equilibrium is described chemically by

$$\delta Fe + L_{III} \underset{\text{heating}}{\overset{\text{cooling}}{\rightleftarrows}} \gamma Fe + MnS$$

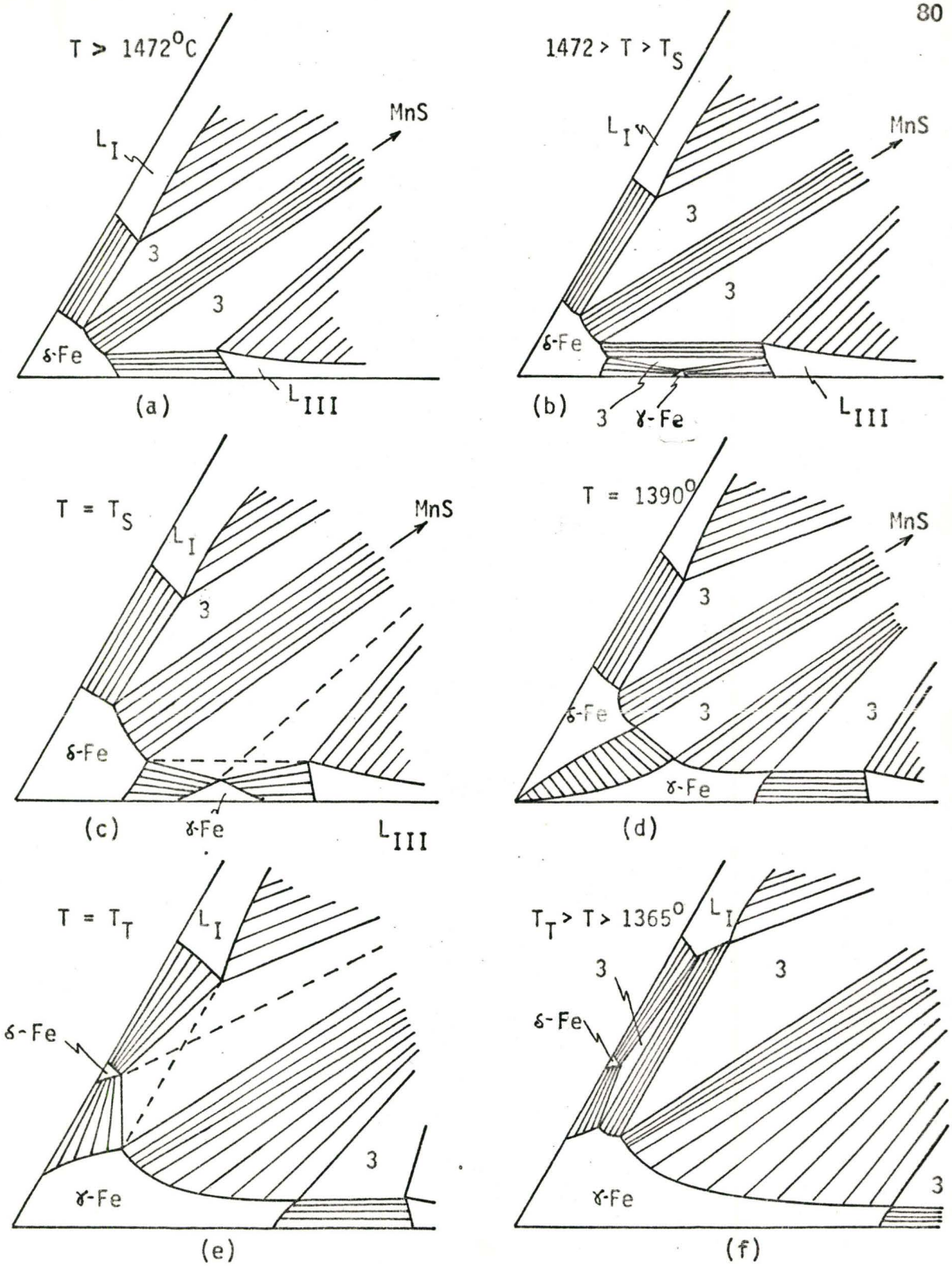

Figure 3.9 A schematic series of isotherms showing the Fe corner of the Fe-Mn-S system in which the phase transitions involving the δ-Fe to γ-Fe alotropic change are illustrated. Note the four-phase equilibrium (class II) at the temperatures T_S and T_T.

and geometrically on the Gibbs' triangle by

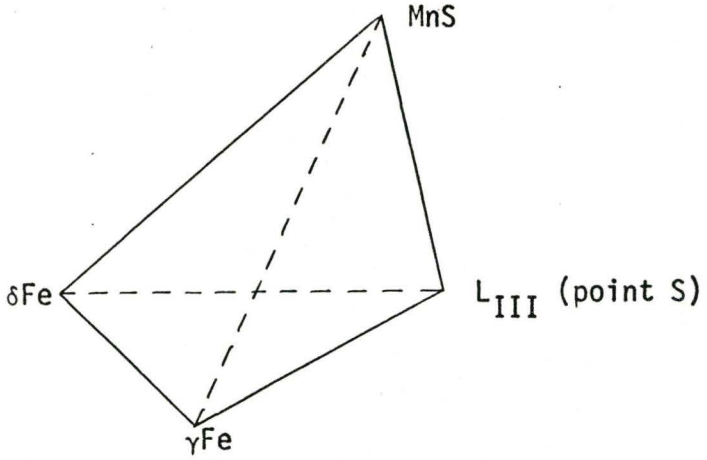

Similarly at the temperature T_T (Figure 3.9e) the four phase equilibrium is described by

$$\delta Fe + MnS \underset{\text{heating}}{\overset{\text{cooling}}{\rightleftharpoons}} Fe + L_I$$

and geometrically by

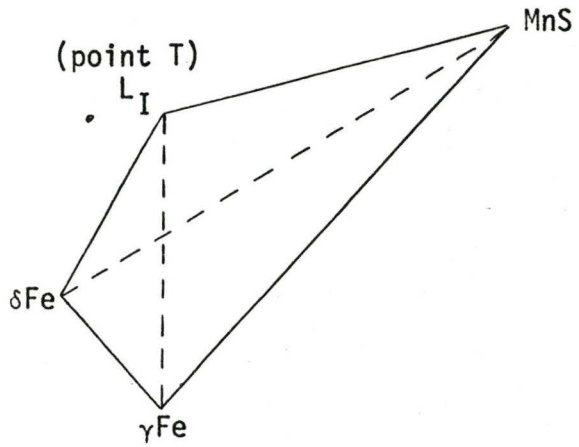

At temperatures T_S and T_T the character of the four phase equilibria are decidedly different than for the ternary eutectic four phase equlibrium. Rhines[52] in his book, Phase Diagrams in Metallurgy, has identified three classes of four phase equilibria: I, II, and III. The above equilibria

are of class II type, whereas the eutectic four-phase equilibrium is a class I type. Class III, not encountered in this system, is the ternary equivalent of a peritectic reaction.

The class II type of equilibrium does not require a temperature minimum at the points S and T, and thus the lines joining S and T to the respective binaries are not troughs but discontinuities in the slope of the liquidus surface. It is of interest to note that the line starting at point S rises with temperature to the Fe-Mn binary, but the line starting at point T falls with temperature to the Fe-S binary.

C. SOLUBILITY THEORY FOR A THREE-COMPONENT SYSTEM

The preceding sections have dealt with the more general, qualitative aspects of the reactions at the Fe-Mn-S liquidus surface. In this section a more rigorous thermodynamic analysis will be made. A solution theory for a three-component system is developed which allows one to quantitatively connect dilute solubilities as a function of composition, temperature and pressure. Although the formalism was developed primarily for solid solutions, in particular for the solubilities of Mn and S in γ-Fe, it will be seen in a later chapter that it can also be usefully applied to the liquidus surface. Because the theory may be used for any three-component system which meets the conditions outlined below, the formalism is kept general (i.e. in terms of components 1, 2, and 3). A more general theory for an n-component system is outlined in Appendix II.

C.1. Assumptions

At the outset it must be made clear that this analysis is applicable to low solubilities and to certain types of phase diagrams. It is assumed firstly that the solubilities of the components in the solvent phase are such that the Wagner formalism, as applied to dilute solutions, is applicable. That is, the activity coefficient for component i in the form of ($\ln \gamma_i$) may be represented by a linear Taylor's expansion where the coefficients of the ensuing terms, ($\partial \ln \gamma_i / \partial X_j = \varepsilon_{ij}$) defined as the Wagner interaction coefficients, are constant. This approximation is usually satisfactory up to $X_i = 0.01$ and in some cases up to $X_i = 0.1$.

Secondly, Figure 3.10 shows a schematic example of the type of diagram to which our analysis applies. Phase I is the solvent phase to which the dilute solution approximation applies. Phase II is the phase which is in thermodynamic equilibrium with phase I and it is assumed that the tie-lines defining the two-phase field on the isotherm all originate from a point on phase II (e.g. constant composition) and radiate to cover the appropriate solubility limits on phase I. This assumption may appear to be highly restrictive, but in fact many interesting situations do exist which adhere to this restriction, and as we shall show, it can be appreciably relaxed without the introduction of serious error.

C.2. The Differential Equation

The Gibbs-Duhem equation may be written for phase P in a system at uniform temperature and pressure as

$$\Sigma X_i^P \, d\mu_i^P = V^P \, dP - S^P \, dT \qquad (3\text{-}37)$$

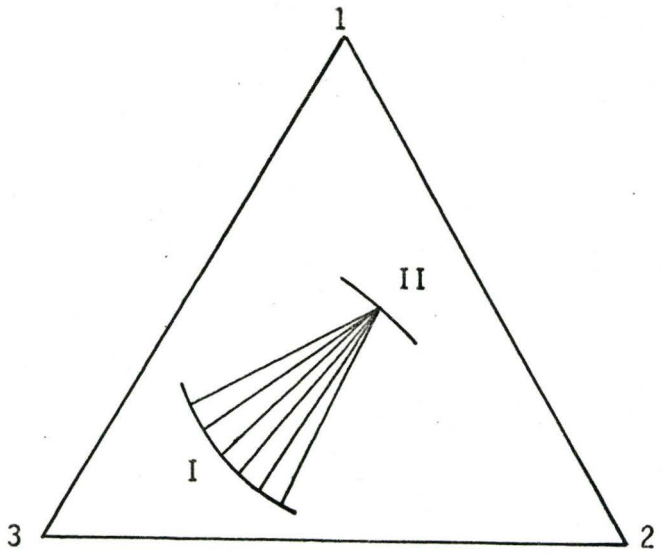

Figure 3.10 Isothermal conditions for two phase equilibrium in a three component system.

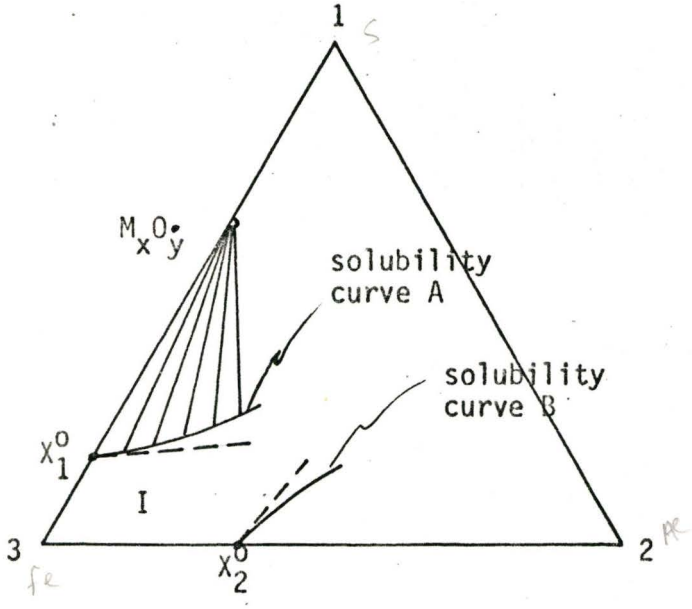

Figure 3.11 Isotherm for a three-component system showing the solubility curves for M_xO_y in equilibrium with phase I.

For the three component system of solutes 1 and 2 dissolved in solvent 3 at constant temperature and pressure, equation 3-37 for phases I and II in equilibrium ($\mu_i^I = \mu_i^{II}$) becomes

$$X_1^I \, d\mu_1 + X_2^I \, d\mu_2 + X_3^I \, d\mu_3 = 0 \tag{3-38}$$

$$X_1^{II} \, d\mu_1 + X_2^{II} \, d\mu_2 + X_3^{II} \, d\mu_3 = 0 \tag{3-39}$$

Recalling that $\Sigma X_i = 1$ and subtracting (3-39) from (3-38) one gets

$$(X_1^{II} - X_1^I)(d\mu_1 - d\mu_3) + (X_2^{II} - X_2^I)(d\mu_2 - d\mu_3) = 0 \tag{3-40}$$

Now according to the Wagner formalism in the linear approximation

$$d\mu_1 = \frac{dX_1}{X_1} + \varepsilon_{11} dX_1 + \varepsilon_{12} dX_2 \tag{3-41}$$

$$d\mu_2 = \frac{dX_2}{X_2} = \varepsilon_{21} \, dX_1 + \varepsilon_{22} dX_2 \tag{3-42}$$

$$d\mu_3 = -dX_1 - dX_2 \tag{3-43}$$

Equations 3-41, 3-42, and 3-43 are derived in Appendix I. Substitution of these three equations into equation 3-40 results after simplification in the following differential equation:

$$\left[\frac{a}{X_1} - bX_1 - cX_2 + p\right] dX_1 + \left[\frac{e}{X_2} - fX_2 - cX_1 + g\right] dX_2 = 0 \tag{3-44}$$

where

$$a = X_1^{II}$$

$$b = (1 + \varepsilon_{11})$$

$$c = (1 + \varepsilon_{21}) = (1 + \varepsilon_{12})$$

$$p = (1 + \varepsilon_{11})X_1^{II} + (1 + \varepsilon_{21})X_2^{II} - 1$$

$$e = X_2^{II}$$

$$f = (1 + \varepsilon_{22})$$

$$g = (1 + \varepsilon_{22})X_2^{II} + (1 + \varepsilon_{21})X_1^{II} - 1$$

In equation 3-44 the mole fractions X_1 and X_2 refer to phase I. The superscript 'I' has been dropped for purposes of visual clarity.

Because $\varepsilon_{12} = \varepsilon_{21}$, equation 3-44 is an exact differential equation and may easily be integrated with respect to the solute mole fractions X_1 and X_2. From this basic differential equation the solubility curves defining the limits of phase I under the prescribed conditions may be calculated.

C.3. Slope of the Solubility Curve at a Binary Limit

Figure 3.11 represents a type of phase diagram commonly encountered. Phase II is a small phase field in which the solubility of component 2 is very small, i.e., $X_2^{II} \to 0$. Also the range of solubility of components 1 and 3 on the binary 1-3 system is small. This describes the condition of a stoichiometric compound of the type M_xO_y where O and M are components 1 and 3, and x and y are small whole numbers.

If in equation 3-44 one lets $e = X_2^{II} = 0$, then one gets

$$\left[\frac{a}{X_1} - bX_1 - cX_2 + p\right] dX_1 + \left[g - cX_1 - fX_2\right] dX_2 = 0 \qquad (3\text{-}45)$$

or

$$\frac{dX_1}{dX_2} = \left[\frac{fX_2 + cX_1 - g}{a - bX_1^2 - cX_1X_2 + pX_1} \right] X_1 \qquad (3\text{-}46)$$

From Figure 3.11 one can see that dX_1/dX_2 is the slope of the solubility curve A of phase I at some point (X_1, X_2) on that curve. The slope at the binary limit is sometimes of interest. For the particular case where $X_2^{II} = 0$, $a = X_1^{II} = 0.5$, (e.g. a stoichiometric compound of the type MO), and $X_1 = X_1^o$ the solubility of 1 in phase I for the 1-3 binary, as $X_2 \rightarrow 0$ is

$$\left.\frac{dX_1}{dX_2}\right|_{X_2 \rightarrow 0} = \left[\frac{(1 + \varepsilon_{21})X_1^o - 0.5\ (1 + \varepsilon_{21}) + 1}{0.5 - (1 + \varepsilon_{11})X_1^{o2} + 0.5\ (1 + \varepsilon_{11})X_1^o - X_1^o} \right] X_1^o \qquad (3\text{-}47)$$

Now for $X_1^o \ll 1$ (in accordance with the Wagner approximation)

$$\left.\frac{dX_1}{dX_2}\right|_{X_2 \rightarrow 0} = (1 - \varepsilon_{21})\ X_1^o \qquad (3\text{-}48)$$

This result states that if one knows the sign and magnitude of the interaction coefficient ε_{21}, then the initial slope of the solubility curve is uniquely determined. It also states that when the interaction parameter is less than unity or negative the initial slope of the solubility curve is positive. That is, the addition of element 2 increases the solubility of element 1 in phase I. When ε_{21} is greater than unity, the slope is negative causing a decrease in the solubility of 1 when 2 is added. When $\varepsilon_{21} = 1$ the slope is zero indicating that the addition of 2 does not affect the solubility of 1, at least for low solubilities of 2 in phase I. When there is no interaction between the solute components ($\varepsilon_{21} = 0$), the slope

is positive as stated above, and equal in magnitude to the value of X_1^o. The smaller the value of X_1^o, the smaller the slope, and as $X_1^o \to 0$, the slope similarly approaches zero, or with respect to the isotherm, the system reduces to the 1-2 binary system.

Morris[53] has used equation 3-48 to estimate the character of the solubility curve in the Fe-Ni-O ternary system. As mentioned previously, equation 3-48 applies to the particular case of $X_1^{II} = 0.5$. Equation 3-49 is a more general form applicable to point X_1^o on Figure 3.11:

$$\left.\frac{dX_1}{dX_2}\right|_{X_2 \to 0} = \left[1 - (1 + \varepsilon_{21})X_1^{II}\right] \frac{X_1^o}{X_1^{II}} \qquad (3\text{-}49)$$

From 3-49 one sees that for

$X_1^{II} = 0.5$ (an MO compound), $dX_1/dX_2 = (1 - \varepsilon_{21})\, X_1^o$

$X_1^{II} = 0.6$ (an M_2O_3 compound), $dX_1/dX_2 = (\frac{2}{3} - \varepsilon_{21})\, X_1^o$

$X_1^{II} = 4/7$ (an M_3O_4 compound), $dX_1/dX_2 = (\frac{3}{4} - \varepsilon_{21})\, X_1^o$

$X_1^{II} = 1$ (pure O), $dX_1/dX_2 = -\varepsilon_{21}\, X_1^o$

It must be remembered that equation 3-49 applies only to the slope as $X_2 \to 0$, and says nothing about the slope (or solubility) as X_2 increases in value.

C.4. Solubility Curve from the 1-3 and 2-3 Binaries

Referring again to Figure 3.11 one can determine by integration the precise equation defining the solubility curve A originating at the

1-3 binary. This curve is also regulated by the previous restrictions placed on phase II. Thus one considers a stoichiometric compound M_xO_y which has a low solubility for component 2. Again $e = X_2^{II} = 0$ in equation 3-44. The integrated result is

$$a \ln X_1 - \frac{bX_1^2}{2} + pX_1 - cX_1X_2 - \frac{fX_2^2}{2} + gX_2 = k \qquad (3\text{-}50)$$

where k is an integration constant. Now for $X_1 \ll 1$, equation 3-50 may be simplified by neglecting the second and third terms so that

$$a \ln X_1 - cX_1X_2 - \frac{fX_2^2}{2} + gX_2 \simeq k \qquad (3\text{-}51)$$

To find k one lets $X_2 = 0$ (and thus $X_1 = X_1^o$) in equation 3-51 to yield

$$k = a \ln X_1^o \qquad (3\text{-}52)$$

Thus the solubility equation is

$$X_1^{II} \ln X_1 - (1 + \varepsilon_{21}) X_1X_2 = \frac{(1 + \varepsilon_{22})}{2} X_2^2 - (1 + \varepsilon_{21}) X_1^{II} X_2 + X_2 + X_1^{II} \ln X_1^o \qquad (3\text{-}53)$$

Figure 3.12 shows plot of this equation for the case in which phase II is a stoichiometric compound of the type MO (i.e. $X_1^{II} = 0.5$) and $X_1^o = 0.01$. A series of solubility curves is drawn for a typical range of values of ε_{21} and ε_{22}. From Figure 3.12 one can see that all the curves are concave upwards. One also notes that the sign and magnitude of ε_{22} is relatively insignificant compared to the sign and magnitude of ε_{21}. An interesting situation occurs when ε_{21} is slightly greater than unity. From equation 3-48 one would predict a negative slope for the solubility equation. That

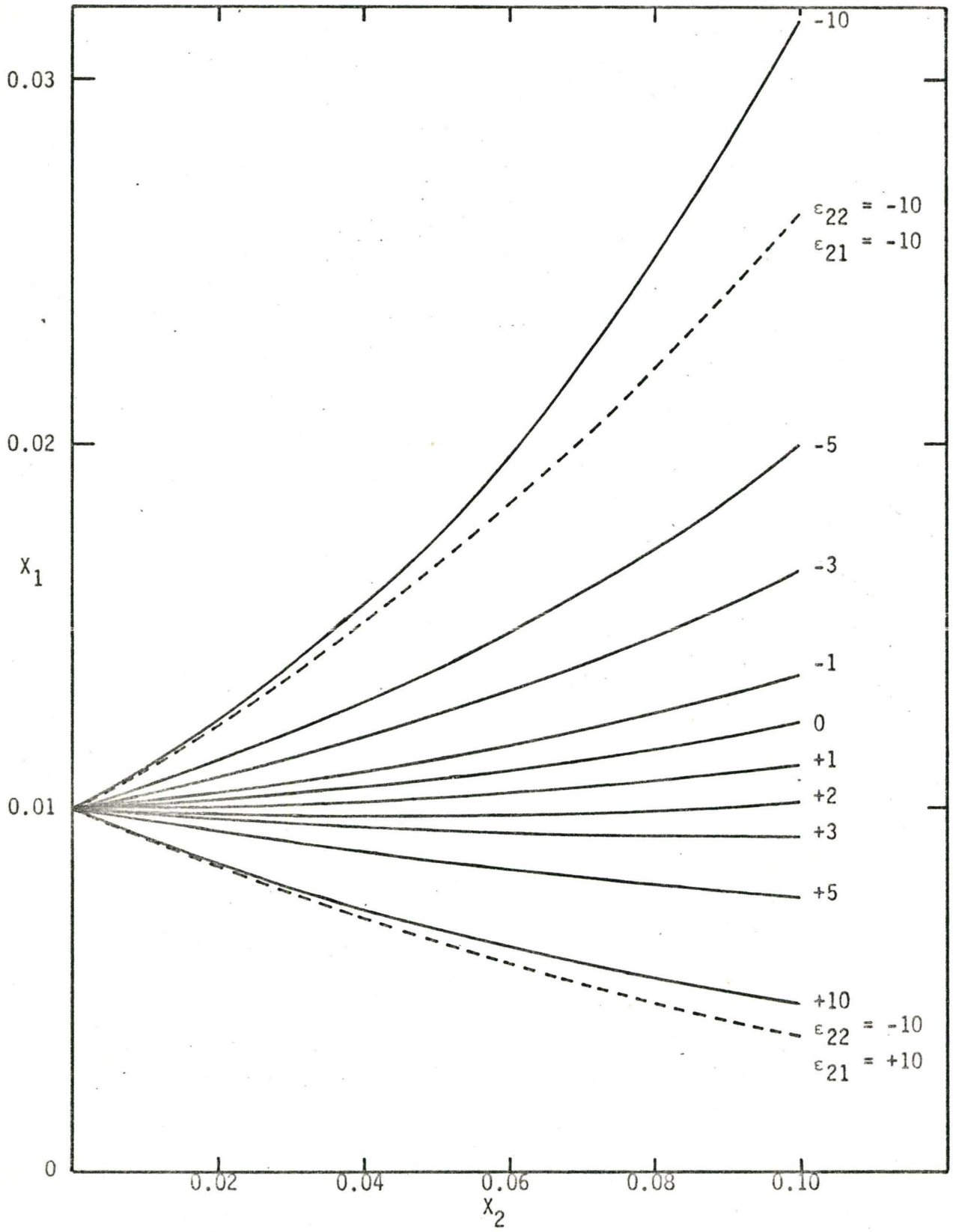

Figure 3.12 Solubility curves for the stoichiometrie compound MO in equilibrium with phase I for ε_{21} = -10 to +10 and ε_{22} = -10 and +10.

is, as X_2 increased in value, X_1 would decrease. But because of the concave nature of the curve it is possible for the slope to change sign with increasing values of X_2 when ε_{21} is slightly greater than unity. This aspect will be dealt with further in section C.6 of this chapter.

It should also be noted that as X_1^o decreases sharply in value the character of the solubility curves also changes significantly. In equation 3-53 one can see that if X_1^o is very small, then the ln terms begin to predominate, and this equation becomes simply

$$X_1^{II} \ln X_1 = X_1^{II} \ln X_1^o \tag{3-54}$$

That is the curve is a straight line parallel to the 3-2 binary. This may also be seen from equation 3-48. For a value of $\varepsilon_{21} = \pm 10$, and $X_1^o = 0.0001$

$$\left.\frac{dX_1}{dX_2}\right|_{X_2 \to 0} \simeq \frac{-}{+} 10^{-3} \tag{3-55}$$

which is approaching a zero slope. Thus for very low solubilities the solubility curve originating from that binary may be drawn as a straight line parallel to the adjacent binary system.

At this point it should be mentioned that the content of section C.3 and this section has been based upon the solubility curve originating at the 1-3 binary as described in Figure 3.11. However a similar analysis can be carried out for both the initial slope and the solubility curve originating at the 2-3 binary system simply by letting $a = X_1^{II} = 0$ in equation 3-44. Then one can find the initial slope dX_1/dX_2 as $X_1 \to 0$ at $X_2 = X_2^o$. The result is shown in equation 3.56

$$\left.\frac{dX_1}{dX_2}\right|_{X_1 \to 0} = \left[\frac{1}{1 - (1 + \varepsilon_{21})X_2^{II}}\right] \frac{X_2^{II}}{X_2^o} \tag{3-56}$$

One can see that equation 3-56 is obtained from 3-49 by exchanging subscripts 1 and 2. Similarly the solubility curve, depicted as curve B in Figure 3.11, may be written as

$$X_2^{II} \ln X_2 - (1 + \varepsilon_{12})\, X_1 X_2 = \frac{(1 + \varepsilon_{11})}{2} X_1^2 - (1 + \varepsilon_{21})\, X_2^{II}\, X_1 + X_1 + X_2^{II} \ln X_2^o \tag{3-57}$$

In this case phase II naturally applies to a phase of small but finite extent lying somewhere along the 2-3 binary.

C.5. Solubility Curve for Equilibria with a Non-Adjacent Binary Phase

It is possible, of course, for more than one phase to be in equilibrium with phase I. In the case considered here another phase, phase III, is in thermodynamic equilibrium with phase I. The location of phase III in the isotherm is immaterial as long as the assumption of a point emission of tie-lines holds. The differential equation is the same as equation 3-44 except that now the definition of 'a' and 'e' refer to phase III and not phase II. In the preceding cases either 'a' or 'e' have been equated to zero before integration. But in this case both 'a' and 'e' have definite, finite values and must, therefore, be retained. Thus the integration of 3-44 yields

$$a \ln X_1 - \frac{bX_1^2}{2} + pX_1 - cX_1X_2 + gX_2 - \frac{fX_2^2}{2} + e \ln X_2 = \text{constant} \qquad (3\text{-}58)$$

where the integration constant, which is generally a function of temperature and pressure, is yet to be determined.

It can be seen that if X_1 and $X_2 << 1$, all the terms in equation 3-50 except the ln terms may be dropped. Thus, to a first approximation

$$a \ln X_1 + e \ln X_2 = \frac{\ln K}{2} \qquad (3\text{-}59)$$

where $\frac{\ln K}{2}$ is the constant. For the particular case where $a = X_1^{III} = 0.5$ and $e = X_2^{III} = 0.5$, (a stoichiometric compound of the type MO on the 1-2 binary) one gets

$$\ln X_1X_2 = \ln K \qquad (3\text{-}60)$$

or

$$X_1X_2 = K \qquad (3\text{-}61)$$

K is now recognized as a typical chemical solubility product. The significance of K can be established by an alternative derivation. Consider the reaction

$$MO = \underline{M} + \underline{O} \qquad (3\text{-}62)$$

for which the equilibrium constant is

$$K' = \frac{a_M a_O}{a_{MO}} \qquad (3\text{-}63)$$

If one equates the activity, a_{MO}, to unity, and substitutes mole fractions for the activities a_M and a_O, then

$$K' = X_M X_O. \qquad (3\text{-}64)$$

or

$$K' = K \tag{3-65}$$

The integration constant, or solubility product K is thus approximately equal to the equilibrium constant of equation 3-62.

A more general case is when $X_1 \ll 1$ (as for the previous case) and X_2 is of significant magnitude. Then one must consider the terms involving X_2 in equation (3-58). The solubility equation becomes

$$a \ln X_1 - cX_1X_2 + gX_2 - \frac{fX_2^2}{2} + e \ln X_2 = \frac{\ln K}{2} \tag{3-66}$$

or substituting for the alphabetic characters

$$X_1^{III} \ln X_1 - (1 + \varepsilon_{21})X_1X_2 + (1 + \varepsilon_{21})X_1^{III} X_2 - X_2 - \frac{(1 + \varepsilon_{22})}{2} X_2^2 + X_2^{III} \ln X_2 = \frac{\ln K}{2} \tag{3-67}$$

In this case the evaluation of K requires more information. In equation 3-67 it is usual that ε_{22} and ε_{21} are not known. Thus to evaluate ε_{22}, ε_{21}, and K requires three sets of solubility values. If ε_{22} is assumed small or equal to zero, which is justified in some systems, then only two sets of solubility values is necessary to find ε_{21} and K. If $\varepsilon_{22} = 0$ and K is known approximately from the equilibrium constant, then only one set is sufficient for an estimation of ε_{21}.

C.6. Points of Minima in the Solubility Curve

In section C.4 it was mentioned that the slope of the curve could start out negative and then become positive. That is, the solubility

curve goes through a minimum with respect to X_1. To locate this minimum we go back to equation 3-46 and equate dX_1/dX_2 to zero, i.e.,

$$\frac{dX_1}{dX_2} = \left[\frac{fX_2 + cX_1 - g}{a - bX_1^2 - cX_1X_2 + pX_1}\right] \quad X_1 = 0 \tag{3-68}$$

or

$$fX_2 + cX_1 - g = 0$$

or

$$X_1|_{min} = \frac{g - fX_2|_{min}}{c} \tag{3-69}$$

Substituting equation 3-69 into the solubility equation 3-53 one gets after simplification

$$a \ln \frac{g - fX_2}{c} + \frac{fX_2^2}{2} = k = a \ln X_1^o \tag{3-70}$$

Assuming that the quadratic term $\frac{fX_2^2}{2} \ll a \ln \frac{g - fX_2}{c}$, then

$$\frac{g - fX_2}{c} = X_1^o \tag{3-71}$$

or

$$X_2|_{min} = \frac{g - cX_1^o}{f} \tag{3-72}$$

$$= \frac{(1 + \varepsilon_{21})(X_1^{II} - X_1^o) - 1}{(1 + \varepsilon_{22})} \tag{3-73}$$

Now generally $X_1^o \ll X_1^{II}$ so that

$$X_2|_{min} = \frac{(1 + \varepsilon_{21}) X_1^{II} - 1}{(1 + \varepsilon_{22})} \tag{3-74}$$

On Figure 3.12 one can see that for $\varepsilon_{21} = 2$, $\varepsilon_{22} = 10$, and $X_1^{II} = 0.5$ that the minimum value of X_1 occurs when

$$X_2 = \frac{(3)\ (0.5) - 1}{II} = 0.045 \tag{3-75}$$

The value of X_2 for a minimum X_1 can be found for the case of section C.5 in the same way. In this case the differential equation 3-44 is rearranged to give

$$\frac{dX_1}{dX_2} = - \frac{\left[\frac{e}{X_2} - fX_2 - cX_1 + g\right]}{\left[\frac{a}{X_1} - bX_1 - cX_2 + p\right]} = 0 \tag{3-76}$$

from which

$$X_1 = \left[\frac{e}{X_2} - fX_2 + g\right] \frac{1}{c} \tag{3-77}$$

Substituting this into the solubility equation 3-66 gives

$$a \ln \left[\frac{e}{X_2} - fX_2 + g\right] \frac{1}{c} + \frac{fX_2^2}{2} + e \ln X_2 = \frac{\ln K}{2} + e \tag{3-78}$$

Again if one assumes that the quadratic term $fX_2^2/2$ is small, then dividing equation 3-78 by 'a' one gets

$$\ln \left[\frac{e}{X_2} - fX_2 + g\right] \frac{1}{c} + \frac{e}{a} \ln X_2 - \frac{\ln K}{2a} - \frac{e}{a} = 0 \tag{3-79$_a$}$$

or

$$\frac{1}{c}\left(\frac{e}{X_2} - fX_2 + g\right)(X_2)^{e/a}(K)^{-1/2a}(2.72)^{-e/a} = 1 \qquad (3\text{-}79b)$$

Equation 3-79b may be rearranged to produce the polynomial

$$fX_2^{\frac{e}{a}+1} - gX_2^{\frac{e}{a}} - eX_2^{\frac{e}{a}-1} + 2.72^{\frac{e}{a}} c K^{\frac{1}{2a}} = 0 \qquad (3\text{-}80)$$

One of the roots of equation 3-80 will be the value of X_2 at which X_1 is a minimum on the solubility curve. The solution of this equation must be done by numerical methods, a common one being Newton's Method. This requires that an initial estimate of X_2 be made, and this value used to calculate a better second approximation. By successive approximations one can dtermine a good value of X_2 at X_1 minimum.

However equation 3-80 can be simplified if the final term in the equation, $(2.72^{e/a} c K^{1/2a})$, is considered to be very much smaller than the other three terms. This can be justified in many systems for which the solubility product, K, is very small (e.g., K = 10^{-7} in the Fe-Mn-S system near 1300^0C). By letting the last term be zero in equation 3-80 one gets

$$fX_2^{\frac{e}{a}+1} - gX_2^{\frac{e}{a}} - eX_2^{\frac{e}{a}-1} = 0 \qquad (3\text{-}80b)$$

Multiplying equation 3-80b by $X_2^{1 - \frac{e}{a}}$ we arrive at the simple quadratic expression

$$fX_2^2 - gX_2 - e = 0 \tag{3-81}$$

from which

$$X_2|_{min} = \frac{g \pm \sqrt{g^2 + 4fe}}{2f} \tag{3-82}$$

That is

$$X_2|_{min} = \frac{\left\{(1 + \varepsilon_{22})X_2^{III} + (1 + \varepsilon_{21})\, X_1^{III} - 1 \pm \sqrt{[\,(1 + \varepsilon_{22})X_2^{III} + (1 + \varepsilon_{21})X_1^{III} - 1]^{\,2} + 4\,(1 + \varepsilon_{22})X_2^{III}}\right\}}{2(1 + \varepsilon_{22})} \tag{3-83}$$

Equation 3-83 is somewhat unwieldy, and can be simplified further with appropriate assumptions. Consider a situation in which $\varepsilon_{22} \to 0$ and ε_{21} has a significant value, or at least when $|\varepsilon_{21}| >> |\varepsilon_{22}|$. Such a situation corresponds to the equilibria for the reactions of a strong deoxidant in steels. In this case equation 3-83 reduces to

$$2X_2|_{min} = \varepsilon_{21}\, X_1^{III} \left[1 \pm \left(1 + \frac{4X_2^{III}}{\varepsilon_{21}^2\, X_1^{III\,2}}\right)^{1/2}\right] \tag{3-84}$$

Applying the binomial theorem to the term in the ( ) bracket gives

$$2X_2|_{min} = \varepsilon_{21}\, X_1^{III} \left[1 \pm \left(1 + \frac{4X_2^{III}}{2\varepsilon_{21}^2\, X_1^{III\,2}}\right) + \ldots . \right] \qquad (3\text{-}85)$$

Since the sign of ε_{21} is negative for this type of reaction, one must adopt the negative sign for X_2 to be a positive value.

Thus

$$2X_2|_{min} = \varepsilon_{21}\, X_1^{III} \left[- \frac{2X_2^{III}}{\varepsilon_{21}^2\, X_1^{III\,2}} \right] \qquad (3\text{-}86)$$

and therefore

$$X_2|_{min} = - \frac{1}{\varepsilon_{21}} \frac{X_2^{III}}{X_1^{III}} \qquad (3\text{-}87)$$

This result is similar to the result obtained by Averin[54] on the basis of equilibrium constant arguments, viz.,

$$N_R = \frac{-x}{\varepsilon_{22}x + \varepsilon_{21}y} \qquad (3\text{-}88)$$

where N_R is the mole fraction of dissolved metal R which produces the minimum oxygen content in liquid iron. x and y are small whole numbers defined by the stoichiometric formula R_xO_y, the phase in equilibrium with the iron. By letting $\varepsilon_{22} = 0$ in 3-88 one sees that the two results are identical.

Figure 3.13 compares equation 3-83 with Averin's approximation for the case where phase III, in equilibrium with phase I, is a stoichiometric

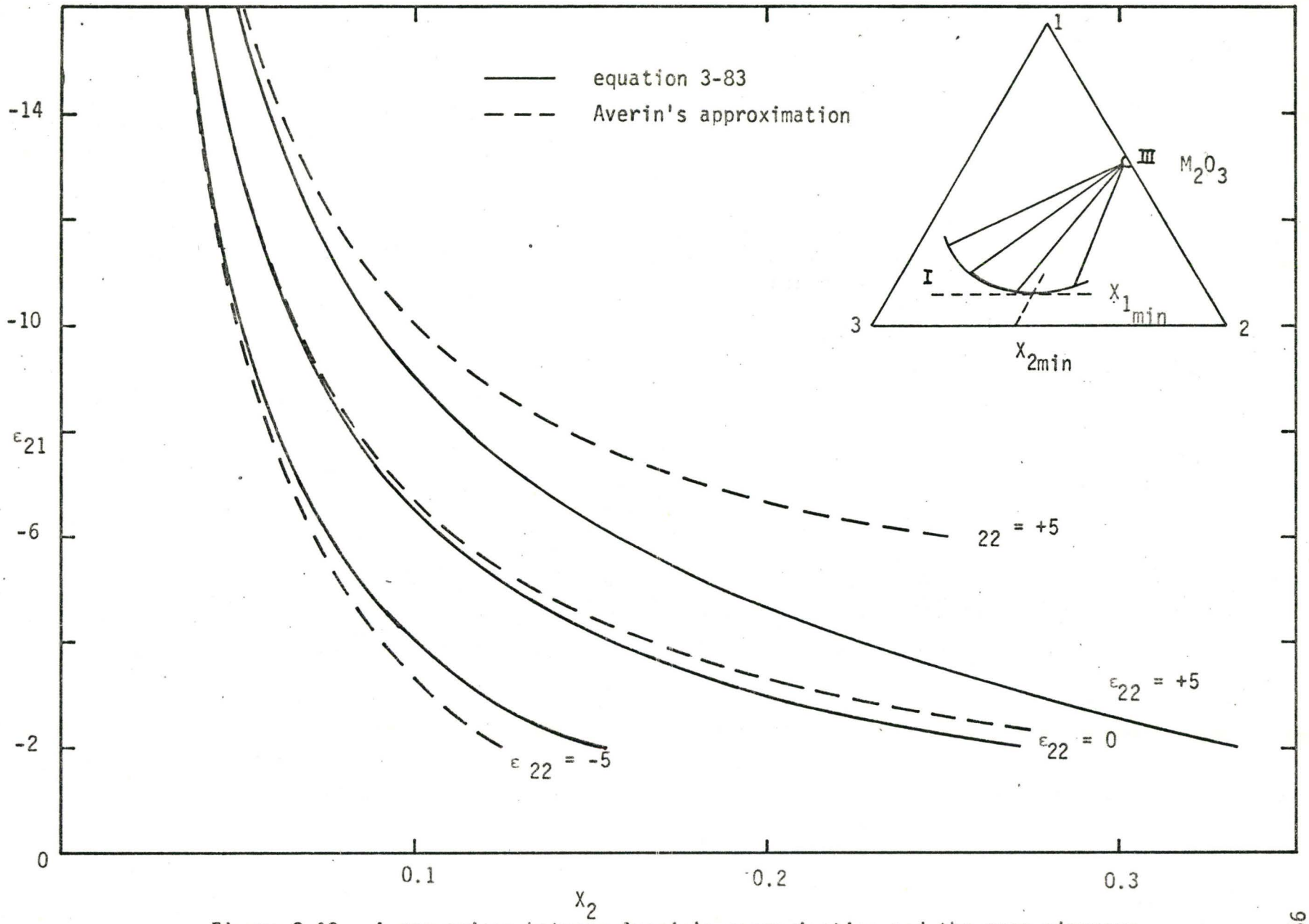

Figure 3.13 . A comparison between Averin's approximation and the more rigorous equation 3-83 for determining the minimum in the solubility curve (i.e., $X_{1\ min}$ and $X_{2\ min}$) using various negative values of the Wagner cross interaction coefficient.

compound on the 1-2 binary of the type M_2O_3 for ε_{22} = -5, 0, and +5. One can see that for higher values of the interaction coefficient ε_{21} (representing a strong deoxidant) the two results are very nearly equal despite different values of ε_{22}. The curves also show that elements with a strong negative interaction in a ternary system produce a minimum in the solubility curve at lower values of X_2 than elements without a strong negative interaction. Also as the interaction weakens, the two results tend to diverge, particularly when ε_{22} is greater than zero. In this case Averin's approximation cannot be considered to be good. On the other hand equation 3-83 cannot be considered to be that accurate either since one is now incorporating values of X_2 in phase I which are probably too large to satisfy the approximation limits.

C.7. The Effect of Pressure on the Solubility

This Gibbs-Duhem analysis can be easily extended to include the effect of pressure on the solubility. The pressure may be due to external forces or to phase interface curvature (capillarity). The analysis for the latter case is well known in binary systems and is known as the Gibbs-Thompson effect.

Consider the original Gibbs-Duhem equation (equation 3-37) in the isothermal case in the form

$$X_1^I \, d\mu_1 + X_2^I \, d\mu_2 + X_3^I \, d\mu_3 = 0 \qquad (3\text{-}89)$$

$$X_1^{III} \, d\mu_1 + X_2^{III} \, d\mu_2 + X_3^{III} \, d\mu_3 = V^{III} \, dP \qquad (3\text{-}90)$$

That is, phase III (suppose this to be a spherical solid precipitate) is acted upon by surface tension while phase I (say a surrounding liquid) is not subject to pressure. Subtracting (3-89) from (3-90) and rearranging as before gives the differential equation

$$\left[\frac{a}{X_1} - bX_1 - cX_2 + p\right] dX_1 + \left[\frac{e}{X_2} - fX_2 - cX_1 + g\right] dX_2 = \frac{V^{III} dP}{RT} \qquad (3\text{-}91)$$

If one assumes V^{III} to be independent of composition and the coefficients on the left to be independent of pressure then this equation remains exact and may easily be integrated. Thus

$$a \ln X_1 - \frac{bX_1^2}{2} + pX_1 - cX_1X_2 + gX_2 - \frac{fX_2^2}{2} + e \ln X_2$$

$$= \frac{\ln K}{2} + \frac{V^{III}}{RT} \int_0^{2\sigma/r} dP = \frac{\ln K}{2} + \frac{V^{III} 2\sigma}{RTr} \qquad (3\text{-}92)$$

where σ and r represent the surface tension and radius of curvature of the spherical phase III respectively.

For ease of discussion one can consider the case where X_1 and X_2 are small, and $X_1^{III} = X_2^{III} = 0.5$, then

$$\ln X_1X_2 = \ln K + \frac{4V^{III}\sigma}{RTr} \qquad (3\text{-}93)$$

or

$$X_1X_2 = K e^{\frac{4V^{III}\sigma}{RTr}} \qquad (3\text{-}94)$$

Figure 3.14 schematically illustrates the effect of pressure due to surface tension. When r is large (i.e., approaching a flat surface) the pressure

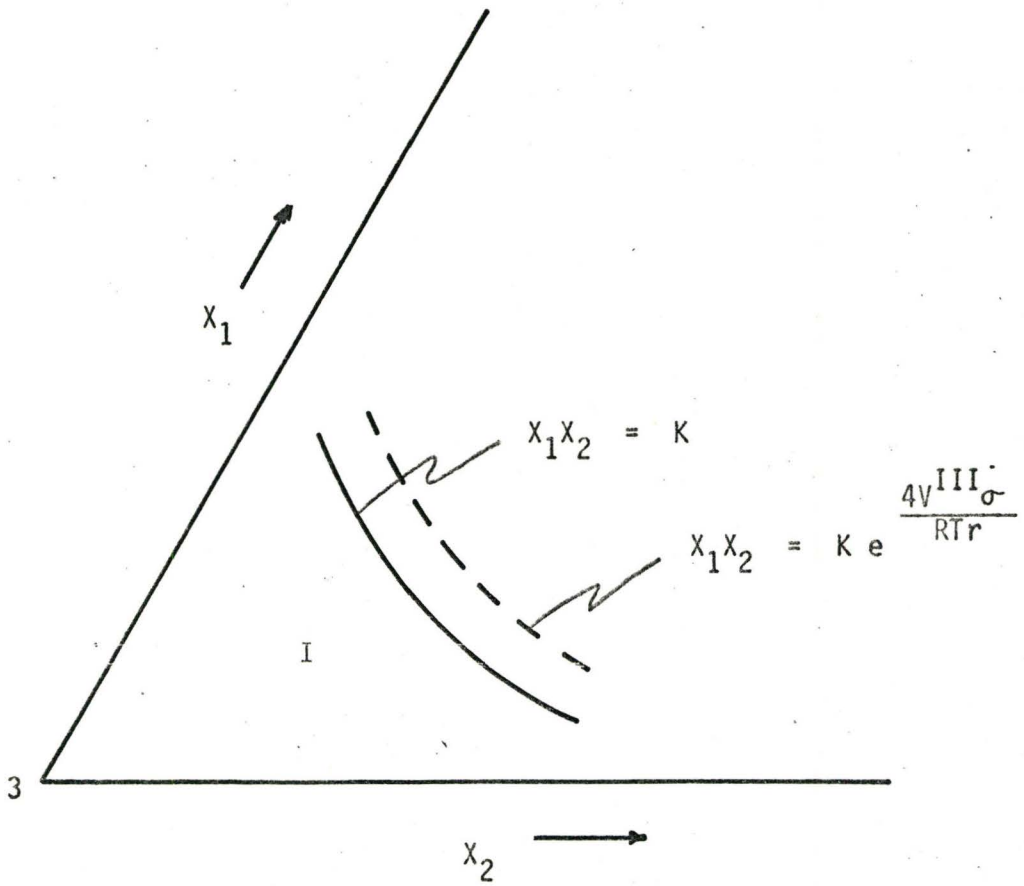

Figure 3.14 A schematic section of a ternary isotherm showing the effect of pressure on the solubility of phase I

term goes to zero and $X_1X_2 \rightarrow K$. This, of course, is the equation derived in section C.5. One sees therefore that the pressure effect is positive, the solubility of phase I increasing as the radius of curvature decreases, a result which was to be expected on the basis of the binary Gibbs-Thomson effect.

C.8. The Effect of Temperature on the Solubility

The Gibbs-Duhem equations for a ternary system at constant pressure but with variable temperature are written as

$$X_1^I \, d\mu_1 + X_2^I \, d\mu_2 + X_3^I \, d\mu_3 = - S^I \, dT \tag{3-95}$$

$$X_1^{III} \, d\mu_1 + X_2^{III} \, d\mu_2 + X_2^{III} \, d\mu_3 = - S^{III} \, dT \tag{3-96}$$

Subtracting equation 3-95 from 3-96, rearranging and using the same notation as before, gives

$$\left[\frac{a}{X_1} - bX_1 - cX_2 + p\right] dX_1 + \left[\frac{e}{X_2} - fX_2 - cX_1 + g\right] dX_2 = - \frac{\Delta S dT}{RT} \tag{3-97}$$

where $\Delta S = (S^{III} - S^I)$. ΔS is related to the isothermal, constant composition heat of formation, Q, of the precipitate III from solution I by

$$\Delta S = \frac{Q}{T} \tag{3-98}$$

Integrating equation 3-97 gives

$$a \ln X_1 - \frac{bX_1^2}{2} + pX_1 - cX_1X_2 + gX_2 - \frac{fX_2^2}{2} + e \ln X_2 = - \frac{Q}{R} \int \frac{dT}{T^2} + \text{constant} \tag{3-99}$$

If one lets the constant be $\frac{\ln K_o}{2}$, and again, for ease of discussion consider X_1 and X_2 small, and $X_1^{III} = X_2^{III} = 0.5$, then equation 3-99 becomes

$$\frac{1}{2} \ln X_1 X_2 = \frac{1}{2} \ln K_o + \frac{Q}{RT} \tag{3-100}$$

or

$$X_1 X_2 = K_o e^{\frac{2Q}{RT}} \tag{3-101}$$

In section C.5 the statement was made that the integration constant ($\frac{\ln K}{2}$) in equation 3-59 is really a function of temperature. By comparing equation 3-61 and 3-101 one sees that

$$K = K_o e^{\frac{2Q}{RT}} \tag{3-102}$$

C.9. Summary

In the preceding it has been demonstrated that the solubility limits of phase I can be theoretically predicted to within a few empirical constants if the restrictions set down in section C.1. can be met. Usually, the binary data X_1^o and X_2^o is available in the literature in the form of phase diagrams. It has been shown that with due regard to standard states the solubility product K(T) is equal to the chemical equilibrium constant which, for many systems, is also available in the literature, and is occasionally given as a function of temperature. The least available data are the interaction coefficients. Most of the values of ε_{21} and ε_{22} which are tabulated are for the ternary alloys of iron, and most of these values are for the liquid state. The parameter ε_{22} has been

shown to have only a small effect on the solubility and thus ε_{21} may be calculated from solubility curves if the other parameters are known. On the other hand it is possible to predict the solubility limits of a solvent phase starting with a minimum of experimental information provided one recognizes the restrictions on the analysis. These procedures are extensively used in our subsequent discussions.

CHAPTER IV

EXPERIMENTAL DESIGN AND PROCEDURES

This chapter describes the experiments used to determine the equilibrium and kinetic data for the Fe-Mn-S system in the temperature range 1200°C to the melting point of iron. The first two sections are concerned with experimental design while the later sections describe the equipment, materials, and particular procedures utilized.

A. EXPERIMENTAL DESIGN FOR THE EQUILIBRIUM STUDIES

The interpretation of phase transformations in the Fe-Mn-S system necessitates a thorough knowledge of phase equilibria within the system. The contents of Chapter II illustrate that such data is scarce. Even that data which is ayailable (Nakao) is incomplete and inconsistent, particularly with respect to the placement of the three phase region (γ-Fe + MnS + FeS) on the 1300°C isotherm.

The obvious experiment to locate the three phase triangle is to produce an equilibrated three phase mixture in which the individual phases are of sufficient area on sectioning to be analysed by electron probe microanalysis. Consequently the logical procedure is to mix together quantities of the three phases concerned, i.e., Fe, MnS, and FeS, in proportions such that the average composition is within the three phase region. It was found, however, that the MnS tended to equilibrate only with the iron and not with the FeS. The FeS, on the other hand, equilibrated

with the iron and because of its wetting properties appeared as a thin film of sulphide surrounding the particles of iron. This film was too limited in area to analyse with the probe. Figure 4.1 illustrates this point.

A second experiment was tried in which only FeS and Mn metal were reacted together. Again the amounts of each were such that the average composition would fall within the three phase region. In this experiment both the Fe and MnS phases would be precipitated and it was hoped that they would be in equilibrium with the FeS phase and with each other. The resultant structure was a good three phase mixture, but the individual phases were too small for accurate probe analysis. The FeS surrounded the Fe and MnS phases and prevented their agglomeration into larger phases. Figure 4.2 shows this situation.

Our most successful experiment involved equilibrating a mixture of iron filings (containing some Mn), powdered FeS and Mn metal. Since both FeS and Mn are in the liquid state at temperature the resultant reaction with the Fe-Mn alloy will be fast. During the reaction a series of localized, finite diffusion couples are set up. The liquid FeS and Mn react together to produce solid MnS with dissolved Fe as a product. Mn in turn reacts with the Fe-Mn alloy to produce Fe with a high Mn content. These two products simultaneously react with each other in an approach to equilibrium. FeS also reacts with the Fe-Mn alloy. Since the initial mixture of constituents has an average composition which falls within the three phase region of the isotherm, a sufficiently long anneal would produce the three phase structure γ-Fe + MnS + FeS. If, however, the system is reacted for a shorter time and quenched, the resultant structure will contain

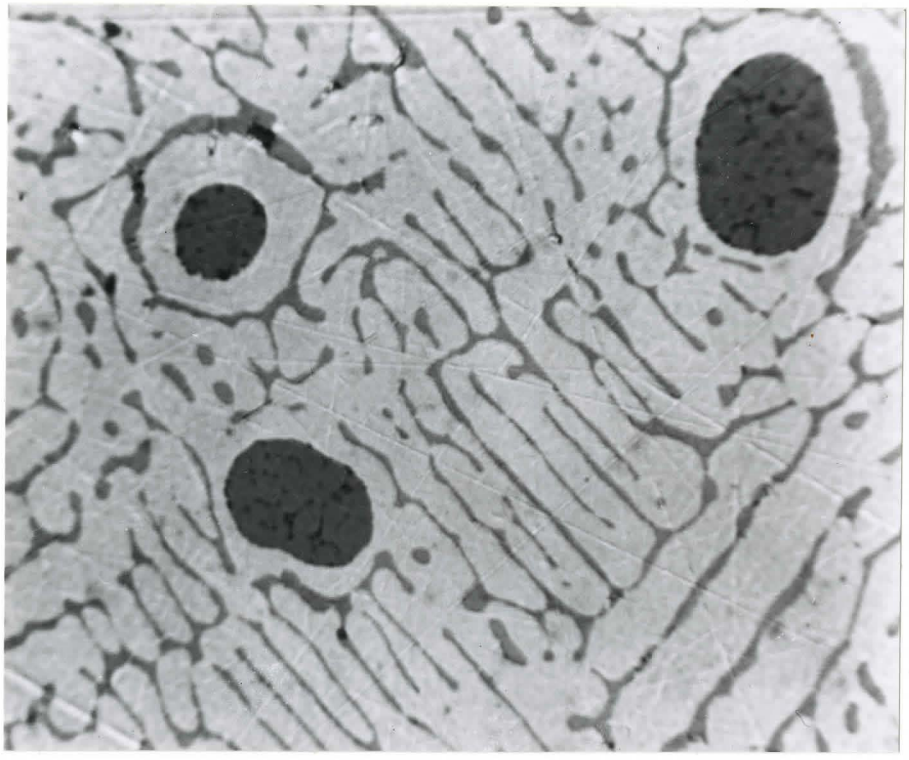

Figure 4.1 Three-phase structure showing the γ-Fe surrounding the MnS precipitates and the FeS film throughout the γ-Fe phase. X620

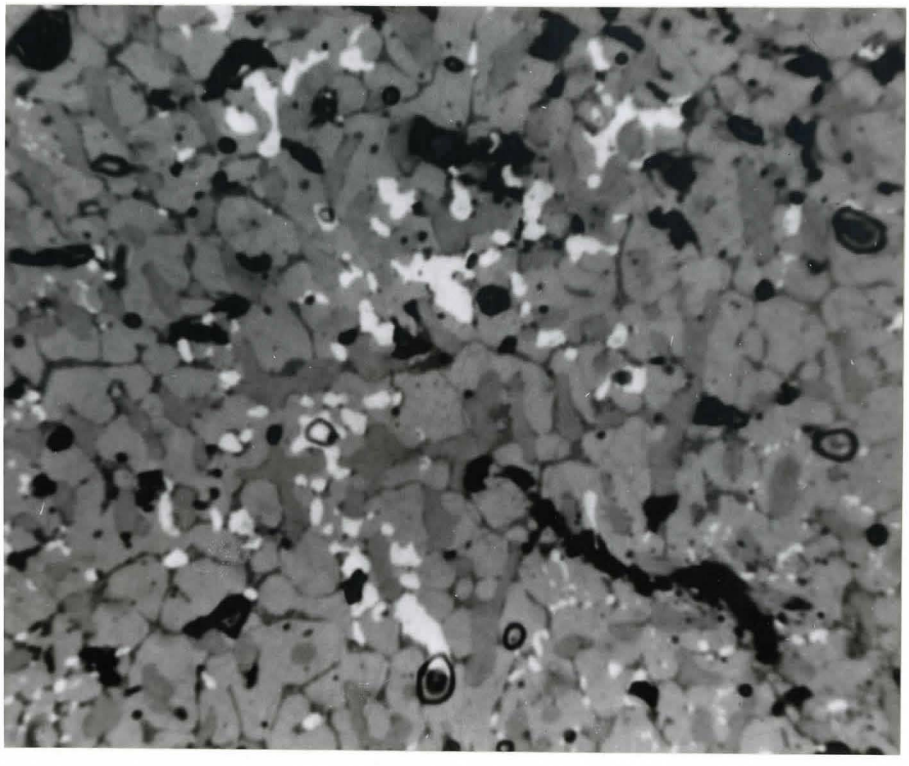

Figure 4.2 Three-phase (γ-Fe + MnS + FeS) equilibrium. X1120

a record of the various processes mentioned above, each phase being in local equilibrium with the next. Such a structure would show a much wider picture of the isotherm when analysed. Thus by carrying out this experiment at various temperatures within the austenite temperature range we were able to rather completely describe the constitution of the Fe-Mn-S system in this region.

The experimental determination of the temperature and composition of the 'eutectic trough maximum' is extremely difficult. The lack of pinpoint temperature measurement, composition fluctuations due to evaporation losses from the liquid, segregation and supercooling effects during quenching, the control of phase size for microprobe analysis, and the analytical error itself, all contributed to the difficulty and conspired to prevent an experimental determination. Consequently, an estimate of its temperature and composition had to be obtained using known binary data, ternary data on the miscibility gap at high temperatures, and the solubility theory of Chapter III.

A few experiments were conducted involving slow solidification and cooling of iron melts with various sulphur and manganese contents followed by a metallographic determination of the type of sulphide and its morphology. While the experiments are anything but definitive with respect to the experimental location of the 'eutectic trough maximum', the results combined with knowledge of commercial practice and Hone's[64] steady state experiments give considerable credence to our semi-empirical estimate.

B. EXPERIMENTAL DESIGN FOR THE KINETIC STUDIES

Table II-3 indicates that cation diffusion data in MnS is limited to one approximate value at one temperature. A program to expand this information was therefore developed. For this purpose there are two types of diffusion couple capable of yielding kinetic data for the diffusion of Fe and Mn in MnS. The first is to weld pure Fe (or an Fe-Mn alloy) to MnS thereby creating a two phase equilibrium condition at the weld interface with simultaneous diffusive interchange of Fe between the metal and sulphide. The second is to make a couple between two different compositions of the same MnS phase; that is, to weld pure MnS to the sulphide (FeMn)S in which the Fe is in solid solution. Both of these methods were utilized in the present studies to determine the kinetics of cation diffusion.

With respect to the first type of couple it became apparent from the equilibrium data that it is more advantageous to use pure Fe rather than an alloy as one terminal since the equilibrium concentration of Fe in MnS is higher when in contact with iron (~4 wt.%). This implies that the iron profile in the MnS can be more accurately determined.

Unfortunately, welding pure Fe to pure MnS is very difficult. Since MnS is brittle, pressure welding tends to crack or shatter the sulphide, and without sufficient pressure one cannot achieve good mechanical contact between the two halves of the couple. Furthermore the welding anneal must be carried out at rather low temperatures because a long welding anneal at a high temperature might alter the initial conditions for diffusion. Nakao experienced similar difficulties with pure Fe, but found that Fe-Mn alloys welded more readily to MnS.

In passing we mention three unsuccessful attempts to form the couple, two of these by pressure. The first involved evaporating a layer of Fe on a flat polished surface of a piece of MnS approximately 3 (mm^3) and welding this to a polished Fe plate. This would ensure a complete Fe to sulphide contact at the interface and permit the weld to occur across an Fe-Fe interface. The attempt was unsuccessful. Parts of the evaporated layer welded to the sulphide, but the layer would not weld to the Fe plate. A longer annealing time would be necessary. However this would permit the Fe layer to diffuse into the sulphide and destroy the ideal initial conditions.

The second attempt involved placing some fine FeS powder in the interface and annealing for a short time above 1200^{o}C. Hopefully the liquid FeS would quickly wet and weld the interface. This again proved unsuccessful because the powder kept the two faces apart and the effect of pressure was lost when the FeS melted.

In the third method a piece of MnS was placed in a shallow, water-cooled copper mold (1/2" diameter x 1/2" deep). A drop of liquid Fe, formed above the mold on the end of a 1/2" diameter iron rod (by induction heating), was allowed to fall into the mold thereby covering the MnS. The water-cooling immediately solidified and cooled the iron droplet. This solid button was then turned upside down in the mold and another drop allowed to fall onto the first one. This ensures that the MnS is completely contained within the iron button, a situation analogous to an inclusion in steels. This procedure was carried out in a hydrogen and argon atmosphere. The result was a perfectly welded diffusion couple but the cooling was not fast enough to prevent both erosion and diffusion

at the Fe/MnS interface.

To surmount the welding difficulty and retain pure Fe as one half of the couple a 'powder metallurgy' technique was finally used. Pure Fe filings were pressed about a solid piece of pure MnS. The result was a small pellet of Fe containing MnS as an "inclusion". This procedure led to good mechanical contact between the Fe and sulphide. This pellet, sealed in an evacuated quartz ampule, was directly reacted at temperature without a prior anneal or weld. This has the disadvantage that one does not know exactly when diffusion begins, i.e., how much time is required to weld the Fe particles to the MnS? This will be discussed in detail in a later chapter, but it can be stated here that the results clearly indicate that welding is essentially instantaneous.

The (FeMn)S:MnS couples were produced in a manner similar to the Fe:MnS couples. Weighed amounts of powdered FeS and MnS were mechanically mixed together to produce an average composition within the solid solution range, then pressed about a solid piece of MnS into small pellets, and reacted at temperature for a known time. Again there is some uncertainty about the exact starting time of diffusion and at time zero the (FeMn)S is obviously not homogeneous. However the fact that FeS is liquid at the reaction temperature means that the pressed powder will sinter immediately and that the pure MnS will be wetted and welded instantly in contact with the sulphide of high Fe potential. Consequently Fe diffusion into pure MnS should start instantly.

During the development of the methodology a pellet of the FeS + MnS mixture at 1300^{o}C was sintered to produce a homogeneous solid solution then an attempt was made to pressure weld this to a piece of MnS. This was

unsuccessful. Both sulphides were brittle and cracked. However the sintering process did lead to a product which was single phase (FeMn)S.

The preceding paragraphs have described the experiments for determination of cation diffusion data in MnS. The following paragraphs describe experiments for the determination of the kinetics of phase transformation between liquid FeS and MnS and between liquid FeS and Fe-Mn alloys.

Nakao's diffusion couples between liquid FeS and solid MnS produced anomolous diffusion profiles in the MnS phase which appeared to be inconsistent with each other and with his equilibrium measurements. This was mentioned in Chapter II. With a view to clarification, diffusion experiments involving couples between FeS and MnS were repeated at 1300°C, and then extended to 1200°C where the rates might be lower and the experiments more easily controllable.

The reaction between liquid FeS and solid Fe-Mn alloys is of interest because of its implications concerning sulphide inclusion equilibria, transformations, and morphology in steels. Thus a series FeS:Fe-Mn diffusion couples annealed at various temperatures for various times was designed to investigate this reaction. It is understood, however, that the corrosive, nature of liquid FeS on steels may prevent one from acquiring high quality kinetic data from such experiments.

One notes that in Table II-3, data for $D_{Mn}^{\delta Fe}$ is absent. Since this information is pertinent to the analysis of phase transformations occurring between the liquid state and the δ-Fe region a program was undertaken to determine $D_{Mn}^{\delta Fe}$. This involved the reaction of Fe:Fe-Mn diffusion couples for known times at temperatures where the δ-Fe structure

(bcc) is stable in both halves of the couples.

C. EXPERIMENTAL APPARATUS

C.1. Furnace Design

The reaction and diffusion experiments were conducted in an electrical resistance, vertical-tube furnace. The heating element consists of 0.050-inch molybdenum wire wound on a 2.1 inch i.d. by 2.3 inch o.d. alumina tube (McDanel AVPT quality). The wound portion of the tube is 22 inches long. It is differentially wound for 5, 4, 4, 4, and 5 inches with 11, 10, 9, 10, and 11 turns per inch, respectively. The element is powered from a 220 volt, 20 amp, AC line through a 280 volt powerstat and control equipment. About 2,500 watts is required to maintain the central zone of the furnace at 1300^{o}C. A protective atmosphere of 3 parts argon and 1 part hydrogen is employed.

A second alumina tube of similar quality, 1.65 inch o.d. and 1.45 inch i.d., placed concentrically inside the winding tube is used as a working tube. The top of this tube is fitted with a water cooled, gas-tight brass fitting with provision for a thermocouple, gas outlet, and port for introducing and lowering the sample to the hot-zone. The bottom of the tube is similarly fitted with a water-cooled, gas-tight fitting with provision for a gas inlet and quenching arrangement. Argon, after passing through the gas train (see Figure 4.3), passes through the working tube.

The quartz ampule containing the sample is connected to a length of 0.020 inch molybdenum wire. The other end of the wire is attached to a 2 inch long by 1/8 inch diameter iron rod. This assembly, about 25

inches in length, slips into a long glass tube and is held in place by a horseshoe magnet attracting the iron through the glass wall of the tube. The upper end of the glass tube is sealed, and the lower end is fitted into a rubber stopper. To charge the furnace this assembly is attached to the top fitting of the working tube so that the ampule is in the upper region of the furnace. After purging the working tube with argon, the ampule is introduced into the hot zone of the furnace by lowering the magnet along the outside of the glass tube. The sample is accurately placed in the hot zone so that it is adjacent to a measuring thermocouple. The bottom connection of the working tube is fitted with an aluminum foil membrane. On removing the magnet, the sample is permitted to fall through the membrane and directly into a quenching medium.

Figures 4.3, 4.4, and 4.5 show the various aspects of the furnace and experimental arrangement.

C.2. Temperature Control and Measurement

The temperature of the furnace is controlled by a Leeds and Northrup Speedomax 'H' 3-Action Current Adjusting (C.A.T.) strip chart recorder and controller in conjunction with a saturable core reactor and magnetic amplifier. A Pt/13 % Rd-Pt thermocouple placed in the hot zone between the two alumina tubes detects any change in the furnace temperature. Any deviation from the set-point temperature is measured by the Speedomax 'H' instrument and the error is relayed to the C.A.T. unit. Depending upon the error direction, the 0-5 ma output of the C.A.T. unit is increased or decreased and then amplified by the magnetic amplifier to proportionately

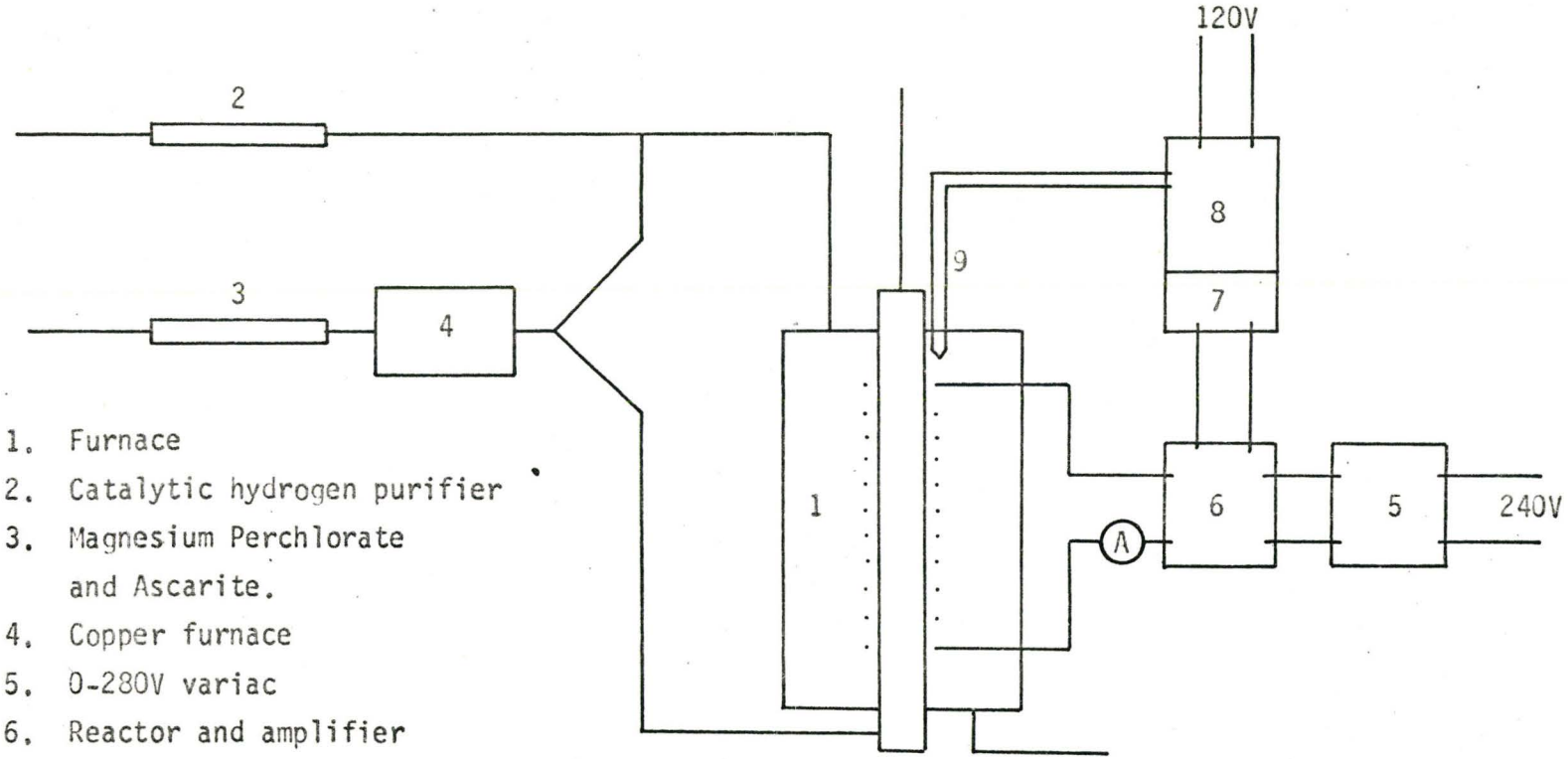

Figure 4.3 Schematic of the apparatus showing the molybdenom resistance furnace, the gas train, and the power supply.

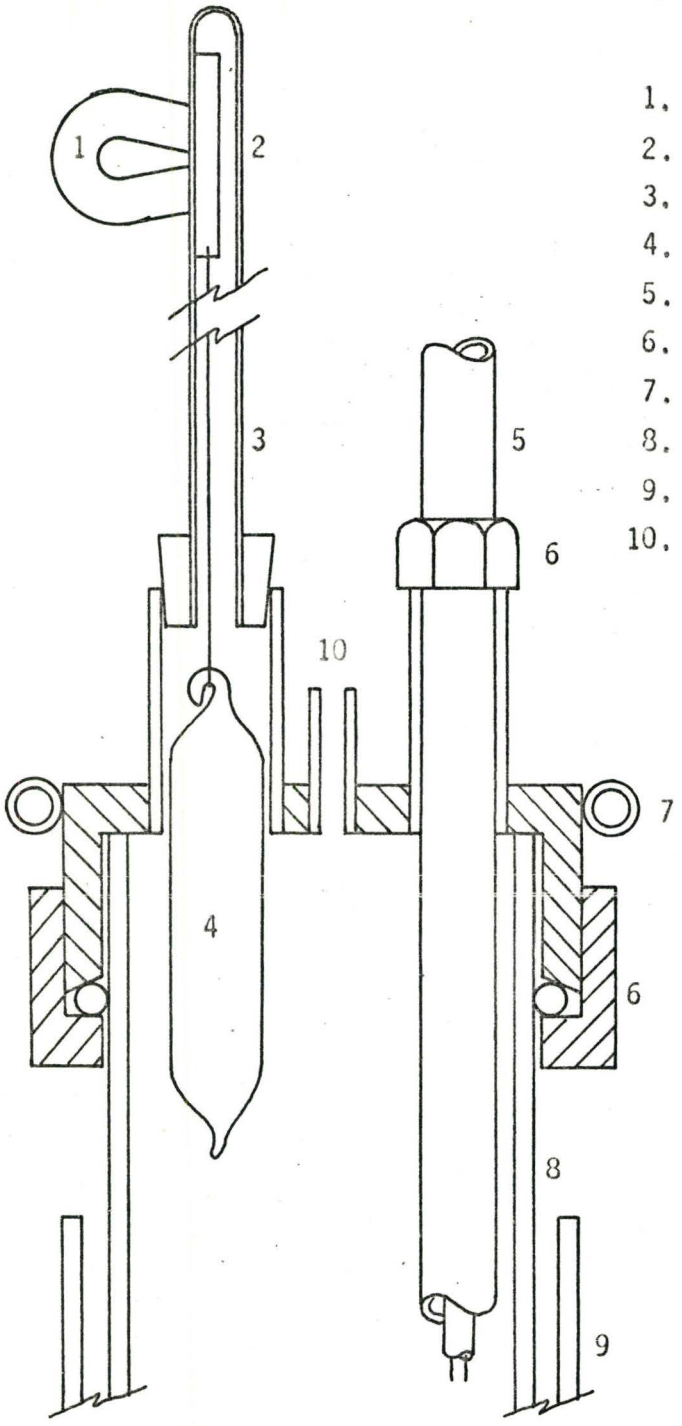

1. Magnet
2. Iron rod
3. Glass tube
4. Quartz ampule
5. Thermocouple sheath
6. O-ring seal
7. Water cooling
8. Alumina working tube
9. Alumina winding tube
10. Gas outlet

Figure 4.4 Brass fitting for the top of the working tube.

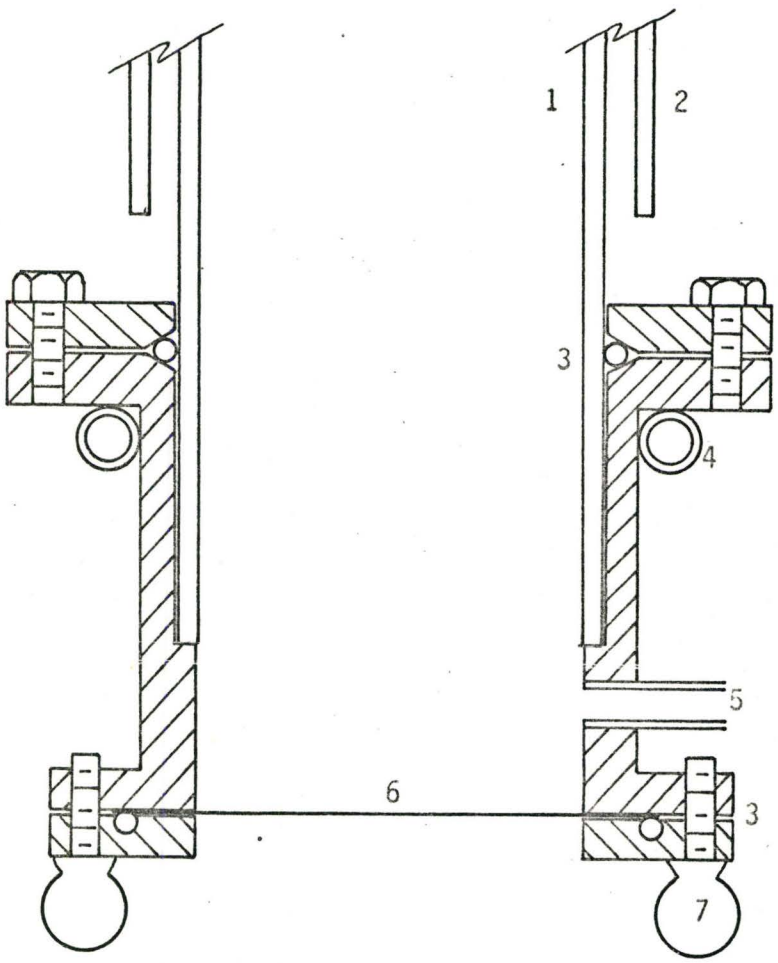

1. Alumina working tube
2. Alumina winding tube
3. O-ring seal
4. Water cooling
5. Gas inlet
6. Aluminum foil membrane
7. Thumbscrew

Figure 4.5 Brass fitting for the bottom of the working tube.

saturate the control winding of the saturable core reactor. This in turn regulates the power input to the furnace element. The 3 control actions, proportional, reset, and rate actions, operate according to the size, duration, and speed of the temperature changes.

The accuracy rating of the controller is quoted as $\pm$ .3% of the electrical span in millivolts. This unit controls from 700° to 1700°C which is equivalent to 13.364 mv. At 1300°C the unit controls within $\pm$ 0.040 mv or $\pm$ 3°C.

The temperature of the sample was measured with a Pt/13 % Rh-Pt thermocouple placed next to the sample in the hot zone. The millivoltage was measured with a thermocouple potentiometer in conjunction with a 0°C cold junction. It was found that the steady state temperature for most runs was maintained within $\pm$ 1°C, and for a few runs to be less than $\pm$ 4°C of the set temperature. The measuring thermocouple was calibrated against a standard thermocouple certified by the National Research Council and found to be identical. The measuring thermocouple was used only during runs and was removed from the furnace at other times. (To optimize the life of the element the furnace was held at 1000°C during periods of non-use.)

D. MATERIALS

D.1. Iron, Manganese, and Fe-Mn Alloys

Two types of iron were used for the equilibrium and kinetic experiments. Vacuum melted iron (Ferrovac E) was used in most instances. Armco iron, having a higher oxygen content, was used for the experiments involving the

eutectic trough maximum equilibrium. Zone refined iron, produced at Battelle Memorial Institute and supplied by the American Iron and Steel Institute was used as the iron standard for electron probe micro analysis. Table VI-1 gives the analysis of the iron samples.

Electrolytic manganese was used in the equilibrium experiments and in the production of the Fe-Mn alloys. Its analysis is also given in Table VI-1.

The iron-manganese alloys were produced by Nakao. The method of production is recorded in his thesis[13], and the following statements paraphrase his description for the alloys employed in this study.

Weighed amounts of electrolytic manganese and Ferrovac E iron, 35 to 45 grams total, were melted in a non-consumable arc furnace using a tungsten electrode under 200 mm Hg of Argon. A titanium getter was used during melting to prevent oxidation of the alloy, and long range segregation was prevented by carrying out four re-melting operations on each button. The buttons were cold rolled to 1.2 mm and homogenized in a vacuum of 10^{-5} mm Hg at 1300°C for 10 days. The chemical analysis of the manganese content is given in Table VI-1.

Table VI-1

Analysis of Fe, Mn, and Fe-Mn alloys. (in p.p.m by weight)

	C	Si	Mn	P	S	Cu	Ni	Cr	V	Mo	Co	H	O	N
Ferrovac E	30	<60	10	30	50	<10	<140	<100	<40	<10	100	5	7.8	2
Battelle Iron	8	<2	1	3	0.6	2	6	10	0.2	0.8	7	0.06	1.5	<0.2
Armco Fe	120		170	50	250								700	

	Mg	Si	Fe	
Electrolytic Manganese	20	3	2	Mn = 99.99 weight per cent

Fe-Mn Alloys (a) 1.08 wt.% Mn (b) 2.15 wt.% Mn (c) 4.05 wt.% Mn

D.2. Synthesis of Iron Sulphide (FeS)

FeS was produced by sulphidizing Fe wire in a stream of H_2S at 800°C for 24 hours. The 0.050" diameter Fe wire is quoted by its suppliers, Thermoelectric Ltd. Brampton, Ont., to be three 9's pure and is the grade used by them to manufacture thermocouples. The sulphide product is a porous crystalline material which easily crumbles to a coarse powder.

The fact that sulphidation takes place in a high sulphur potential means that the sulphide product will probably be a sulphur excess (or metal deficit) sulphide.

D.3. Synthesis of Manganese Sulphide

Manganese sulphide (MnS) may exist as one of three structures. α-MnS, the stable modification, is a green cubic (NaCl structure) form with a melting point at approximately 1610°C. The two other forms are β-MnS, which also has a cubic structure, and γ-MnS, which has an hexagonal structure. These last two modifications are metastable in nature. At 200°C these two forms, which are red in colour, start to transform to the green stable form.

The stable form, α-MnS, is available commerically. However it is invariably supplied as a powder at a high price. Unfortunately MnS oxidizes with time and Chao et al[55] report that the oxidation product is a sulphate, $MnSO_4$. There is also a possibility that the powdered sulphide will quickly convert to Mn(OH)S in moist air. A similar conversion has been reported to occur with NiS[56]. In any case, oxidation is an undesirable affect, because upon subsequent heat-treatment the oxygen replaces some of the

sulphur and the product becomes a mixture of MnS and MnO. To prevent this the powdered, freshly-produced sulphide must be melted and solidified into a large lump (to reduce the surface area) and stored in an oxygen and moisture free atmosphere. We found that these undesirable effects had occurred with the commercial sulphide and as a result a method had to be developed for producing MnS in our laboratory.

Following is a summary of some of the reported methods for producing MnS. Each method produces a powder form but it is possible to melt and solidify the powder before oxidation takes place.

1) Chao et al[55] report a method in which MnS is produced by the deoxidation of reagent grade manganese sulphate with S. S is vaporized at 410°C and brought into contact with $MnSO_4$ powder at 900°C. The effective reaction is

$$MnSO_4 + S_2 \overset{900^{\circ}C}{\rightleftharpoons} MnS + 2SO_2$$

This method was rejected because it was found that deoxidation was generally incomplete and unreduced sulphate remaining in the product would react with the MnS to produce MnO.

2) Other investigators have produced MnS by reacting powdered Mn and S together in evacuated silica tubes. Le Bot and Quan[57] reacted Mn powder with an excess of S for 12 hours at 485°C. The product was quenched and the excess S removed with carbon disulphide. This procedure was repeated four times. The end product is a crystalline form of MnS with a slight excess of manganese.

Keisling and Westman[48] compressed stoichiometric amounts of S and Mn powders into pellets, sealed them in evacuated silica tubes and heated

them for 48 hours at 1150°C until equilibrium was established. They often found it necessary to crush, recompress, and reheat the product for another 24-48 hours.

This method produces a good product but the process is slow and potentially dangerous. It is possible for large S pressures to build up in the sealed tubes if care is not exercized during heating. These tubes have been known to explode.

3) Classen[56] reports a wet method for producing MnS. This is based on the observation that MnS may be precipitated from a basic solution with H_2S.

A boiling solution of 10 gm of $MnCl_2.4H_2O$ in 500 ml of water containing a small amount of $K_2C_2O_4$ is reacted with an excess of 50% NH_3 solution and saturated at its boiling point with H_2S. The reactions can be summarized as

$$MnCl_2 + NH_4OH = Mn(OH)_2 + NH_4Cl$$
$$Mn(OH)_2 + H_2S = MnS + H_2O$$

The potassium oxalate prevents the oxidation of $Mn(OH)_2$. Although this method is easy and produces a powdered form of MnS, the precipitate is wet and subsequent filtering, washing, and drying is tedious and can lead to oxidation.

4) Lorenz and Schulz[58] used a method in which the metal chloride is reacted with H_2S at 600°C. The reaction is

$$MnCl_2 + H_2S \overset{600^o}{\rightleftarrows} MnS + 2HCl$$

This is the method we finally adopted to produce MnS. All of the other

methods were tried but were rejected for the reasons described.

A weighed quantity of $MnCl_2.4H_2O$ (20gm) is slowly heated under purified argon in a horizontal tube furnace to 300°C. This procedure drives off the water of hydration. H_2S is then introduced and the temperature raised to 600°C. Although the reaction appears to go to completion within 3-4 hours, usually more than 12 hours was allowed. The system is then cooled to room temperature in a sustained flow of H_2S and subsequently flushed with argon.

The melting and solidification is carried out as soon after production as possible. The melting is done in a graphite crucible by induction heating under purified argon. The resultant solid MnS is stored in an evacuated dessicator until use. Neither X-ray diffraction nor microscopic examination revealed other phases in the product.

E. SPECIAL EXPERIMENTAL PROCEDURES

The following paragraphs describe the methods used to seal unreacted samples in silica tubes, and the methods used to prepare the reacted samples for micro-probe and microscopic analysis. These are standard experimental methods and will not be dwelt upon in detail.

The method of sealing involved evacuating and backfilling with hydrogen a closed end quartz tube (10 mm o.d.) containing the sample. By repeating this process five times for each sample the partial pressure of gaseous oxygen remaining in the final evacuated sealed ampule was negligible. This method was used for every equilibrium and kinetic experiment involving evacuated ampules.

Sample preparation for the micro-probe involved mounting each sample in 1" diameter lucite or bakelite blocks, then sectioning and polishing each to a 0.1 micron lap finish. It was not necessary to etch the polished surfaces since each phase is distinctly visible in the as-polished condition. However each sulphide sample was vapor deposited with a thin layer of carbon to facilitate better electron conduction during micro-probe analysis.

E.1. Three Phase Equilibrium and the Ternary Isotherm

Weighed amounts of Fe-4% Mn alloy filings, electrolytic Mn, and powdered FeS were mixed together so that the average composition of the mixture would be within the limits of the three phase region (γFe + MnS + FeS). Table IV-2 lists the total weight and the average composition of the mixture before reaction. Each mixture was sealed in an evacuated silica tube and individually reacted at the temperature and time given in Table IV-2. The quenched samples were then prepared for micro-probe analysis.

Table IV-2

Experimental Conditions for Three Phase Equilibrium

	Total weight of sample	Average Composition, wt% Fe	Mn	S	Reaction Temperature °C	Reaction Time Min.
1.	0.2142 g	61.6	11.4	27.0	1191	> 60*
2.	0.2253 g	66.3	7.2	26.5	1251	125
3.	0.3616 g	73.9	6.3	19.8	1298	61
4.	0.4032 g	65.6	12.0	22.4	1336	60
5.	0.3333 g	69.3	11.5	19.2	1379	47
6.	0.3114 g	61.3	13.4	25.3	1419	40

* It was planned to react sample No. 1 for several hours because Mn is solid at 1191°C. However the sample accidently fell into the quench medium after an unknown reaction time between 1 hr. and 3 hrs.

E.2. Eutectic Trough Maximum

Each experiment involved melting ~200 gm of Armco Fe rod (1" diameter) by high frequency induction heating in a recrystallized alumina crucible (50 cc capacity) in an argon atmosphere. When molten, 0.2 gm. of aluminum was added to deoxidize the liquid iron. To each was added a predetermined quantity of electrolytic Mn and FeS. Each melt was then permitted to slowly solidify and cool by gradually reducing the power input. The resultant cylindrical ingot was cut in half along its central axis. One half was polished for microscopic examination, the other half was sampled for chemical analysis. The sampling involved drilling three holes perpendicular to the central axis through the half ingot (top, center, and bottom), and analysing the turnings for Mn and S. Table IV-3 lists the total weight of each ingot and the final Mn and S contents.

Table IV-3

Total Weight and Final Composition of Ingots

	Weight	Composition wt%		at %	
	gms	Mn	S	Mn	S
1.	268	1.55	0.073	1.57	0.127
2.	205	0.97	0.129	0.99	0.224
3.	210	0.58	0.167	0.59	0.290

E.3 Diffusion Couples

Fe:Fe-Mn

Plates of Fe (Ferrovac 'E') and Fe-Mn alloy (1 cm^2 x 1.2 mm thick) were polished to a 0.1 micron finish. The initial coarse polishing served

to remove any Mn depleted surface zone due to the homogenization treatment. Each diffusion couple was formed by pressure welding an Fe plate to an alloy plate in an hydrogen atmosphere at 1000°C for two hours. Each couple was suspended in the furnace at the temperature and time cited in Table IV-4. The quenched samples were sectioned, mounted, and polished for micro-probe examination.

The 4 wt.% Mn alloy couple was formed and reacted at the intermediate temperature and to assure a reasonable temperature span and ensure that the crystal structure of both sides of the couple remained bcc (δ-Fe region), the 2 wt.% Mn alloy was used for the lower and higher temperature experiments.

Table IV-4

Experimental Conditions for Fe:Fe-Mn Diffusion Couples

Couple	Temperature	Time
Fe: Fe - 2%Mn	1446°C	30 min.
Fe: Fe - 4%Mn	1478°C	60 min.
Fe: Fe - 2%Mn	1494°C	30 min.

Fe:MnS

Each couple was made by compressing (about 60,000 psi) iron filings (Ferrovac 'E') surrounding a piece of MnS to form a pellet 1/4" diameter x 3/8" long. Each pellet was separately sealed in an evacuated silica tube. An ampule containing an Fe:MnS couple and an ampule containing an (FeMn)S:MnS couple were simultaneously reacted at the temperature and time cited in Table IV-5. The quenched couples were then prepared for micro-probe analysis.

(FeMn)S:MnS

Weighed amounts of powdered MnS and FeS were mechanically mixed so that the iron content of the mixed sulphide was 11.0 wt.% Fe. This powder, surrounding a piece of MnS, was then compressed to form a pellet. The subsequent procedure is exactly as described for the Fe:MnS couples (see Table IV-5).

Table IV-5

Experimental Conditions for the Fe:MnS and (FeMn)S:MnS Couples

Reaction Temperature, ^{o}C	Reaction Time, Min.
1253	36
1300	122
1298	64
1299	36
1301	16
1299	5
1349	36
1406	16

FeS:MnS

A solid piece of MnS was sealed in an evacuated silica tube with powdered FeS. Sufficient FeS was added so that the MnS would be completely immersed in a pool of liquid FeS at temperature. Each couple was reacted at the temperature and time cited in Table IV-6. The resultant quenched samples were then prepared for micro-probe analysis.

Table VI-6

Experimental Conditions for the FeS:MnS Diffusion Couples

Reaction Temperature, ^{o}C	Reaction Time, Min.
1203	16
1204	37
1206	61
1296	7
1299	15
1294	27
1298	30

FeS:Fe-4%Mn

Each couple was formed by surrounding a 1 cm^2 x 1.2 mm thick Fe - 4 wt.% Mn alloy plate with sufficient quantity of powdered FeS in an evacuated silica tube. Each plate was polished on both sides to a 0.1 micron finish. The couples were reacted for the times and temperatures cited in Table VI-7.

Table VI-7

Experimental Conditions for the FeS:Fe-4%Mn Diffusion Couples

Reaction Temperature, ^{o}C	Reaction Time, Min.
1200	15
1197	30
1203	60
1297	15
1297	30
1298	60

Table IV-7 Cont'd.

Reaction Temperature, °C	Reaction Time, Min.
1400	15
1395	30
1393	60
1444	4
1442	7
1441	12

F. ELECTRON MICRO-PROBE ANALYSIS

In recent years considerable literature has appeared on the application of the micro-probe and the analysis of the raw data so our discussion will be brief. There are two general methods of analysing the raw data. One is to compare the experimental data with that determined for known alloy standards. This method is excellent for binary systems, but is inconvenient for ternary systems because of the large number of alloy standards of various compositions required. The second method is to mathematically correct the measured intensities on the basis of data acquired for the pure components of the ternary system. In this study pure Fe, Mn, MnS, and FeS were used as the standards.

In practice three different corrections must be made to the measured intensities. These corrections account for fluorescence, mass absorption, and atomic number difference effects. In the case of the Fe-Mn-S system it was found that the correction for fluorescence effects was insignificant, and was consequently neglected. C.W. Haworth[59] suggests that the absorption and atomic number corrections may be combined according to the following equation.

$$k_A^m = C_A M \qquad (4\text{-}1)$$

where

$$k_A^m = \frac{I_{ABC}^A}{I_A} = \frac{\text{measured characteristic X-ray intensity of A in alloy ABC}}{\text{measured characteristic X-ray intensity of the known amount of A in a standard}}$$

C_A = concentration of A in the alloy ABC (weight fraction)

M = the theoretical correction one makes to the relative intensity due to absorption and atomic number affects.

From equation 4-1 one can calculate theoretical correction curves of k_A^m versus C_A. For the methodology to do this, as suggested by Haworth, the reader is referred to an outline entitled "The Electron Probe Microanalyser"[59]. Figure 4.6 shows the curves used to determine the concentration of Fe and Mn in the sulphides of Fe and Mn from the measured relative intensity data.

It should be noted that the Fe alloys, containing Mn and S, are treated as binary Fe-Mn alloys. The S content, being so low, cannot be measured in the alloys by the micro-probe technique, and its minute concentration does not significantly affect the Fe and Mn corrections. The calculations indicate that the relative intensities of Fe and Mn in the Fe-Mn alloys require only minute corrections.

With respect to the sulphide corrections Nakao has shown that varying the S concentration in the sulphides does not affect the corrections one makes to the Fe and Mn in the sulphides. Consequently the theoretical curves were calculated on the basis that the sulphides contained 36.4 wt.% S.

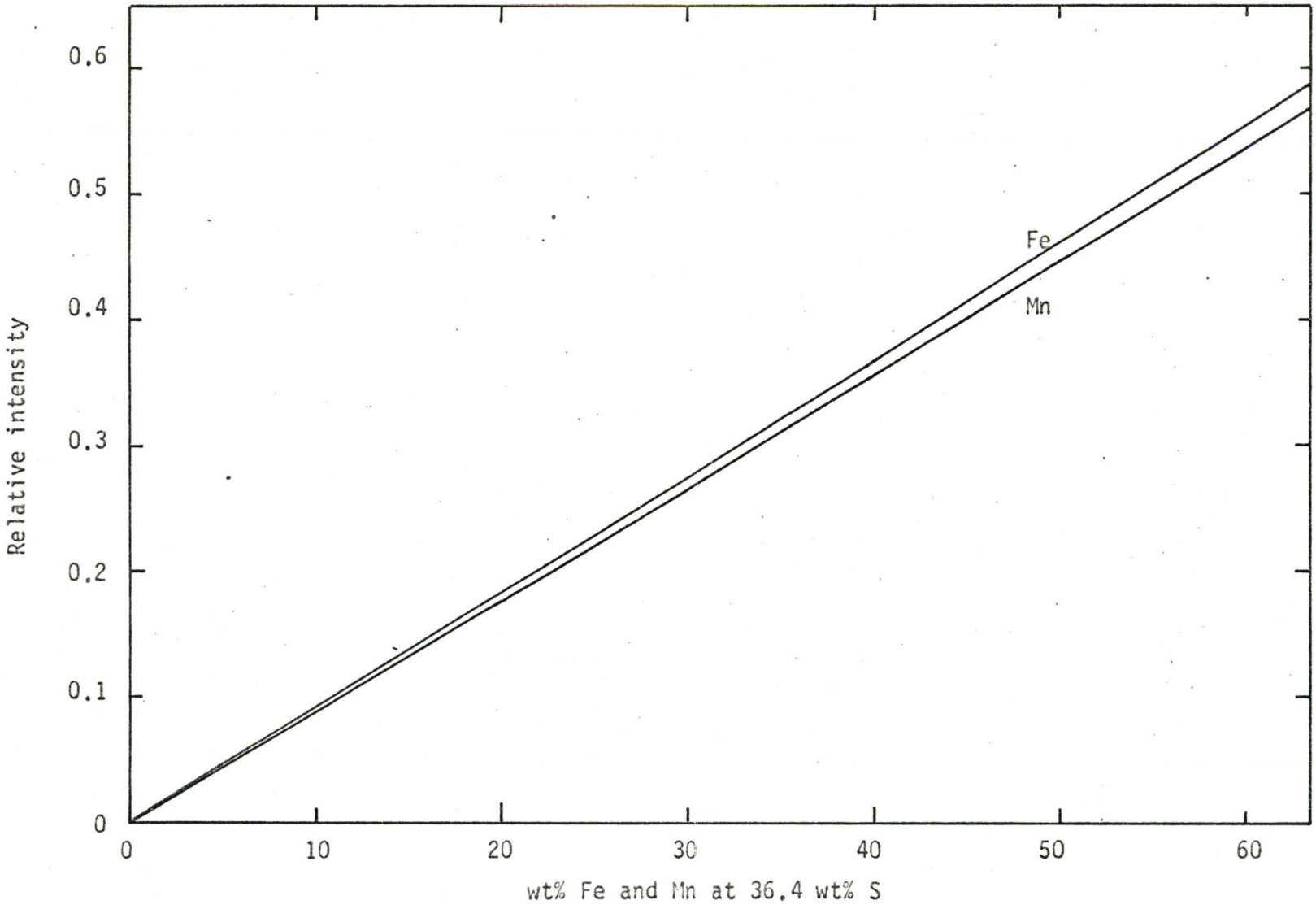

Figure 4.6 Measured relative intensity versus wt% Mn and Fe in their respective sulphides for 36.4 wt% S

From Figure 4.6 one sees that the average correction to the Fe or Mn content in an iron or manganese sulphide is about 10% greater than the measured relative intensity.

The S analysis in the sulphides was generally obtained by difference, i.e.,

$$\text{wt.\% S} = 100 - (\text{wt.\% Fe} + \text{wt.\% Mn}) \qquad (4\text{-}2)$$

CHAPTER V

Fe-Mn-S PHASE DIAGRAM; RESULTS AND DISCUSSION

A. THE TERNARY ISOTHERM AND THE THREE PHASE REGION (γ-Fe + MnS + FeS)

Of the equilibration experiments in the austenite temperature range the 1300°C isotherm was studied most thoroughly. This abetted comparison with Nakao's data at 1300°C and, since this temperature is strongly representative of the region, the amount of experimentation needed at other temperatures was reduced.

A.1. The 1300°C Isotherm

Figure 5.1 shows the quenched-in structure of the specimen reacted at 1300°C for 61 minutes. Recalling that the initial constituents were Fe filings, Mn, and FeS, the latter two being liquids at 1300°C, one can infer the steps in the reactions leading towards equilibrium. The probe results indicate that the liquid FeS (light gray phase at the bottom of the micrograph) reacted with the liquid Mn (initially in the region of the lacy, white phase at the top of the micro) to form MnS (the darker gray phase comprising most of the micrograph). The Fe filings and the Fe rejected from the FeS simultaneously reacted with the liquid Mn to increase the latter's Fe content. The Fe content continually increased until the liquid Mn-Fe alloy transformed to a solid Fe-Mn alloy (the lacy, white phase). Of course this solid alloy was simultaneously seeking equilibrium with the

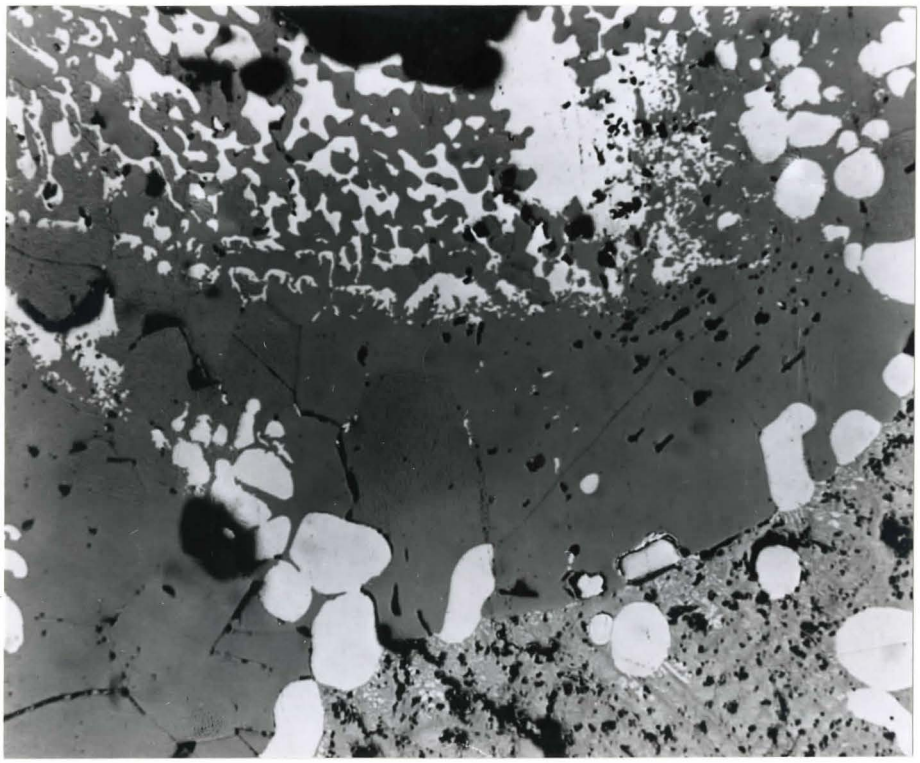

Figure 5.1 The microstructure of the unequilibrated sample reacted at 1298^{o}C. X160

surrounding MnS phase. If the equilibrium time had been longer, the whole structure would appear as a distinct three phase equilibrium between γ-Fe, MnS, and FeS. However, for this short time this occurs only at the MnS/FeS interface where the white globular iron phase is also present. In the other regions of the reaction zone there is a series of local equilibria between the MnS and the Fe-Mn alloy. By measuring the concentrations of adjacent phases by electron probe microanalysis a series of tie-lines are established in this two phase region. The Mn content of the alloy changes from 46 wt.% Mn at the top of the Fe-Mn phase field to nearly zero Mn at the FeS/MnS front. The results are listed in Table V-1 and plotted in Figure 5.2.

As mentioned, the three phase equilibrium between γ-Fe, MnS and FeS exists only near the bottom of the micro near the FeS/MnS front. The determination of the corners of the three phase region can thus be acquired by measuring the compositions of the three phases where obvious three phase equilibrium occurs. This data is also listed in Table V-1 and plotted in Figure 5.2. (The FeS phase appears as a finely dispersed Fe + FeS eutectic structure since it is impossible to prevent the eutectic breakdown even with our speed of quench. The compositions of FeS quoted represent the average for the two-phase room temperature mixture.)

The notable aspect of the MnS-Fe(Mn) tie-lines reported in Figure 5.2 is that nearly the entire concentration range of the Fe-Mn alloy is in equilibrium with substantially pure MnS, and similarly, the concentration range of the MnS from a few wt.% Fe to about 16.6 wt.% Fe (the MnS corner of the three phase region) is in equilibrium with nearly pure γ-Fe. Such behaviour might have been inferred from the tie-lines in the miscibility gap

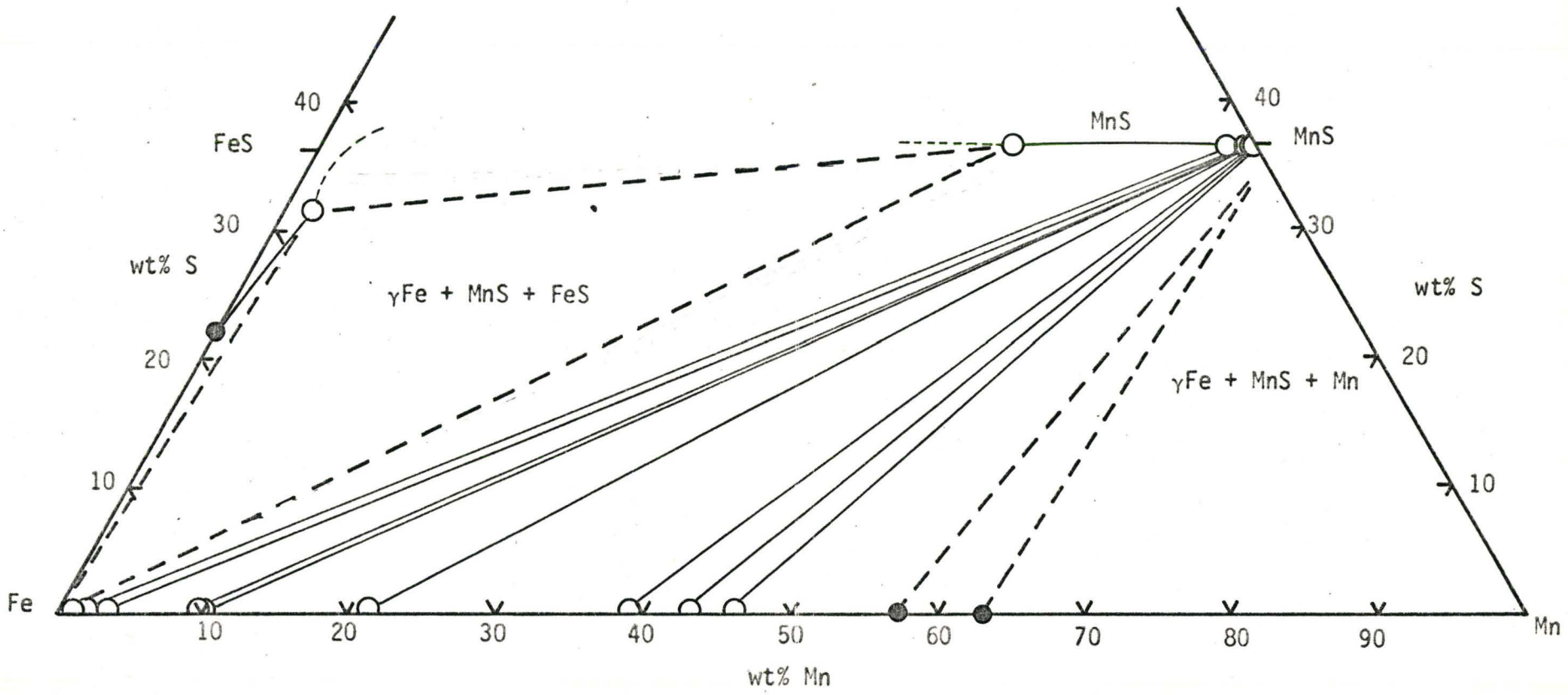

Figure 5.2 The 1300°C isotherm for the Fe-Mn-S system as determined experimentally (o) and from known binary data (●).

Table V-1

1300°C Equilibrium Experiment

Microprobe Data and Results

Standard		Fe Counts	Mn Counts
Initial	Fe	10971	90
	Mn	35	41848
	MnS	19	21894
	FeS	6407	127
Final	Fe	10699	40280
	MnS	17	24466
	FeS	6175	125

Tie-lines in the (γFe + MnS) two-phase region

Tie-Line	Fe		Mn		S
1. Fe	6233	57.07 wt.%	18746	45.93 wt.%	
MnS	40	0.22	23128	63.00	36.78 wt.%
2. Fe	6547	59.95	17494	42.89	
MnS	42	0.24	22975	62.58	37.18
3. Fe	7294	66.82	15771	38.69	
MnS	60	0.42	23241	63.31	36.27
4. Fe	90000	82.69	8631	21.13	
MnS	44	0.26	23488	63.98	35.76
5. Fe	10115	93.17	3971	9.62	
MnS	66	0.48	22601	61.56	38.00
6. Fe	10063	92.69	4090	9.93	
MnS	47	0.29	23565	64.19	35.52
7. Fe	10642	98.17	1383	3.21	
MnS	228	2.10	22635	61.73	36.17
8. Fe	10997	101.44	409	0.78	
MnS	123	1.05	22425	61.09	37.87
9. Fe	10961	101.11	722	1.57	
MnS	72	0.54	22900	62.38	37.08
10. Fe	11074	102.21	186	0.22	
MnS	1779	17.83	16228	44.45	37.72
MnS Corner of three-phase triangle	1621	16.23	17054	46.66	37.11
	1581	15.65	17856	48.80	35.55
	1675	16.59	17300	47.28	36.13
	1679	16.63	17651	48.24	35.13

Average (including tie-line No.10) 16.6 wt.% Fe, 47.1 wt.% Mn, 36.3 wt.% S

Table V-1 Cont'd.

	Fe		Mn		S
FeS Corner of three-phase triangle	6639	67.04 wt.%	477	0.94 wt.%	32.02
	6518	65.82	668	1.44	32.74
	6639	67.04	454	0.87	32.09
	6960	70.28	422	0.79	28.93
Average		67.5 wt.% Fe		1.0 wt.% Mn	31.4 wt.% S

(Figure 2.7) and indeed is generally to be expected for two phase fields which cut diagonally across a phase diagram. Nakao's failure to recognize this led him to an incorrect interpretation of his data as is later discussed.

The S content of the Fe-Mn alloy is too low to be accurately measured by micro-probe analysis. The average reading obtained with the probe over the Fe-Mn composition range of nearly pure γ-Fe to 46 wt.% Fe was 0.057 wt.% S. This is about a magnitude higher than would be expected from a theoretical extrapolation of Turkdogan's dilute Fe-Mn solution data (see section A.2.2) so must be regarded as unreliable.

Since the sulphur content of Fe-Mn alloys is extremely low one can confidently say that the compositions of the lower two corners of the (γ-Fe + MnS + Mn) three phase region are very close to the Fe-Mn binary two phase compositions (γ-Fe + Mn). The upper corner of this region is stoichiometric MnS with 0.32 $\pm$ 0.09 wt.% Fe substituted for Mn in the cation lattice. The compositions of the corners of this three phase region are given in Table V-2.

The compositions of the corners of the most important three phase region (γ-Fe + MnS + FeS) are also given in Table V-2. The iron content of the MnS corner is seen to be 16.6 wt.% Fe which is significantly different than Nakao's value of 39.4 wt.% Fe. As we shall see later the discrepancy is due to Nakao's misunderstanding of the limitations of the pseudo-binary concept. As we shall also see, the present equilibrium data together with equilibrium data acquired during the course of our kinetic experiments will permit a clearer discussion of this point (see Chapter VII).

The FeS corner obtained is not significantly different than Nakao's value. The solubility of Mn in liquid FeS is low (1.01 wt.% Mn) and the S content, though less than the 36.48 wt.% S stoichiometric value of pure FeS, is not as low as earlier anticipated on the basis of qualitative free energy surface arguments.

Table V -2

Compositions of the Corners of the Three-Phase Triangles (γ-Fe + MnS + FeS) and (γ-Fe + MnS + L_{III}) at 1300°C.

Three-Phase Triangle	Fe wt.%	Mn wt.%	S wt.%
γ-Fe	99.9	0.039	0.042
+			
MnS	16.6 $\pm$ 0.6	47.1 $\pm$ 0.7	36.3
+			
FeS	67.6 $\pm$ 1.4	1.0 $\pm$ 0.2	31.4
γ-Fe	44 $\pm$ 1	56 $\pm$ 1	~0.05
+			
MnS	0.32 $\pm$ 0.09	63.1 $\pm$ 0.7	36.6
+			
L_{III}	38 $\pm$ 1	62 $\pm$ 1	~0.05

A.2. The Solubility of S and Mn in γ-Iron

The determination of the S and Mn concentrations in the Fe corner of the three-phase triangle was not feasible using electron micro-probe analysis. Accordingly we have used the thermodynamic solubility theory outlined in Chapter III in combination with the experimental data of Turkdogan et al[9] reported in Chapter II to develop a semi-empirical expression for the solubility as a function of temperature.

The corner of this triangle may be defined at any temperature as the intersection of the solubility curve emanating from the Fe-S binary and the solubility curve of γ-Fe in equilibrium with MnS. In Chapter III the former curve was obtained from an integration of the Gibbs-Duhem equation as

$$X_1^{II} \ln X_1 - (1 + \varepsilon_{21}) X_1 X_2 = \frac{(1 + \varepsilon_{22})}{2} X_2^2 - (1 + \varepsilon_{21}) X_1^{II} X_2 + X_2 + X_1^{II} \ln X_1^o \tag{3-53}$$

In this case component 1 = S and component 2 = Mn. It was pointed out that as X_1^o becomes small (X_S^o = 0.00073 at 1300°C), the ln terms predominate, and thus

$$X_1^{II} \ln X_1 = X_1^{II} \ln X_1^o \tag{3-54}$$

or

$$X_S = X_S^o \tag{5-1}$$

This means that the solubility curve for S in γ-Fe on the ternary isotherm can be approximated by a straight line beginning at $X_S = X_S^o$ on the Fe-S binary and running parallel to the Fe-Mn binary. The temperature dependence of this solubility is simply the temperature dependence of X_1^o on the Fe-S binary.

The solubility curve for MnS in γ-iron was defined as

$$X_1^{III} \ln X_1 - (1 + \varepsilon_{21}) X_1 X_2 = \frac{(1 + \varepsilon_{22})}{2} X_2^2 - (1 + \varepsilon_{21}) X_1^{III} X_2 + X_2 - X_2^{III} \ln X_2 + \frac{\ln K}{2} \tag{3-67}$$

Assuming the MnS phase (i.e., phase III) to be stoichiometric and having negligible iron content(as evident from the tie-line direction in Figure 5.2)

one can let $X_S^{MnS} = X_{Mn}^{MnS} = 0.5$. It remains to determine the coefficients ε_{Mn}^{S}, ε_{Mn}^{Mn}, and the integration constant K in this equation.

A.2.1 The Determination of ε_{Mn}^{Mn} from Binary Fe-Mn Activity Data

The definition of ε_{Mn}^{Mn} derives from the Taylor Series expansion of $\ln_{Mn}$ as follows.

$$\ln\gamma_{Mn}\Big|_{X_{Mn}\to 0} = \ln\gamma_{Mn}^{o} + X_{Mn}\left.\frac{d\ln\gamma_{Mn}}{dX_{Mn}}\right|_{X_{Mn}\to 0} + \ldots. \qquad (5\text{-}2)$$

where γ_{Mn} is the activity coefficient of Mn in Fe, and γ_{Mn}^{o} is a constant to be identified with the Henry's law coefficient. Usually second order terms and higher are neglected. The term $(d\ln\gamma_{Mn}/dX_{Mn})$ is abbreviated as ε_{Mn}^{Mn}. It is important to note that this expansion is written for $X_{Mn}\to 0$. In familiar notation, equation 5-2 becomes

$$\ln\gamma_{Mn} = \ln\gamma_{Mn}^{o} + X_{Mn}\varepsilon_{Mn}^{Mn} \qquad (5\text{-}3)$$

One can relate ε_{Mn}^{Mn} to the α function defined in Darken and Gurry[60] which, for the Fe-Mn system, is

$$\alpha = \frac{\ln\gamma_{Mn}}{X_{Fe}^2} \qquad (5\text{-}4)$$

α is considered a constant, independent of composition, over the entire range of composition. From equation (5-4) one gets

$$\ln\gamma_{Mn} = \alpha X_{Fe}^2 = \alpha(1 - X_{Mn})^2$$

$$= \alpha(1 - 2X_{Mn} + X_{Mn}^2) \qquad (5\text{-}5)$$

Since ε_{Mn}^{Mn} is defined for $X_{Mn} \rightarrow 0$ one can neglect the second order term, X_{Mn}^2, and write equation (5-5) as

$$\ln\gamma_{Mn} = \alpha - 2\alpha X_{Mn} \tag{5-6}$$

The equivalence of equations 5-3 and 5-6 permits one to write

$$\varepsilon_{Mn}^{Mn} = -2\alpha \tag{5-7}$$

and

$$\ln\gamma_{Mn}^{o} = \ln k = \alpha \tag{5-8}$$

Roy and Hultgren[81] have determined the activity of Mn in γ-Fe over the entire concentration range at 1177°C (1450°K). Their data is plotted is Figure 5.3 as the activity, a_{Mn}, versus mole fraction X_{Mn}. To find α one applies equation 5-4 to their data. The results are plotted in Figure 5.4 as α versus mole fraction X_{Mn}. One notes in Figure 5.4 that α is not independent of composition. Up to $X_{Mn} = 0.5$, α appears to be either a constant or linearly dependent upon X_{Mn}, depending upon one's interpretation of the point scatter. For constant α the average value up to $X_{Mn} = 0.5$ (dashed line in Figure 5.4) is

$$\alpha = 0.48 \tag{5-9}$$

from which

$$\varepsilon_{Mn}^{Mn} = -0.95 \tag{5-10}$$

and

$$k = 1.61 \tag{5-11}$$

For a linear dependence of α up to $X_{Mn} = 0.5$, then using linear regression analysis, α is

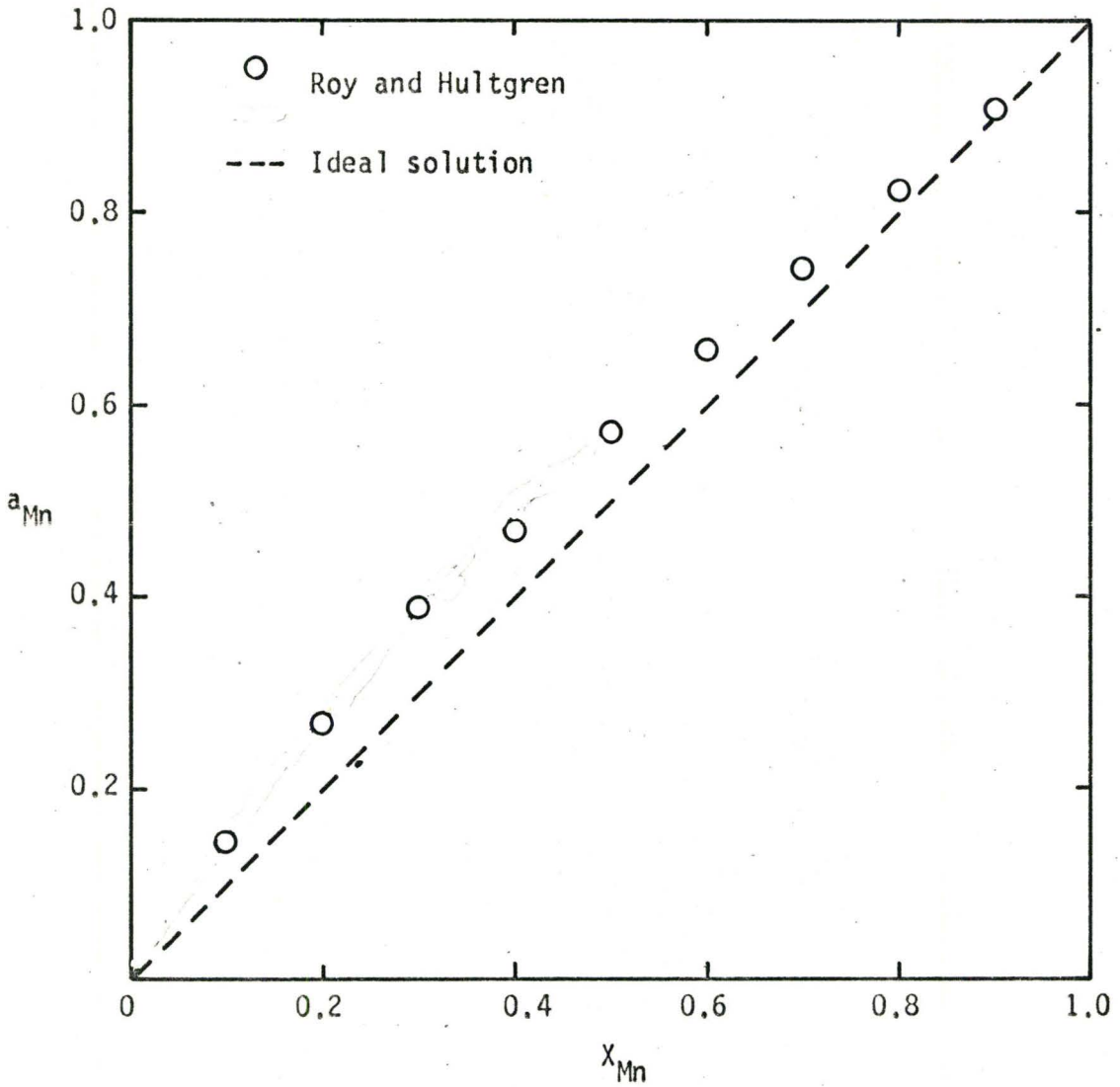

Figure 5.3 The activity of Mn in Fe at 1177°C after Roy and Hultgren[81].

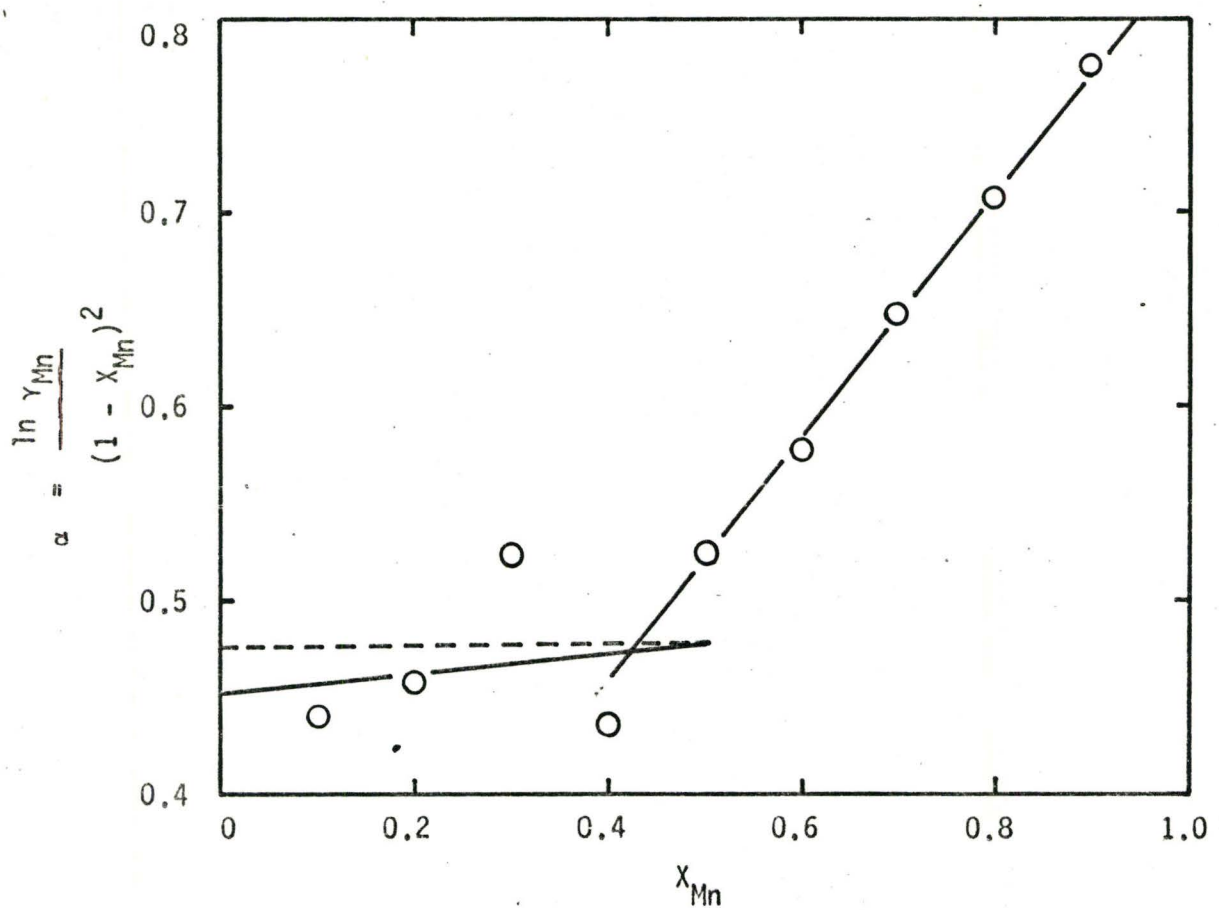

Figure 5.4 A plot of the α function versus the mole fraction of Mn, X_{Mn}, from the data of Roy and Hultgren.

$$\alpha = 0.051\ X_{Mn} + 0.45 \qquad (5\text{-}12)$$

Since ε_{Mn}^{Mn} is defined for $X_{Mn} \to 0$, then equation 5-12 yields

$$\alpha = 0.45 \qquad (5\text{-}13)$$

from which

$$\varepsilon_{Mn}^{Mn} = -0.90 \qquad (5\text{-}14)$$

and

$$k = 1.57 \qquad (5\text{-}15)$$

Because the maximum number of significant figures justified by the data is one, we have accepted a value of $\varepsilon_{Mn}^{Mn} = -1$ for our calculations.

A.2.2. The Evaluation of ε_{Mn}^{S} and K(T)

Using the thermodynamic equation 2-16 one can write an expression relating wt.% S and wt.% Mn in γ-Fe as

$$\log[\%S] = \log K_2 - \log [\%Mn] - \log f_{MnS}^{S} \qquad (5\text{-}16)$$

(In equation 2-16 a_{MnS} is assumed to be unity). By choosing a value of [%Mn] at a temperature T one can calculate numerical values for $\log f_{Mn}^{S}$ and $\log K_2$ from Turkdogan et al's equations 2-17 and 2-18, respectively. Using [%Mn] = 0.4 and 1.30, the corresponding values of [%S] were calculated from equation 5-16 at 1100, 1200, 1300, and 1335°C. These values are listed in Table V-3.

At any one temperature two sets of compositions (%Mn, %S) are necessary, when converted to (X_{Mn}, X_S), to determine the interaction

coefficient ε_{Mn}^{S} and the integration constant K in the solubility equation 3-67. Using $\varepsilon_{Mn}^{Mn} = -1$ and the values of (X_{Mn}, X_S) in Table V-3, ε_{Mn}^{S} and K were determined for the corresponding temperatures. These values are also listed in Table V-3.

In Chapter III we showed the temperature dependence of the integration constant, K, to be

$$K = K_o \; e^{\frac{2Q}{RT}} \tag{3-102}$$

Thus a plot of the empirical values of lnK versus 1/T (T in ^oK) should yield a straight line. This is done in Figure 5.5, and the temperature dependence of K determined from this line is

$$K = 0.16 \exp(-41722/RT) \tag{5-17}$$

Thus the heat of precipitation of MnS in γ-Fe is Q = -20861 calories/mole.

Having determined the coefficients it is now possible to determine the point of intersection of the two solubility curves. This has been done graphically at the four temperatures shown in Figure 5.6. At 1300^{o}C the point of intersection, and thus the composition of the Fe corner of the three phase triangle, is X_{Mn} = 0.00039 and X_S = 0.00073, (0.039 wt.% Mn, 0.042 wt.% S).

Our value is to be compared with the value proposed by Nakao (X_{Mn} = 0.00153, X_S = 0.000157), also shown in Figure 5.6 along with Turkdogan et al's experimental data. Nakao's value of X_{Mn} was based on the results of an Fe:MnS diffusion couple which are graphically shown in Figure 2.19. His misunderstanding of the tie-line direction in the (γFe + MnS) two-phase region led him to interpret the interface value of 0.2 wt.% Mn in γ-Fe in

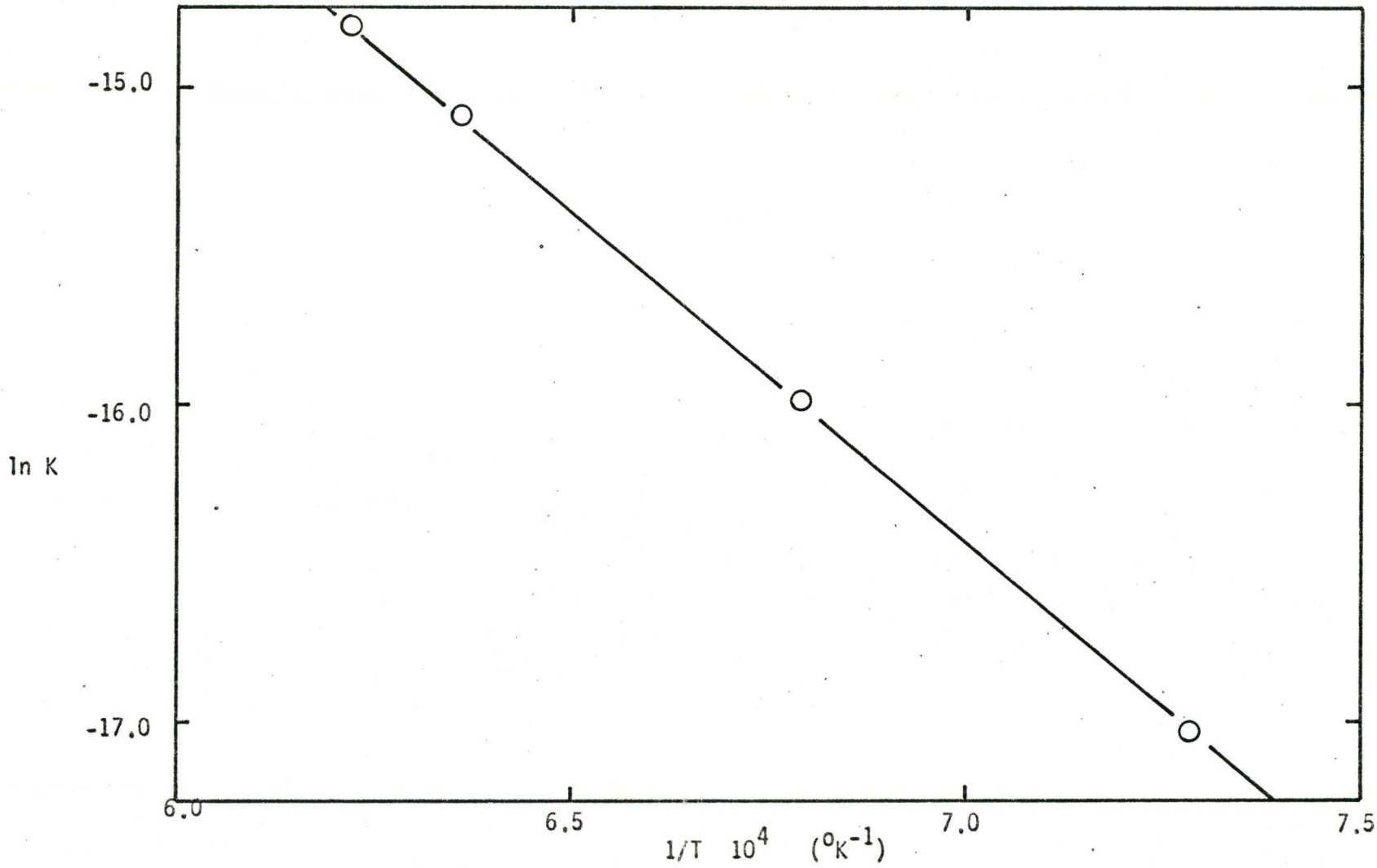

Figure 5.5 The plot of ln K, as calculated from the solubility equation using the results of Turkdogan et al, as a function of the absolute temperature.

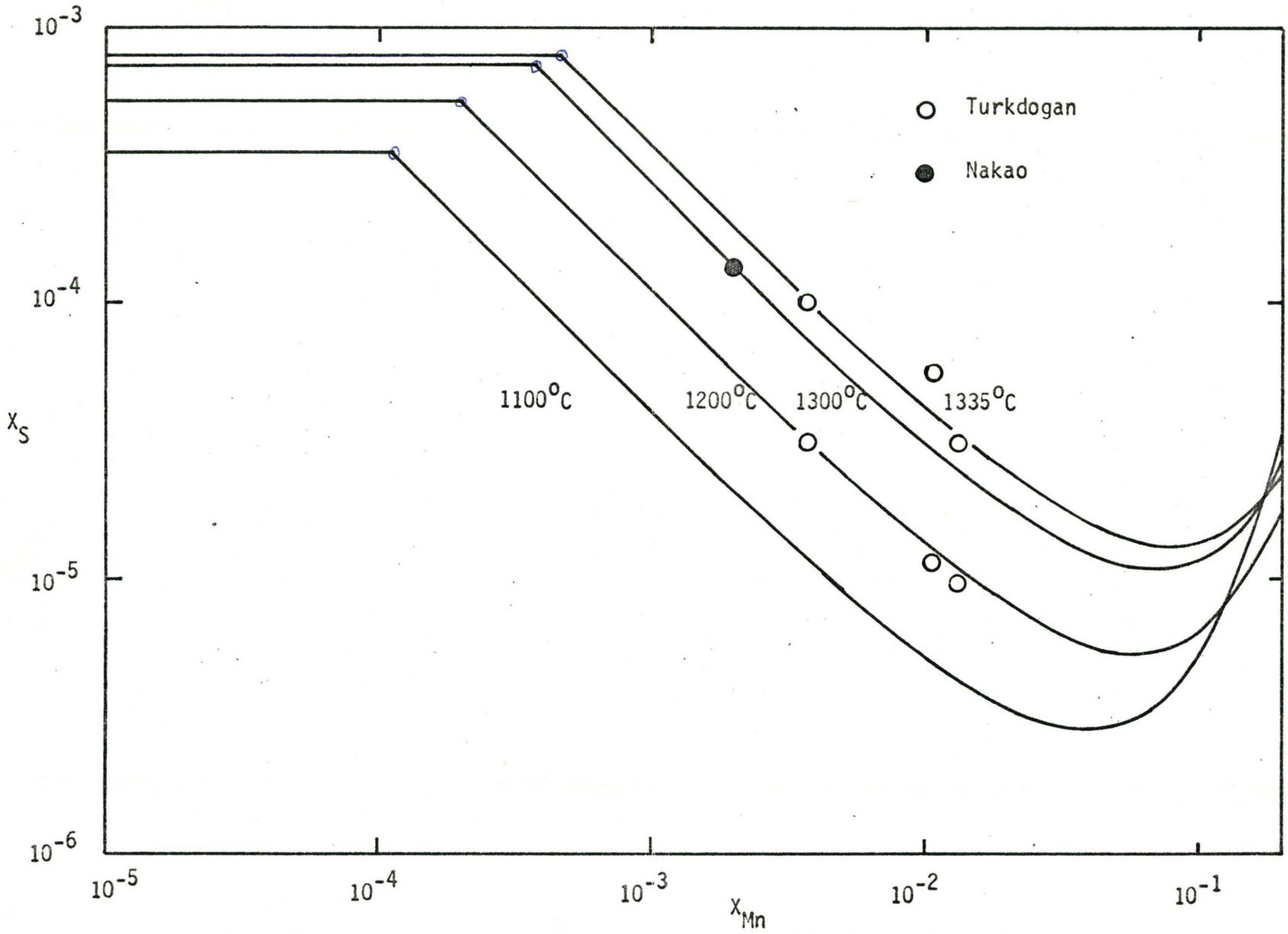

Figure 5.6 The solubility of Mn and S in γ-Fe

Figure 2.19 to be only slightly greater than the three-phase equilibrium value, and thus to a guess of 0.15 wt.% Mn for this value. He did not believe, however, that the MnS was in chemical equilibrium with the γ-Fe at the interface. Our results show that the interface was in equilibrium, and thus from his value of 0.2 wt.% Mn we can determine the equilibrium amount of sulphur from Figure 5.6 and these coordinates represent a tie-line in the two-phase region at 1300°C. This tie-line is

γ-Fe (0.2 wt.% Mn, 0.008 wt.% S) = MnS (3.7 wt.% Fe, 59.4 wt.% Mn)

(The MnS end of the tie-line is acquired from the results of our Fe:MnS kinetic experiments to be discussed later.)

It is interesting to note that the four curves equilibrating γ-Fe and MnS are nearly linear for X_{Mn} <0.01 (1 at % Mn). This was predicted in Chapter III where it was shown that a chemical solubility product could be used at low concentrations. That is

$$X_S \, X_{Mn} = K \qquad (3\text{-}61)$$

which, of course, plots as linear on log-log paper. Also, each of the curves passes through a minimum in the region of X_{Mn} = 0. 1 (10 at% Mn), the precise position of which can be calculated from the solubility theory of Chapter III.

These solubility curves have been extended to 20 at% Mn which is undoubtedly well beyond the validity of the Wagner approximation. However the facts that the Fe-Mn system is nearly ideal over the entire concentration range and the low S solubilities in this region ($X_S < 10^{-4}$), imply that the calculated values of X_S from 10 to 20 at% Mn are reasonable representations of the S contents in this region.

Temp °C	[%Mn]	[%S]	X_{Mn}	X_S	ε^S_{Mn}	ln K
	0	0.02046	0	0.000357		(- 17.0294)
1100°	0.40	0.000604	0.004066	0.0000105	(- 13.8135)	
	1.30	0.000210	0.013213	0.0000037	- 13.8	- 17.0
	0	0.0310	0	0.00005408		
1200	0.40	0.001671	0.0040669	0.0000292	(- 9.5929)	(- 15.9895)
	1.30	0.000569	0.0132124	0.0000099	- 9.6	- 16.0
	0	0.04167	0	0.0007268		(- 15.0982)
1300	0.40	0.004060	0.0040659	0.0000708	(- 8.1981)	
	1.30	0.001356	0.0132123	0.0000237	- 8.2	- 15.1
	0	0.0456	0	0.0007953		
1335	0.40	0.005397	0.0040658	0.0000942	(- 7.3687)	(- 14.8091)
	1.30	0.001792	0.0132123	0.0000313	- 7.4	- 14.8

Table V-3

Tabulation of the calculated values for X_{Mn}, X_S, ε^S_{Mn}, and ln K.

Thus, with the exception of the FeS-MnS "pseudo-binary" section, the 1300°C isotherm for the Fe-Mn-S system has been quantitatively described. The examination of the pseudobinary in Chapter VIII plus additional data from the kinetic experiments will complete the record of the current constitutional knowledge of this isotherm.

A.3. The Three-Phase Region at Temperatures Below and Above 1300°C

The 1300°C experiment was most informative because during the anneal the couple did not attain uniform activity and so a broad range of local equilibria was recorded. Of the other five equilibrium experiments, the three performed at 1190, 1251, and 1336°C went to completion as illustrated by their microstructures, Figures 5.7, 5.8 and 5.9, respectively. The equilibrated three-phase structure in each case implies that the only data obtainable are the corners of the three-phase triangle on the isotherm at each temperature. This data is tabulated for the FeS and MnS corners in Table V-4, V-5 and V-6.

Again the S and Mn contents in γ-Fe were too small to measure, so we rely on the semi-empirical curves of Figure 5.6 for this data. From the data we see that within the experimental error the FeS corner is invariant in composition throughout the experimental temperature range. However the composition of the MnS corner does vary with temperature, the variation being limited to the Fe and Mn contents. The S content, within the accuracy of the measurements, remains fixed at the stoichiometric value. Figure 5.10 shows the change in Fe content in MnS as a function of temperature.

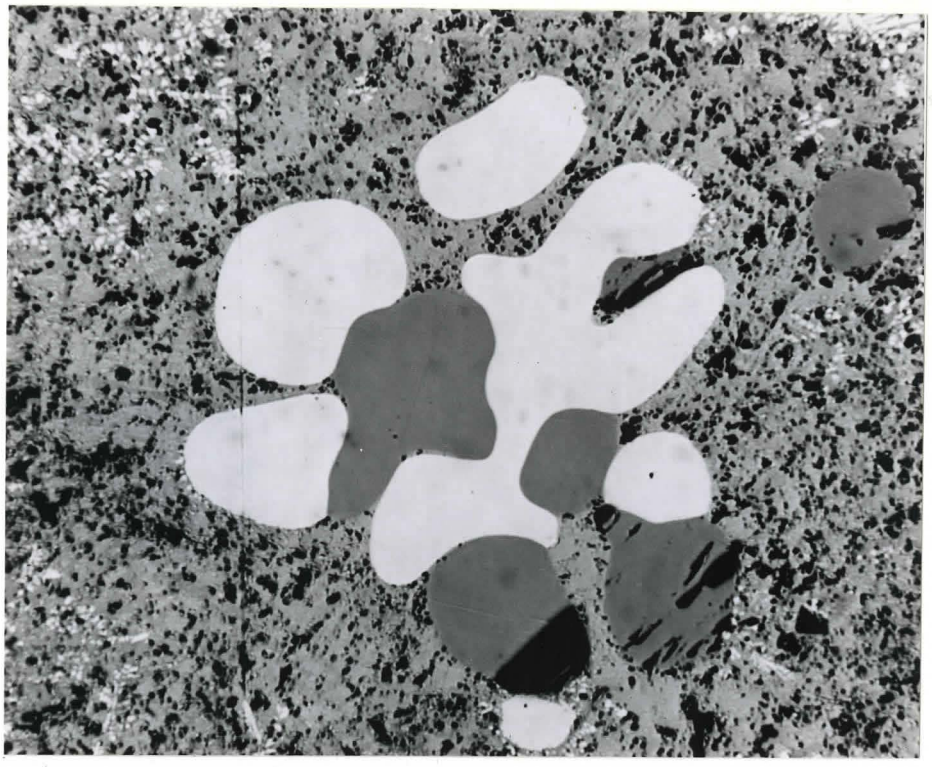

Figure 5.7 Three-phase (γ-Fe + MnS + FeS) equilibrium. at 1190°C. X225

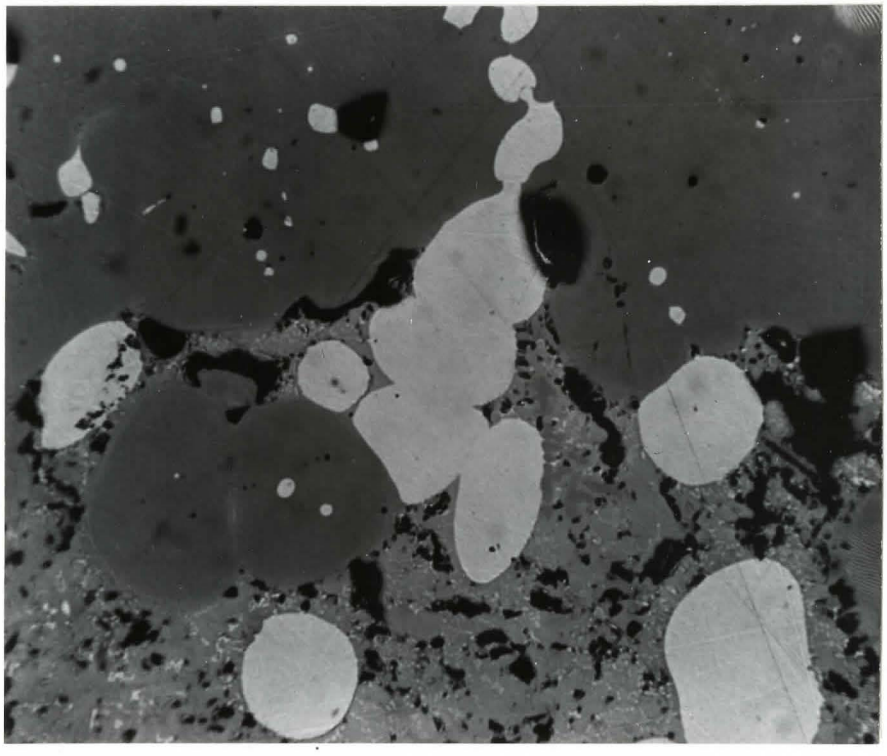

Figure 5.8 Three-phase (γ-Fe + MnS + FeS) equilibrium 1251°C. X225

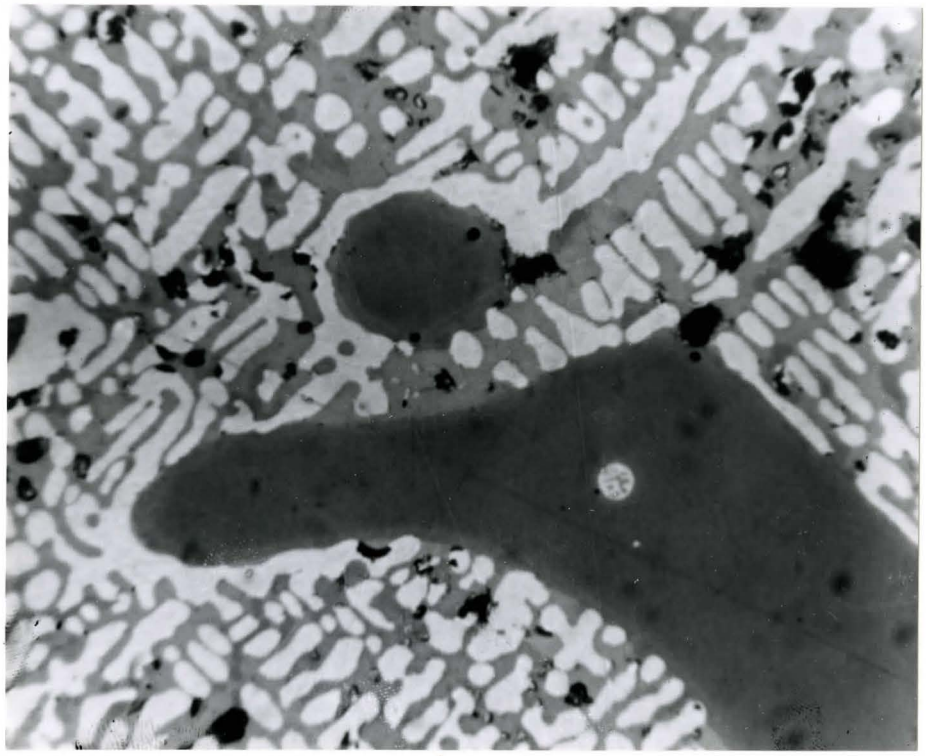

Figure 5.9 Three-phase (γ-Fe + MnS + FeS) equilibrium at 1336^{o}C. X225

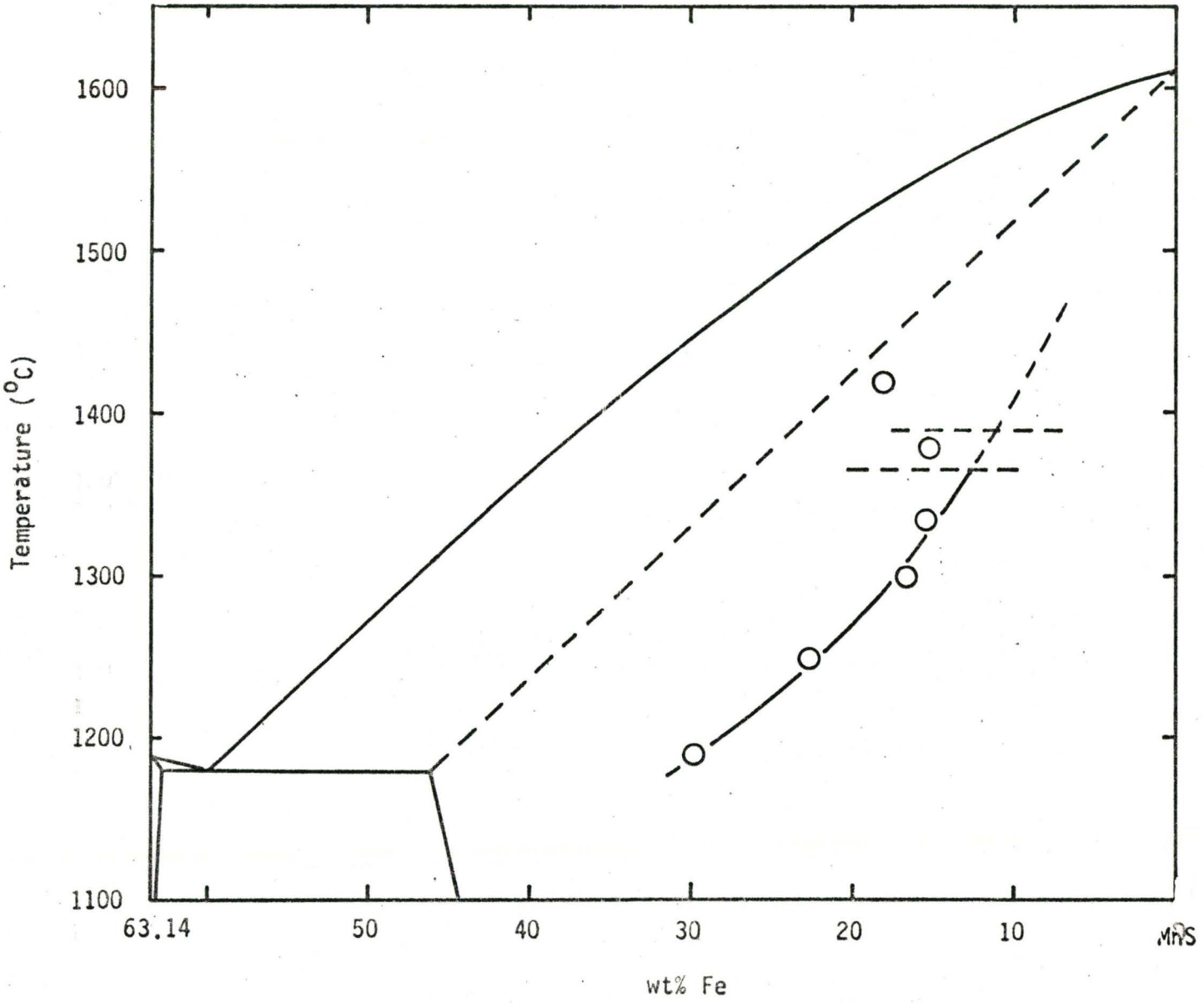

Figure 5.10 The variation of the MnS corner of the (γ-Fe + MnS + FeS) three-phase triangle with temperature in relation to the FeS-MnS pseudo-binary diagram. The Fe content is plotted at constant S composition (36.86 wt% S).

We have superimposed the FeS-MnS 'pseudo-binary' diagram of Shibata onto Figure 5.10 to show its relation to the temperature variation of the MnS corner of the (γ-Fe + MnS + FeS) three-phase triangle. As will be seen in Chapter VIII the MnS phase in the 'pseudo-binary' has its lowest S content at the stoichiometric value, and it is at this S content that the MnS corner of the three-phase field contacts the MnS solid solution field of the 'pseudo-binary'.

We know from the discussion in Chapter III, (see Figure 3.9e and f) that the (γ-Fe + MnS + FeS) region originates at a temperature above 1365°C (the Fe-S extectic temperature), but probably below 1390°C (the δFe $\rightleftarrows$ γFe temperature). Thus the curve in Figure 5.10 must terminate between 1365 and 1390°C. The composition at which it terminates can be estimated by assuming the curve can be extrapolated to the melting point of MnS. From Figure 5.10 this composition is stoichiometric MnS with approximately 12 wt.% Fe replacing Mn in the cation lattice.

The preceding discussion implies that the experiment performed at 1419°C could not possibly have led to equilibrium as a (γ-Fe + MnS + FeS) three phase structure, and its microstructure, Figure 5.11, clearly illustrates this. Figure 3.9, illustrating the δFe(Mn,S) $\rightleftarrows$ γFe(Mn,S) phase changes shows that both δ-Fe and γ-Fe are stable at 1419°C, along with solid MnS and L_I. (In Chapter VIII it will be shown that L_I and L_{II}, the two immiscible liquids, become the single FeS liquid just above 1365°C).

The matrix material in the microstructure is a fine, dendritic (Fe + MnS + FeS) structure. The massive gray band is MnS. The light globules are revealed at a higher magnification (Figure 5.12) to be a two phase structure (Fe + FeS). This microstructure can be explained as follows.

At 1419°C the two-phase globules form a three-phase equilibrium at the MnS (band) interface between Fe, MnS, and L_I, and in Figure 3.9b the only three phase region containing these three phases is that containing δ-Fe. The matrix surrounding the globules and MnS band at 1419°C was probably liquid L_I which, during quenching, dissociated into the fine dendritic Fe and MnS phases in FeS. Thus there are threeequilibria involved; the (δ-Fe + L_I) equilibrium within the globules, the (δ-Fe + MnS + L_I) equilibrium between the globules and the MnS band, and the (MnS + L_I) equilibrium between the matrix and the MnS band. The tie-lines in the two-phase fields must be very near to the three-phase field boundaries.

Unfortunately, because of the fine structure, the MnS phase was the only phase of sufficient area to analyse. This composition is presented in Table V-8 and Figure 5.10. In Figure 5.10 this composition is tothe left of the extended curve. This is to be expected, since at a slightly lower temperature, at $T = T_T$, the three-phase regions (δ-Fe + MnS + L_I) and (γFe + δFe + Mn) react to give (γFe + MnS + L_I) as one of the product three phase regions (see Figure 3.11e).

The equilibrium experiment performed at 1379°C is within the temperature range at which the (γ-Fe + MnS + L_I) three-phase field originates (see Figures 3.9d, e, and f). Because we do not know if $T = T_T$ is above or below 1379°C, we cannot state whether or not the at-temperature microstructure of this experiment could contain this three-phase reaction. However the resultant microstructure, Figure 5.13, is two-phase (L_I + MnS), indicating that the average composition of the sample is somewhere in the (L_I + MnS) two-phase field. Again the L_I phase has decomposed to Fe

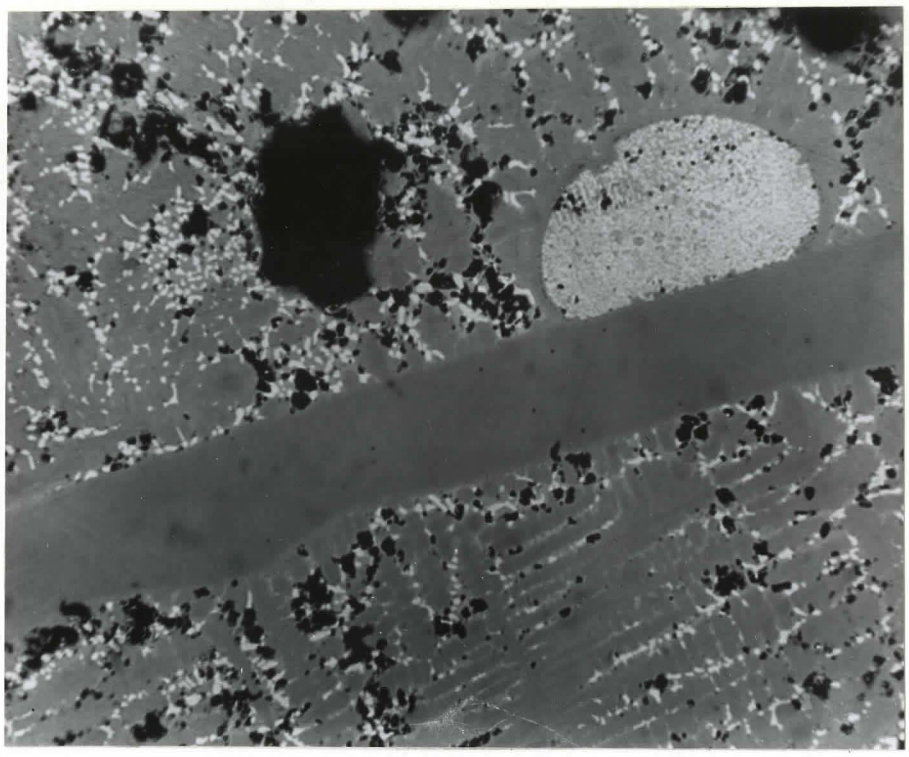

Figure 5.11 The microstructure of the sample reacted at 1419°C. A MnS band and a Fe rich globule are present in a (Fe + MnS + FeS) matrix. X225

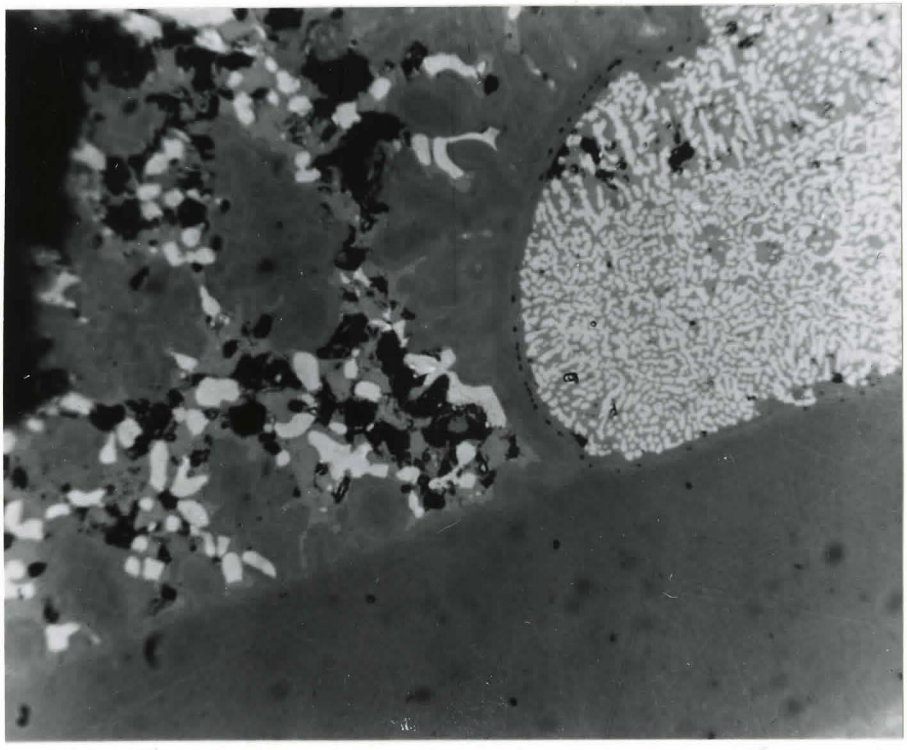

Figure 5.12 The Fe rich globule in figure 5.11 is seen to be the two-phase structure (Fe + FeS). X620

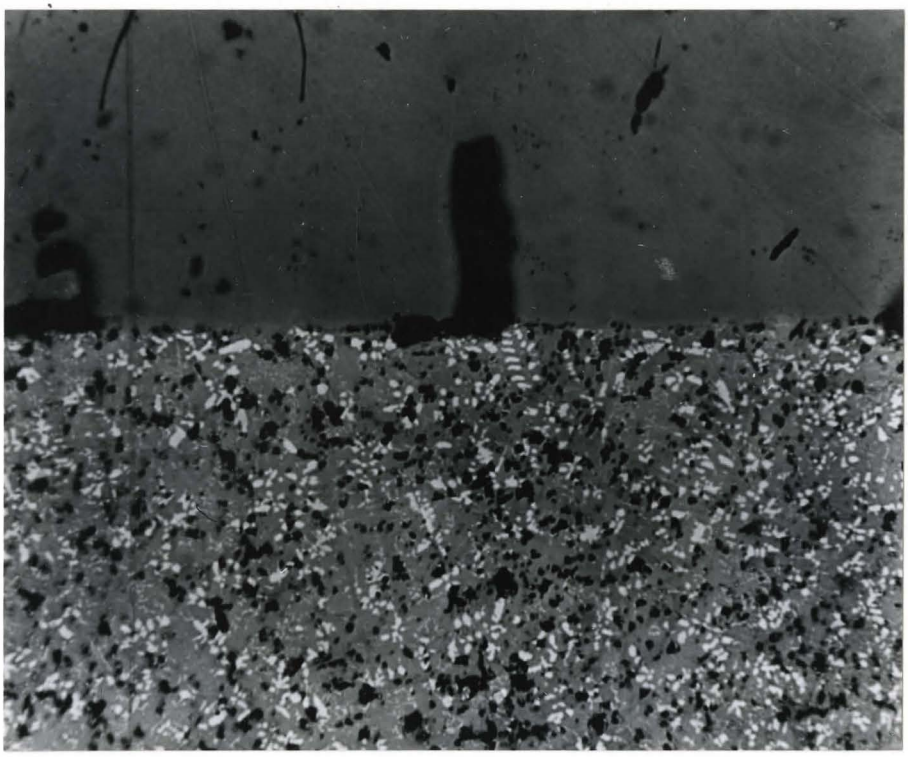

Figure 5.13 Two-phase (FeS + MnS) equilibrium of the sample reacted at 1379^{o}C. X225

Table V-4

1190°C Equilibrium Experiment
Microprobe Data and Results

Standard		Fe Counts	Mn Counts
Initial	Fe	8705	26
	Mn	117	28925
	MnS	78	16214
	FeS	4885	45
Final	Fe	8679	30
	Mn	116	28268
	MnS	73	16070
	FeS	5198	57

MnS Corner of the Three-Phase Triangle

Fe		Mn		S
2589	31.46 wt.%	8160	32.17 wt.%	36.37 wt.%
2593	31.51	8319	32.43	36.06
2602	31.62	8226	32.07	36.31
2245	27.18	9375	35.92	35.90
2264	27.42	9144	36.01	36.57
2528	30.73	8319	32.76	36.51
2370	28.75	9109	35.87	35.38
Average	29.8 wt.% Fe		34.0 wt.% Mn	36.2 wt.% S

FeS Corner of the Three-Phase Triangle

Fe		Mn		S
5914	74.44 wt.%	187	0.54 wt.%	25.02 wt.%
5190	65.33	129	0.31	34.36
5229	65.82	492	1.75	32.43
4976	62.63	465	1.65	35.72
5549	69.85	160	0.43	29.72
5304	66.76	151	0.40	32.84
5560	69.99	179	0.51	29.50
Average	69.1 wt.% Fe		0.8 wt.% Mn	30.1 wt.% S

Table V-5

1251°C Equilibrium Experiment

Microprobe Data and Results

Standard	Fe Counts	Mn Counts
Initial Fe	7601	19
Mn	113	28561
MnS	64	16112
FeS	4430	33
Final Fe	7812	27
Mn	102	30282
MnS	61	17103
FeS	4510	45

MnS Corner of Three-Phase Triangle

Fe		Mn		S
1607	21.76 wt.%	11171	42.71 wt.%	35.53 wt.%
1777	24.15	10208	39.07	36.78
1688	22.90	10755	41.12	35.98
1572	21.27	11231	42.94	35.79
Average	22.5 wt.% Fe	41.5 wt.% Mn		36.0 wt.% S

FeS Corner of Three-Phase Triangle

Fe		Mn		S
4776	67.80 wt.%	100	0.24 wt.%	31.96 wt.%
5109	72.53	181	0.55	24.92
4638	65.85	250	0.81	33.34
4769	67.71	364	1.26	31.03
Average	68.5 wt.% Fe	0.7 wt.% Mn		30.8 wt.% S

Table V-6

1336°C Equilibrium Experiment

Microprobe Data and Results

Standard	Fe Counts	Mn Counts
Initial Fe	11325	95
Mn	41	41761
MnS	75	23549
FeS	6182	143
Final Fe	11220	96
Mn	36	43476
MnS	22	24376
FeS	5919	157

MnS Corner of the Three-Phase Triangle

Fe		Mn		S
1626	15.41 wt.%	18372	48.38 wt.%	36.21 wt.%
1609	15.25	18166	47.84	36.91
1719	16.31	18286	48.21	35.48
1629	15.44	18535	48.87	35.69
1520	14.39	17966	47.31	38.30
Average	15.4 wt.% Fe	48.1	wt.% Mn	36.5 wt.% S

FeS Corner of the Three-Phase Triangle

Fe		Mn		S
6186	60.04 wt.%	377	0.61 wt.%	39.95 wt.%
7015	68.09	499	0.93	30.98
6089	59.10	750	1.60	39.30
6073	58.94	777	1.67	39.39
6102	59.23	875	1.98	38.79
Average	61.1 wt.% Fe	1.4	wt.% Mn	37.6 wt.% S

Table V-7

1379°C Equilibrium Experiment

Microprobe Data and Results

Standard	Fe Counts	Mn Counts
Initial Fe	9820	81
Mn	16	41369
MnS	8	23393
FeS	5581	149
Final Fe	9809	98
Mn	18	41929
MnS	11	23626
FeS	5614	142

MnS Side of Two-Phase Region

Fe		Mn		S
1382	15.16 wt.%	18322	49.42 wt.%	35.42 wt.%
1386	15.21	18716	50.49	34.30
1377	15.11	19299	52.06	32.83
1411	15.48	18894	50.97	33.55
1400	15.36	18065	48.74	35.90
1348	14.79	18491	49.89	35.32
Average	15.1 wt.% Fe		50.3 wt.% Mn	34.6 wt.% S

FeS Side of Two-Phase Region

Fe		Mn		S
5740	63.99 wt.%	737	1.61 wt.%	34.40 wt.%
5874	65.49	332	0.51	34.00
5908	65.87	607	1.26	32.87
6041	67.35	513	1.00	31.65
6108	68.10	468	0.90	31.00
5976	66.63	671	1.43	31.94
Average	66.2 wt.% Fe		1.1 wt.% Mn	32.6 wt.% S

Table V-8

1419°C Equilibrium Experiment

Microprobe Data and Results

Standard	Fe Counts	Mn Counts
Initial Fe	9627	94
Mn	27	55420
MnS	16	31220
Final Fe	9552	94
Mn	23	55383
MnS	13	31325

MnS Phase

Fe		Mn	
1469	16.45 wt.%	24124	48.93
1459	16.27	24254	49.19
1613	18.00	23685	48.03
2122	23.74	21455	43.51
1969	22.04	22028	44.68
1535	17.12	24498	49.68
1487	16.58	24813	50.32
1467	16.36	24711	50.12
1910	21.37	22229	45.08
1430	15.94	24709	50.11
1502	16.75	24462	49.61
1467	16.36	24460	49.61

Average 18.1 wt.% Fe 48.2 wt.% Mn 33.7 wt.% S

dendrites and FeS upon quenching. The probe data was acquired from the FeS/MnS interface regions, and thus the compositions, Table V-7, represent a tie-line in the two-phase region. The fact that the MnS end of this tie-line, as plotted in Figure 5.10 is just to the left of the three-phase equilibrium curve implies that this tie-line is near the (iron + MnS + L_I) three phase triangle shown in Figure 3.9d or 3.9f. In these figures we note that the iron phase of the three-phase triangle is δ-Fe and γ-Fe, respectively.

B. THE EUTECTIC TROUGH MAXIMUM

B.1. The Calculation of the Eutectic Trough Maximum

The temperature, T_c, and the composition, (X^c_{Mn}, X^c_S), at the eutectic trough maximum, see Figure 5.17, can be uniquely evaluated in terms of the binary solubilities and the solubility product for the MnS liquidus in the following way. On an isotherm the δ-Fe liquidus may be approximated by a line according to Hone et al[62], and at a temperature just above T_c the liquidus may be written as

$$X_S = mX_{Mn} + b \qquad (5\text{-}18)$$

where

$$m = -\left(\frac{X^o_S + a}{X^o_{Mn} + a}\right) \quad \text{and} \quad b = (X^o_S + a)$$

X^o_S and X^o_{Mn} are the binary solid solubilities (mole fractions) and 'a' is the solute concentration difference between the binary solidus and liquidus. At constant T the value of 'a' is the same for both binaries, and indeed

is the same for any solute element dissolved in δ-Fe in dilute concentrations. (This can be seen from the van't Hoff equation, equation 2.1. Since T_{tr} and ΔH_{tr} refer to the pure solvent, then $\Delta[S]$ is the same for any dilute solute at constant ΔT).

The MnS liquidus is described as a solubility product,

$$X_S \, X_{Mn} = K \tag{5-19}$$

Eliminating X_S between equations 5-18 and 5-19 one gets

$$m \, X_{Mn}^2 + b \, X_{Mn} - K = 0 \tag{5-20}$$

or

$$X_{Mn} = \frac{- b \pm \sqrt{b^2 + 4mK}}{2m} \tag{5-21}$$

At T_c the two curves must be tangential and thus the solution of equation 5-20 must be a single value of X_{Mn}, i.e., $X_{Mn} = X_{Mn}^c$.
This occurs when

$$b^2 + 4mK = 0 \tag{5-22}$$

It follows that

$$X_{Mn}^c = - \frac{b}{2m} = - \left(\frac{X_S^o + a}{2}\right) \left(- \frac{X_{Mn}^o + a}{X_S^o + a}\right)$$

$$= \frac{X_{Mn}^o + a}{2} \tag{5-23}$$

and thus

$$X_S^c = \frac{X_S^o + a}{2} \tag{5-24}$$

That is, point C occurs at the mid-point of the δ-Fe liquidus.

The solidus end of the tie-line, PC, can now be determined using the binary distribution coefficients, k_{Mn} and k_S, which Hone et al[62] have shown to be constant for the (δ-Fe + L_I) two phase region in the Fe-Mn-S ternary system. That is

$$X^P_{Mn} = k_{Mn}\, X^C_{Mn} = \frac{X^o_{Mn}}{2} \tag{5-25}$$

and

$$X^P_S = k_S\, X^C_S = \frac{X^o_S}{2} \tag{5-26}$$

That is, point P is exactly mid-point on the δ-Fe solidus.

The extension of the tie-line PC into the (MnS + L_I) region must go straight to MnS. The slope of the tie-line PC is

$$S_{PC} = \frac{X^C_S - X^P_S}{X^C_{Mn} - X^P_{Mn}} = \frac{\frac{X^o_S + a}{2} - \frac{X^o_S}{2}}{\frac{X^o_{Mn} + a}{2} - \frac{X^o_{Mn}}{2}} = \frac{a}{a} = 1 \tag{5-27}$$

The slope of the tie-line MnS-C is

$$S_{MnS} = \frac{X^{MnS}_S - X^C_S}{X^{MnS}_{Mn} - X^C_{Mn}} = \frac{\frac{1}{2} - \frac{X^o_S + a}{2}}{\frac{1}{2} - \frac{X^o_{Mn} + a}{2}} = \frac{1 - (X^o_S + a)}{1 - (X^o_{Mn} + a)} \tag{5-28}$$

and since $(X^o_S + a)$ and $(X^o_{Mn} + a)$ are both $\ll 1$, then $S_{MnS} \simeq 1$.

To determine T_C we use the fact that the slopes, dX_S/dX_{Mn}, of both liquidus curves must be equal at point C. From equation 5-18, dX_S/dX_{Mn} is

$$\frac{dX_S}{dX_{Mn}} = m = -\left(\frac{X_S^o + a}{X_{Mn}^o + a}\right) \tag{5-29}$$

and from equation 5-19

$$\frac{dX_S}{dX_{Mn}} = -\frac{K}{X_{Mn}^2} = -\frac{4K}{(X_{Mn}^o + a)^2} \tag{5-30}$$

At point C, $X_{Mn} = (X_{Mn}^o + a)/S$. By equating 5-29 and 5-30, and simplifying one gets

$$4K = (X_S^o + a)\,(X_{Mn}^o + a) \tag{5-31}$$

However K, $(X_S^o + a)$, and $(X_{Mn}^o + a)$ are functions of temperature as follows

$$K = K_o\, e^{\frac{2Q}{RT}} \tag{3-102}$$

$$(X_S^o + a) = \frac{T - 1535}{M} \tag{5-32}$$

$$(X_{Mn}^o + a) = \frac{T - 1535}{N} \tag{5-33}$$

Equation 3-102 is derived in Chapter III. Equations 5-32 and 5-33 follow from the fact that the liquidus curves are linear in the Fe-S and Fe-Mn binary systems, M and N being the slopes of the liquidus lines in the Fe-S and Fe-Mn systems, respectively, and 1535^oC being the melting point of iron.

Substituting 3-102, 5-32 and 5-33 into 5-31 at $T = T_C$ gives

$$4K^o\, e^{\frac{2Q}{RT_C}} = \frac{(T_C - 1535)^2}{MN} \tag{5-34}$$

To graphically determine T_C one plots $F_1(T) = 4K_o e^{\frac{2Q}{RT}}$ as a function of T, and $F_2(T) = (T - 1535)^2/MN$ as a function of T. The intersection ($T < 1535^oC$) of the two curves occurs at T_C. Using the following numerical values for the parameters the graphical determination of T_C is shown in Figure 5.16.

$2Q = -40,100$ cal. (see Chapter II)

$K_o = 14.08$ (see Chapter II)

$N = -529.66$ (see Figure 5.14)

$M = -1686.91$ (see Figure 5.15)

$k_{Mn} = 0.699$ (see Figure 5.14)

$k_S = 0.0418$ (see Figure 5.15)

The temperature T_C and the compositions of the points C, P, and the binary points are listed in Table V-9 and plotted in Figure 5.17.

Table V-9

Calculated Temperature and Compositions at the Eutectic Trough Maximum

$T_C = 1509^oC$	$X^o_{Mn} + a = 0.0491$
$X^C_{Mn} = 0.0245$	$X^o_S + a = 0.0154$
$X^C_S = 0.00771$	$X^o_{Mn} = 0.0343$
$X^P_{Mn} = 0.0171$	$X^o_S = 0.000644$
$X^P_S = 0.000322$	

The accuracy of a calculation of this type is dependent upon the assumptions and approximations, the binary phase diagram data, and the value of the solubility product used. Of these, the value of the solubility product has the greatest effect upon the calculated value of T_C and (X^C_{Mn}, X^C_S). The reliability of $2Q = -40,100$ cal/mole will be discussed in Chapter VIII,

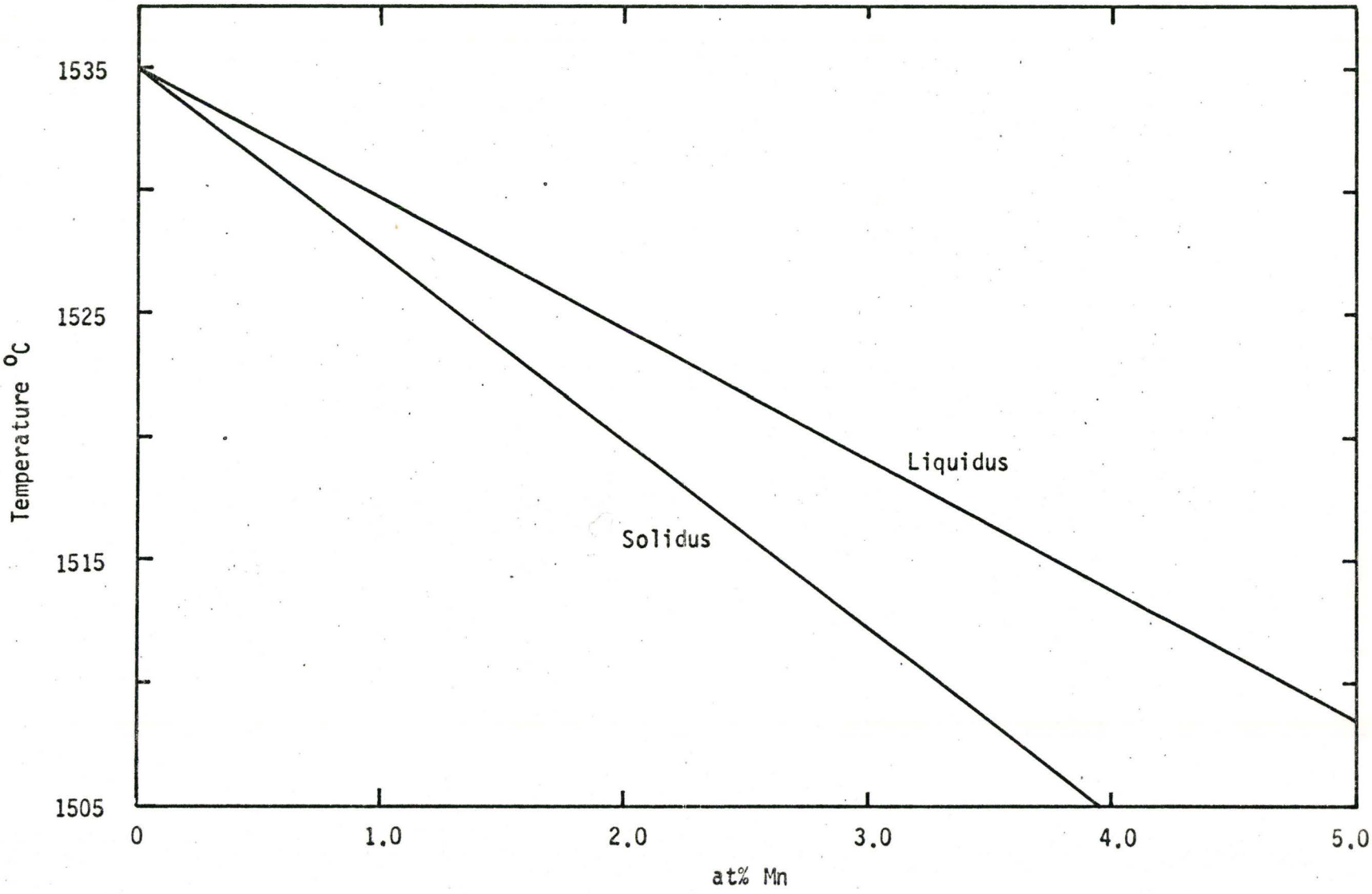

Figure 5.14 Binary Fe-Mn phase diagram showing the solidus and liquidus curves.

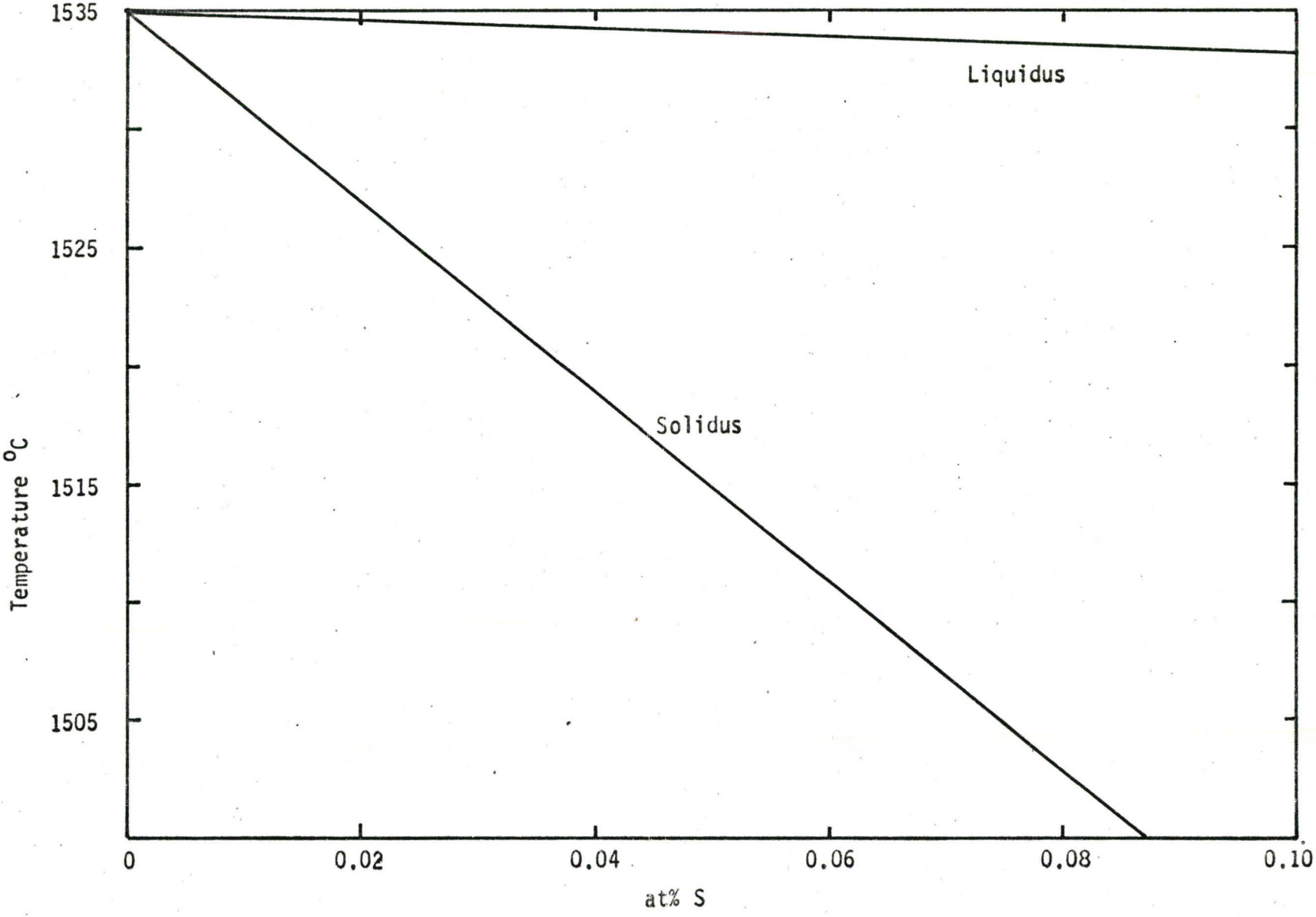

Figure 5.15 Binary Fe-S phase diagram showing the solidus and liquidus curves

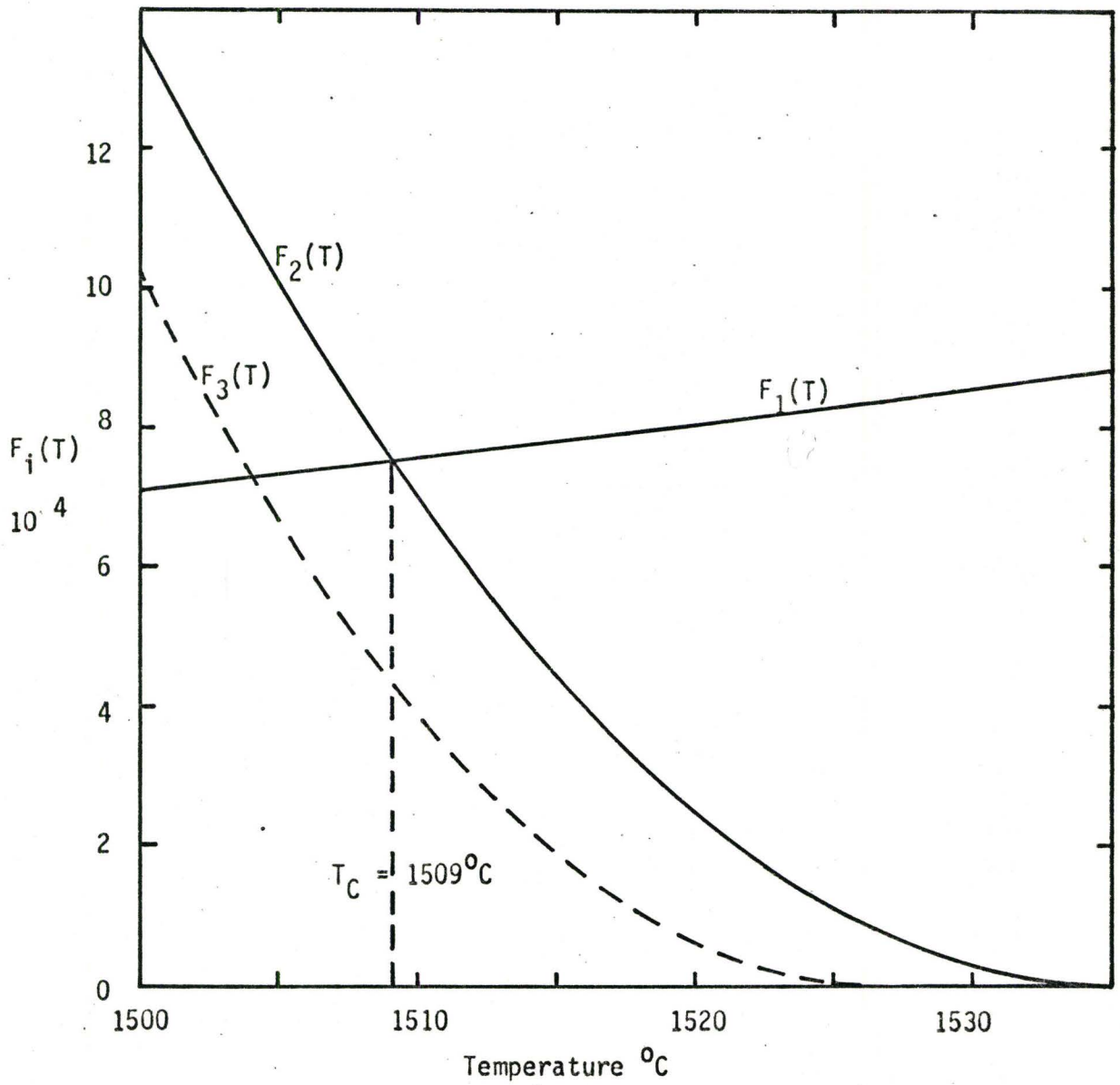

Figure 5.16 The graphical determination of T_C

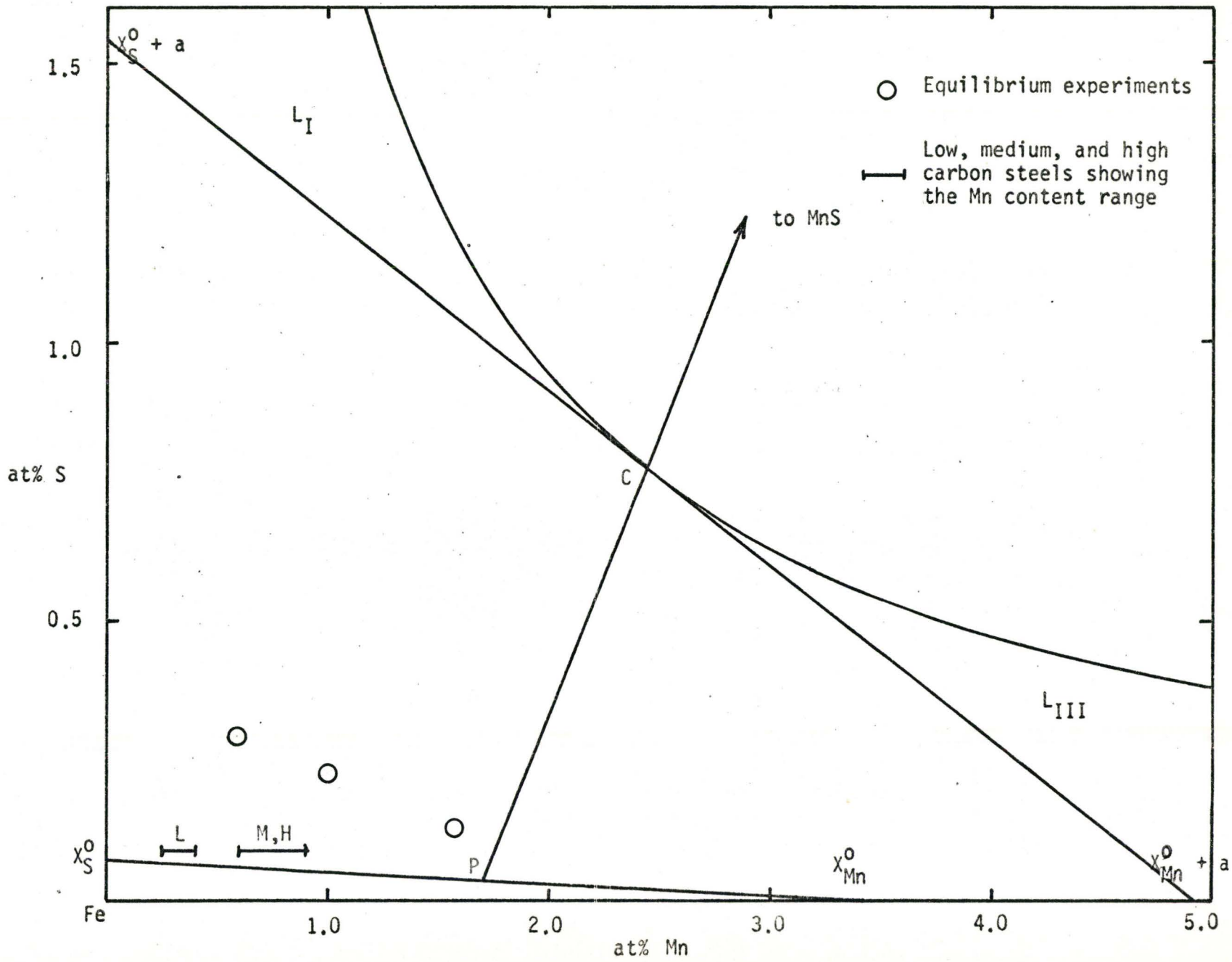

Figure 5.17 At T_C = 1509°C the MnS phase in direct reaction with δ-Fe along the tie-line PC.

We note here that a variation of ± 10 kcal/mole can lead to ± 5°C change in T_C, and a corresponding change in X^C_{Mn} and X^C_S. Similarly a change of K_o by ± 5 can impose a ± 5°C change in T_C. While it is difficult to numerically assess the accuracy of the estimate it is our opinion an educated guess on the bounds of T_C to be ± 10°C and on X^C_{Mn} and X^C_S to be ± 0.005 and ± 0.0005, respectively.

The results of the experiments to locate X^C_{Mn} and X^C_S experimentally are inconclusive. The observed microstructures suggest the initial presence of FeS inclusions which had evidently transformed to MnS during slow cooling of the ingots. The position of the tie-line PC in figure 5.17 in relation to the Mn and S contents of the melts (open circles) is consistent with that course of events.

B.2. Metastable γ-Fe and T_C

In view of the fact that the melting point of metastable γ-Fe is only 9°C below the melting point of δ-Fe as calculated from Fe-X binary phase diagrams[63], and that it is proportionately less as solute is added, it is conceivable that the MnS phase in this system could directly react with γ-Fe rather than δ-Fe if a small amount of supercooling occurred during solidification. Hone[64], in analysing his steady state solidification experiments for this same Fe-Mn-S system, considers this possibility. Thus it is of interest to determine the temperature T'_C and composition (X^C_{Mn}, X^C_S) at which MnS first directly with γ-Fe.

The previous analysis can be applied. If the metastable melting point of γ-Fe is 1526°C, then we can estimate the γ-Fe solidus and liquidus lines on the Fe-Mn binary by representing them as straight lines between 1526°C and the peritectic concentrations, X_{Mn} = 0.102 and 0.13 at 1472°C. From this we can calculate a value of N' = - 392.3 and k_{Mn} = 0.785.

This is more difficult for the Fe-S binary because metastable γ-Fe must exhibit retrograde solid solubility. We can, however, assume that M does not change considerably, and thus M' = - 1687. Using M' and the above Fe-Mn data we can estimate k_S = 0.0755.

To find T_C' graphically we plot the new function $F_3(T) = (T - 1526)^2/M'N'$ against T, and the temperature at which $F_3(T)$ intersects $F_,(T)$ is T_C'. This is shown in Figure 5.16, and one sees that T_C' = 1504°C. As one would expect, this is only slightly lower than the stable δ-Fe temperature, T_C = 1509°C.

CHAPTER VI

INTERDIFFUSION AND Fe-Mn-S PHASE TRANSFORMATION

RESULTS AND DISCUSSION

A. Fe:Fe-Mn DIFFUSION COUPLES

The results of the three Fe:Fe-Mn diffusion couples reacted at 1446, 1478, and 1494°C are tabulated in Table VI-1 and plotted in Figures 6.1, 6.2, and 6.3. The figures show the observed concentration of Mn in δ-Fe (circles) as a function of the diffusion distance as measured from the initial Fe/Fe-Mn interface. The chemical diffusion coefficient for Mn in δ-Fe, $D_{Mn}^{\delta Fe}$, was determined by fitting an error function curve (solid line) to the equilibrium data. The error function is represented by equation 6-1.

$$\frac{C - C_o}{C_s - C_o} = \text{erfc}\left(\frac{x}{2\sqrt{Dt}}\right) \qquad (6\text{-}1)$$

where C is the concentration at a distance x from the interface in centimeters after a time t in seconds. C_s is the composition at the interface, C_o is the composition at t = 0, and D is the diffusion coefficient. The experimental values of $D_{Mn}^{\delta Fe}$ at the three temperatures are listed in Table VI-2.

Table VI-2

The Diffusion Coefficient of Mn Diffusion in δ-Fe.

Temperature °C	Reaction Time secs.	D_{Mn}^{Fe}, cm^2/sec
1446	1800	1.073×10^{-7}
1478	3600	1.57×10^{-7}
1494	1800	1.87×10^{-7}

In analysing the temperature dependence of $D_{Mn}^{\delta Fe}$ the usual Arrhenius analysis was applied to the diffusion coefficients. The result is shown in Figure 6-4 in which (ln D) is plotted against the reciprocal of the absolute temperature. From the line drawn through the three points equation 6-2 was obtained.

$$D_{Mn}^{\delta Fe} = D_o e^{-\frac{\Delta H}{RT}} = 0.264\, e^{\frac{-59500}{RT}} \qquad (6\text{-}2)$$

Although the points show a very good fit to a straight line, it is unwise to put great reliance on values of D_o and the activation energy, ΔH, based on only three data points spread over a temperature range of 48°C.

Table VI-3 shows the temperature dependence of iron and cobalt diffusing in δ-Fe as determined by James and Leak[41]. Our own values for Mn are shown as well and one notes that both D_o and ΔH for Mn compare well with those of Co and Fe.

Table VI-3

The Diffusion Coefficients of Mn, Fe, and Co Diffusing in Fe.

Diffusing Species	D_o cm^2/sec	ΔH cal/mole
Mn (in δ-Fe)	0.264	-59,500
Fe (in δ-Fe)	2.01	-57,500
Co (in δ-Fe)	6.38	-61,400
Fe (in δ-Fe)	2.01	-57,500
Co (in δ-Fe)	6.38	-61,400

Also included in Table VI-3 is D_o and ΔH for Co and Fe diffusion in α-Fe. This data shows that the temperature dependence in α-Fe, for both Co and Fe, extrapolates to the δ-Fe range, and vice versa. Now if Mn follows the same trend, and there is no reason to believe it should not, then one might

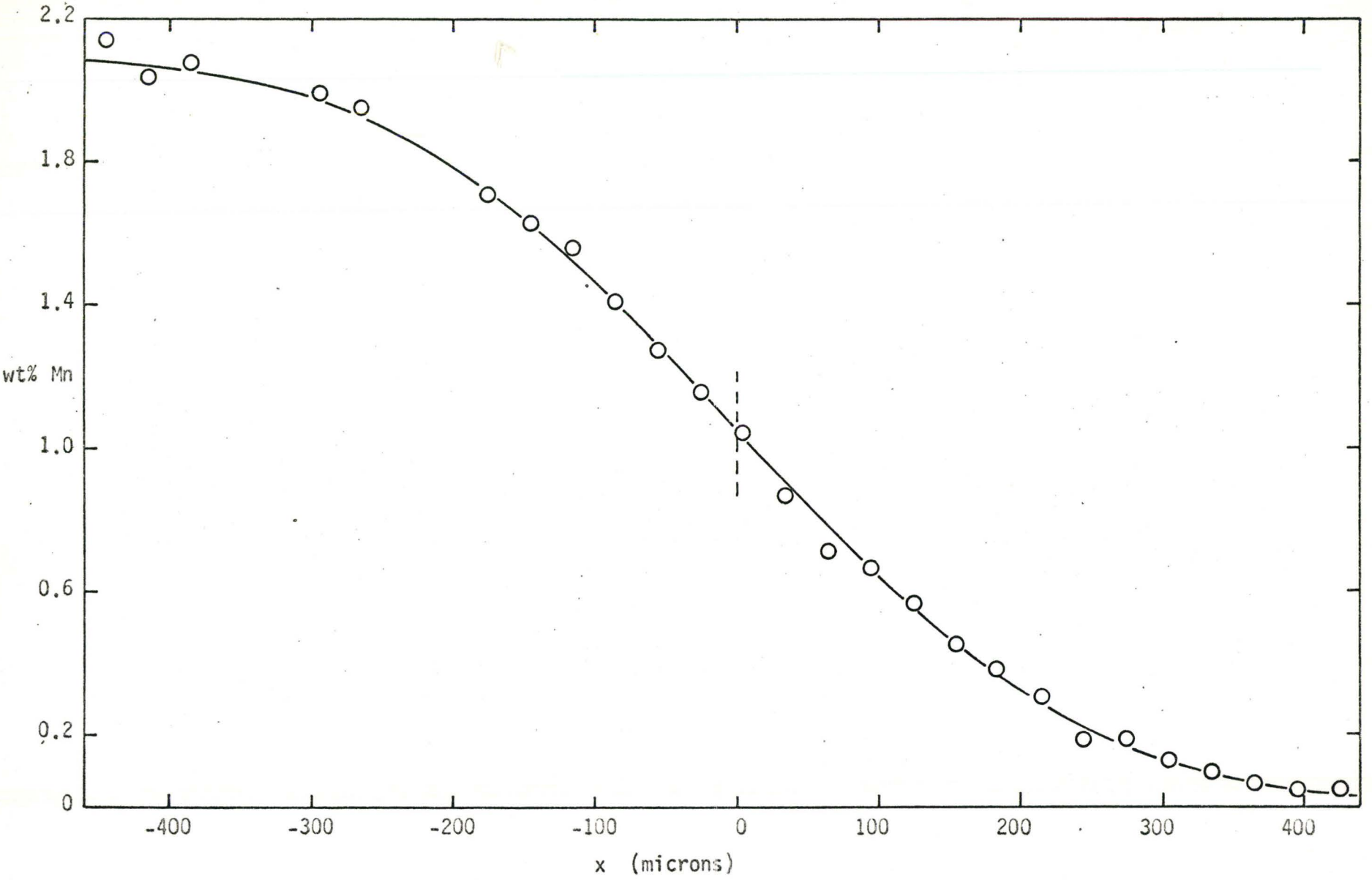

Figure 6.1 Mn concentration-penetration curve for the Fe:Fe-2.05Mn diffusion couple reacted at 1446°C for 1800 seconds.

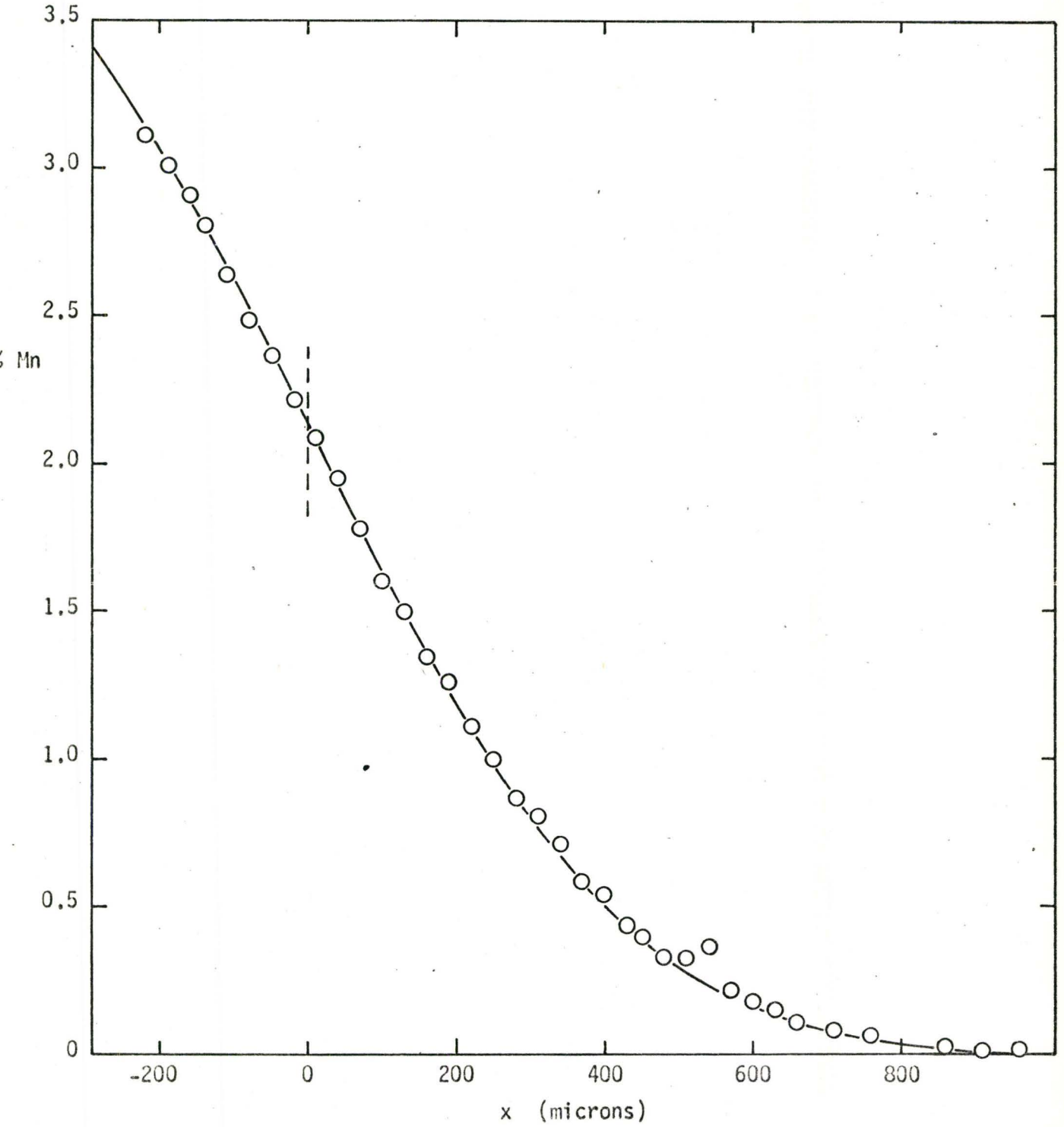

Figure 6.2 Mn concentration-penetration curve for the Fe;Fe-4.15Mn diffusion couple reacted at 1478°C for 3600 seconds.

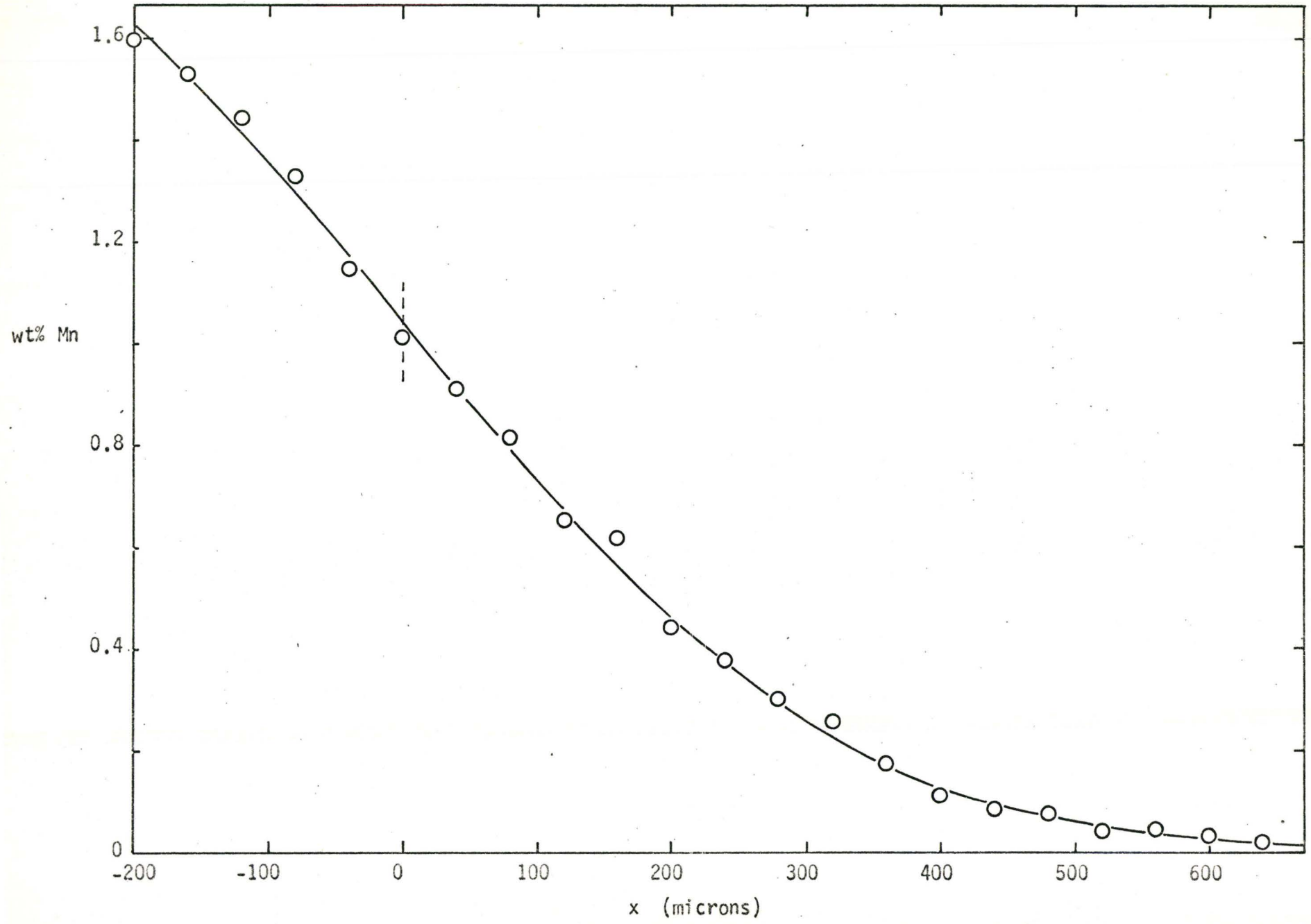

Figure 6.3 Mn concentration-penetration curve for the Fe:Fe-2.05Mn diffusion couple reacted at 1494°C for 1800 seconds

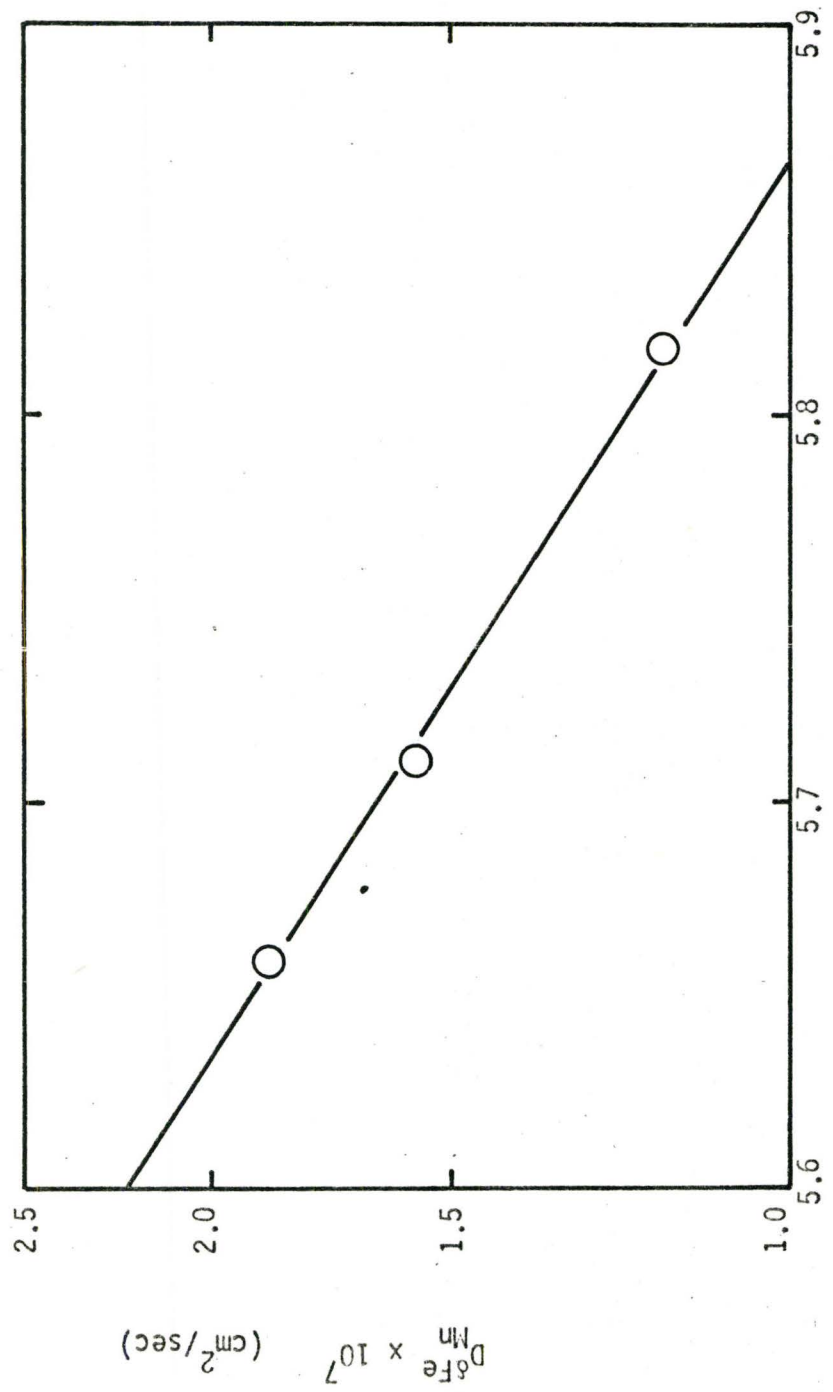

Figure 6.4 The temperature dependence of $D^{\delta Fe}_{Mn}$.

Table VI-1

Fe:Fe-2.15 Mn Diffusion Couples, 1446°C for 1800 seconds.

Micro-probe Data and Results

Standard		Fe	Mn
Initial	Fe	11220	22
	Mn	37721	62
Final	Fe	12042	21
	Mn	37139	57

Distance from Interface (microns)	Counts	% Mn
455	32	0.032
425	37	0.045
395	36	0.043
365	43	0.061
335	56	0.096
305	68	0.13
275	92	0.19
245	90	0.19
215	163	0.30
185	134	0.38
155	189	0.45
125	233	0.57
95	269	0.66
65	286	0.71
35	345	0.87
5	404	1.02

Distance from Interface (microns)	Counts	% Mn
Interface = 0		
-25	455	1.16
-55	499	1.28
-85	547	1.41
-115	605	1.56
-145	630	1.63
-175	661	1.71
-205	650	1.68
-235	685	1.77
-265	752	1.95
-295	768	1.99
-325	817	2.13
-355	819	2.13
-385	800	2.08
-415	785	2.04
-445	823	2.14

Table VI-1 Cont'd.

Fe:Fe-4.05 Mn Diffusion Couple, 1478°C for 3600 sec.

Standard	Fe	Mn
Initial Fe	20423	95
Mn		
Final Fe	22485	101

Distance from Interface (microns)	Counts	% Mn
1010	103	0.01
960	115	0.02
910	115	0.02
860	123	0.03
760	154	0.07
710	168	0.08
660	192	0.11
630	227	0.15
600	253	0.18
570	291	0.22
540	426	0.38
510	393	0.33
480	389	0.33
450	450	0.40
430	491	0.44
400	578	0.54
370	625	0.59
340	729	0.71
310	818	0.81
280	876	0.87
250	992	1.00
220	1096	1.12
190	1235	1.27
160	1305	1.35
130	1443	1.50
100	1536	1.61
70	1691	1.78
40	1853	1.96
10	1970	2.09
Interface	2087	
-20	2222	2.22
-50	2328	2.37
-80	2466	2.49
-110	2617	2.64
-140	2704	2.81
-160	2798	2.91
-190	2885	3.01
-220	2803	3.11

Table VI-1 Cont'd.

Fe:Fe-2.15 Mn Diffusion Couple, 1494°C for 1800 seconds

Probe Data and Results

Standard		Fe	Mn
Initial	Fe	10954	18
	Mn	40899	62
Final	Fe	11168	14
	Mn	37124	53

Distance from Interface (microns)	Counts	% Mn
720	18	0.01
680	21	0.02
640	23	0.02
600	26	0.03
560	33	0.05
520	30	0.04
480	43	0.07
440	48	0.09
400	58	0.11
360	82	0.17
320	115	0.26
280	132	0.30
240	162	0.38

Distance from Interface (microns)	Counts	% Mn
200	187	0.44
160	256	0.62
120	271	0.66
80	334	0.82
40	373	0.92
Interface = 0	411	1.02
-40	463	1.15
-80	533	1.34
-120	577	1.44
-160	613	1.53
-200	639	1.60
-240	697	1.75
-280	687	1.72

in the absence of other information, estimate $D_{Mn}^{\alpha Fe}$ by extrapolating from the δ-Fe range to the α-Fe range.

B. CATION DIFFUSION IN MANGANESE SULPHIDE

The cation diffusion coefficients in MnS were determined from the Fe:MnS and (FeMn)S:MnS diffusion couples. In the following two sections the observations and results of these experiments are presented separately. Since the two results are related, their full discussion will be reserved until section B.3.

B.1. Fe:MnS Diffusion Couples

We recall from Chapter V that the solubility of Mn and S in γ-Fe is too small to be accurately measured by electron probe microanalysis. As a result only the concentration profiles in the MnS side of the Fe:MnS diffusion couples were measured and recorded. This data is tabulated in Tables VI-4 to VI-11, and plotted in Figures 6.5 to 6.11. To determine the cation diffusion coefficients, equation 6-1 was fitted to the experimental points for each of the eight Fe:MnS diffusion couples. The diffusion coefficients, D_{Fe}^{MnS}, are listed in Table VI-12.

There were five Fe:MnS diffusion couples reacted in the region of $1300^{o}C$ ($1299.4 \pm 1^{o}C$) for five different times. To determine the average D_{Fe}^{MnS} at $1300^{o}C$, the value of x when $(x/2\sqrt{Dt}) = 0.5$, was plotted against $\sqrt{t}$ for each of the five times. This is shown in Figure 6.12, and the slope of the straight line through these points (the line must also pass through the origin) is then equal to $\sqrt{\bar{D}_{Fe}^{MnS}}$. The value of $\bar{D}_{Fe}^{MnS}$ is also listed in Table VI-12.

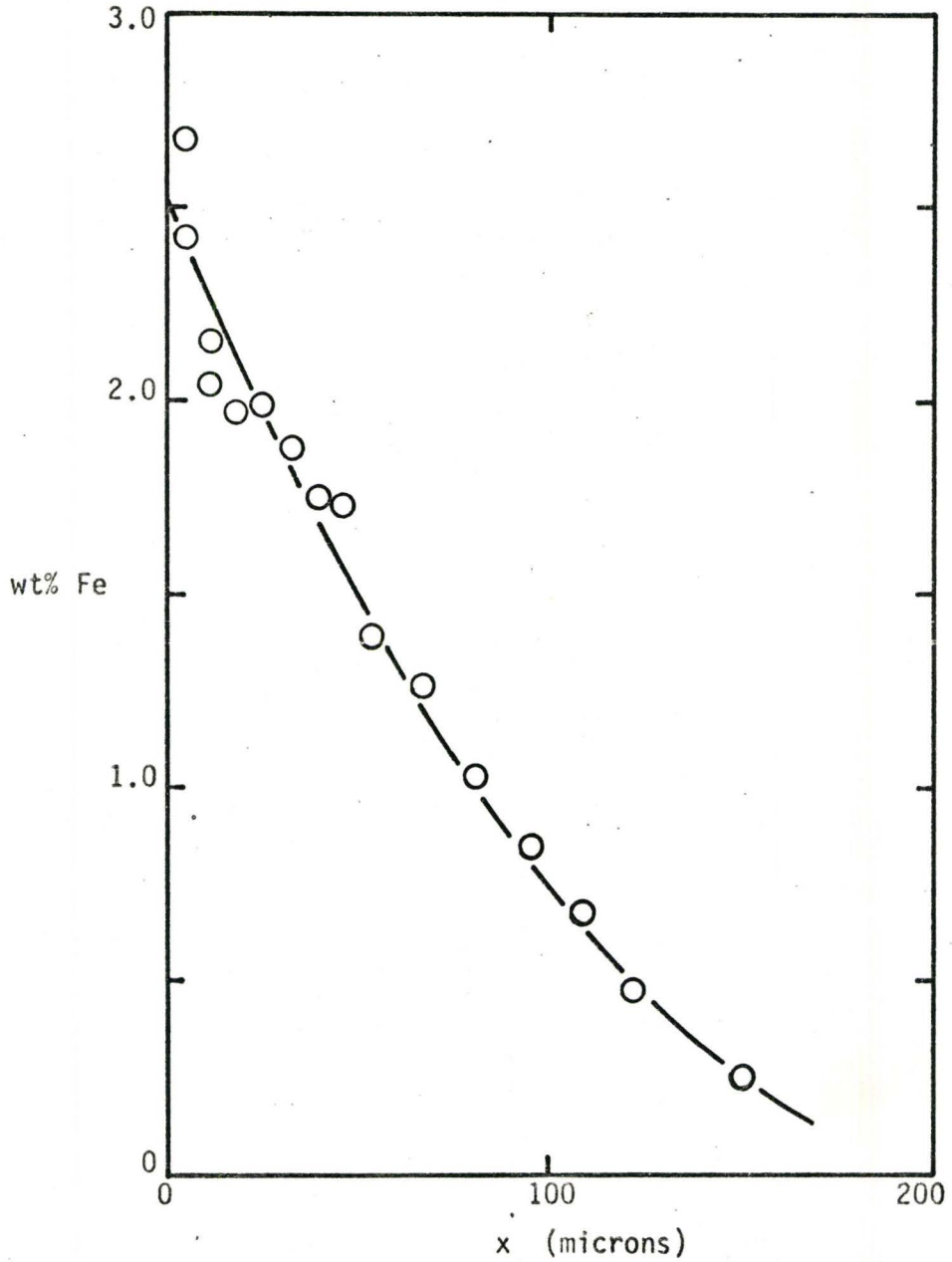

Figure 6.5 Fe concentration-penetration curve for the MnS side of the Fe:MnS diffusion couple reacted at 1253°C for 2160 seconds.

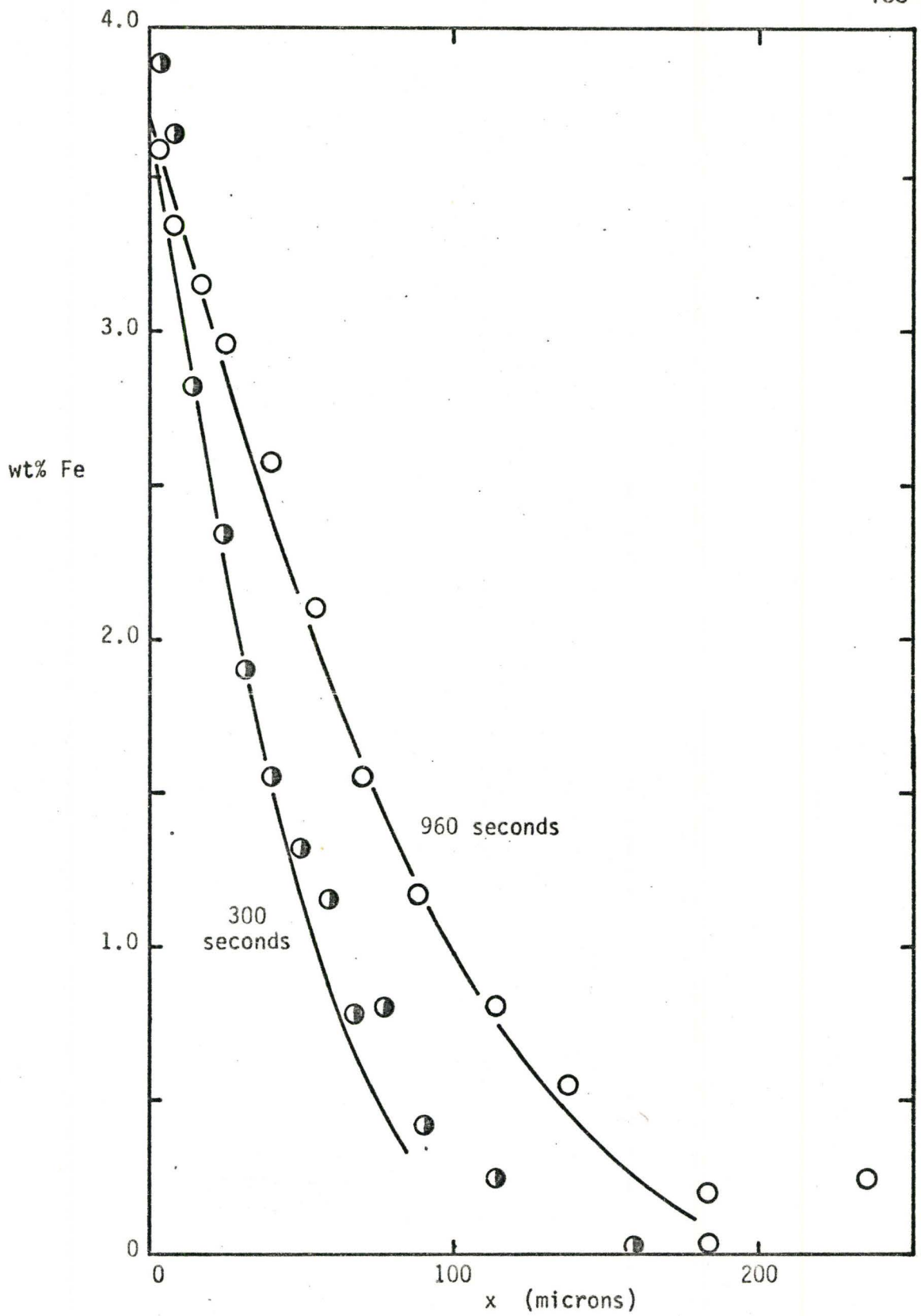

Figure 6.6 Fe concentration-penetration curves for the MnS side of the Fe:MnS diffusion couples reacted at 1299 and 1301°C, for 300 and 960 seconds, respectively.

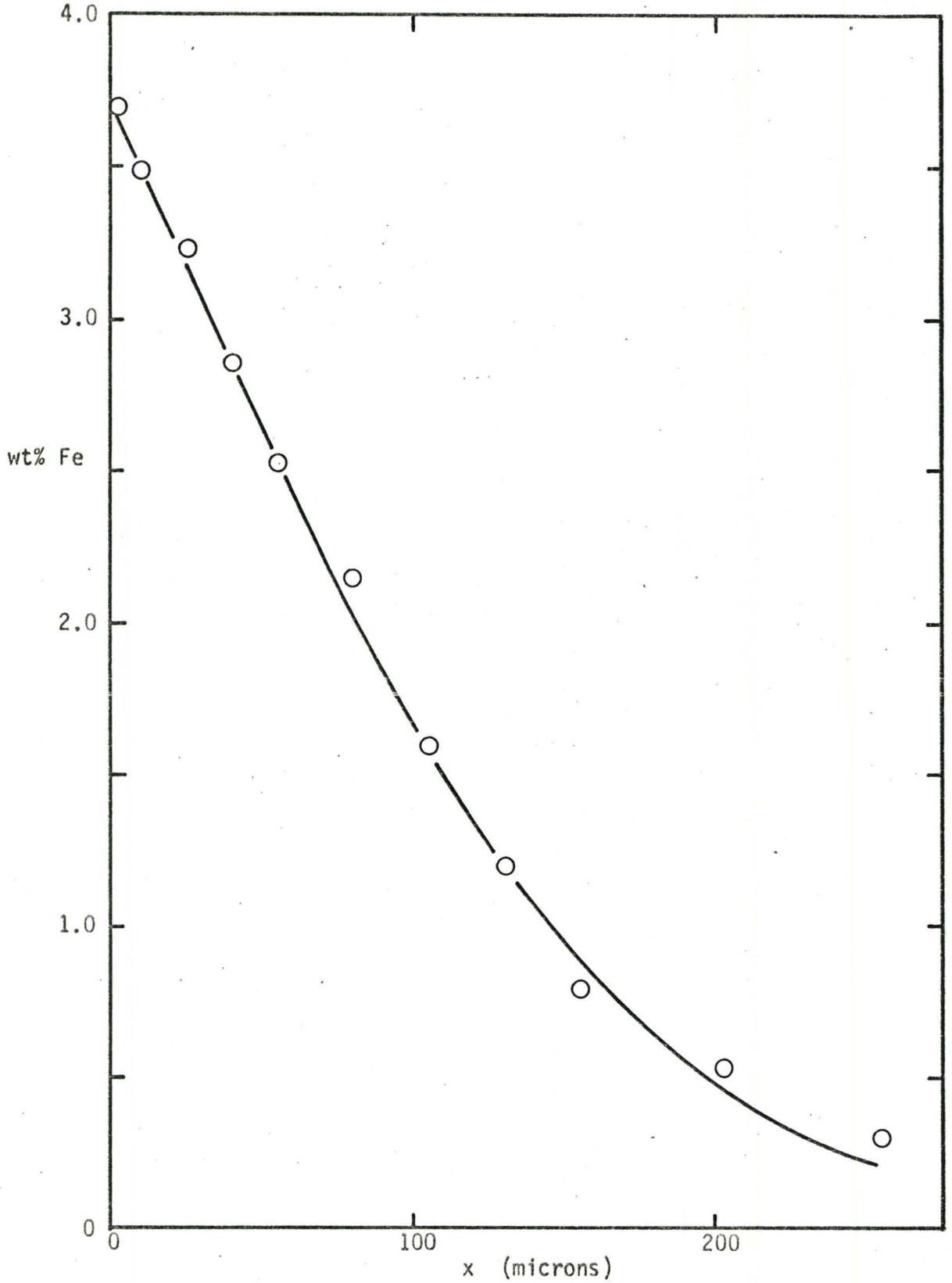

Figure 6.7 Fe concentration-penetration curve for the Mns side of the Fe:MnS diffusion couple reacted at1299^{0}C for 2160 seconds.

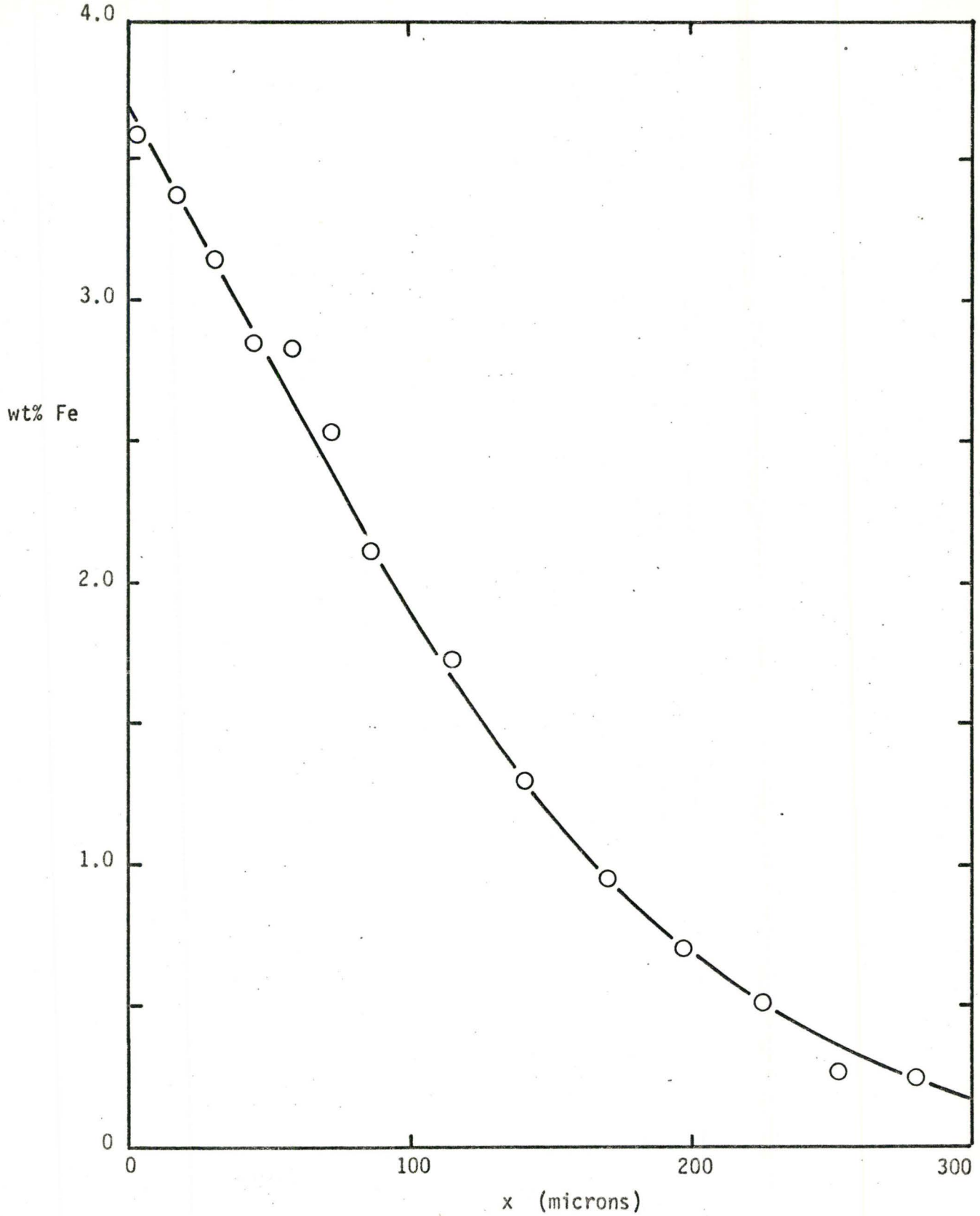

Figure 6.8 Fe concentration-penetration curve for the MnS side of the Fe:MnS diffusion couple reacted at 1298°C for 3840 seconds.

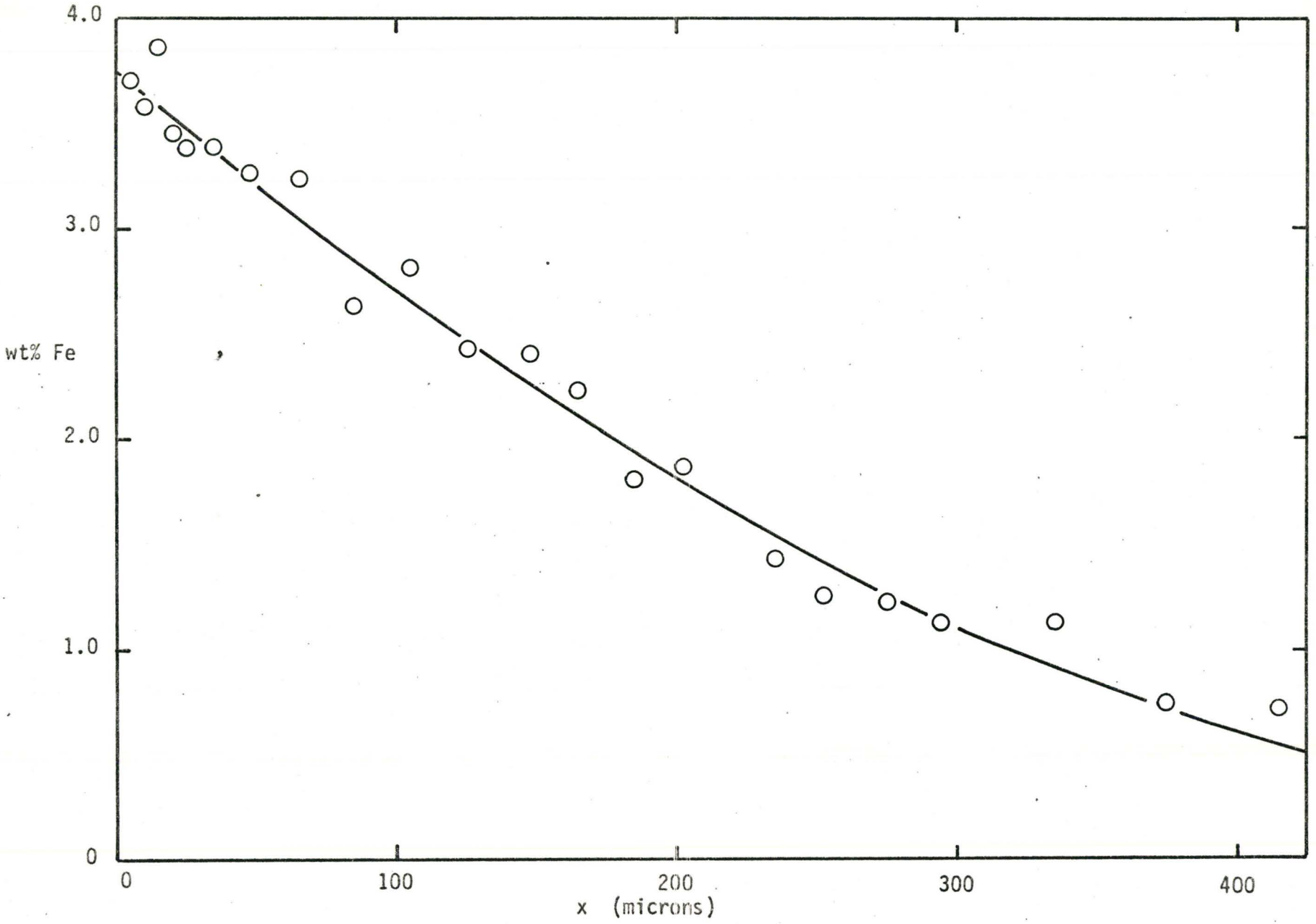

Figure 6.9 Fe concentration-penetration curve for the MnS side of the Fe:MnS diffusion couple reacted at 1300°C for 7260 seconds.

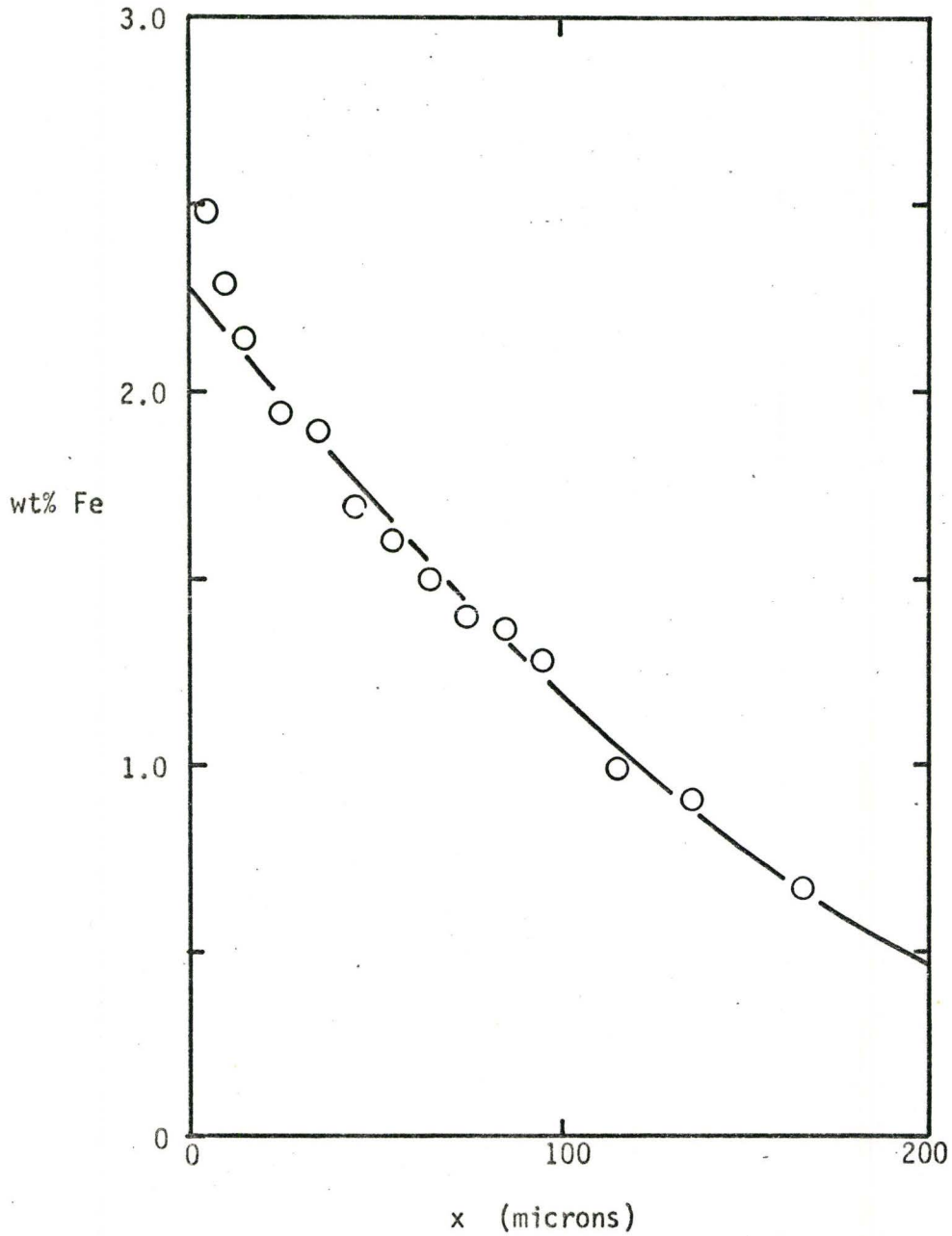

Figure 6.10 Fe concentration-penetration curve for the MnS side of the Fe:MnS diffusion couple reacted at 1349°C for 2160 seconds.

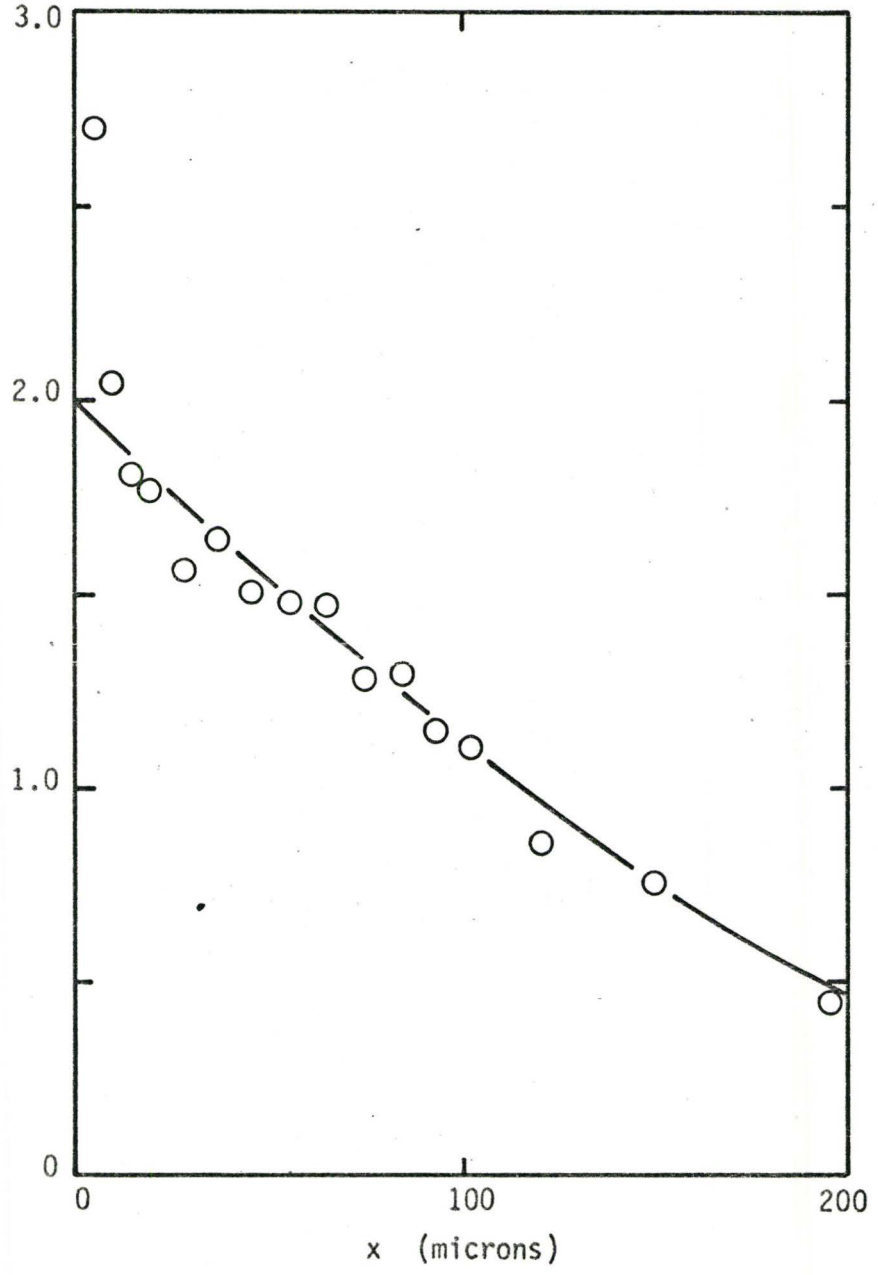

Figure 6.11 Fe concentration-penetration curve for the MnS side of the Fe:MnS diffusion couple reacted at 1406°C for 960 seconds.

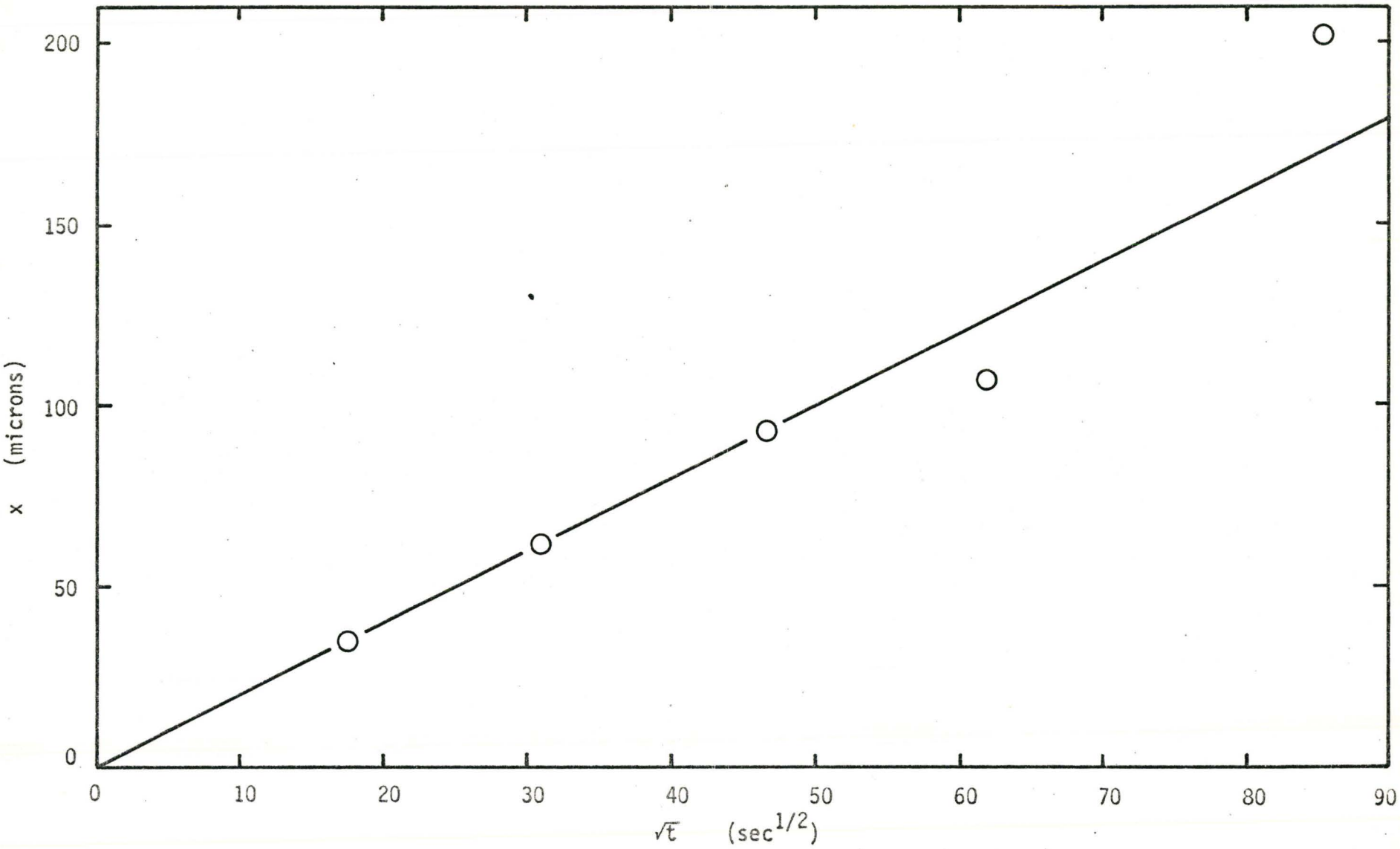

Figure 6.12 x versus $\sqrt{t}$ for the five Fe:MnS diffusion couples at 1300°C for the condition when $x/\sqrt{Dt} = 1$.

Table VI-4

Fe:MnS Diffusion Couple, 1253°C, 36 Minutes

Micro-Probe Data and Results of MnS Side

Standard	Fe Counts	Mn Counts
Initial Fe	18273	20
Mn	78	20894
MnS	47	12392
Final Fe	18397	16
Mn	66	20458
MnS	39	10890

Distance from Interface (microns)	Fe		Mn		S
5	497	2.68 wt.%	11092	60.14 wt.%	37.18 wt.%
5	389	2.04	10686	57.94	40.02
12	408	2.15	11034	59.83	38.02
12	453	2.42	10827	58.71	38.87
19	376	1.97	11150	60.46	37.57
26	380	1.99	11066	60.00	38.07
32	362	1.88	11078	60.07	38.05
39	340	1.75	11020	59.75	35.50
46	337	1.73	11065	60.00	38.27
53	278	1.39	11113	60.26	38.35
67	257	1.27	11283	61.18	37.55
81	218	1.03	11204	60.75	38.22
95	187	0.85	11387	61.74	37.41
108	158	0.68	11248	60.99	38.33
122	125	0.48	11568	62.72	36.80
150	87	0.26	11671	63.28	36.46

Table VI-5

Fe:MnS Diffusion Couple, 1299°C, 5 Minutes

Micro-Probe Data and Results for MnS Side

Standard	Fe Counts	Mn Counts
Initial Fe	15101	16
Mn	65	20989
MnS	40	11898
Final Fe	14668	14
Mn	61	19109
MnS	41	10744

Distance from Interface (microns)	Fe	Mn		S
5	3.89 wt.%	10444	58.40 wt.%	37.71 wt.%
8	3.65	10610	59.33	37.02
14	2.82	10889	60.89	36.29
25	2.35	10868	60.77	36.88
32	1.91	10923	61.08	37.01
41	1.56	11147	62.33	36.11
50	1.32	11267	63.00	35.68
59	1.16	11220	62.74	36.10
68	0.78	11159	62.40	36.82
77	0.81	11269	63.01	36.18
91	0.42	11374	63.60	35.98
114	0.25	11238	62.84	36.91
159	0.04	11403	63.76	36.20

Table VI-6

Fe:MnS Diffusion Couple, 1301°C, 16 Minutes

Micro-Probe Data and Results of MnS Side

Standard	Fe Counts	Mn Counts
Initial Fe	15437	20
Mn	66	16313
MnS	44	9802
Final Fe	15034	19
Mn	69	15689
MnS	38	8222

Distance from Interface (microns)	Fe		Mn		S
3	547	3.59 wt.%	8481	59.42	36.99
8	518	3.35	8555	59.94	36.71
17	484	3.15	8694	60.91	35.94
25	418	2.68	8789	61.58	35.74
39	402	2.57	8651	60.61	36.82
54	336	2.10	8661	60.73	37.17
69	260	1.56	8766	61.42	37.02
88	206	1.17	8952	62.72	36.11
113	155	0.81	9036	63.31	35.88
137	120	0.56	8946	62.68	36.76
186	69	0.20	9012	63.14	36.66
186	49	0.06	8829	61.86	38.08
235	76	0.25	9000	63.06	36.69

Table VI-7

Fe:MnS Diffusion Couple, 1299°C, 36 Minutes

Micro-Probe Data and Results for MnS Side

Standard	Fe Counts	Mn Counts
Initial Fe	16706	15
Mn	60	
MnS	38	
Final Fe	15651	22
Mn	67	
MnS	39	

Distance from Interface (microns)	Fe		Mn		S
3	592	3.70 wt.%	9315	56.98 wt.%	39.32 wt.%
10	559	3.48	9307	56.93	39.59
25	522	3.23	9489	58.04	38.73
40	465	2.85	9408	57.55	39.60
55	437	2.52	9435	57.71	39.77
80	361	2.15	9660	59.09	38.76
105	278	1.60	8819	53.95	44.45
130	220	1.20	9094	55.63	43.17
155	195	1.04	9773	59.78	39.18
180	134	0.63	9814	60.03	39.34
205	117	0.53	10239	62.63	36.84
255	85	0.31	10307	63.05	36.64
305	56	0.11	10322	63.14	36.75
405	46	0.05	10311	63.07	36.88

Table VI-8

Fe:MnS Diffusion Couple, 1298°C, 64 Minutes

Micro-Probe Data and Results of MnS Side

Standard	Fe Counts	Mn Counts
Initial Fe	17079	23
Mn	63	21988
MnS	35	11939
Final Fe	16752	18
Mn	57	20067
MnS	40	10581

Distance from Interface (microns)	Fe		Mn		S
3	597	3.58 wt.%	10866	57.93 wt.%	38.49 wt.%
17	565	3.37	11104	59.20	37.43
31	531	3.15	11226	58.85	37.00
44	483	2.85	11307	60.28	36.87
58	462	2.71	11528	61.46	35.85
72	434	2.53	11488	61.25	36.22
86	369	2.11	11524	61.44	36.45
114	309	1.73	11655	62.19	36.08
141	244	1.31	11699	62.37	36.32
169	188	0.96	11789	62.85	36.19
197	147	0.70	11748	62.63	36.67
225	119	0.52	11996	63.96	35.52
252	80	0.27	11947	63.69	36.04
280	76	0.25	11843	63.14	36.61

Table VI-9

Fe:MnS Diffusion Couple, 1300°C, 122 Minutes

Micro-Probe Data and Results for MnS Side

Standard	Fe Counts	Mn Counts
Initial Fe	7127	26
Mn	22	13827
MnS	14	7512
Final Fe	6761	21
Mn	18	12479
MnS	8	7300

Distance from Interface (microns)	Fe		Mn		S
5	247	3.70 wt.%	6828	58.20 wt.%	38.10 wt.%
10	239	3.58	6910	58.90	37.52
15	257	3.86	6853	58.41	37.73
20	231	3.45	6809	58.03	38.52
25	226	3.37	6813	58.07	38.56
35	226	3.37	6807	58.02	38.61
45	219	3.26	6895	58.77	37.97
65	217	3.23	6952	59.25	37.52
85	179	2.63	7006	59.71	37.66
105	191	2.82	7126	60.74	36.44
125	166	2.43	7141	60.86	36.71
145	165	2.41	7219	61.53	36.06
165	154	2.24	7151	60.95	36.81
185	127	1.81	7431	63.34	34.85
205	131	1.88	7406	63.12	35.00
235	103	1.43	7317	62.36	36.21
255	92	1.26	7484	63.79	34.95
275	90	1.23	7343	62.59	36.18
295	84	1.13	7408	63.14	35.73
335	84	1.13	7375	62.86	36.01
375	59	0.74	7523	64.12	35.14
415	58	0.73	7510	64.01	35.26

Table VI-10

Fe:MnS Diffusion Couples, 1349°C, 36 Minutes

Micro-Probe Data and Results for MnS Side

Standard	Fe Counts	Mn Counts
Initial Fe	18319	18
Mn	60	21076
MnS	32	11631
Final Fe	18581	20
Mn	57	19158
MnS	37	11029

Distance from Interface (microns)	Fe		Mn		S
2	552	3.03 wt.%	10706	59.66 wt.%	37.31 wt.%
5	458	2.48	11012	61.37	36.15
10	426	2.29	11111	61.91	35.79
15	399	2.14	10985	61.22	36.64
25	366	1.94	11083	61.76	36.30
35	358	1.89	11013	61.37	36.74
45	323	1.69	11034	61.49	36.82
55	308	1.60	10984	61.21	37.19
65	291	1.50	11126	62.00	36.50
75	273	1.40	11176	62.28	36.32
85	268	1.37	11169	62.24	36.39
95	254	1.28	11328	63.13	35.64
115	203	0.99	11282	62.87	36.14
135	190	0.91	11330	63.14	35.95
165	149	0.67	11487	64.01	35.32

Table VI-11

Fe:MnS Diffusion Couple 1406°C, 16 Minutes

Micro-Probe Data and Results for MnS Side

Standard	Fe Counts	Mn Counts
Initial Fe	18837	19
Mn	49	16579
MnS	24	9481
Final Fe	18333	12
Mn	45	16126
MnS	24	8953

Distance from Interface (microns)	Fe		Mn		S
5	488	2.70 wt.%	8761	60.06 wt.%	37.24 wt.%
9	374	2.04	8946	61.33	36.63
14	335	1.81	9052	62.06	36.13
19	328	1.77	8961	61.43	36.80
28	292	1.56	8322	57.05	41.39
37	306	1.64	8900	61.01	37.35
46	281	1.50	9039	61.97	36.53
56	278	1.48	8976	61.54	36.98
65	276	1.47	8977	61.54	36.99
74	243	1.28	9055	62.08	36.64
84	246	1.29	9145	62.69	36.02
93	220	1.14	9466	64.90	33.96
102	215	1.11	9210	61.77	37.12
121	171	0.86	8304	56.93	42.21
149	155	0.76	9289	63.68	35.56
195	102	0.45	9217	63.19	36.36

The temperature dependence of D_{Fe}^{MnS} is determined from Figure 6.13 in which the diffusion coefficients are plotted as a function of 1/T. From the line through these points one can determine

$$D_{Fe}^{MnS} = 69.4 \exp(-62{,}000/RT) \qquad (6\text{-}3)$$

As mentioned one can also extract equilibrium data from these kinetic measurements. The interface compositions of the Fe and MnS represent a tie-line in the (γ-Fe + MnS) two-phase field. At 1300°C, Figures 6.6 to 6.9 show the Fe content in MnS to be 3.7 wt.% Fe. Unfortunately the S content in the γ-Fe cannot be measured, and the diffusion times are too short for Mn to penetrate into the γ-Fe far enough to measure its profile or interface value. However Nakao, using a diffusion time of 35 hours, was able to determine the Mn (0.2 wt.%) interface content in γ-Fe. This was pointed out in Chapter V. The S concentration in the MnS does not change over the diffusion distance and it remains near the stoichiometric value of 36.86 wt.% S.

Table VI-12

The Diffusion Coefficient of Fe in MnS for Fe:MnS Diffusion Couples.

Temperature (°C)	Reaction Time (sec)	D_{Fe}^{MnS} (cm^2/sec.)
1253	2160	2.08×10^{-8}
1299	300	4.08×10^{-8}
1301	960	4.07×10^{-8}
1299	2160	4.00×10^{-8}
1298	3840	3.01×10^{-8}
1300	7260	5.63×10^{-8}
$\overline{D}_{Fe}^{MnS}$ at 1300°C		3.96×10^{-8}
1349	2160	5.81×10^{-8}
1406	960	1.53×10^{-7}

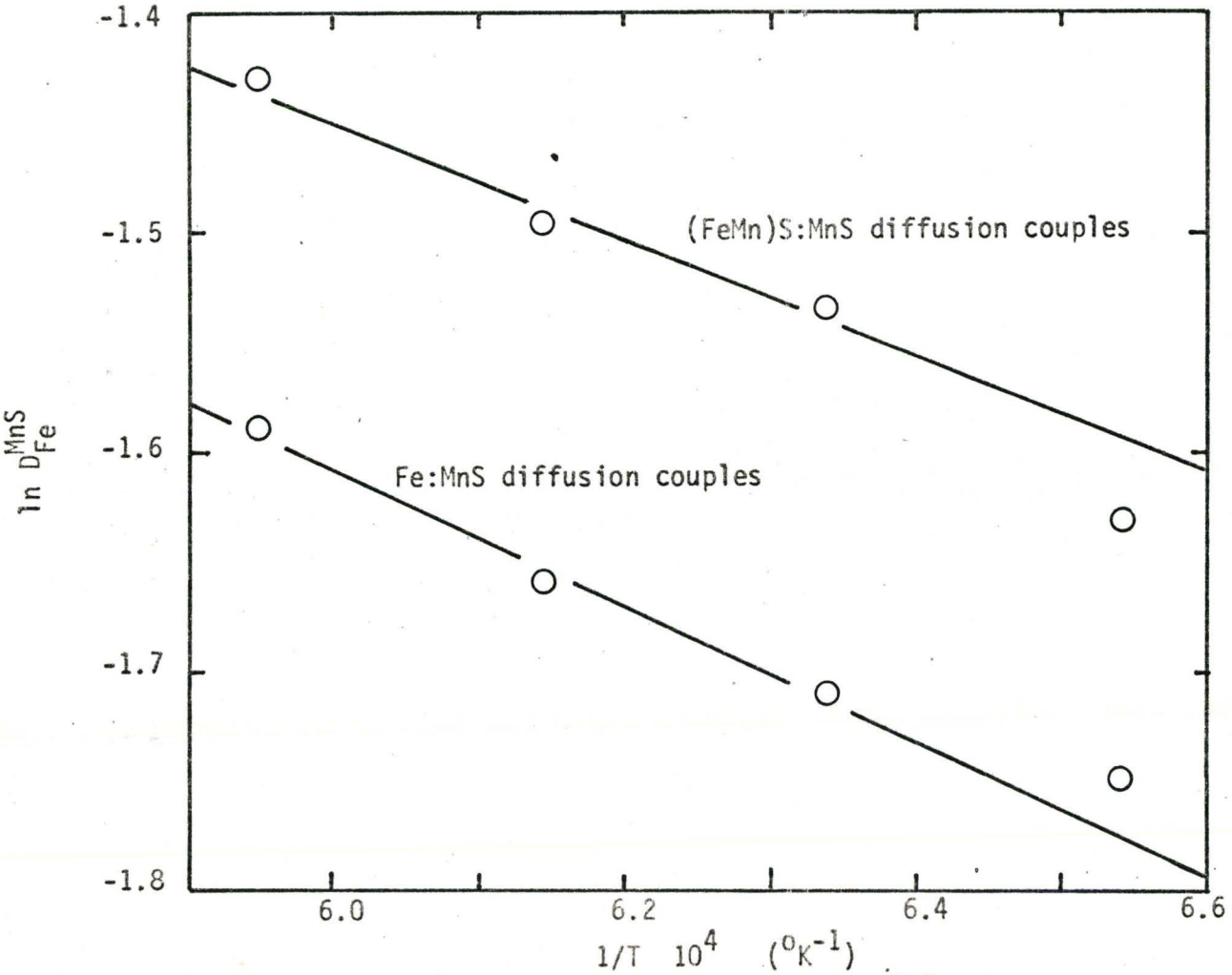

Figure 6.13 The temperature dependence of D_{Fe}^{MnS} determined from the (FeMn)S:MnS and Fe:MnS diffusion couples.

B.2. (FeMn)S:MnS Diffusion Couples

The analysis of the data for the eight (FeMn)S:MnS diffusion couples is essentially the same as that performed on the Fe:MnS couples, with the exception that one is now able to measure the concentration profiles on both sides of each couple. This data is tabulated in Tables VI-13 to VI-20 and plotted in Figures 6.14 to 6.21. One notes that the points for the (FeMn)S side of the interface are scattered. This is because of the porosity in the (FeMn)S resulting from the powder technique used to produce the couples. The same sort of porosity exists in the Fe side of the Fe:MnS couples.

As with the Fe:MnS experiments there were five (FeMn)S:MnS couples reacted at 1300°C. To find the average D_{Fe}^{MnS} for these couples the diffusion distance x at $x/2\sqrt{Dt} = 0.5$ was plotted against $\sqrt{t}$. This is shown in Figure 6.22, and $\bar{D}_{Fe}^{MnS}$ at 1300°C is determined from the slope of the line through the points in this figure. $\bar{D}_{Fe}^{MnS}$ is included in Table VI-21, along with the diffusion coefficients for the various times and temperatures.

The temperature dependence of Fe diffusion in MnS is shown in Figure 6.13 in which ln D is plotted against 1/T. The line through the points is represented by equation 6-4.

$$D_{Fe}^{MnS} = 0.756 \exp(-53{,}000/RT) \qquad (6\text{-}4)$$

B.3. Discussion of the Kinetic Data for the Fe:MnS and (FeMn)S:MnS Diffusion Couples

The tabulated diffusion coefficients result from application of equation 6-1 to the experimental data. This equation implies that the interface in both

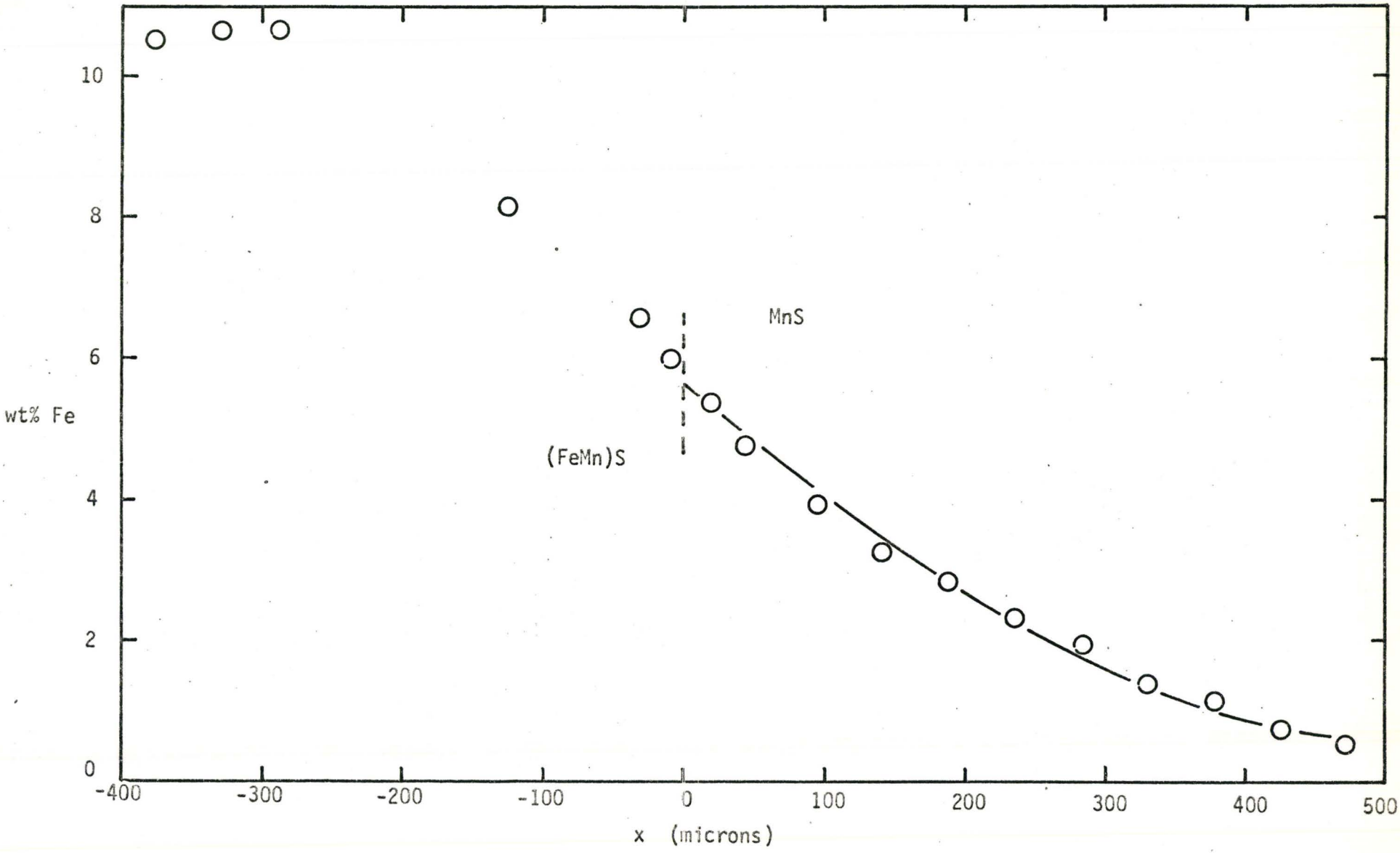

Figure 6.14 Fe concentration-penetration curve for the (FeMn)S:MnS diffusion couple reacted at 1253°C for 2160 seconds.

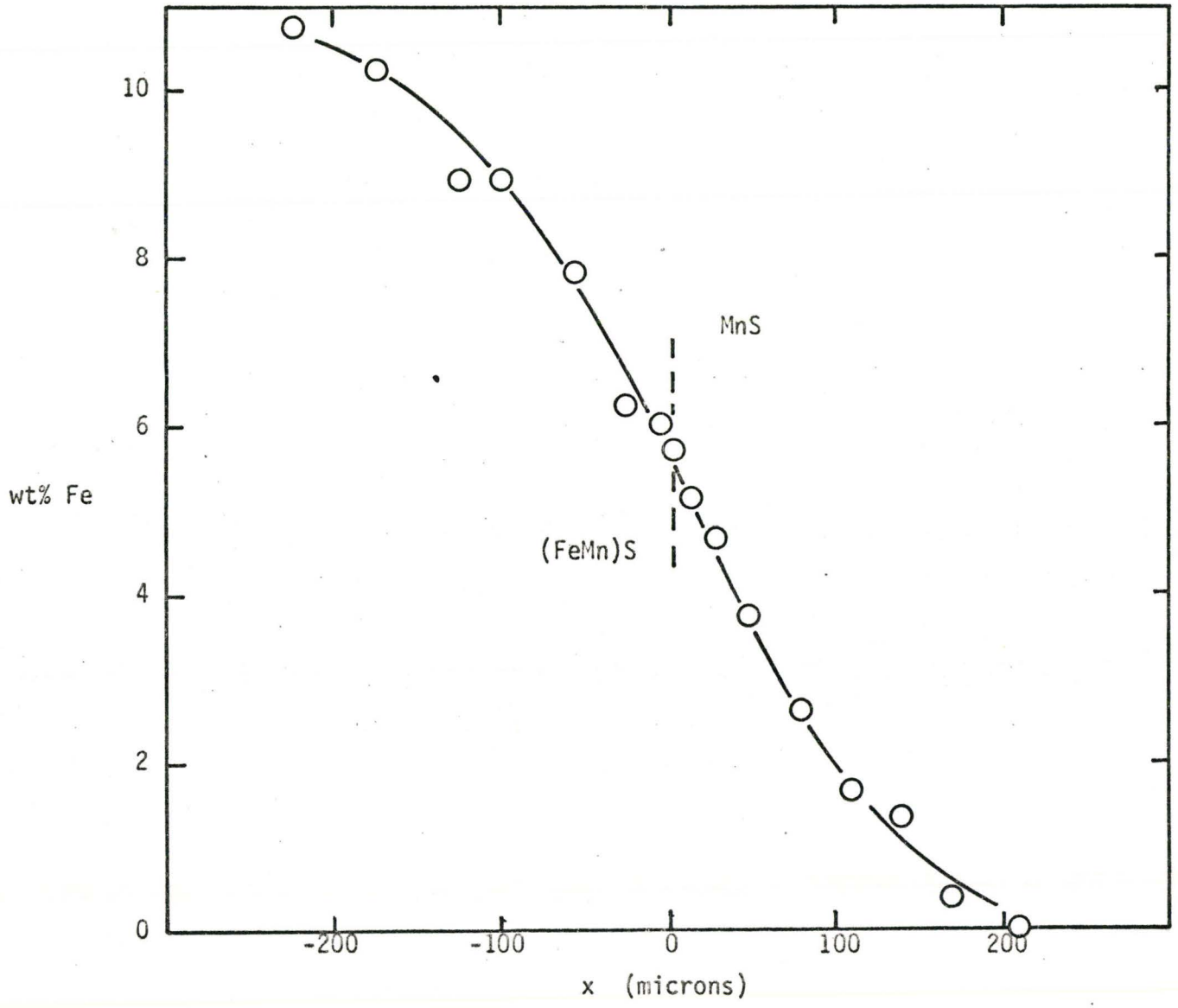

Figure 6.15 Fe concentration-penetration curve for the (FeMn)S:MnS diffusion couple reacted at 1299°C for 300 seconds.

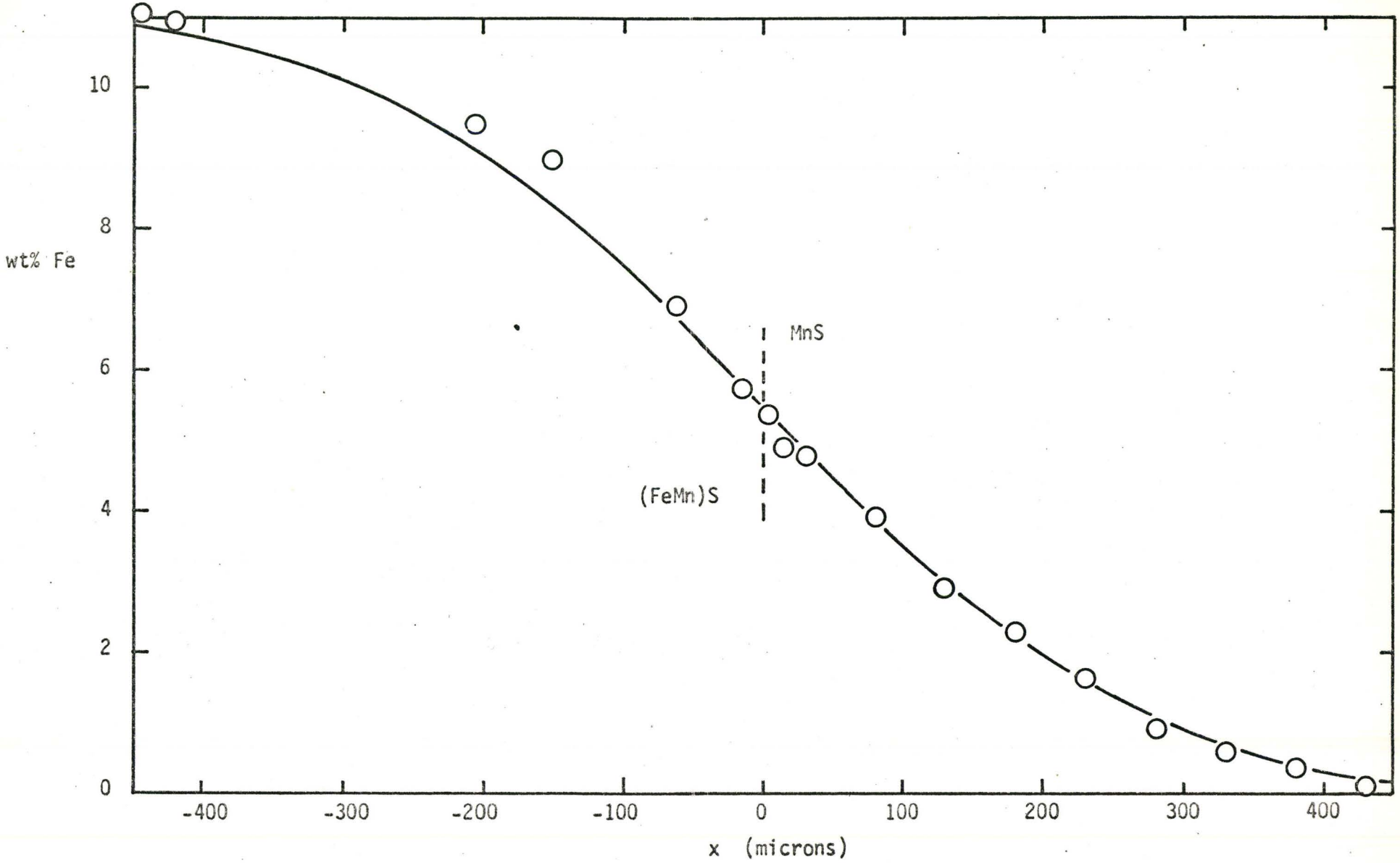

Figure 6.16 Fe concentration-penetration curve for the (FeMn)S:MnS diffusion couple reacted at 1301°C for 960 seconds.

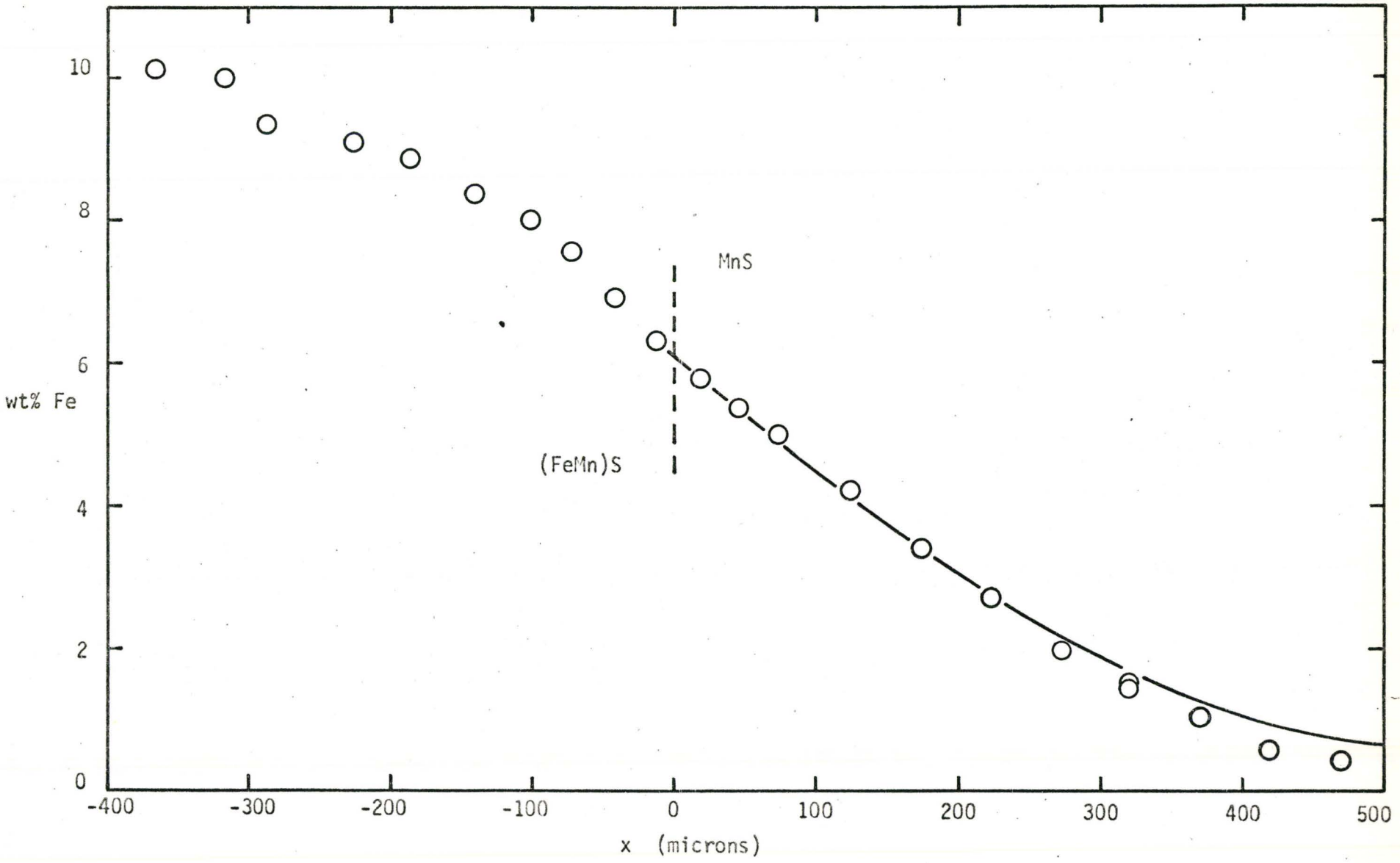

Figure 6.17 Fe concentration-penetration curve for the (FeMn)S:MnS diffusion couple reacted at 1299°C for 2160 seconds.

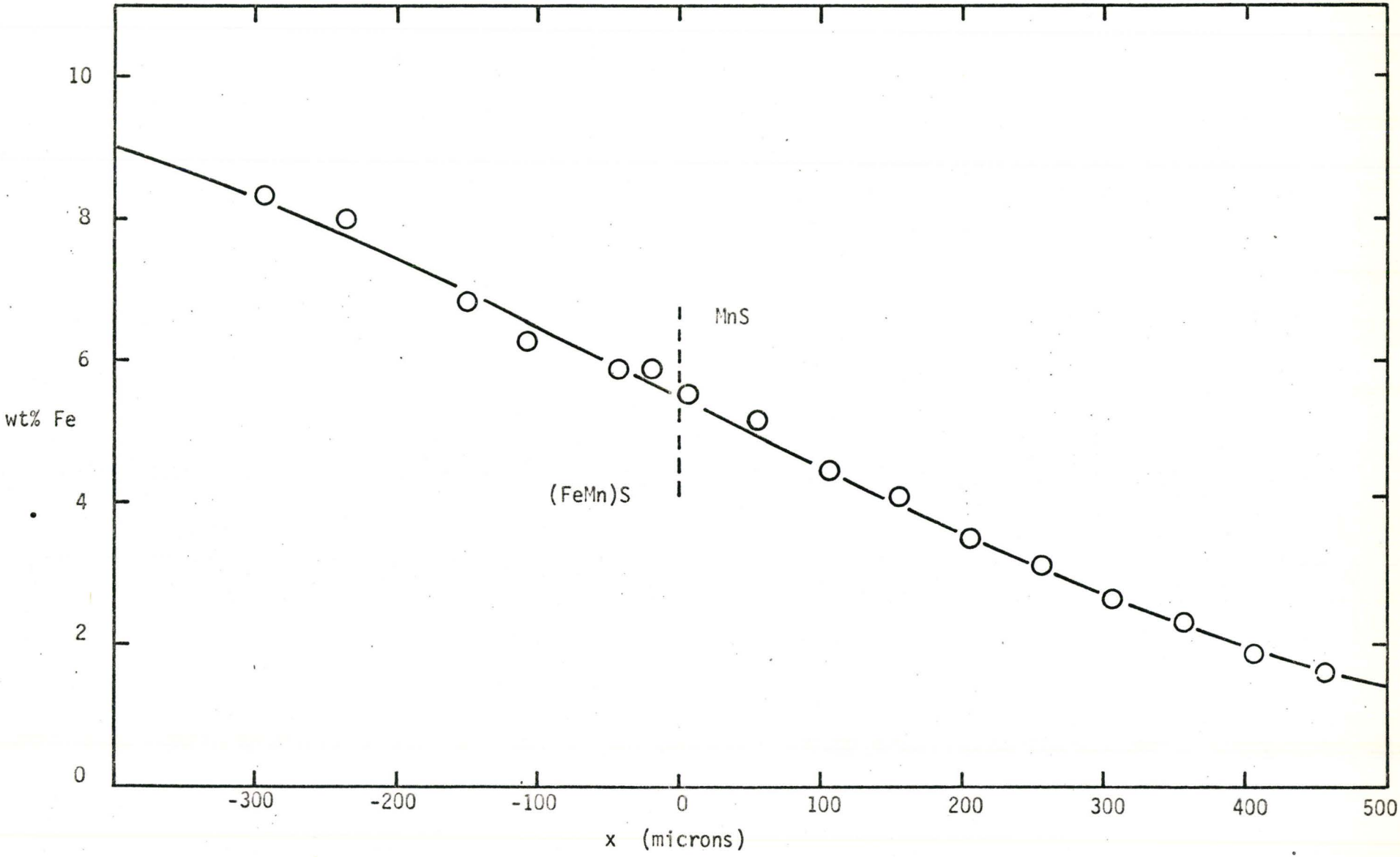

Figure 6.18 Fe concentration-penetration curve for the (FeMn)S:MnS diffusion couple reacted 1298°C for 3840 seconds.

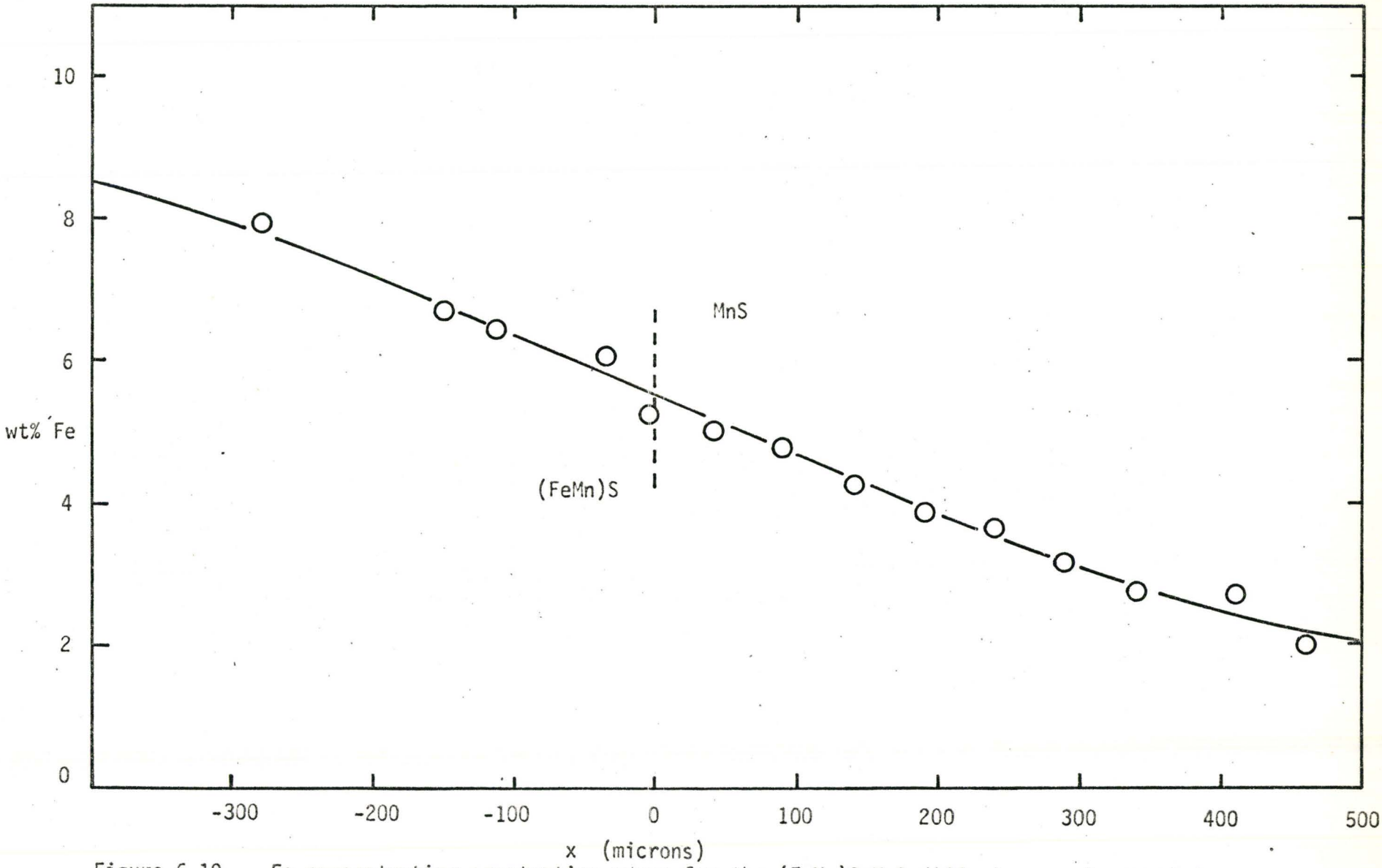

Figure 6.19 Fe concentration-penetration curve for the (FeMn)S:MnS diffusion couple reacted at 1300°C for 7260 seconds.

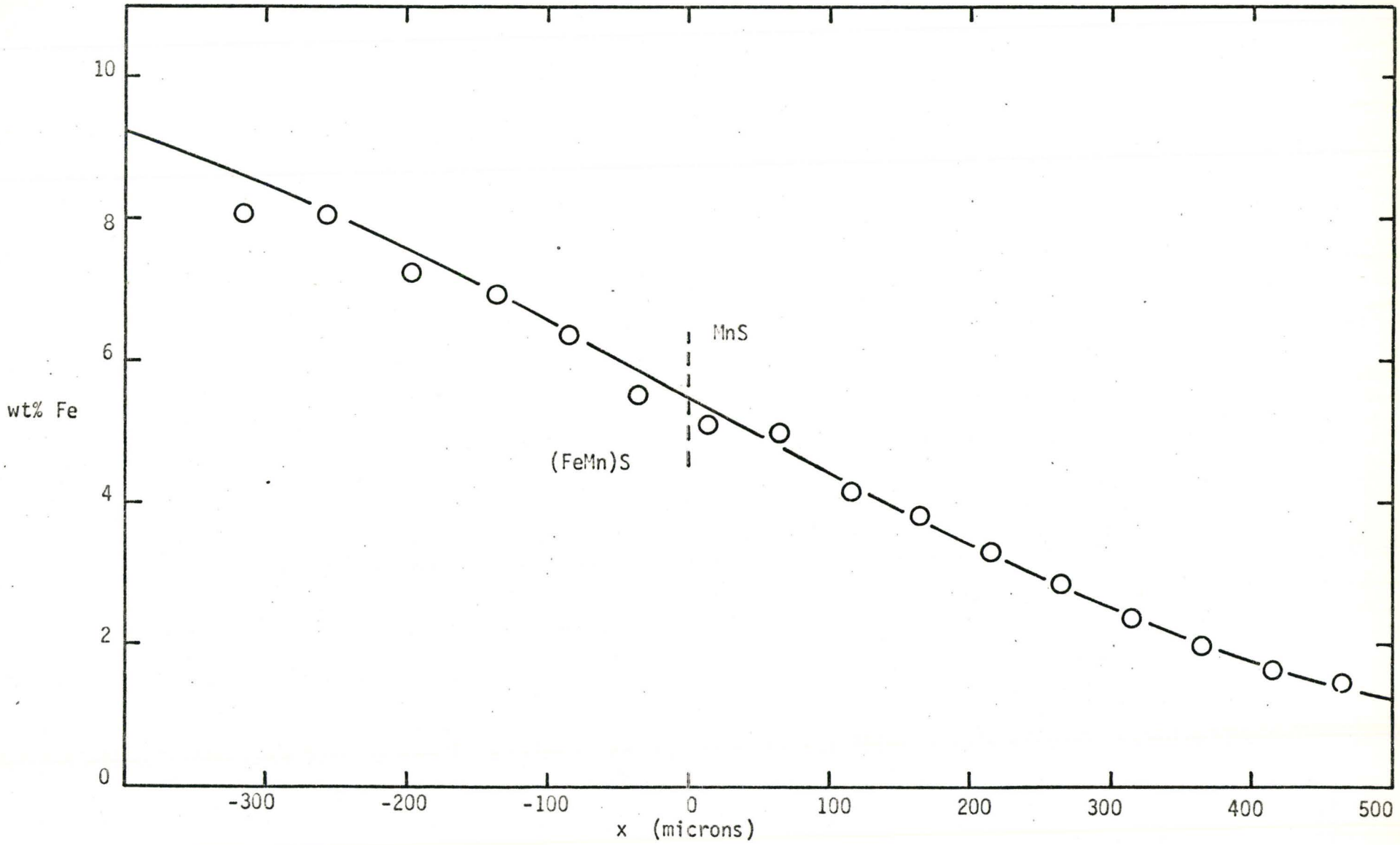

Figure 6.20 Fe concentration-penetration curve for the (FeMn)S:MnS diffusion couple reacted at 1349°C for 2160 seconds.

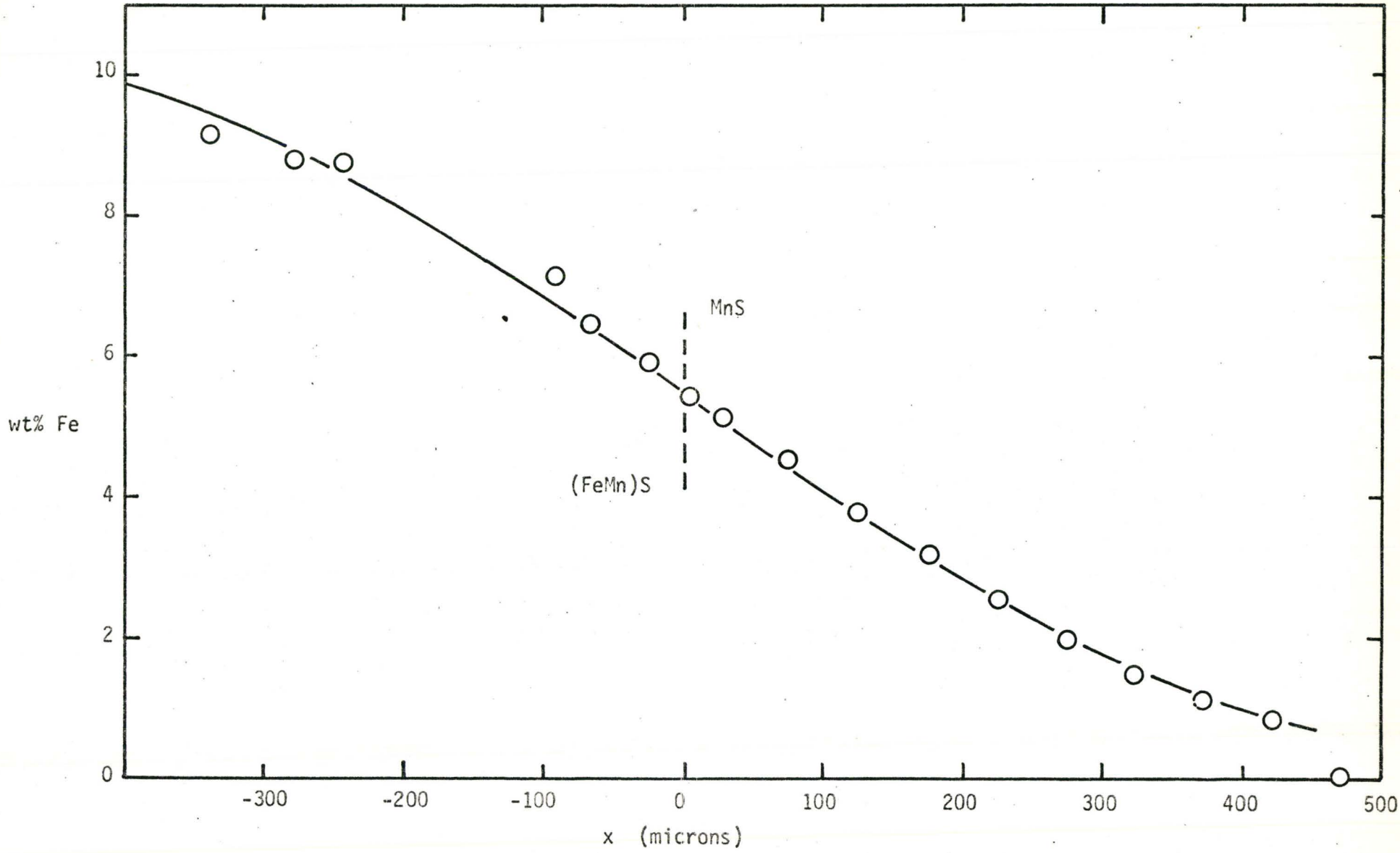

Figure 6.21 Fe concentration-penetration curve for the (FeMn)S:MnS diffusion couple reacted at 1406°C for 960 seconds.

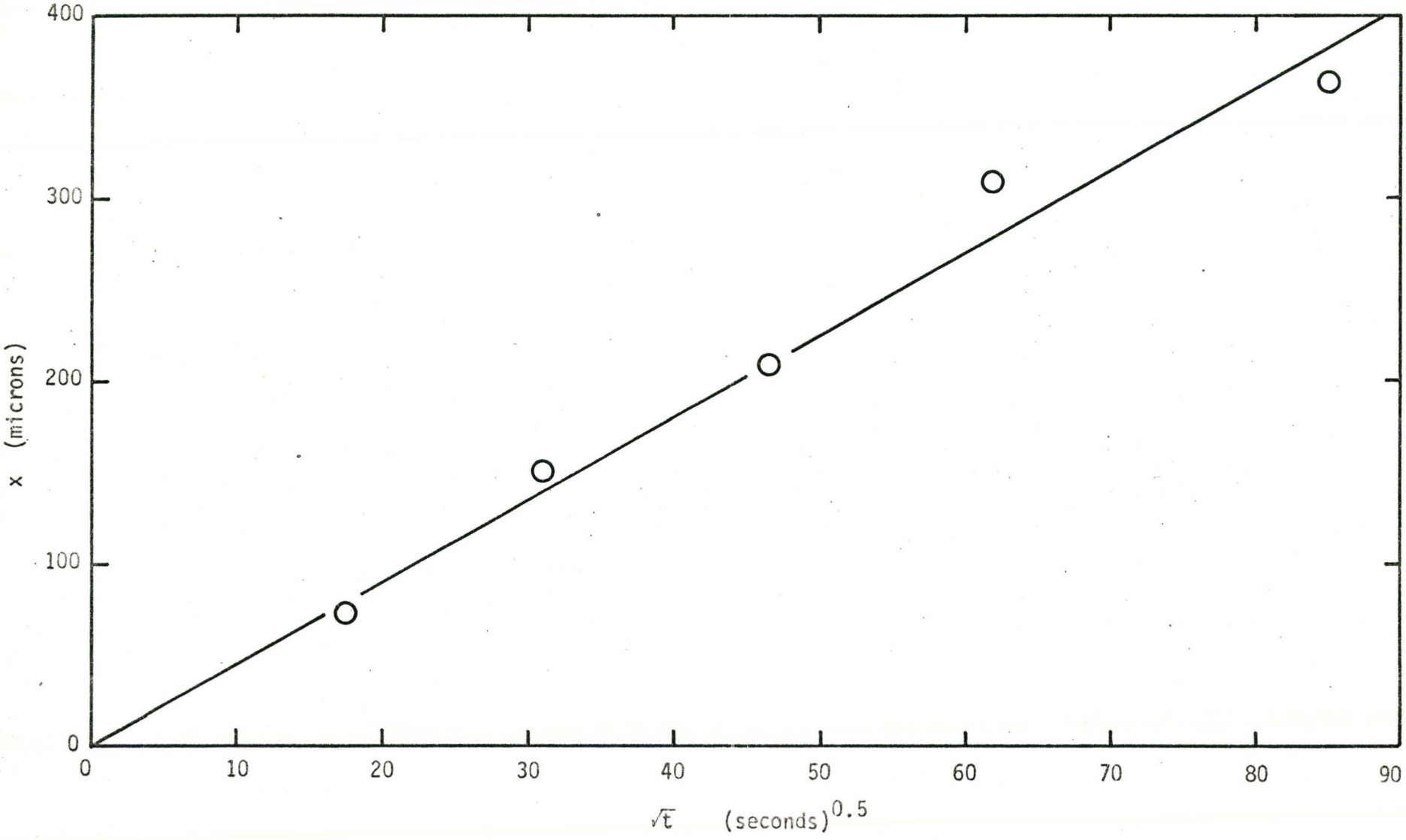

Figure 6.22 X versus $\sqrt{t}$ for the five (FeMn)S:MnS diffusion couples at 1300°C for the condition when $x/\sqrt{Dt} = 1$.

Table VI-13

(FeMn)S:MnS Diffusion Couple, 1253°C, 16 Minutes

Micro-Probe Data and Results

Standard	Fe Counts
Initial Fe	29142
Mn	228
MnS	152
Final Fe	28089
Mn	238
MnS	144

Distance (microns)	Fe	
471	291	0.54 wt.%
424	352	0.77
377	451	1.15
330	517	1.40
283	657	1.93
235	769	2.35
188	896	2.84
141	1008	3.26
94	1195	3.97
47	1409	4.78
19	1568	5.38
Interface		
-9	1728	6.01
-31	1878	6.58
-124	2292	8.16
-289	2962	10.67
-330	2958	10.65
-377	2920	10.51

Table VI-14

(FeMn)S:MnS Diffusion Couple, 1299°C, 5 Minutes

Micro-Probe Data and Results

Standard	Fe Counts
Initial Fe	15962
Mn	89
MnS	59
Final Fe	15215
Mn	96
MnS	56

	Distance (microns)	Fe	
	210	64	0.04 wt.%
	168	117	0.41
	138	256	1.38
	108	300	1.69
MnS	78	512	2.76
	48	597	3.76
	28	731	4.70
	14	796	5.15
	3	879	5.73
	Interface		
	-5	923	6.04
	-26	959	6.29
(FeMn)S	-56	1183	7.85
	-99	1340	8.95
	-124	1342	8.96
	-175	1523	10.24
	-225	1595	10.74

Table VI-15

(FeMn)S:MnS Diffusion Couple, 1301°C, 16 Minutes

Micro-Probe Data and Results

Standard		Fe Counts
Initial	Fe	15018
	Mn	49
	MnS	32
Final	Fe	14690
	Mn	57
	MnS	30

Distance (microns)	Fe	
532	43	0.09 wt.%
432	50	0.14
382	86	0.40
332	116	0.62
282	162	0.96
232	255	1.64
182	344	2.29
132	430	2.92
82	566	3.92
32	685	4.79
16	701	4.91
4	767	5.39
Interface		
-15	817	5.76
-60	976	6.92
-151	1258	9.00
-205	1325	9.49
-418	1555	10.95
-444	1538	11.05

Table VI-16

(FeMn)S:MnS Diffusion Couple, 1299°C, 36 Minutes

Micro-Probe Data and Results

Standard		Fe Counts
Initial	Fe	29452
	Mn	234
	MnS	152
Final	Fe	30753
	Mn	238
	MnS	156

	Distance (microns)	Fe	
	518	234	0.29 wt.%
	469	279	0.45
	420	318	0.59
	371	443	1.04
	322	554	1.44
	273	704	1.98
	224	909	2.72
	175	1109	3.44
	126	1327	4.23
MnS	76	1540	5.00
	47	1647	5.39
	18	1755	5.78
	Interface		
	-12	1902	6.32
(FeMn)S	-41	2079	6.96
	-71	2251	7.59
	-100	2368	8.03
	-139	2478	8.40
	-185	2611	8.89
	-226	2677	9.13
	-287	2751	9.39
	-316	2923	10.02
	-365	2959	10.15

Table VI-17

(FeMn)S:MnS Diffusion Couple 1298°C, 64 Minutes

Micro-Probe Data and Results

Standard	Fe Counts
Initial Fe	15861
Mn	60
MnS	33
Final Fe	15643
Mn	58
MnS	31

Distance (microns)	Fe	
507	238	1.42 wt.%
457	267	1.62
407	339	1.90
357	374	2.36
307	420	2.68
257	487	3.14
207	540	3.51
157	628	4.12
107	679	4.47
57	782	5.18
7	834	5.54
Interface		
-18	886	5.92
-43	885	5.90
-106	944	6.30
-151	1023	6.85
-236	1190	8.01
-293	1238	8.34

Table VI-18

(FeMn)S:MnS Diffusion Couple, 1300°C, 122 Minutes

Micro-Probe Data and Results

Standard	Fe Counts
Initial Fe	12851
Mn	36
MnS	21
Final Fe	12383
Mn	33
MnS	23

Distance (microns)	Fe	
460	255	2.01 wt.%
410	339	2.73
340	341	2.75
290	390	3.17
240	445	3.64
190	472	3.88
140	516	4.25
90	577	4.79
40	602	5.00
Interface		
-5	630	5.24
-36	726	6.07
-113	768	6.43
-149	798	6.69
-279	944	7.96
-452	1168	9.89
-625	1271	10.78

Table VI-19

(FeMn)S:MnS Diffusion Couple, 1349°C, 36 Minutes

Micro-Probe Data and Results

Standard	Fe Counts
Initial Fe	16273
Mn	105
MnS	52
Final Fe	15263
Mn	103
MnS	66

	Distance (microns)	Fe	
	665	147	0.61 wt.%
	565	182	0.85
	515	216	1.08
	465	272	1.47
	415	295	1.63
	365	346	1.98
MnS	315	406	2.39
	265	478	2.89
	215	540	3.32
	165	613	3.82
	115	660	4.15
	65	784	5.00
	15	801	5.12
	Interface		
	-35	865	5.56
	-85	785	6.39
(FeMn)S	-135	1065	6.95
	-197	1144	7.25
	-257	1229	8.08
	-315	1231	8.10
	-480	1511	10.03
	-585	1492	9.90

Table VI-20

(FeMn)S:MnS Diffusion Couple, 1406°C, 16 Minutes

Micro-Probe Data and Results

Standard		Fe
Initial	Fe	29182
	Mn	226
	MnS	148
Final	Fe	27338
	Mn	230
	MnS	163

	Distance (microns)	Fe		
	519	164	0.03	wt.%
	470	172	0.06	
	421	377	0.85	
MnS	372	452	1.14	
	323	546	1.50	
	274	673	1.99	
	225	827	2.58	
	176	991	3.21	
	126	1140	3.79	
	77	1338	4.55	
	28	1494	5.15	
	4	1564	5.42	
	Interface			
	-25	1696	5.93	
	-67	1834	6.46	
	(FeMn)S			
	-91	2011	7.15	
	-243	2423	8.74	
	-278	2434	8.78	
	-338	2535	9.17	

Table VI-21

The Diffusion Coefficient of Fe in MnS for the (FeMn)S:MnS Diffusion Couples

Temperature (^{o}C)	Reaction Time (sec)	D_{Fe}^{MnS} (cm^2/sec)
1253	2160	1.01×10^{-7}
1299	300	1.88×10^{-7}
1301	960	2.42×10^{-7}
1299	2160	2.04×10^{-7}
1298	3840	2.50×10^{-7}
1300	7260	1.84×10^{-7}
	$\bar{D}_{Fe}^{MnS}$ at $1300^{o}C$	2.04×10^{-7}
1349	2160	3.36×10^{-7}
1406	960	5.00×10^{-7}

types of diffusion couples is stationary. Such an assumption is justified for the Fe:Fe-Mn diffusion couples analysed in section A in which Fe and Mn diffuse by a direct binary interchange across the interface. However, in the Fe:MnS couples a ternary system is involved in which the amount of Mn and S diffusing into the Fe phase is limited by their low solubilities and the lower diffusion rate of Mn in γ-Fe. An approximate mass balance using a Zener analysis for the Fe diffusing in the 1300^{o}C couple reacted for 122 minutes indicates that the interface will have moved about 5 to 6 microns into the Fe phase. This assumes no counter diffusion of Mn and S into the Fe phase. However the samples show considerable MnS in the porous Fe side, a situation analogous to internal precipitation which Nakao observed in his Fe-Mn:MnS diffusion couples. The amount of this internal precipitation will counterbalance the diffusion of Fe into the MnS, and consequently minimize the interface movement. Thus the assumption that the interface is stationary in the Fe:MnS couples is justified within the accuracy of the diffusion measurements.

With respect to the (FeMn)S:MnS couples, the diffusing species are moving in the same phase in either side of the interface. Assuming that the S concentration does not vary, then these couples are analogous to binary Fe-Mn diffusion couples, and again the stationary interface concept is justified. However, as we shall see below the cation vacancy concentration must be considered, and if this concentration is different on either side of the interface then it is probable that the interface will move. However the experimental evidence indicates that such movement is small.

Figure 6.13 which shows the temperature dependence of D_{Fe}^{MnS}, clearly reveals that the diffusion coefficients determined from an Fe:MnS and an

(FeMn)S:MnS couple at any one temperature differ by about a factor of ten. This is a real difference, and is not associated with experimental errors.

The difference in D_{Fe}^{MnS} between the Fe:MnS and the (FeMn)S:MnS diffusion couples must be explained on the basis of the defect structure of the sulphide. The literature contains very little information concerning the defect structure of MnS, and the present experiments were not designed to quantitatively determine this. Consequently one must draw analogies between MnS and the sulphides of other metals for which information is available.

The range of stoichiometric deviation in pure MnS is unknown. It has, however, been classed as semiconductive[65], and evidence indicates that it is metal deficit (p-type) compound[66]. This is consistent with the character of the sulphides of the neighboring transition metals. In these sulphides the deviation from stoichiometry is achieved by creating vacancies on the cation sites, the charge neutrality being maintained by creating two M^{3+} ions for each M^{2+} vacancy. The ease of ionizing an M^{2+} ion to an M^{3+} ion is directly related to the occurrence of nonstoichiometry. If a compound is not stoichiometric, the excess or deficit of charge is compensated for by changing the valence of the ions involved. This is easily done in FeO for example. In AgBr the energy required to change the valence is quite large. Thus the appreciable non-stoichiometric deviation in FeO and lack of it in AgBr.

To obtain a theoretical estimate of the deviation from stoichiometry in MnS, the ionization potentials, $M^{2+} \rightarrow M^{3+}$, of the neighboring transition metals can be compared with that of Mn. This is shown in Table VI-22.

Table VI-22

Ionization Potentials (electron volts) from the Handbook of Physics[67]

Element	Atomic Number	Electron Configuration	Stage of Ionization (M^+)	(M^{2+})	(M^{3+})	Largest Deviation in the Sulphides[4]
Cr	24	2,8,12,2	6.76	16.49	30.95	50 to ~60 at% S
Mn	25	2,8,13,2	7.43	15.64	33.69	-
Fe	26	2,8.14,2	7.90	16.18	30.64	50 to 56 at% S
Co	27	2,8,15,2	7.86	17.05	33.49	50 to 52.5 at% S
Ni	28	2,8,16,2	7.63	18.15	36.16	50 to 52 at% S
Cu	29	2,8,17,2	7.72	20.29	36.83	50 to 51 at% S

To ionize from M^{2+} and M^{3+} is easiest for Cr and Fe. This is exemplified by the fact that FeS, like FeO, has a large solubility range and CrS is a series of ordered structures existing from CrS to Cr_2S_3. Cu has the highest potential shown and has the narrowest phase field. Co and Mn have about the same ionization potential which is some 10% greater than Fe. Thus one can imagine the stoichiometric deviation of MnS to be less than FeS, and about the same as CoS, i.e., about 2.5 at%.

The general defect equation for a metal deficit (or sulphur excess) compound, using FeS as an example, is

$$2Fe^{2+} + \frac{1}{2} S_2(g) = 2Fe^{3+} + S^{2-} + V_{Fe}$$

where V_{Fe} represents the cation vacancies. FeS, with its large stoichiometric deviation, will have a large cation vacancy concentration in which as much as 6 at% of the Fe sites can be vacant. Since the present FeS used was produced under a high sulphur potential (H_2S) it is reasonable to assume

that a large number of cation vacancies existed in the material. MnS, also produced under a high sulphur potential, will also contain a significant cation vacancy concentration although not as high as the FeS. Mixing the two sulphides (11 wt% Fe in MnS) will result in an (FeMn)S sulphide containing more vacancies than the pure MnS, but no more than was present in the FeS.

Diffusion between the two sulphides probably occurs by a cation-vacancy exchange mechanism. The vacancies involved are not only those described by the non-stoichiometric defect equation (extrinsic vacancies), but also the thermally induced vacancies (intrinsic vacancies) normally found in the compound. The diffusivity of the cation must then be dependent upon the concentrations of both types of defect. Using Shewmon's notation[68] for the cation tracer diffusion coefficient D_T, we can write

$$D_T = \gamma \; a_o^2 \; N_{vc} \; w_T \tag{6-5}$$

in which D_T is proportional to the product of the square of the lattice constant a_o, the cation vacancy concentration N_{vc}, and the tracer cation jump frequency w_T. Shewmon shows that at high temperatures when the intrinsic vacancy concentration N_{vc}^o is much greater than the impurity concentration N_{im}, then $N_{vc} = N_{vc}^o$, and thus

$$D_T = \gamma \; a_o^2 \; N_{vc}^o \; w_T \tag{6-6}$$

$$= D_o \exp\left(-\frac{\Delta H_S/2 - \Delta H_m}{RT}\right) \tag{6-7}$$

where ΔH_S is the molar enthalpy of a formation of a pair of intrinsic

vacancies, and ΔH_m is the molar enthalpy (heat of activation) associated with the jump frequency. The variation of D_T with temperature stems from the fact that both N_{vc}^o and w_T vary with temperature.

At lower temperatures where $N_{im} >> N_{vc}^o$ then $N_{vc} = N_{im}$, and thus

$$D_T = \gamma \ a_o^2 \ N_{im} \ w_T \tag{6-8}$$

Now N_{im} is not temperature dependent and consequently

$$D_T = D_o' \exp\left(-\frac{\Delta H_m}{RT}\right) \tag{6-9}$$

where $D_o' = N_{im} D_o$. The temperature dependence of D_T (and thus the diffusivity of the non-radioactive cations) is schematically illustrated in Figure 6.23. In the higher temperature range the intrinsic vacancy concentration dominates D_T. At lower temperatures the extrinsic vacancy concentration dominates, and the greater the impurity content, the greater is the value of D_o'.

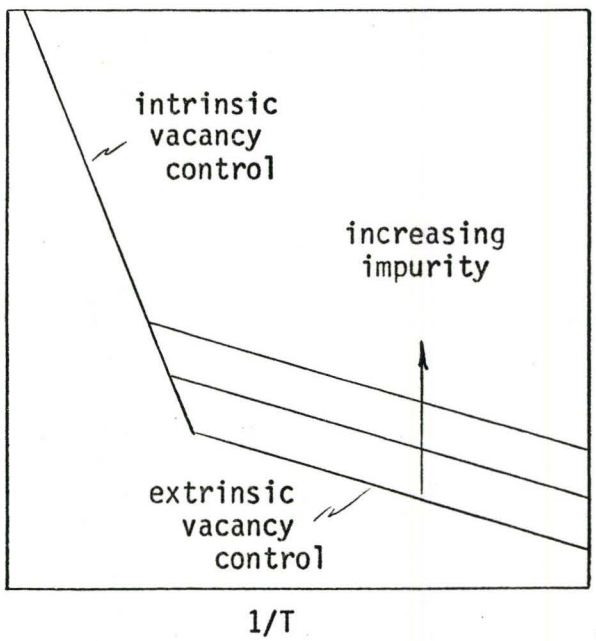

Figure 6.23
The temperature dependence of the tracer diffusion coefficient for intrinsic and extrinsic vacancy control.

Thus the observation that the D_{Fe}^{MnS} associated with the (FeMn)S:MnS diffusion couples is about a factor of ten greater than the D_{Fe}^{MnS} associated with the Fe:MnS diffusion couples can be attributed to a difference in the S content (or the cation vacancy content) in the two couples near the interface. The S content of the Fe:MnS couples is supposed to be near the stoichiometric value, while the S content of the (FeMn)S:MnS couples is greater than the stoichiometric amount, and may be as much as 2.5 at% greater.

C. THE FeS:MnS DIFFUSION COUPLES

The results of the liquid iron sulphide: solid manganese sulphide diffusion couples at 1200°C and 1300°C are tabulated in Tables VI-23 to VI-29 and plotted in Figures 6.24 to 6.27. The purpose of these experiments was to clarify the anomolous cation diffusion kinetics which Nakao observed in solid MnS in similar experiments done at 1300°C. For this reason the figures show only the MnS side of each diffusion couple. One's first impression of the present results is that the anomolies are still unresolved. However in the light of our other investigations together with a more comprehensive understanding of the Fe-Mn-S ternary system we can account for Nakao's and our observations.

Considering the four 1300°C experiments, our first observation is that the Fe concentration in MnS at the interface in each of these is 42 wt.% Fe, a value in agreement with Nakao. We also note that as the diffusion time increases from 7 to 30 minutes that the Fe content in the MnS at any given diffusion distance is increasing as it should, except for the diffusion couple reacted for 15 minutes. This couple exhibits very steep

cation gradients, much steeper than the gradient observed for the couple reacted for 7 minutes. Also, with the exception of the 15 minute couple, the diffusion distances are very large for a solid state diffusion process. The cation diffusion profile in the 7 minute experiment conforms to what one would expect from the error function equation, equation 6-1, except that there is a definite inflection in the plotted curves. The 27 minute experiment has a profile which corresponds roughly to an error function penetration curve. The 30 minutes experiment, on the other hand, has a profile which begins as an error function but which quickly levels to high, uniform Fe and Mn contents.

Many of these same anomolies were also observed by Nakao, and he was not able to adequately explain them. Our explanation is based on two new pieces of information. The first concerns the character of the 'pseudo-binary'. We recall from Chapter II the statement that a true FeS-MnS pseudo-binary can only exist if the FeS_x and MnS_x terminal compositions are such as to fall on the extensions of a single tie-line within the (FeS + MnS) two-phase field. (This criterion is investigated in detail in Chapter VII). The second piece of information is the observed microstructure of the FeS:MnS diffusion couples. Figures 6.28 and 6.29 are representative of the microstructures of the FeS/MnS interface and MnS interior of all the diffusion couples, with the exception of the 15 minute, 1300°C FeS:MnS diffusion couple which is shown in Figure 6.30.

Metallographically one observes that the initial MnS phase for the 7, 27, and 30 minute experiments has become a two-phase mixture of FeS and MnS. The 15 minute couple, on the other hand, remains as single phase MnS except for a little FeS penetration (~10 microns) at the interface region.

The two phase structure is a result of a composition instability at the FeS/MnS interface resulting from the initial (t = 0) interface compositions of FeS and MnS failing to correspond to the end points of a common tie-line in the two-phase field. That is, the above tie-line criterion for the FeS_x-MnS_x pseudo-binary has been violated. In attempting to attain a common tie-line one, or both phases, becomes supersaturated with respect to the other. This supersaturation is relieved by precipitation, the precipitation morphology, in this case, being related to the crystal structure of the solvent phase. Kirkaldy and Brown[69] have discussed this phenomenon using the 'virtual path' concept, and Harrison and Wagner[70] have observed similar effects in Cu-Ni (solid): Ag(liquid), Au-Cu (solid): Bi (liquid), and Ag-Au (solid): AgCl (liquid) diffusion couples.

In our case the FeS has quite obviously caused instability on the MnS side of the interface and has quickly penetrated deeply into the MnS phase along grain boundaries and within the MnS grains in directions associated with the cubic structure of solid MnS. The fact that the estimated Fe diffusion coefficients from the 7 and 27 minute experiments have effective values of $\sim 1.2 \times 10^{-6}$ and $\sim 1.5 \times 10^{-6}$ cm^2/sec, respectively, attest to the fact that diffusion rates nearing those of liquids (D is approximately, 10^{-5} cm^2/sec in liquids) are involved. Indeed, we are undoubtedly measuring the diffusion penetration of liquid FeS rather than solid state diffusion into solid MnS. The inflection in the 7 minute profile could be associated with a particularly course precipitate such as evolves along a grain boundary. The constant Fe and Mn contents in the 30 minute experiment is a result of the impingement of the Fe gradients from opposite sides of the MnS phase. In the Figure 6.28 one also notices that the FeS

side of the couples has also become two phase. This is due to its low Mn solubility and consequent conversion to MnS as the Mn diffuses from the MnS side of the couple.

The 15 minute couple is unique in that its initial interface composition closely conformed to the pseudo-binary tie-line criterion. No interface instability is observed, and the diffusion of iron into the MnS is therefore a solid state process. An estimate of D_{Fe}^{MnS} is 1.0×10^{-8} cm^2/sec at 1300^oC, which is in agreement with the value determined at 1300^oC in the present Fe:MnS diffusion couples. This implies that the S content at the FeS/MnS interface in this couple must have been very close to the stoichiometric value. Nakao had a similar observation, Figure 2.18, from which he estimated $D_{Fe}^{MnS} = 2 \times 10^{-7}$ cm^2/sec. This value is in agreement with the value determined from the present (FeMn)S:MnS diffusion couples, thus the interface S content of his couple must have been greater than the stoichiometric value.

At 1200^oC one expects the penetration rates to be slower, but the results in Tables VI-27 to VI-29 imply the opposite. We observe that there is always interface instability and associated penetration of FeS into the MnS and the amount of Fe in the MnS is greater than that observed at 1300^oC for similar times and distances. After 37 and 60 minutes, complete saturation has occurred, and after 16 minutes the Fe content is nearing saturation. In all cases impingement of the Fe entering from opposite sides of the MnS phase has occurred. The reason for the faster penetrations at 1200^oC must be associated with a more severe instability associated with the changed constitution at 1200^oC.

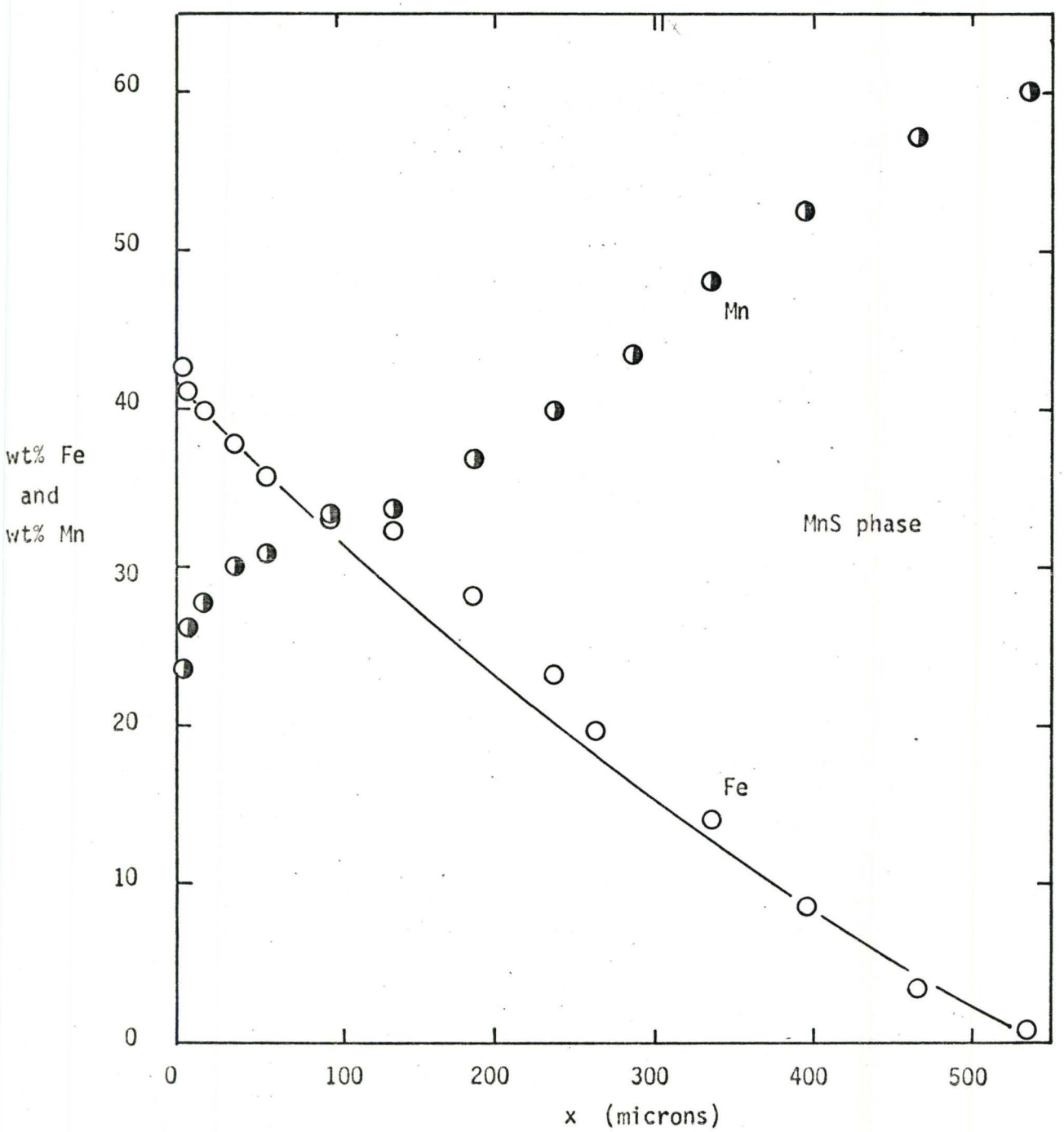

Figure 6.24 Fe and Mn concentration-penetration curves for the FeS:MnS diffusion couple reacted at 1300°C for 7 minutes.

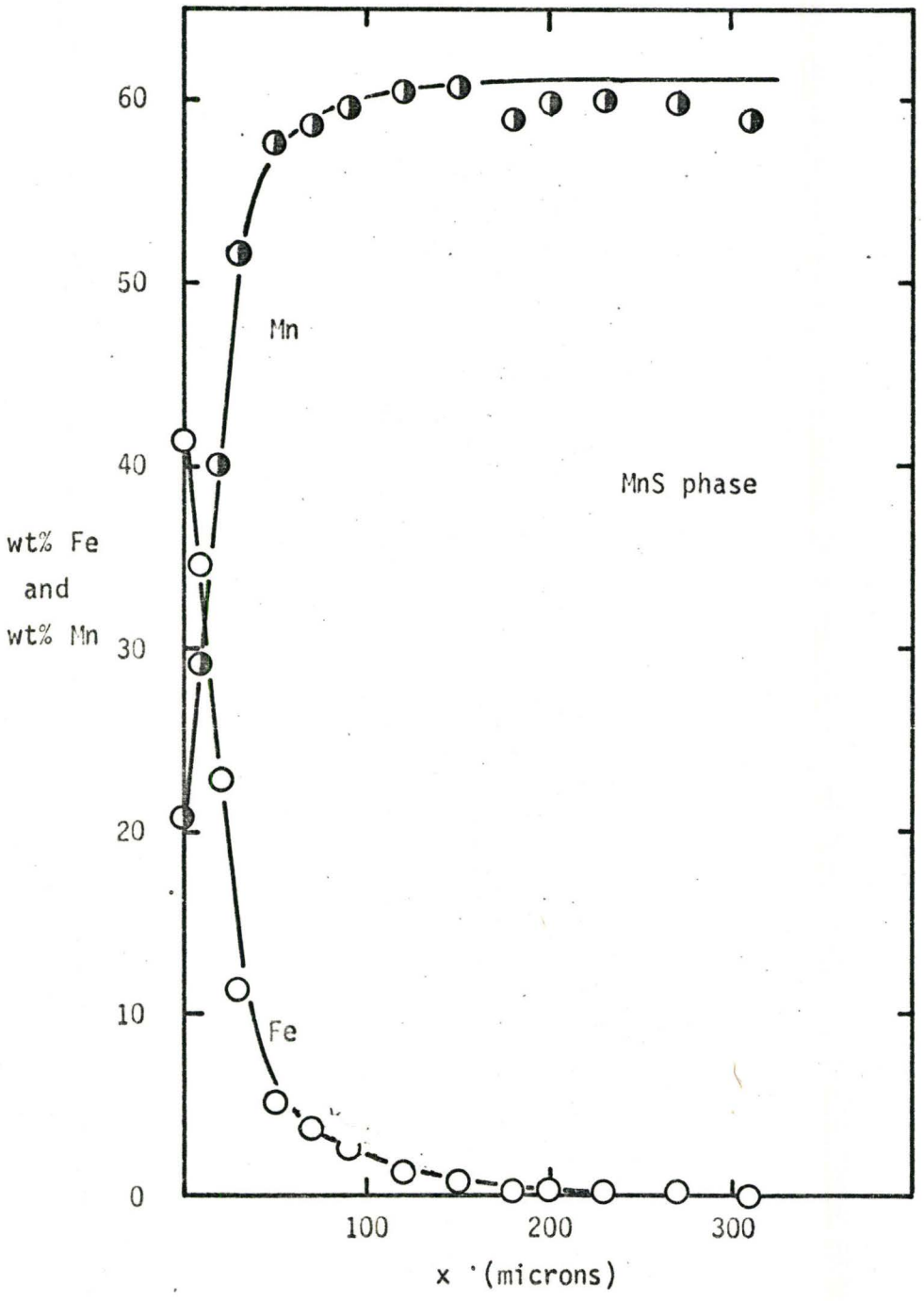

Figure 6.25 Fe and Mn concentration-penetration curves for the FeS:MnS diffusion couple reacted at 1300°C for 15 minutes.

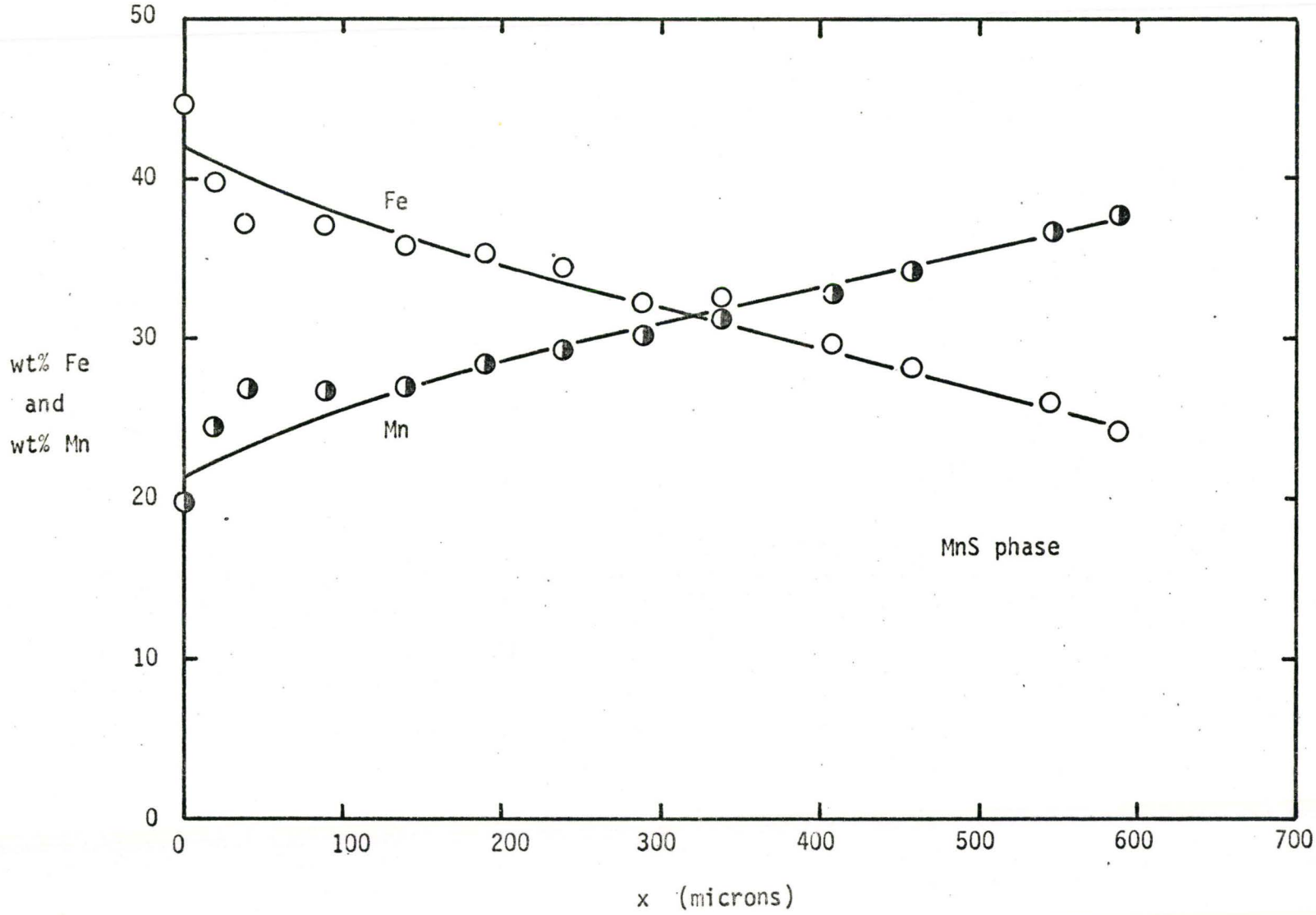

Figure 6.26 Fe and Mn concentration-penetration curves for the FeS:MnS diffusion couple reacted at 1300°C for 27 minutes.

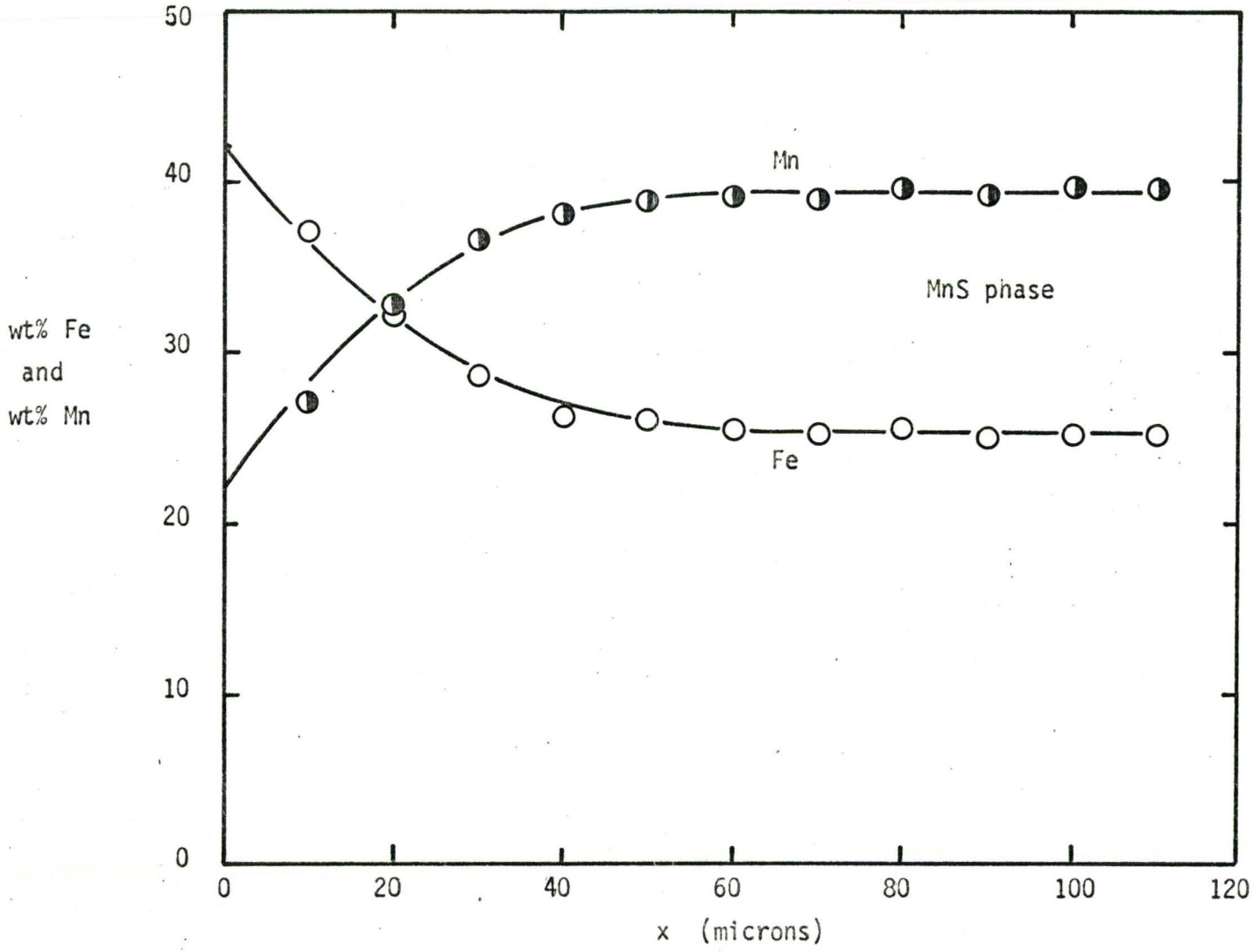

Figure 6.27 Fe and Mn concentration-penetration curves for the FeS:MnS diffusion couple reacted at 1300°C for 30 minutes.

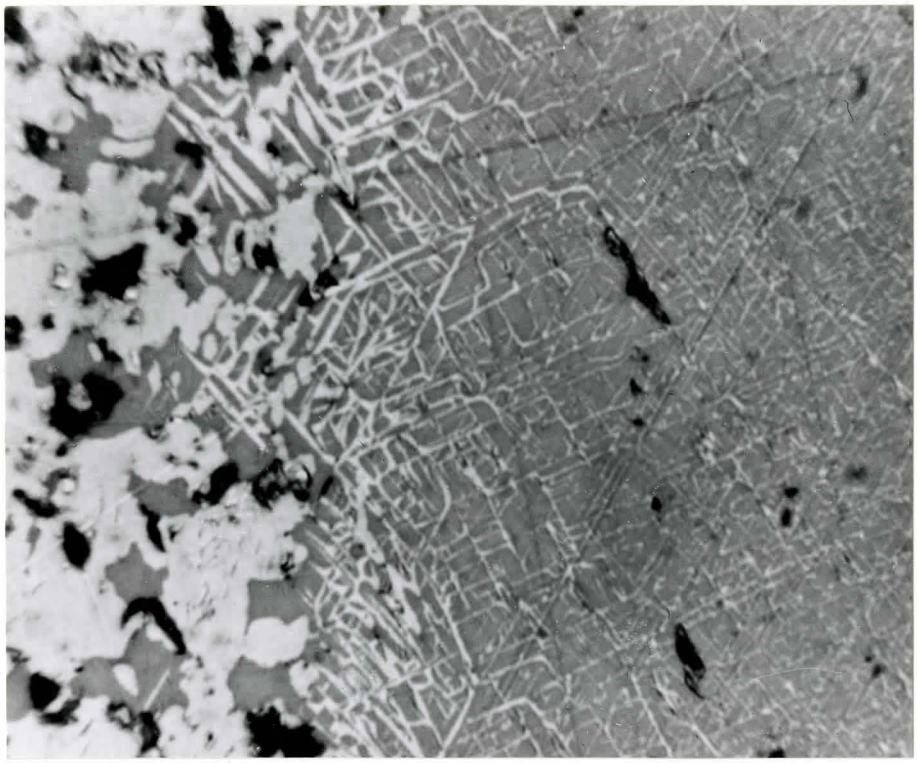

Figure 6.28 Typical interface region of the FeS:MnS diffusion couples reacted for 7, 27, and 30 minutes at 1300°C. X1120

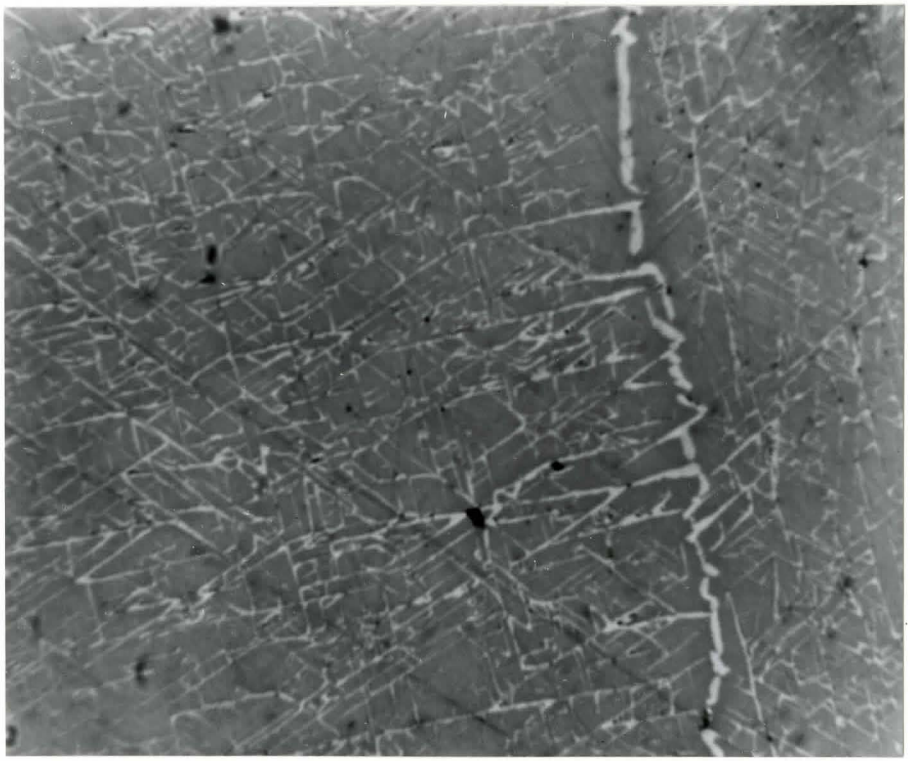

Figure 6.29 Typycal microstructure of the MnS interior of the FeS:MnS diffusion couples reacted for 7, 27, and 30 minutes at 1300°C. X1120

Figure 6.30 The interface of the FeS:MnS diffusion couple reacted at 1300^{o}C for 15 minutes. X1120

Table VI-23

FeS:MnS Diffusion Couple, 1295°C, 7 Minutes

Micro-Probe Data and Results of MnS Phase

Standard	Fe Counts	Mn Counts
Initial Fe	7813	36
Mn	160	27167
MnS	101	15973
Final Fe	8185	45
Mn	162	29238
MnS	108	16626

Distance from Interface (microns)	Fe		Mn	
3	3246	42.77 wt.%	5897	23.64 wt.%
6	3122	41.09	6576	26.35
16	3034	39.89	6895	27.63
36	2873	37.70	7544	30.23
56	2732	35.74	7708	30.85
96	2538	33.10	8383	33.55
136	2489	32.43	8420	33.70
186	2185	28.26	9253	36.99
236	1828	23.39	9994	39.95
286	1564	19.80	10913	43.58
336	1153	14.19	12071	48.15
396	736	8.63	13199	52.59
466	364	3.50	14388	57.26
536	177	0.97	15146	60.07

Table VI-24

FeS:MnS Diffusion Couple, 1299°C, 15 Minutes

Micro-Probe Data and Results of MnS Phase

Standard	Fe Counts	Mn Counts
Initial Fe	7688	41
Mn	144	28478
MnS	100	14641
Final Fe	8368	44
Mn	157	30307
MnS	112	16239

Distance from Interface (microns)	Fe		Mn	
0	3164	41.50 wt.%	5400	20.78 wt.%
10	2658	34.59	7549	29.02
20	1804	22.97	10455	40.10
30	956	11.47	13523	51.69
50	498	5.29	15112	57.70
70	386	3.77	15366	58.67
90	306	2.70	15630	59.62
120	215	1.47	15865	60.51
150	176	0.97	15913	60.69
180	129	0.31	15460	59.03
200	141	0.47	15693	59.92
230	130	0.32	15703	60.03
270	133	0.36	15509	59.35
310	114	0.11	15503	59.00

Table VI-25

FeS:MnS Diffusion Couple, 1294°C, 27 Minutes

Micro-Probe Data and Results

Standard	Fe Counts	Mn Counts
Initial Fe	7885	39
Mn	148	26516
MnS	101	14526
Final Fe	7953	39
Mn	151	26666
MnS	93	15688

Distance from Interface (microns)	Fe		Mn	
0	3344	44.67 wt.%	4685	19.93 wt.%
18	2997	39.89	5770	24.55
38	2804	37.20	6347	27.00
88	2798	37.11	6299	26.77
138	2697	35.73	6607	28.08
188	2672	35.38	6702	28.48
238	2620	34.67	6917	29.39
288	2456	32.38	7119	30.22
338	2472	32.60	7382	31.33
408	2265	29.76	7765	32.96
458	2165	28.39	8080	34.30
546	1986	25.90	8643	36.64
588	1875	24.38	8909	37.77

Table VI-26

FeS:MnS Diffusion Couple, 1300°C, 30 Minutes

Micro-Probe Data and Results

Standard	Fe Counts	Mn Counts
Initial Fe	10934	98
Mn	23	56035
MnS	12	31947
Final Fe	10814	105
Mn	25	56555
MnS	13	31609

Distance from Interface (microns)	Fe		Mn	
10	3730	37.20 wt.%	13647	27.30 wt.%
20	3218	32.07	16422	32.85
30	2841	28.27	18333	36.67
40	2648	26.34	19106	38.22
50	2634	26.20	19437	38.88
60	2576	25.62	19596	39.20
70	2547	25.33	19520	39.05
80	2575	25.61	19846	39.70
90	2529	25.15	19616	39.24
100	2546	25.32	19725	39.46
110	2550	25.36	19850	39.71

Table VI-27

FeS:MnS Diffusion Couple, 1203°C, 16 Minutes

Micro-Probe Data and Results of MnS Side

Standard		Fe Counts	Mn Counts
Initial	Fe	8226	33
	Mn	142	48603
	MnS	103	26914
Final	Fe	8888	43
	Mn	175	49087
	MnS	106	28378

Distance from Interface (microns)	Fe		Mn	
9	3730	49.92 wt.%	5519	13.1 wt.%
137	3572	47.75	6642	15.5
237	3278	43.70	8548	20.1
287	3100	41.25	8938	20.9
337	3119	41.51	8792	20.6
387	2773	36.70	11235	26.5
437	3041	40.43	9427	22.1
487	3093	41.15	8939	20.8
537	3232	43.06	8694	20.3
587	3398	45.40	7718	17.7
637	3729	49.96	5568	13.0
687	3317	44.28	8108	18.9
777	3664	49.07	5910	13.9
opposite interface at 791 microns				

Table VI-28

FeS:MnS Diffusion Couple, 1204°C, 37 Minutes

Micro-Probe Data and Results of MnS Side

Standard	Fe Counts	Mn Counts
Initial Fe	8203	35
Mn	143	27236
MnS	100	15654
Final Fe	8617	37
Mn	154	28539
MnS	88	15829

Distance from Interface (microns)	Fe		Mn	
0	3436	43.34 wt.%	4675	18.99 wt.%
43	3599	45.45	4011	16.29
93	3573	45.11	4433	18.00
193	3685	46.56	4072	16.54
293	4085	51.75	3121	12.67
393	3615	45.66	4450	18.07
593	3509	44.28	4702	19.11
703	3453	43.56	4905	19.92
793	2962	37.11	6868	27.89
893	4174	52.91	3364	13.66
975	3557	44.90	5281	21.45
Opposite interface at 1021 microns				

Table VI-29

FeS:MnS Diffusion Couple, 1206°C, 61 Minutes

Micro-Probe Data and Results for MnS Side

Standard	Fe Counts	Mn Counts
Initial Fe	8751	31
Mn	143	27435
MnS	92	15504
Final Fe	8971	36
Mn	129	28435
MnS	87	16033

Distance from Interface (microns)	Fe		Mn	
27	4005	48.18 wt.%	3931	15.94 wt.%
227	4059	48.85	4006	16.24
427	4006	48.19	4151	16.83
632	4065	48.92	3976	16.12
815	3869	46.51	4931	19.97
Opposite interface at 835 microns				

D. Fe-Mn:FeS DIFFUSION COUPLES

Although the Fe-Mn:FeS diffusion couple experiments do not yield the quantitative kinetic information which was anticipated due to the effect of interface instability between the Fe-Mn alloy and the liquid FeS, they provide considerable insight into the qualitative character of the reactions. The source of the instability can be demonstrated with the aid of Figure 6.31 in which a trace, ABCDE, of the average composition change from the pure FeS side to the alloy side of the diffusion couple is drawn schematically on the 1300°C isotherm. This carries the implication that there exists a two-phase mixture between points B and C and points C and D along the path, the compositions of the phases being given by the intersecting tie-lines and the relative amounts of phase being given by the lever rule. It is worth noting that since the micrographs and our probe measurements unmistakably identify such a path (see Figure 6.31), and since the activity must decrease in the direction A to E, it must also decrease along the phase boundaries in the directions G to H or F to C. This is not inconsistent with the known negative sign of the interaction parameter, ε_{Mn}^{S}, (see Table V-3).

Returning to the micrograph (Figure 6.32) we can see that the FeS must have been supersaturated with γ-Fe resulting in the breakdown of the interface by the dendritic or cellular growth of Fe into the liquid FeS. The development of this instability simultaneously causes the interface to recede towards the Fe side of the couple.

At 1400°C and 1440°C, this reaction was so fast that the Fe-Mn plate in these experiments was completely dissolved and a fine three-phase equilibrium structure evolved. At 1200°C and 1300° the reaction was

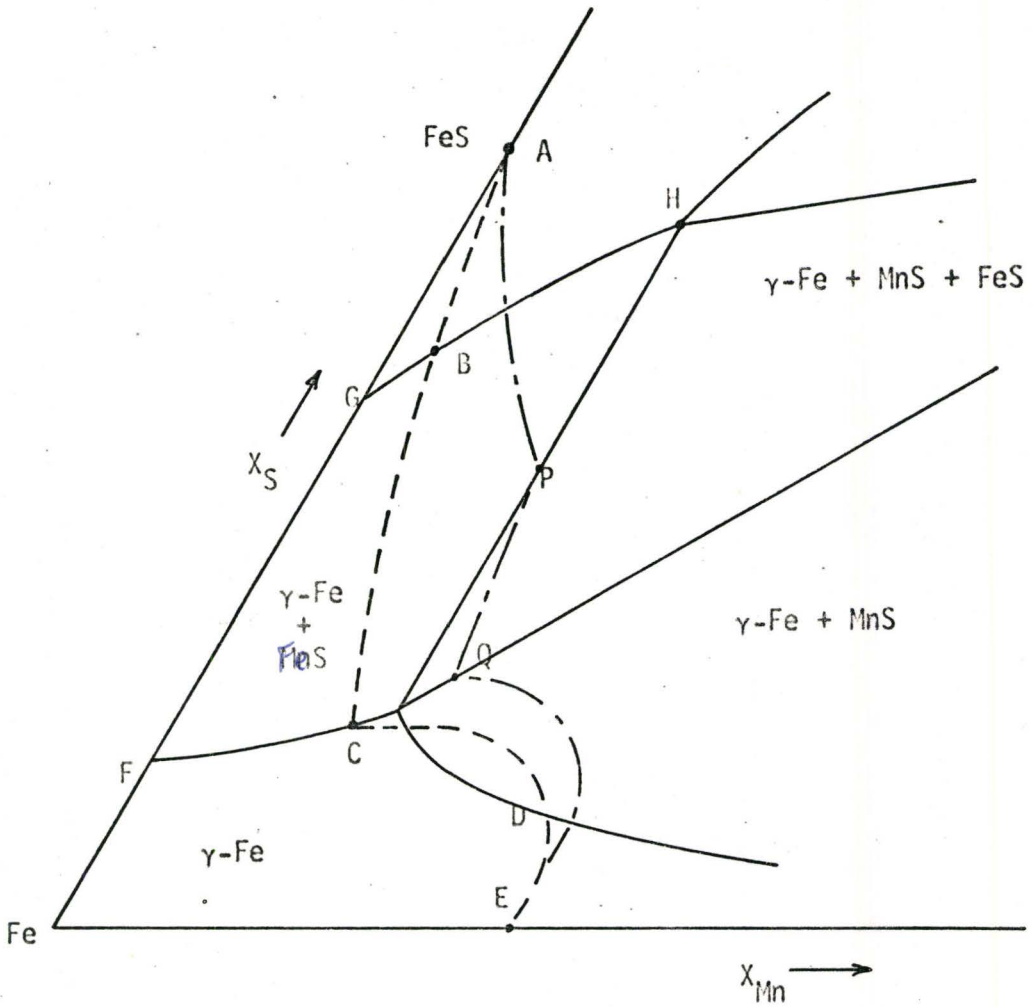

Figure 6.31 Schematic composition paths, ABCDE, for the Fe-Mn:FeS diffusion couples schematically drawn on the 1300°C isotherm.

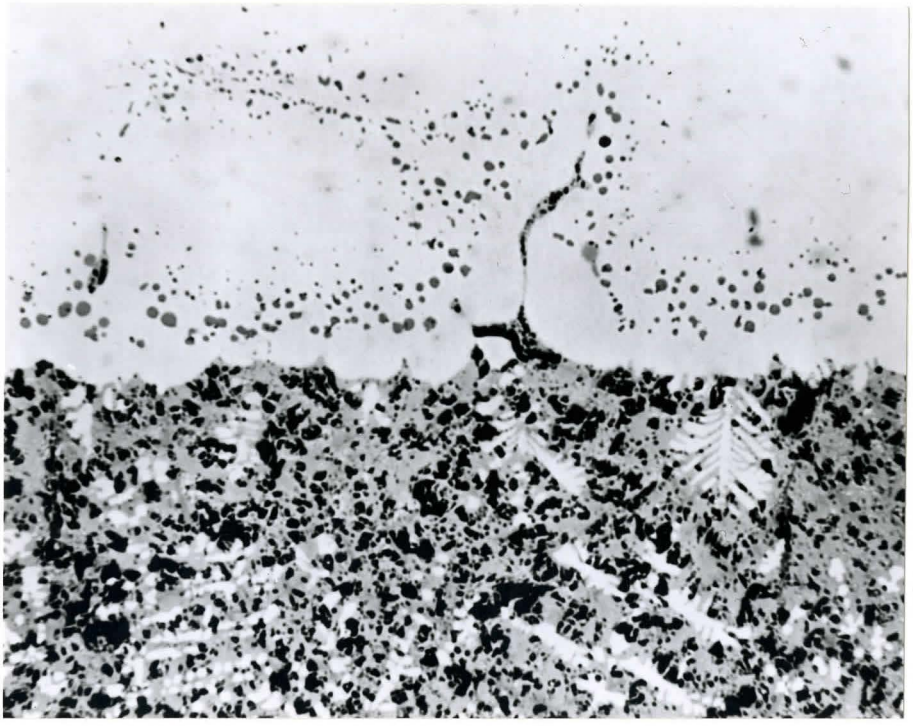

Figure 6.32 Interface region of the FeS:Fe-4.15Mn diffusion couple reacted at 1300°C for 60 minutes. X225

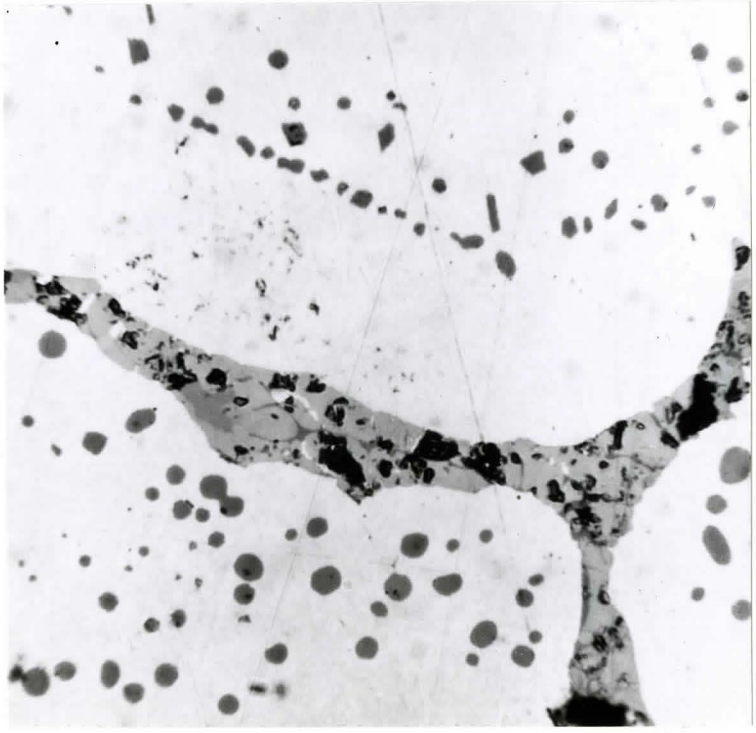

Figure 6.34 MnS precipitates in the Fe side of the FeS:Fe-4.15Mn diffusion couple. X620

successfully arrested. Figure 6.32 shows the microstructure of the FeS/Fe-Mn interface at 1300°C after a 60 minute reaction time. The microstructures of the other two experiments at 1300°C, and the three at 1200°C are similar to Figure 6.30 though the reaction is not so far advanced. In Figure 6.32 we can observe the Fe dendrites growing from the interface into the FeS and the simultaneous penetration of FeS into the Fe-Mn alloy along a grain boundary. Also present are inclusions of MnS which have internally precipitated in the alloy. This is due to the intrusion of the path into the (γ-Fe + MnS) field along the line CD. This intrusion is caused by the fast inward diffusion of S in relation to the slow counter diffusion of Mn in γ-Fe, leading to a curved 'virtual path' (see Kirkaldy and Brown[69], Nakao[13]). As γ-Fe becomes super-saturated with Mn and S and the precipitation of MnS occurs, the MnS precipitate having a composition in equilibrium with the surrounding γ-Fe, S continues to diffuse, new precipitates are formed, and the precipitation front correspondingly moves into the γ-Fe. Simultaneously the Mn content of the γ-Fe behind this front decreases as line CD implies. This is observed in Table VI-30 and Figure 6.33 which present the results of a micro-probe analysis for Mn in γ-Fe starting from the FeS/Fe-Mn interface, passing through the precipitate band, and extending beyond the precipitation front.

In Figure 6.33 it is seen that the MnS precipitate free zone near the interface is nearly depleted of Mn. This represents the γ-Fe area just beneath the three-phase triangle and through which ABCDE passes in Figure 6.31. As the Mn content in the γ-Fe increases in the precipitate zone from nearly zero to 2-3 wt.% Mn at the precipitate front, one expects

that the Fe content of the MnS precipitates correspondingly decreases, as indicated by the tie-lines in the (γ-Fe + MnS) two phase field in Figure 5.2. We know from the equlibrium experiments that the Fe content of MnS in equilibrium with an Fe-4 Mn alloy is practically zero. Thus the first precipitates to form at the precipitation front must be nearly pure stoichiometric MnS. On the other hand, those precipitates near the FeS/Mn-Fe interface should contain considerable Fe because the Mn content of the γ-Fe is extremely low. In Table VI-30 we present the compositions of some of these larger precipitates, and indeed, we observe that the Fe content is 15-18 wt.% Fe. (Because the measured precipitates are only about 10 microns in diameter one can expect considerable interference from the surrounding Fe phase during the measurements. Thus the tabulated compositions can only be regarded as rough estimates.)

An interesting observation concerning the MnS internal precipitates is that their morphology changes across the precipitation zone. Those near the precipitation front, i.e., the newest precipitates, are small and have a definite crystallographic form (see Figure 6.34) while those on the FeS side of the zone are larger and are globular in shape. This morphology change presents an interesting nucleation and growth problem, the analysis of which is outside the scope of the present investigation.

Because of the large amount of FeS used in the 1200 and 1300^{o}C experiments, and because the diffusion of Mn in liquid FeS is very fast, the FeS did not become saturated with Mn at the FeS/Fe-Mn interface. If the reaction times had been larger, and/or had the amount of FeS been smaller, saturation would have occurred and the composition trace would

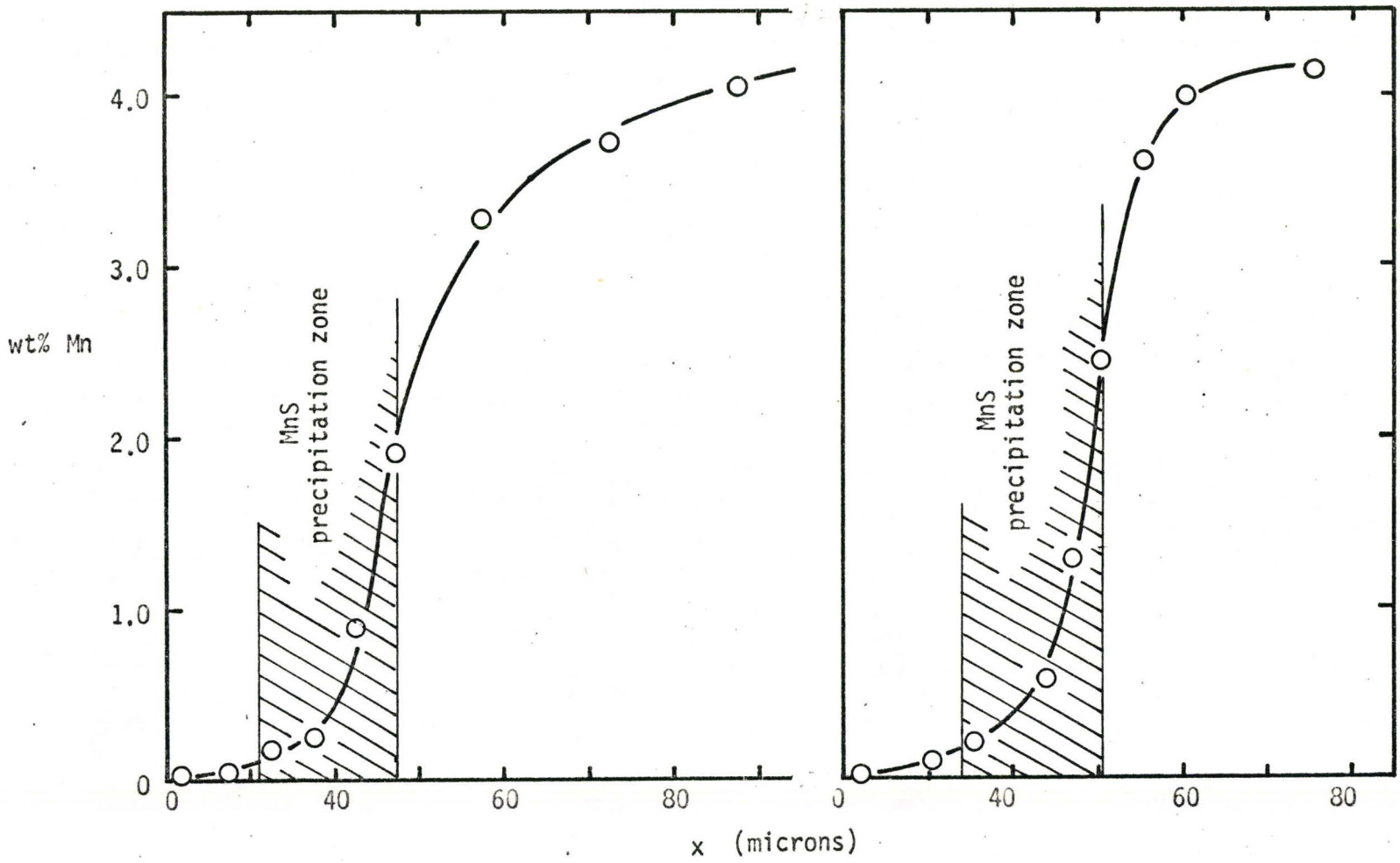

Figure 6.33 Mn concentration-penetration curve for the Fe-4.15Mn:FeS diffusion couple reacted at 1300^{0}C for 60 minutes.

Table VI-30

FeS:Fe-4 wt.% Mn Diffusion Couple

Reacted at 1298°C for 60 Minutes

Micro-Probe Data and Results for Fe-Mn Side

Standard	Fe Counts	Mn Counts
Initial Fe	8324	33
Mn	126	30105
MnS	88	17069
Final Fe	8236	32
Mn	139	29813
MnS	81	16579

Trace No. 1

Diffusion Distance from Interface		Mn
4 microns	42	0.03 wt.%
15	48	0.05
25	86	0.18
35	109	0.24
45	294	0.88
55	605	1.92
75	1009	3.28
105	1144	3.73
135	1243	4.06

Ppte. Zone between 22 and 55 microns

Trace No. 2

Diffusion Distance from Interface		Mn
4 microns	42	0.03 wt.%
21	67	0.11
31	99	0.22
48	208	0.59
54	415	1.28
61	760	2.44
71	1107	3.61
81	1229	4.00
111	1273	4.15

Ppte. Zone between 28 and 61 microns

MnS Precipitates in γ Fe

	Fe		Mn		S
1.	1583	18.0 wt.%	11731	39.4 wt.%	42.6 wt.%
2.	1582	18.0	12622	42.4	39.6
3.	1366	15.4	13224	44.4	40.2

then be represented by APQDE in Figure 6.31. That is, MnS as well as Fe would dendritically precipitate in the FeS. This has obviously occurred in the 1400 and 1440^{o}C experiments where the solid state diffusion rates are faster. Nakao, who in similar experiments involving longer times and lesser amounts of FeS invariably observed MnS precipitation as well as Fe precipitation in the FeS zone, noted that this behaviour simulated very well the process of conversion of L-FeS → MnS in Mn containing steels (see Chapter VIII).

CHAPTER VII

THE TERNARY DIAGRAM IN THE REGION OF THE IRON SULPHIDE - MANGANESE SULPHIDE 'PSEUDO-BINARY'

The term pseudo-binary is apostrophized in the above title because it was shown in Chapter II that a true pseudo-binary section cannot exist between stoichiometric FeS and MnS, and that pseudo-binary planes in the Fe-Mn-S ternary system can only be accommodated by a special set of paired non-stoichiometric FeS_X-MnS_X compositions. In this chapter we investigate the character of the ternary diagram at temperatures where liquid iron sulphide exists in equilibrium with solid manganese sulphide. The methodology of investigation involves qualitatively predicting a ternary isotherm in the region of the pseudo-binary using the free energy concepts discussed previously, and then comparing this isotherm with information culled from equilibrium and kinetic data in the literature and from the present investigation.

In Chapter III it was stated that the simple liquid free energy curve on the Fe-S binary system transforms to liquid-liquid immiscibility at lower temperatures, but that one of the liquids is metastable with respect to solid iron. This is implied by the shape of the Fe-S binary phase diagram, schematically shown in Figure 7.1a. We view the Fe-S phase diagram in relation to the Fe-Mn-S system as represented by the Gibb's triangle inset in Figure 7.1a. We note that the slope of the γ-Fe liquidus curve, dT/dX_S, approaches zero as the liquidus curve nears the extectic temperature (1365°C). When $dT/dX_S = 0$, one has the point of imminent immiscibility or the critical point. By extrapolating this liquidus curve (dashed curve in Figure 7.1a)

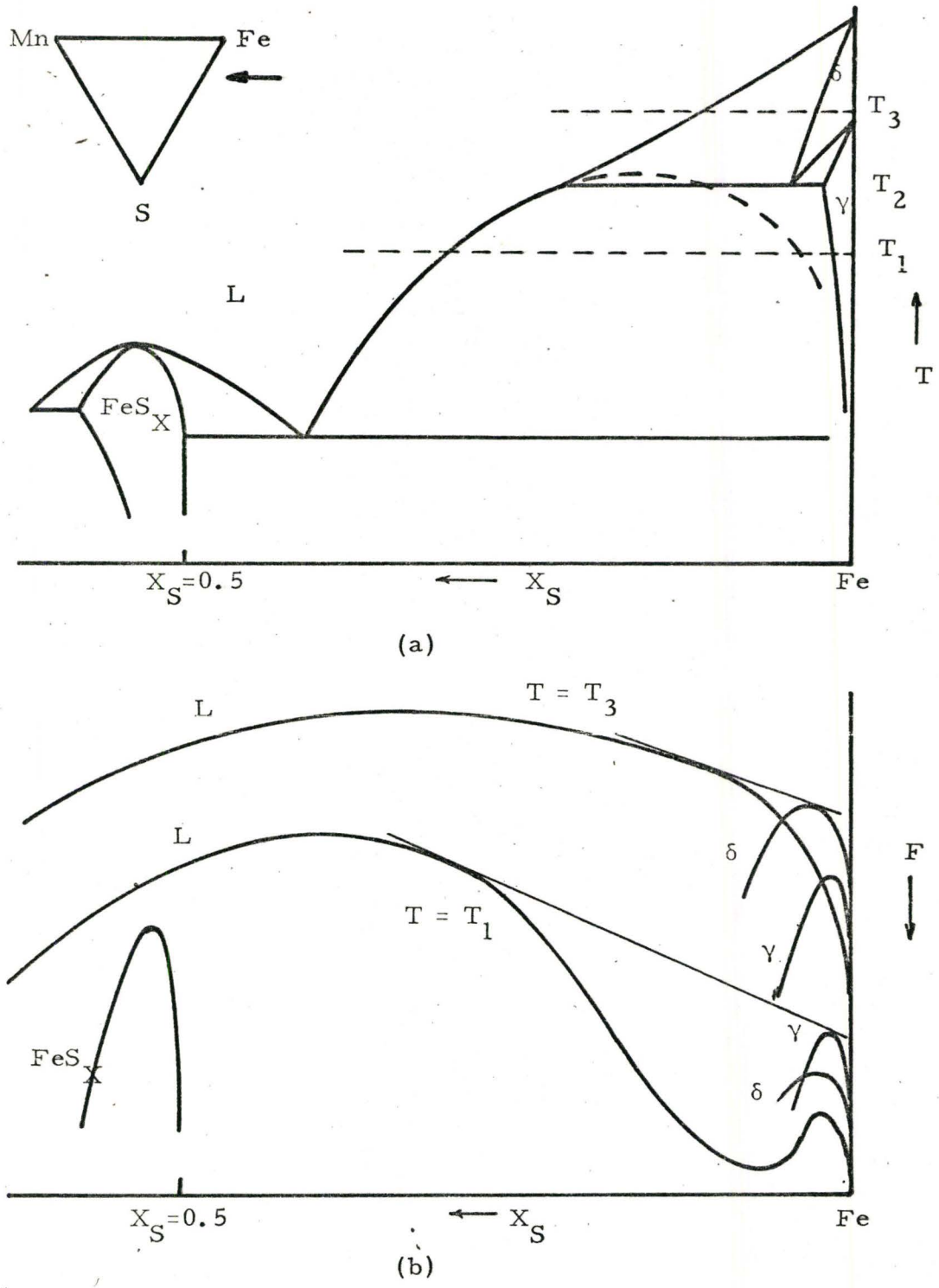

Figure 7.1 Schematic representation of the Fe-S binary phase diagram and the associated free energy-composition diagram at the temperatures T_1 and T_3.

we find that $dT/dX_S = 0$ just above 1365°C. Qualitatively, we may expect metastable immiscibility at temperatures and compositions beneath the dashed line.

Figure 7.1b schematically shows the associated free energy curves for the Fe-S binary. (In maintaining our ternary convention the curves are drawn upside down). At a temperature T_3 above T_2, the temperature of imminent immiscibility, the liquid free energy curve is everywhere concave downwards. At a temperature T_1 (say 1300°C) the curve suggests immiscibility, but the emergent iron phase makes it metastable. One can now see the strong symmetry between the Fe-S and Mn-S binary systems, the Mn-S system having a stable miscibility gap. In fact the stable miscibility gap on the Mn-S binary is connected to the metastable miscibility gap on the Fe-S binary through the Fe-Mn-S ternary system. At some composition and temperature within the ternary system the metastable miscibility gap emanating from the Fe-S binary becomes stable. This is in fact point K on the liquidus surface of Figure 3.2. It is interesting to note that point K was estimated by Korber (see Chapter II) to occur close to the Fe-S binary (5 wt.% Mn, 22 wt.% S) at 1370°C, just 5°C above the extectic temperature. Point K is defined by $dT/dX_S = 0$ on the ternary phase diagram, and $d^2F = d^3F = 0$ on the free energy surface. The locus of all such points in the ternary phase diagram describes a curve traversing the ternary from the Mn-S to the Fe-S binary. The terminal of this curve on the Mn-S binary occurs at a high temperature, probably >1800°C, and at a S content which is probably >25 at% S (the extreme relative stability of solid MnS in this system is probably reflected in this composition). The terminal of this curve on the Fe-S binary occurs at a temperature above 1365°C, and at a composition <19 at% S (the liquid

extectic composition). From these inferences the projection of the critical curve onto the Gibb's triangle can be estimated. This is the dashed curve traversing the liquidus surface of Figure 3.2.

On the basis of the above discussion one can make certain predictions concerning the character of the pseudo-binary region, especially with respect to the (FeS + MnS) two-phase region, and the composition of the FeS corner of the (γ-Fe + FeS + MnS) three-phase triangle at 1300^{o}C. We begin by reproducing, in Figure 7.2, the liquid and solid free energy curves corresponding to the temperature T_1 in Figure 7.1b. The liquid curve is labelled F_o and is associated with the Fe-S binary. As Mn is added to the system, the free energy increases and the miscibility gap widens. This is shown by the curves F_1 and F_2, which we will assume represent Mn contents of X_{Mn} = 0.01 and 0.02, respectively. F_3 represents the liquid free energy curve on the Mn-S binary, and F_4 represents the solid MnS free energy curve. The curves AB and CD represent the locus of points defined by $dF_{FeS}/dX_S = 0$ and $dF_{L_1}/dX_S = 0$, where FeS $\equiv L_{II}$ and L_I are the two immiscible liquids.

As one now adds small amounts of Mn to γ-Fe, the γ-Fe free energy curve rises slowly because the Fe-Mn system is nearly ideal. Also the sulphur content remains small, and thus one can keep the γ-Fe free energy surface fixed in Figure 7.2, that is fixed with respect to the FeS liquidus surface. Our investigations at 1300^{o}C indicate that with small additions of Mn the curve AB must rise and swing quickly towards higher sulphur. This is based on the location of the FeS corner of the three phase triangle (X_{Mn} = 0.01) in relation to the Fe-S binary liquidus composition. The three phase triangle is represented in Figure 7.2 as the triangle PQR. As the temperature of the system increases the swing of AB to higher sulphur will be moderated by a

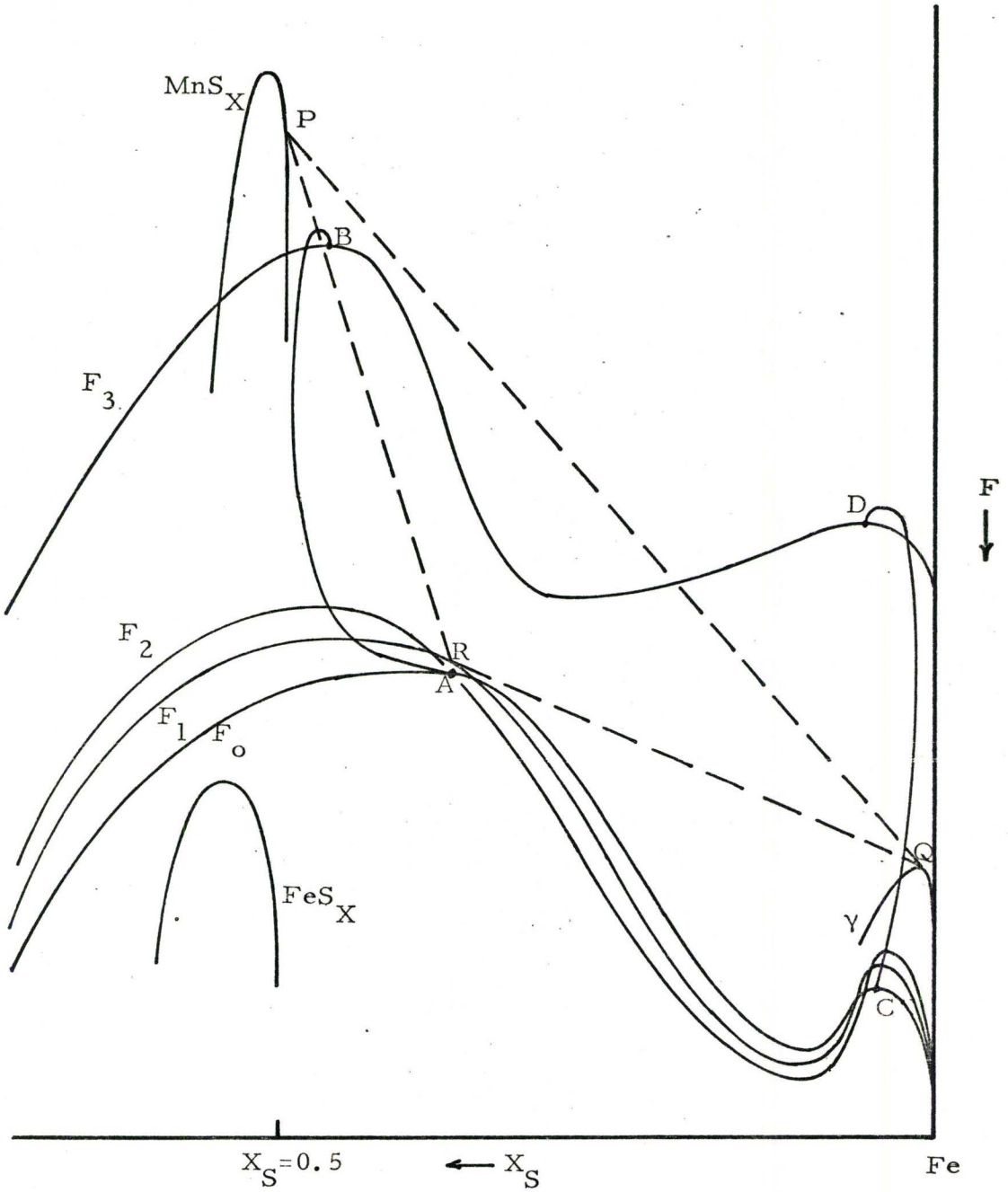

Figure 7.2 Free energy-composition diagram of the Fe-Mn-S system as viewed from the Fe-S binary side.

narrowing of the miscibility gap. This was also observed in our investigations whereby the composition of the FeS corner remained invariant with increasing temperature.

To show how the boundaries of the two-phase region (FeS + MnS) are determined an additional figure, Figure 7.3, is employed. In Figure 7.3 we view the free energy surfaces schematically from the Fe-Mn binary and look towards increasing sulphur contents. The γ-Fe curve is closest to the Fe-Mn binary. The curve CD, occurring at low sulphur contents, is just behind the γ-Fe curve (the dashed part of CD indicates this). CD, of course, represents the top of the liquid ridge depicting the proximity of the metal rich boundary of the miscibility gap. The curve AB represents the top of the ridge depicting the proximity of the high sulphur boundary of the miscibility gap. The MnS curve is behind AB. The three phase triangle is also shown by the triangle PQR. The important aspect of this diagram is that a common tangent between the MnS and AB curves is tangent to the AB curve at a point very close to the FeS binary.

The boundaries of the two-phase region (FeS + MnS) are determined by putting an imaginary tangent plane in contact with the MnS and FeS free energy surfaces at points P and R in Figure 7.1b and/or 7.2 and rotating this plane towards higher sulphur. It is obvious that the plane describes a path encircling the peaked MnS free energy surface. The trace on the liquid FeS surface is not so obvious.. We can infer, however, that because the curves F_1 and F_2 display little curvature until above X_S = 0.5, and because the curve AB rises sharply for small Mn contents in Figure 7.3 that the rotating tangent plane will trace a path on the FeS surface nearly parallel to the Fe-S binary until above X_s = 0.5, and then swing sharply across the

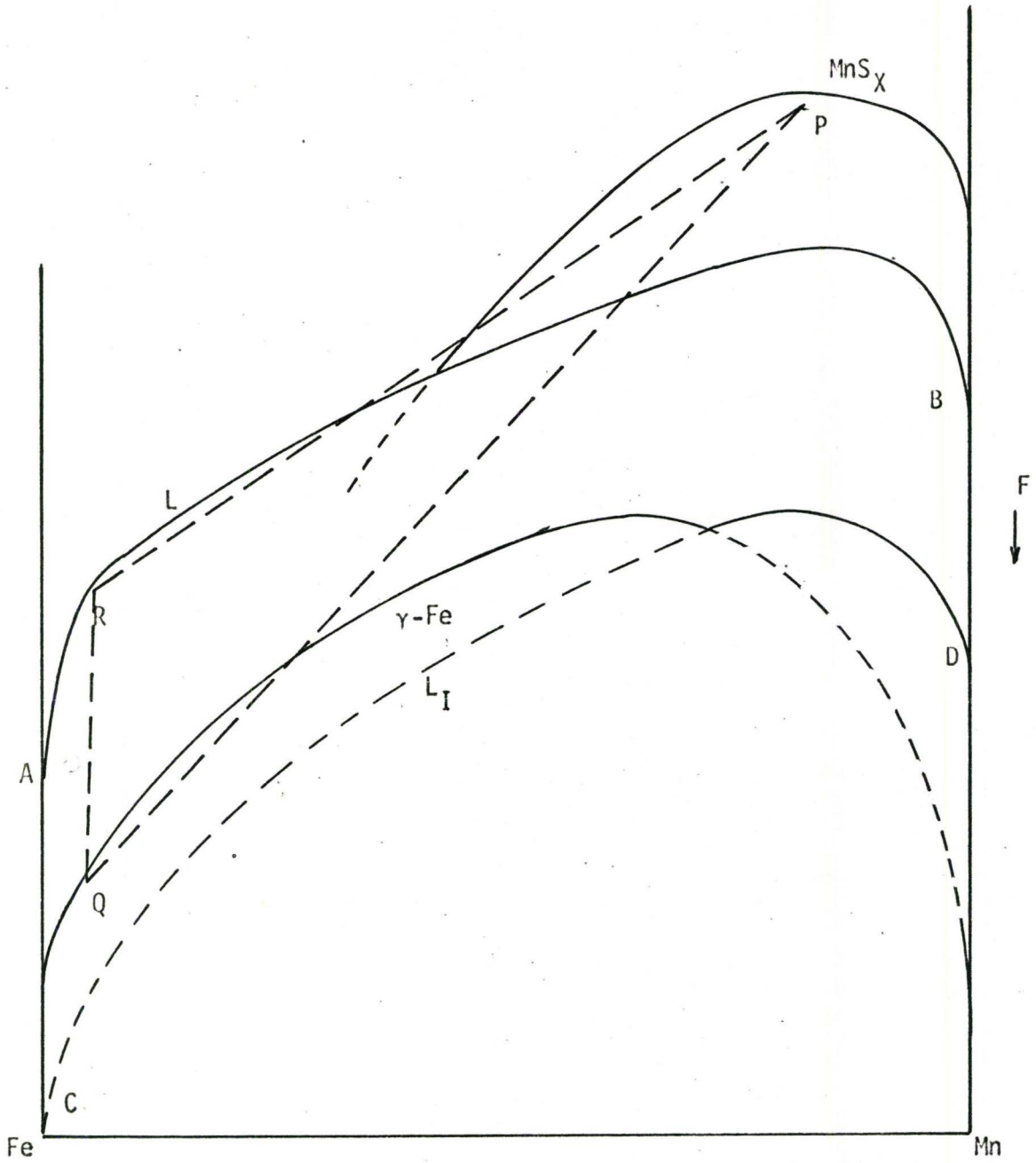

Figure 7.3 Schematic free energy-composition diagram of the Fe-Mn-S system as viewed from the Fe-Mn binary.

ternary system, behind the MnS surface to the Mn-S binary.

With this qualitative theoretical information and the experimental data mentioned at the beginning of this chapter, the section of the 1300°C isotherm showing the pseudo-binary region may be constructed.

The phase extent of pure MnS is unknown. However, through analogy with related sulphides, the cation diffusion results, and their subsequent interpretation, we have inferred that manganese sulphide is a metal deficit sulphide with a formula MnS_X in which $1 \leq (X = \frac{N_S}{N_{Mn}}) \leq 1.1$ (see Chapter VI). In Figure 7.4 the sulphide limits are therefore shown as from 50 to 52.5 at% S.

More is known about the solid solubility of iron in MnS. However the data of various investigators at first sight appear to be in disagreement. A similar statement can be made with respect to the Mn content of liquid FeS. As we shall see below, the disagreement can be ascribed to faulty interpretation rather than to a true discrepancy.

The composition of the FeS and MnS corners of the (γ-Fe + MnS + FeS) three-phase triangle at 1300°C are 0.9 at% Mn, 54.8 at% Fe) and (37.1 at% Mn, 12.9 at% Fe), respectively. These coordinates represent the bounding tie-line of the (FeS + MnS) two-phase region. From Shibata's phase diagram, Figure 2.5, one notes that the liquidus at 1300°C occurs at approximately 25.5 wt% MnS (~13 at% Mn). Shibata did not determine the solidus of this diagram. The S content of his starting materials (mixtures of MnS and FeS) were reported as stoichiometric. However during the course of his experiments he used a 'molten glass' slag on top of the liquid sulphide to prevent oxidation. Being molten, the glass must have been a type of borosilicate glass which, among other compounds in trace amounts, contains about 25% $CaO + Na_2O$. Thus the glass slag is an acid slag having a low basicity

index (about 0.33). With respect to liquid steels, acid slags are not desulpherizers but they do dissolve Mn, and probably Fe, from the melts. They undoubtedly react in a similar manner with the liquid sulphides, especially when one considers that CaS is more stable than FeS and MnS. Consequently it is conceivable that the glass slag Shibata used to prevent oxidation of his liquid sulphide changed the nominal composition of his sulphide in the general direction indicated by the arrow on his data point in Figure 7.4.

Nakao determined, from his FeS:MnS diffusion couple data, that the MnS phase could contain about 42 wt.% Fe (33 at% Fe) in solid solution at 1300°C. Although he does not quote a corresponding value for the Mn dissolved in liquid FeS, one can see from Figure 2.18 due to Nakao that he detected Mn contents lying between 2 and 12 wt.% Mn in the FeS phase which contained considerable dendritic MnS as a finely dispersed second phase. The high Mn values are evidently due to the probe spot measurements averaging over both phases. The low value (~2 at% Mn) must therefore represent the Mn content of the FeS. The S content of his MnS phase can be estimated by comparing his value of $D_{Fe}^{MnS} = 2 \times 10^{-7}$ cm^2/sec, measured from Figure 2.18, and the results of the present Fe:MnS and (FeMn)S:MnS diffusion couples which give D_{Fe}^{MnS} at 1300°C as 3.96×10^{-8} and 2.04×10^{-7} cm^2/sec, respectively. Our second value, which agrees with Nakao's, was attributed to a S excess MnS_X (i.e., $X > 1$), while the former value was attributed to diffusion in stoichiometric MnS_X ($X = 1$). Thus the S content of his FeS:MnS couples would appear to be greater than the stoichiometric amount.

Measurements from the present FeS:MnS diffusion couples show that the Fe content of MnS is also about 42 wt.% Fe (33 at.% Fe). A measurement of

the diffusion coefficient from one of these couples at 1300°C gave $D_{Fe}^{MnS} = 1.0 \times 10^{-8}$ cm^2/sec. Since this value is in agreement with the D_{Fe}^{MnS} value determined in the stoichiometric MnS, one can conclude that the S content of our FeS:MnS diffusion couples is very close to 50 at% S.

From this evidence one infers that the average S content in Nakao's FeS-MnS experiments was slightly greater than in the present FeS-MnS experiments, but because the probe could not resolve these slight differences they do not show up in the tabulated results.

Referring again to Nakao's thesis, we record the reported composition of the MnS in his five equilibrium experiments (see Table VII-1). Because Nakao thought that the top of the three-phase triangle must lie on the stoichiometric line he concluded that the first four listed values for Fe in MnS had not attained equilibrium with the coexisting phases, γ-Fe and FeS. At the same time, because the fifth value agreed closely with the composition determined in his FeS:MnS diffusion couple measurements, he assumed that this represented the three-phase equilibrium value. That his conclusion was in error can be seen by plotting his data, as in Figure 7.4, which clearly indicates that equilibrium was attained in each case, and that each of the four points corresponds to a tie-line in the (FeS + MnS) two-phase region. His measurements for the FeS side of these tie-lines are also listed in Table VII-1 and are plotted in Figure 7.4.

Despite the impressionistic character of some of this data it gives, with the exception of the two-phase region sweeping behind the MnS phase, some substance to the structure of the isotherm which one predicts from qualitative free energy considerations. If one assumes as well that at these

TABLE VII-1

The Composition of the MnS and FeS Corner of the (Fe + MnS + FeS) Three-Phase Triangle, after Nakao[13].

Phase	wt%				at%	
	Fe	Mn	S	Total	Fe	Mn
	22.4	40.0	36.4	98.8	17.7	32.2
	24.2	41.1	35.6	100.9	18.7	32.1
MnS	30.7	31.2	36.0	97.9	24.6	25.4
	32.4	30.0	34.3	96.7	26.2	24.9
	39.4	23.6	36.8	99.8	30.9	32.2
	59.7	0.72	35.0	95.42	49.2	0.6
	65.6	1.34	34.0	100.94	52.0	1.1
FeS	62.6	0.60	35.3	98.5	50.2	0.5
	62.2	0.59	35.7	98.49	49.8	0.5
	67.0	0.71	34.9	102.61	52.1	0.6

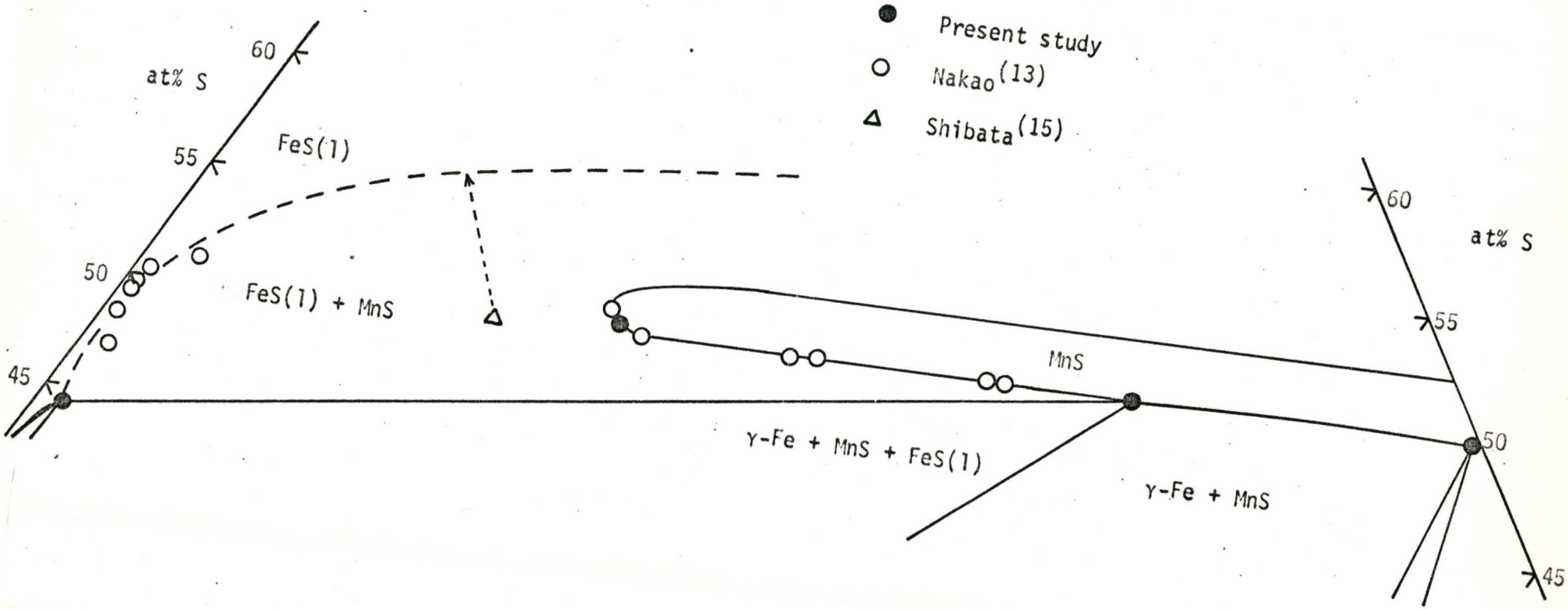

Figure 7.4 The pseudo-binary region of the 1300°C isotherm in the Fe-Mn-S ternary system.

high temperatures there are no other stable phases* other than the liquid phase and the gaseous sulphur phase, the latter occurring at the pure sulphur corner, then the liquidus curve of the two-phase region must swing behind the solid MnS phase and traverse the isotherm to the Mn-S binary as indicated by the dashed line in Figure 7.4.

The foregoing construction supports our earlier statement that a true pseudo-binary between the stoichiometric compounds, FeS and MnS, does not exist. If one is going to refer to a pseudo-binary between iron sulphide and manganese sulphide then one must write the terminal compounds as FeS_x and MnS_x such that the straight line between them on an isotherm coincides with a tie-line in the (FeS + MnS) two-phase region and that this line remains within the solubility fields of the FeS (solid or liquid) and MnS phases.

---

* It is known that the solid compounds FeS_2 and MnS_2 exist [4], but in all probability they have transformed to the liquid state at lower temperatures.

CHAPTER VIII

COMPILATION AND DISCUSSION OF RESULTS

A. A COMPILATION OF THE Fe-Mn-S ISOTHERMS

We present the Fe-Mn-S ternary system as a series of isotherms between and including 1200 and 1630°C in Figures 8.1 to 8.11. Each isotherm is representative of either a particular phase change or is characteristic of a temperature range between phase changes. Each isotherm will be briefly discussed with respect to the phases which are stable at that temperature and the distinguishing characteristic of that isotherm.

To facilitate the discussion, we emphasize now that all the binary solubility data is taken from the binary phase diagrams referenced in Chapter II. These data points are represented by a closed circle, ●, on each isotherm. The data points determined in the present study, and the data points uniquely calculated on the basis of information taken from the literature are represented by open circles, o. Regions on the isotherms which exhibit solubilities too low to be graphically presented are schematically drawn on the isotherms.

The solubility of Mn and S in liquid Fe, δ-Fe, and γ-Fe are given by the following three semi-empirical equations in which K is the solubility product, $X_{Mn}\ X_S$, for solid stoichiometric MnS in equilibrium with the respective Fe phase.

liquid Fe $$K = 14.08 \exp\left(-40{,}100 \frac{\text{cal}}{\text{mole}} / RT\right) \qquad (8\text{-}1)$$

δ-Fe $$K = 0.53 \exp\left(-40{,}900 \frac{\text{cal}}{\text{mole}} / RT\right) \qquad (8\text{-}2)$$

$$\gamma\text{-Fe} \qquad K = 0.16 \exp\left(-41{,}720 \frac{\text{cal}}{\text{mol}} / RT\right) \tag{8-3}$$

Equation 8-1 is determined from the combined data of Meyer and Schulte[26], Korber and Oelsen[29], and Sherman and Chipman[32]. It is noted that the phase in equilibrium with liquid Fe is the S and Mn rich liquid L_{II} which is unstoichiometric MnS. In principle a more complicated equation should be used for this K. However, since the composition of L_{II} is close to MnS, and since the tie-line direction remains very closely the same, we suppose that equation 8-1 is a sufficiently good approximation. Equation 8-3 is derived via the solubility theory of Chapter III and the experimental data of Turkdogan et al[9]. Equation 8-2 is an estimate. The enthalpy term is taken as the average of the δ-Fe and liquid Fe enthalpy terms. Using this enthalpy term and the composition point $X^P_{Mn} = 0.0171$ and $X^P_S = 0.000322$ (see Chapter V) we can calculate the leading coefficient in equation 8-2.

We can obtain a check on the enthalpy term , 2Q, in the exponent of the equations by comparison with values estimated from thermo-chemical data. The solubility of Mn and S in liquid Fe can be chemically described by adding together the following three reactions and their associated standard free energies of reaction.

$$Mn\ (l) + \frac{1}{2} S_2(g) = MnS(S); \quad \Delta F_1^\circ \tag{8-4}$$

$$[Mn] = Mn(l); \quad \Delta F_2^\circ \tag{8-5}$$

$$[S] = \frac{1}{2} S_2(g); \quad \Delta F_3^\circ \tag{8-6}$$

The addition gives

$$[Mn] + [S] = MnS(S) \; ; \quad \Delta F^\circ \qquad (8\text{-}7)$$

where

$$\Delta F^\circ = \Delta F_1^\circ + \Delta F_2^\circ + \Delta F_3^\circ \qquad (8\text{-}8)$$

and

$$\Delta F_1^\circ = -69{,}300 + 19.19\,T \qquad (71)$$

$$\Delta F_2^\circ = 9.11T \qquad (72)$$

$$\Delta F_3^\circ = 31{,}520 - 5.27T \qquad (73)$$

Since these all have the standard form $\Delta F_i^0 = \Delta H_i^0 - T\,\Delta S_i^0$ we infer that

$$\Delta H^0 = \Sigma \Delta H_i^0 = -69{,}300 + 31{,}520 = -37{,}780 \text{ cal/mole}$$

Now since ΔH^0 is expressed per mole of product MnS, and since Q is expressed per 1/2 mole of product MnS (1/2 mole of reactants Mn and S in solution), therefore

$$Q = \Delta H/2 = -18{,}890 \text{ cal/mole}$$

This is to be compared with the value from equation 8-1, viz.,

$$Q = -40{,}100/2 = -20{,}050 \text{ cal/mole}$$

which is a satisfactory check, if not a precise one. There is no way of knowing whether the discrepancy lies in the solubility or thermo-chemical data.

The 1630°C Isotherm

Stable Phases: Liquid L_I (low sulphur content)

Liquid L_{II} (high sulphur content)

Characteristic: A large miscibility gap emanating from the Mn-S binary and penetrating into the Fe corner covers most of the isotherm. The tie-line directions in the miscibility gap are indicative of the Fe-MnS phase equilibria at lower temperatures. The tie-lines radiate from the Mn and S rich liquid L_{II} to span the entire Fe-Mn liquid solution range up to the tie-line z. At the tie-line z the remaining tie-lines become more evenly distributed until immiscibility disappears at K.

The 1600°C Isotherm

Stable Phases: Liquid L_I, Liquid L_{II}, MnS (M.P. 1610°C)

Characteristic: The MnS phase has crystallized but it is not in direct contact with the miscibility gap. The limits of the miscibility gap have been determined by Meyer and Schulte[26], Korber and Oelsen[29] and Sherman and Chipman [32] at 1600°C and are represented on the isotherm. The tie line z is estimated from this data to have the terminal compositions,

L_I (4.5 at% Mn, 0.7 at% S) and L_{II} (7 at% Fe, 46 at% S)

The 1575°C Isotherm

Stable Phases: Liquid L_I, Liquid L_{II}, MnS.

Characteristics: 1575°C is just below the Mn-S binary monotectic reaction temperature (1580°C). The direct reaction between solid MnS and L_I has occurred which results in the formation of the three-phase triangle (L_I + L_{II} + MnS). The L_I corner moves across the isotherm with decreasing temperature until it penetrates deep into the Fe-corner of the isotherm above the melting point of Fe.

The 1530°C Isotherm

Stable Phases: Liquid L_I, Liquid L_{II}, MnS, δ-Fe (M.P. 1535°C)

Characteristics: The δ-Fe phase has just crystallized, but it has not reacted directly with the MnS phase.

The 1509°C Isotherm

Stable Phases: Liquid L_I, Liquid L_{II}, Liquid L_{III}, MnS, δ-Fe

Characteristics: At 1509°C the δ-Fe and MnS directly react with each other as a true pseudo-binary eutectic reaction along the common tie-line P-C-MnS. The eutectic composition at C is 2.45 at% Mn and 0.771 at% S.

The 1500°C Isotherm

Stable Phases: Liquid L_I, Liquid L_{II}, Liquid L_{III}, MnS, δ-Fe.

Characteristics: The common tie-line at 1509°C has split into the three-phase fields (δ-Fe + MnS + L_I) and (δ-Fe + MnS + L_{III}), and the two-phase field (δ-Fe + MnS).

The 1470°C Isotherm

Stable Phases: Liquid L_I, Liquid L_{II}, Liquid L_{III}, MnS, δ-Fe, γ-Fe.

Characteristics: The γ-Fe has interjected itself from the Fe-Mn binary through the peritectic reaction at 1472°C creating the three phase field (δ-Fe + γ-Fe + L_{III}), and the (δ-Fe + γ-Fe) and (γ-Fe + L_{III}) two-phase fields.

The 1465°C Isotherm

Stable Phases: L_I, L_{II}, L_{III}, MnS, δ-Fe, γ-Fe.

Characteristics: The three-phase fields (δ-Fe + MnS + L_{III}) and (δ-Fe + γ-Fe + L_{III}) meet and split into the (δ-Fe + γ-Fe + MnS) and (γ-Fe + MnS + L_{III}) three-phase fields through a four-phase equilibrium. The temperature, 1465°C, is an estimate based on the argument that it must lie just

below the Fe-Mn binary peritectic temperature.

The 1370°C Isotherm

Stable Phases: L, L_{III}, MnS, δ-Fe, γ-Fe.

Characteristics: The (L_I + L_{II}) two-phase liquid miscibility gap, a remnant of the higher temperature miscibility gap, disappears along with its associated phase fields, and the single liquid L is now essentially liquid FeS.

Also the three phase fields (δ-Fe + γ-Fe + MnS) and (δ-Fe + γ-Fe + L) have met and split into the (δ-Fe + γ-Fe + L) and (γ-Fe + MnS + L) three-phase fields through a four-phase equilibrium. Again this temperature of transition is an estimate based on the argument that it must lie just above the binary Fe-S extectic temperature at 1365°C.

The 1360°C Isotherm

Stable Phases: L, L_{III}, MnS, δ-Fe.

Characteristics: The δ-Fe phase has disappeared through the Fe-S binary extectic reaction at 1365°C.

The 1300°C Isotherm

Stable Phases: L, L_{III}, MnS, γ-Fe

Characteristics: This isotherm is representative of the entire austenitic temperature range where the only phases present are L, L_{III}, MnS, and γ-Fe.

At 1244°C Mn crystallizes; at slightly less than 1232°C (the Mn-Fe binary eutectic reaction temperature) the liquid L_{III} disappears through the ternary eutectic reaction L_{III} = γ-Fe + MnS + Mn; at 1188°C the lowest melting point constituent $FeS_{1.09}$ crystallizes; and at slightly less than 988°C (the Fe-S binary eutectic reaction temperature) the liquid L disappears through the ternary reaction L = γ-Fe + MnS + FeS.

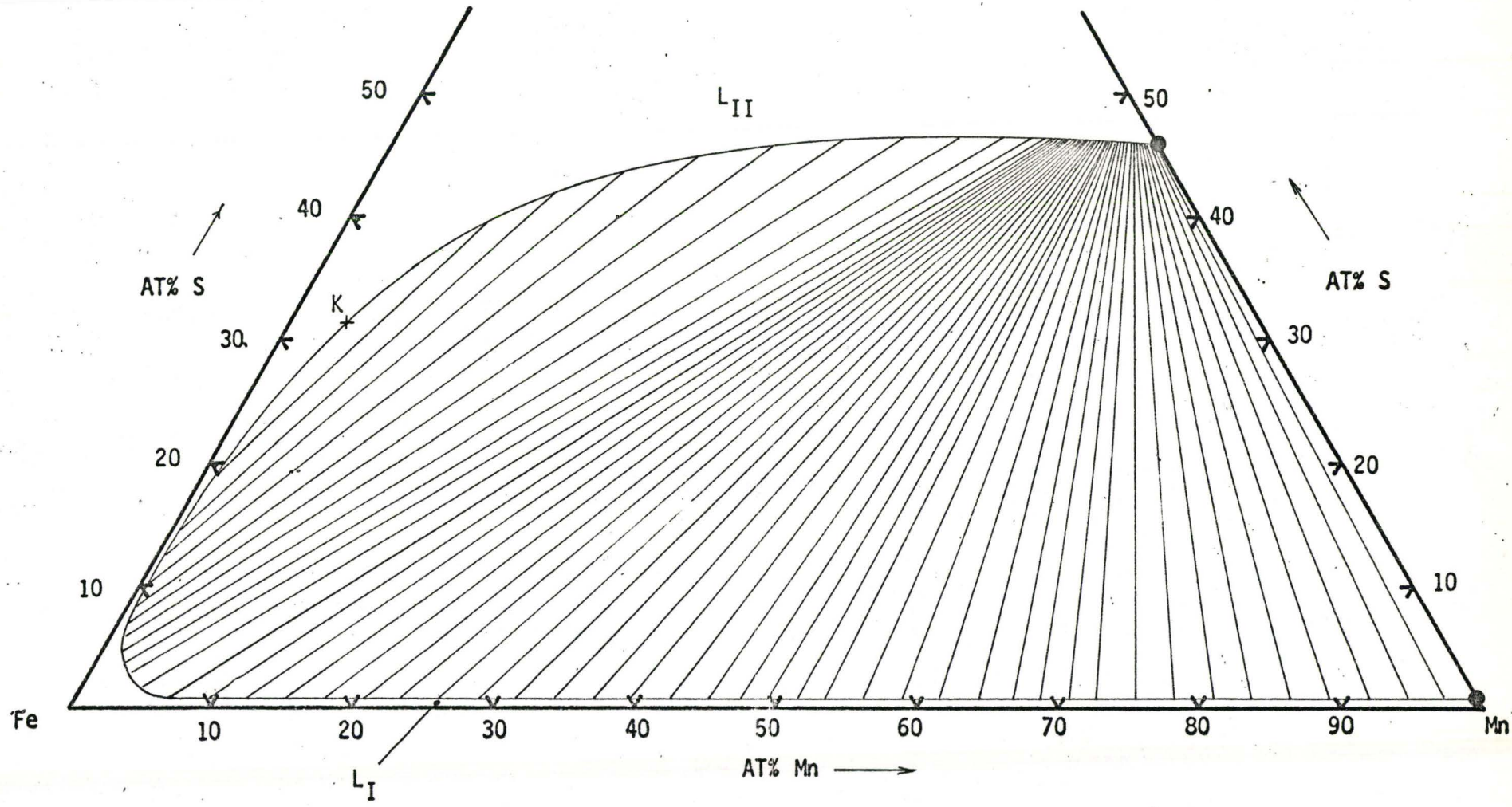

Figure 8.1 The 1630°C isotherm for the Fe-Mn-S system.

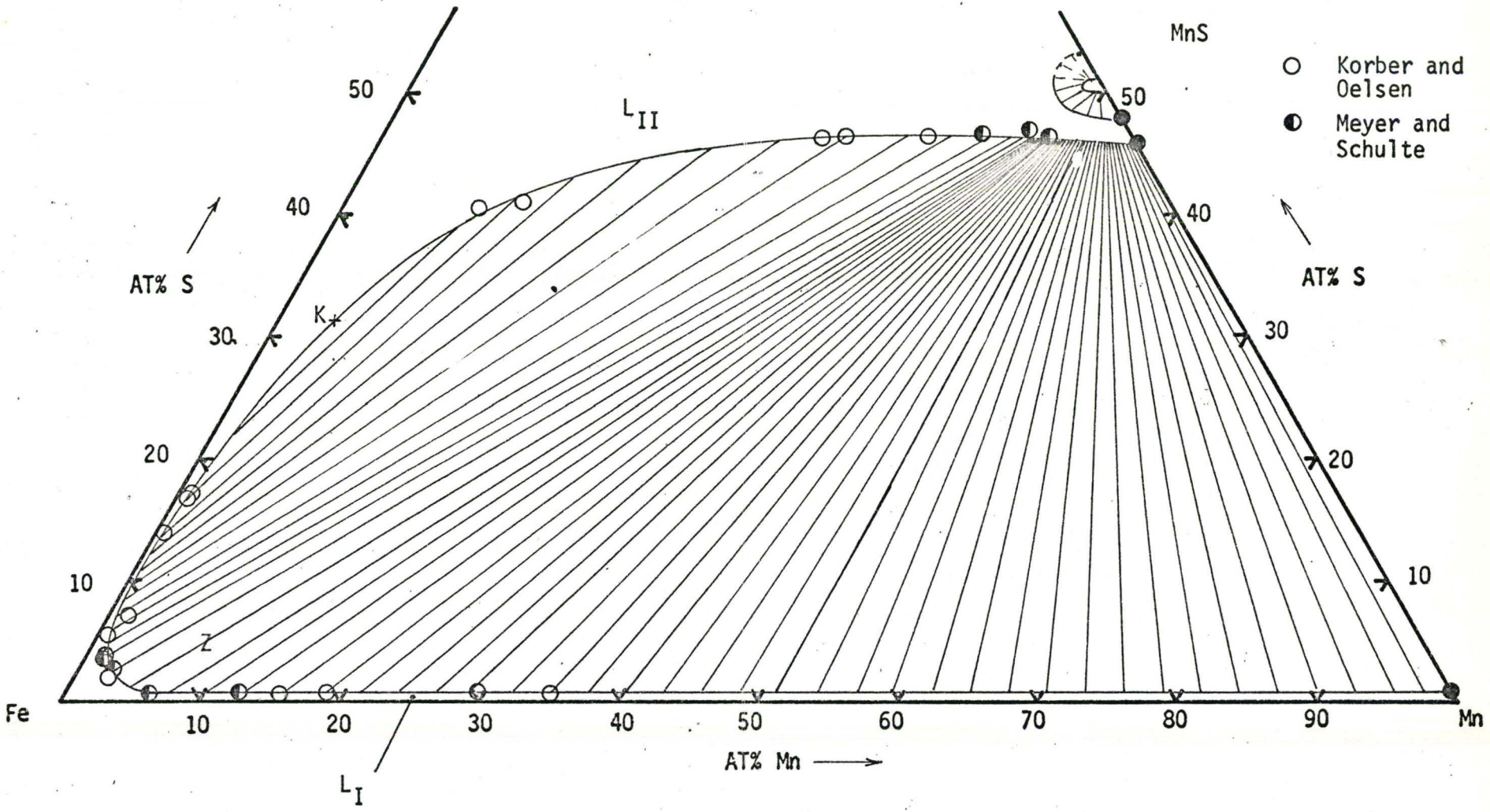

Figure 8.2 The 1600°C isotherm for the Fe-Mn-S system.

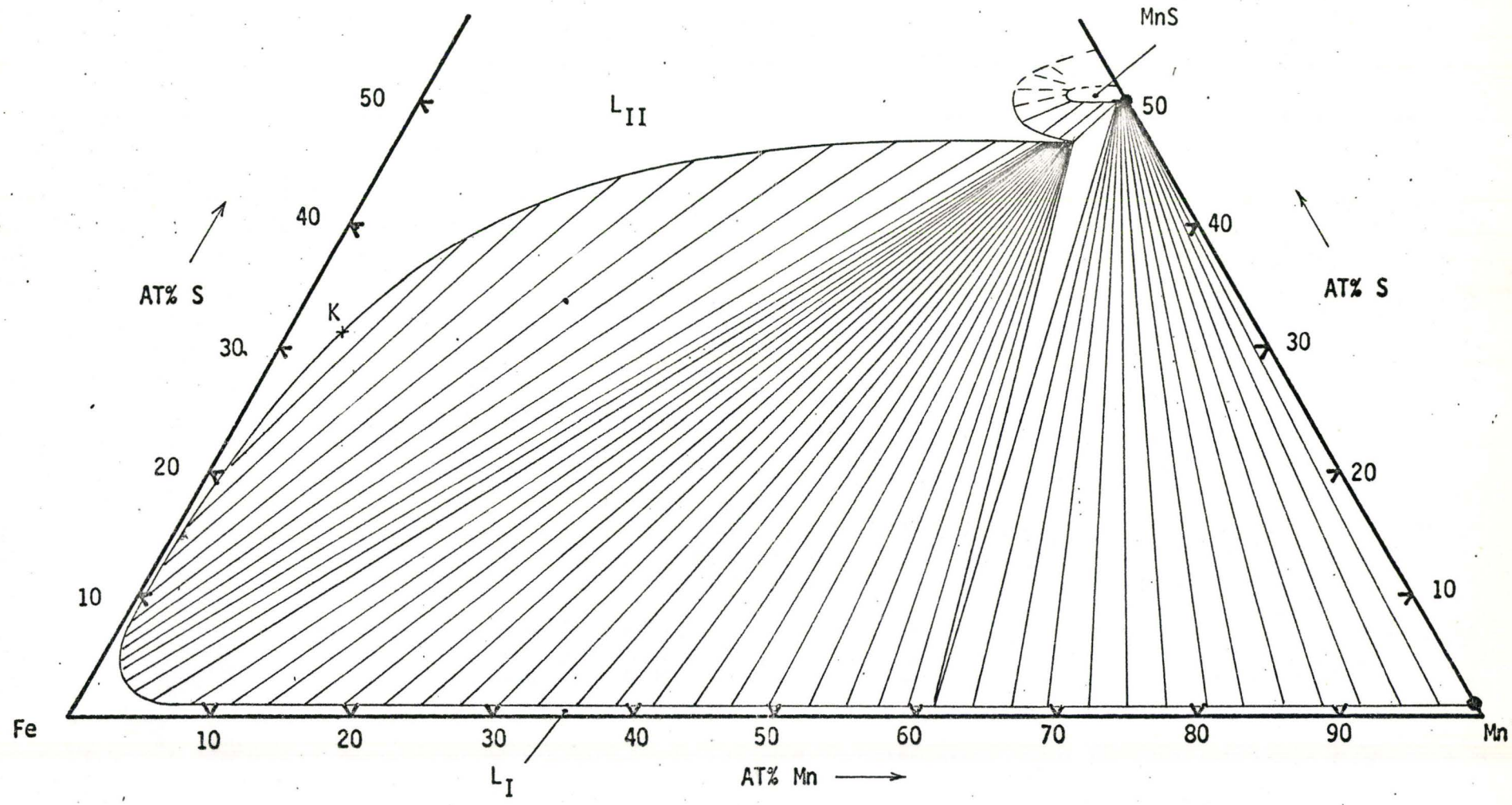

Figure 8.3 The 1575°C isotherm for the Fe-Mn-S system.

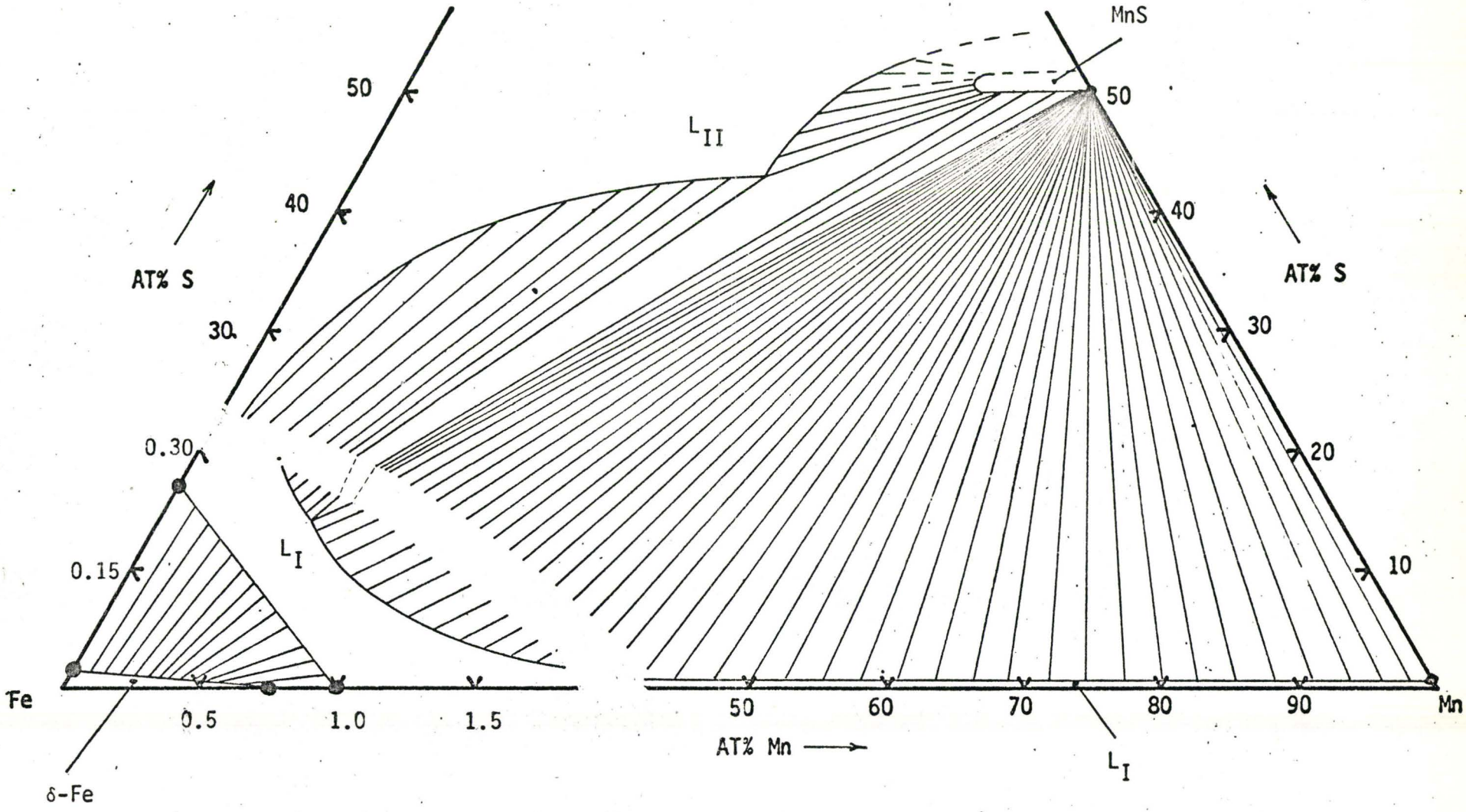

Figure 8.4 The 1530°C isotherm for the Fe-Mn-S system.

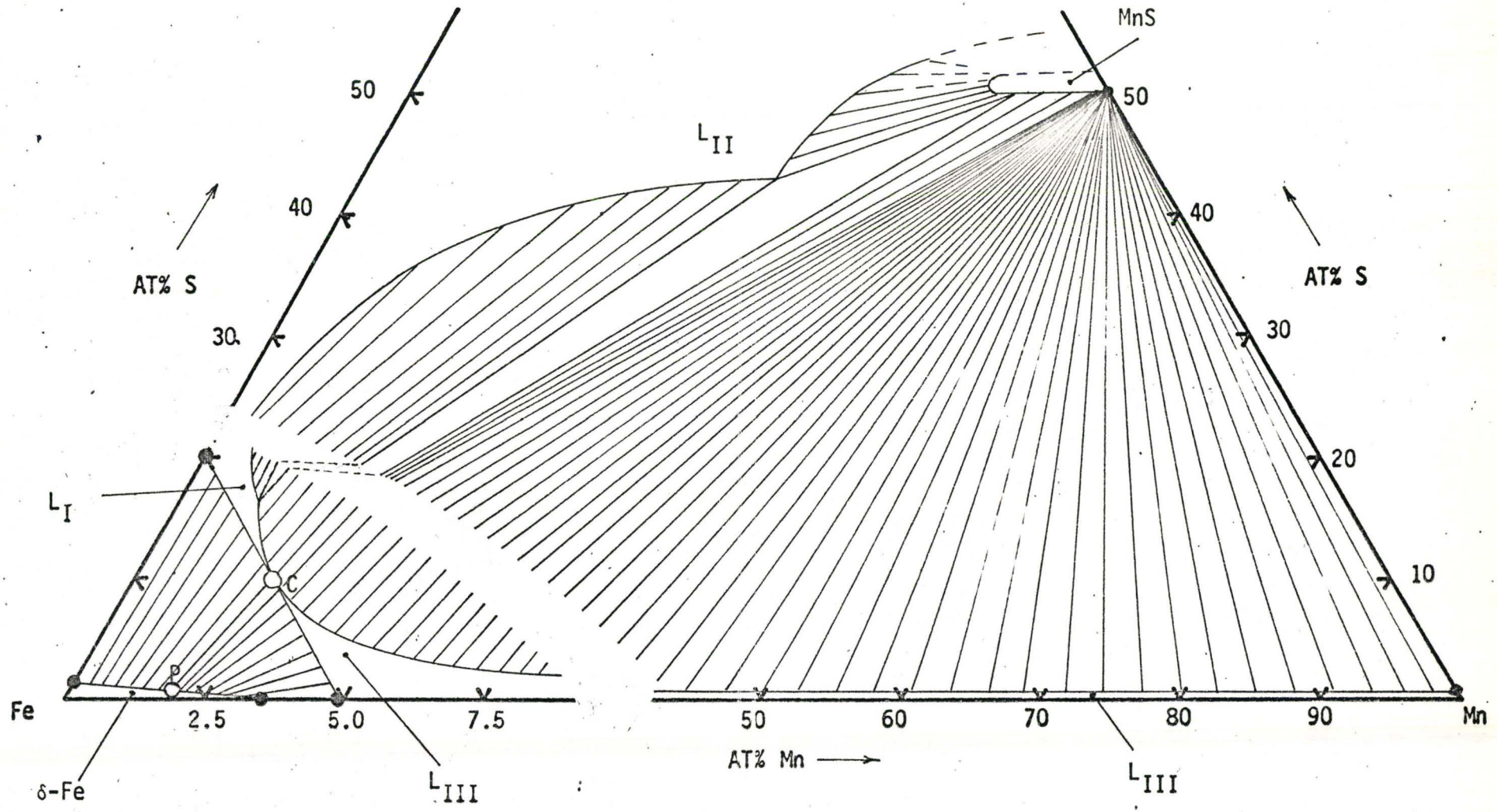

Figure 8.5 The 1509°C isotherm for the Fe-Mn-S system.

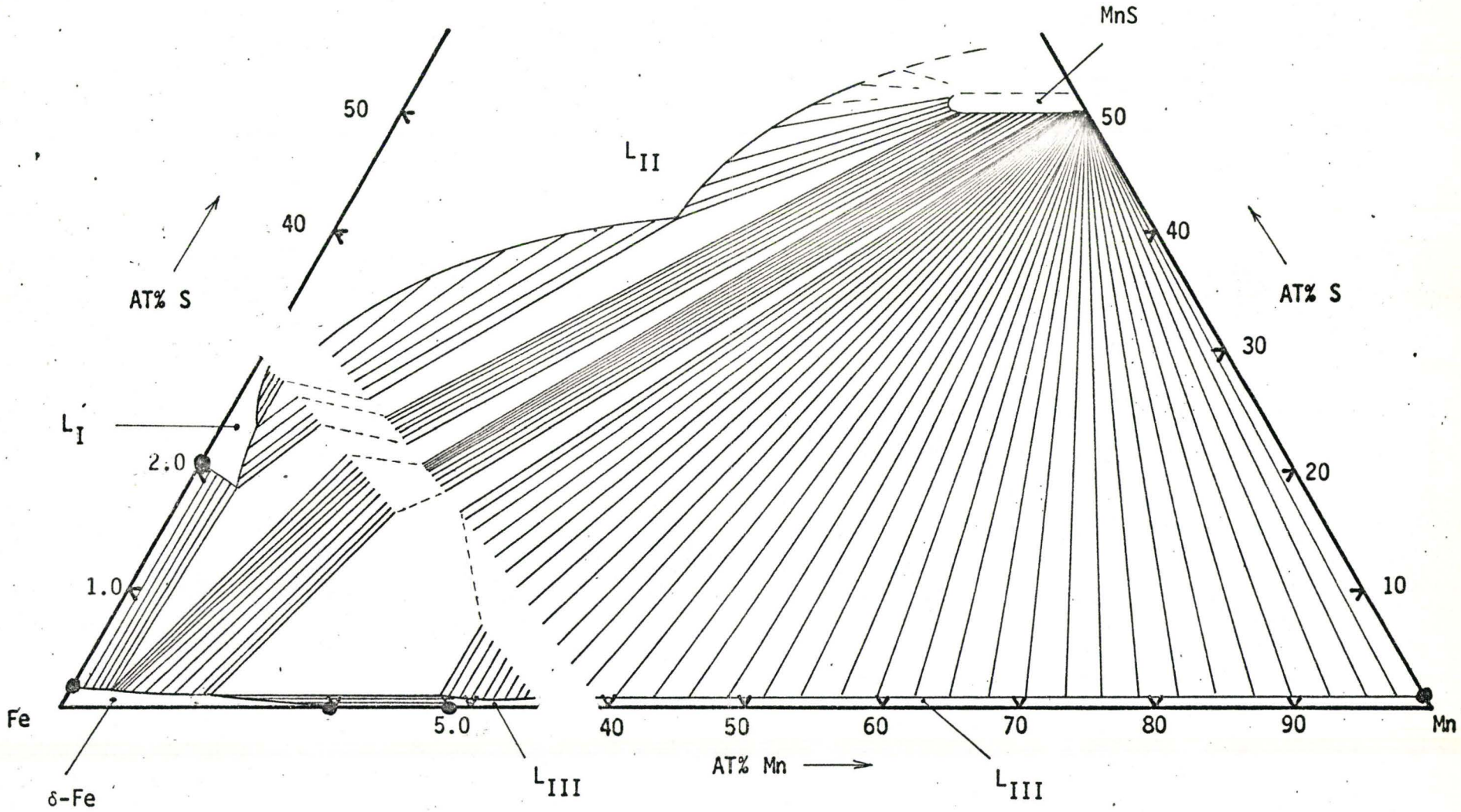

Figure 8.6 The 1500°C isotherm for the Fe-Mn-S system.

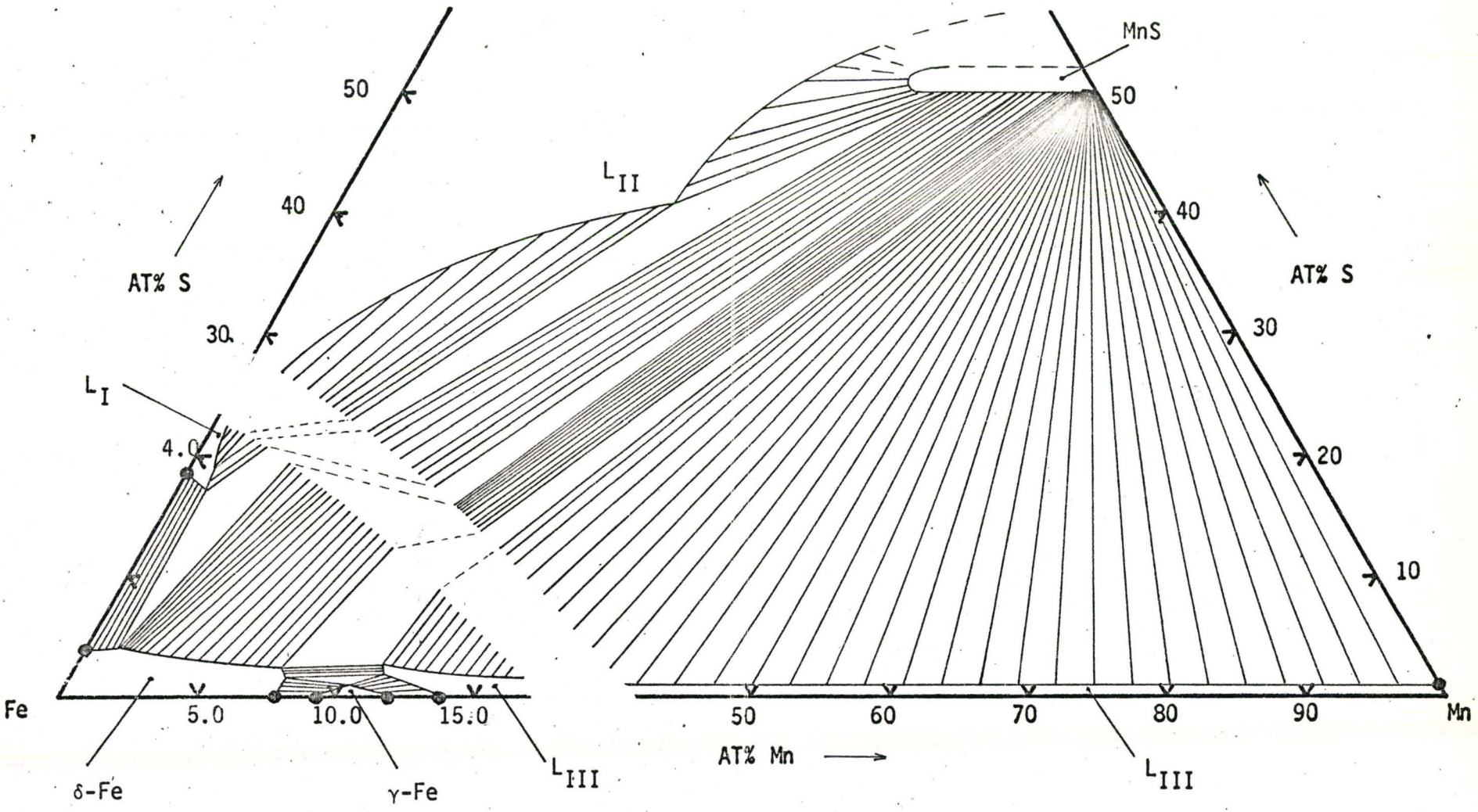

Figure 8.7 The 1470°C isotherm for the Fe-Mn-S system.

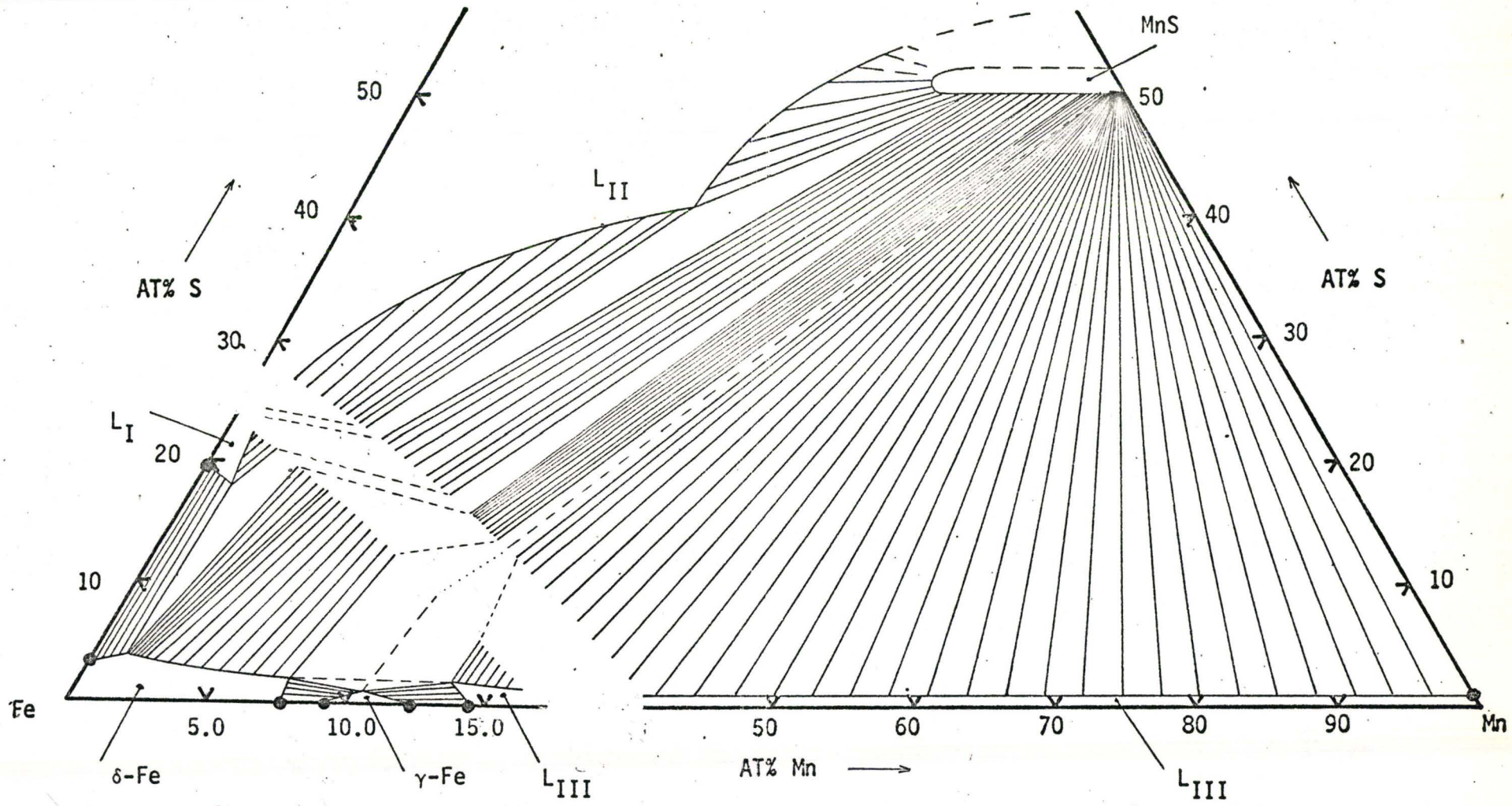

Figure 8.8 The 1465°C isotherm for the Fe-Mn-S system.

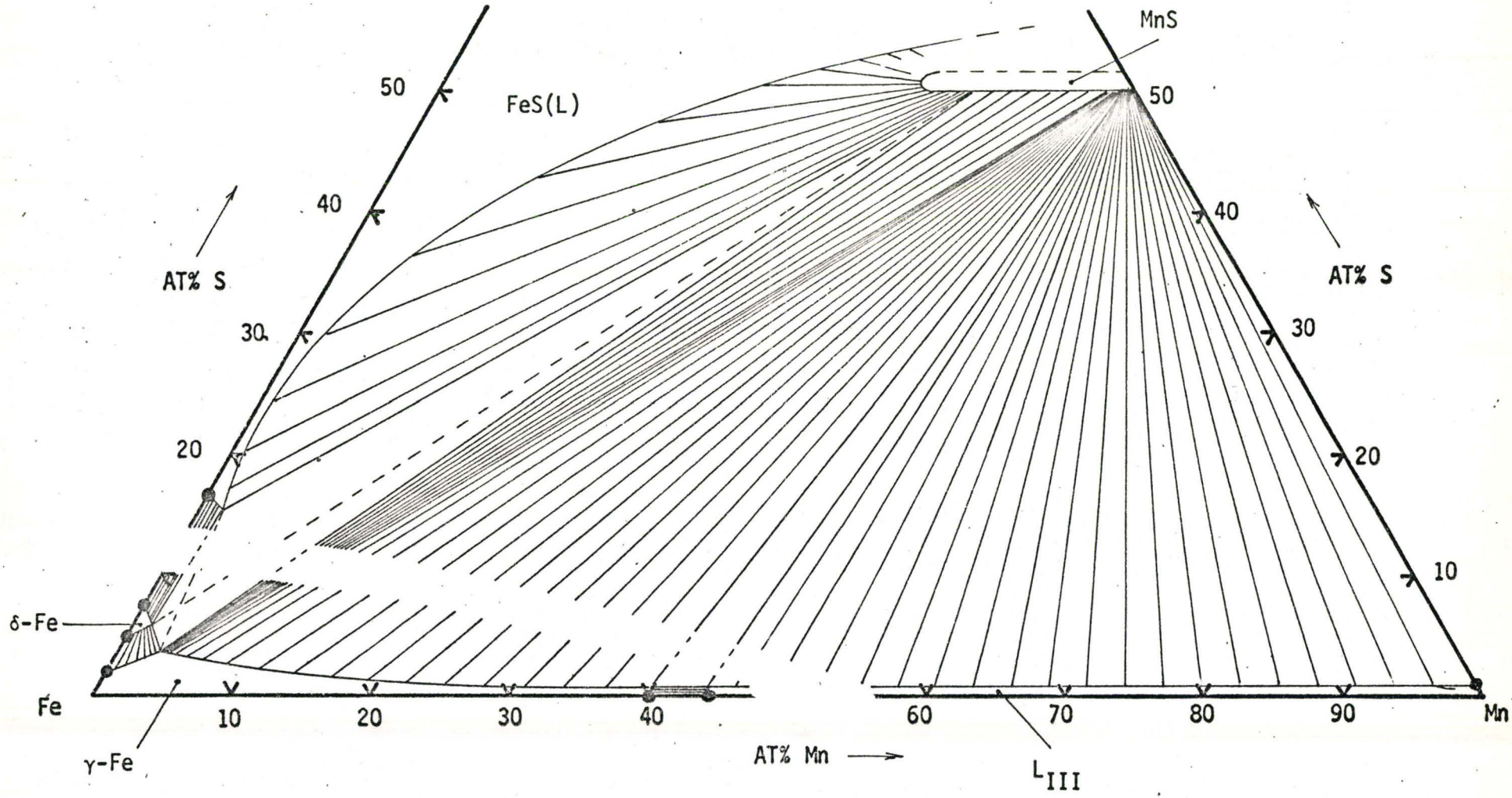

Figure 8.9 The 1370°C isotherm for the Fe-Mn-S system

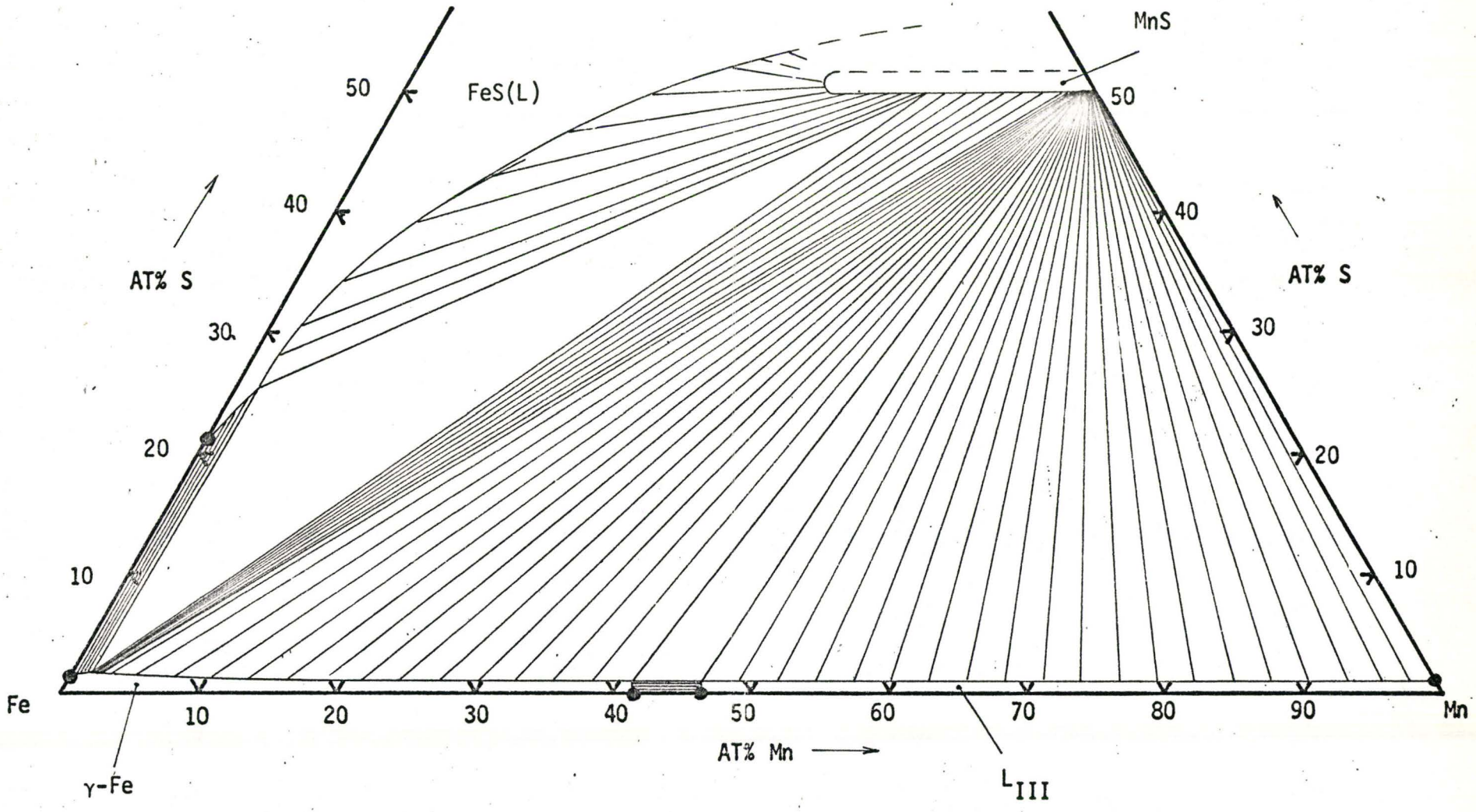

Figure 8.10 The 1360°C isotherm for the Fe-Mn-S system.

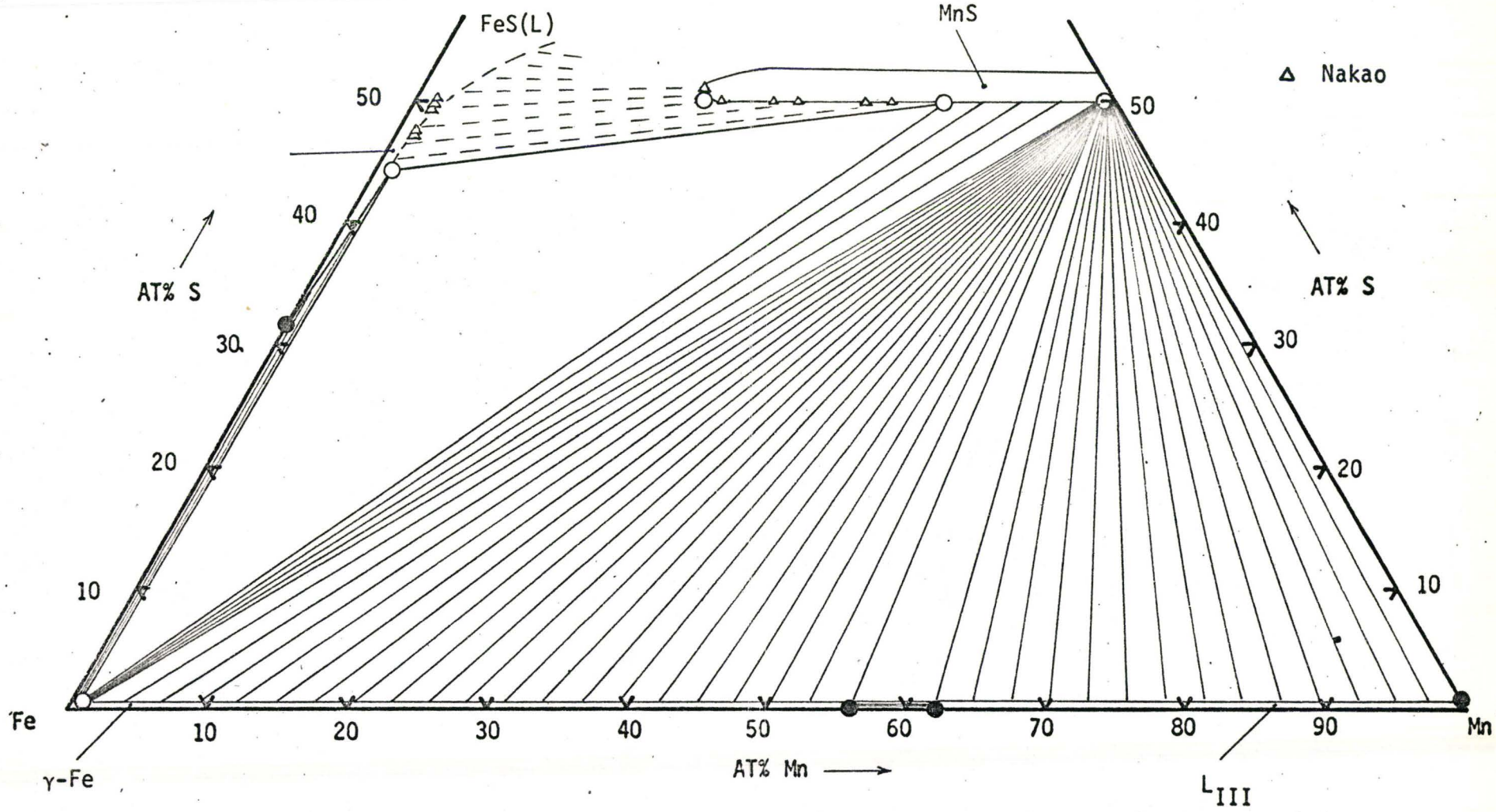

Figure 8.11 The 1300°C isotherm for the Fe-Mn-S system.

B. THE Fe-Mn-S SYSTEM AND COMMERCIAL STEELS

B.1. The Significance of the Eutectic Trough Maximum

In our literature review attention was drawn to the practical significance of the temperature and composition at which δ-Fe first directly reacts with MnS. It was stated that during the solidification of an Fe-Mn-S alloy, the remaining liquid becomes enriched in Mn and S. When the composition of the liquid reaches the eutectic trough, the further solidification of this liquid must be in the downward direction of the eutectic trough. Depending on which side of the tie-line PC in Figure 5.17 this occurs, the direction is either towards lower S and higher Mn contents, or towards higher S and lower Mn contents. We can now investigate this quantitatively by relating the tie-line PC to the Mn and S contents of commercial carbon steels. A cursory perusal of steel specifications shows us that the vast majority of carbon steels have nominal Mn and S contents which lie to the left of the tie-line PC as calculated for the ternary Fe-Mn-S system. This is illustrated in Figure 5.17 for typical low, medium, and high carbon steels. That is, based solely on our calculated tie-line, one would expect the solidification products of steels to contain FeS in all cases. However FeS is only observed as a room temperature phase in low carbon steels[74]. This result can be explained by examination of the quaternary effect of carbon on the Fe-Mn-S system and by noting the strong tendency for FeS to transform to MnS at temperatures below the liquidus.

B.1.1. The Quaternary Effect of Carbon on the Fe-Mn-S System

Experiments (see Chapter II) show that the solubility of Mn and S

in liquid iron decreases when carbon is added. Since the data is for carbon saturated iron we cannot make direct inferences as to the carbon composition dependence. However using solubility theory we can predict the functional dependence of the solubility product, K, on the carbon content.

In Appendix II the solubility theory of Chapter III was generalized to multi-component systems. For the four-component system, Fe-C-Mn-S, equation II-3 becomes

$$\left[\frac{X_{Mn}^{MnS}}{X_{Mn}} + f_{Mn}\right] dX_{Mn} + \left[\frac{X_S^{MnS}}{X_S} + f_S\right] dX_S + \left[\frac{X_C^{MnS}}{X_C} + f_C\right] dX_C = 0 \qquad (8\text{-}9)$$

where f_i (i = Mn, S, C) is defined by equation II-4. Since carbon has negligible solubility in MnS[12], then $X_C^{MnS} = 0$, and the integrated form of equation 8-9 is

$$X_{Mn}^{MnS} \ln X_{Mn} + f_{Mn} X_{Mn} + X_S^{MnS} \ln X_S + f_S X_S + f_C X_C = \text{constant} \qquad (8\text{-}10)$$

Let the constant = (ln K)/2. For small X_{Mn}, X_S and X_C we see that the $f_{Mn} X_{Mn}$ and $f_S X_S$ terms are small compared to the respective ln terms and may be neglected. However there is no corresponding ln term for $f_C X_C$ and we must therefore retain this term. The integrated form of f_C contains quadratic and linear terms involving X_i. If we neglect the quadratic terms (because $X_i << 1$), then the approximate integrated form of equation II-4 for carbon is

$$f_C \simeq [(\varepsilon_C^{Mn} + 1) X_{Mn}^{MnS} + (\varepsilon_C^{S} + 1) X_S^{MnS} + (\varepsilon_C^{C} + 1) X_C^{MnS} - 1] X_C \qquad (8\text{-}11)$$

For $X_C^{MnS} = 0$, and $X_{Mn}^{MnS} = X_S^{MnS} = 0.5$ equation 8-11 reduces to

$$\ln X_{Mn} + \ln X_S + 2(\varepsilon_C^{Mn} + \varepsilon_C^S) X_C = \ln K \qquad (8\text{-}12)$$

Now the temperature dependence of K is given by $K = K_o \exp(2Q/RT)$, so equation 8-12 becomes

$$K = X_{Mn} X_S = K_o \, e^{\frac{2Q}{RT}} \, e^{-2X_C(\varepsilon_C^{Mn} + \varepsilon_C^S)} \qquad (8\text{-}13)$$

At 1560°C the values of ε_C^{Mn} and ε_C^S are -1.4 and 11.2, respectively[75]. Since these values do not change appreciably with temperature the solubility product for the liquid Fe-C-Mn-S system may be represented by

$$X_{Mn} X_S = 14.08 \, e^{\frac{-40,100}{RT}} \, e^{-19.6 X_C} \qquad (8\text{-}14)$$

Thus the effect on the solubility product of carbon additions is to lower K by reducing the effective value of K_o exponentially with X_C.

It now remains to show quantitatively how the temperature and composition at which MnS first directly reacts with δ-Fe is affected by carbon. To do this we utilize the theory outlined in Chapter V to calculate the ternary reaction temperature and compositions, T_C and (X_{Mn}^C, X_S^C), and to modify this to the quaternary case. Referring to Figure 8.12, an isothermal representation of the Fe corner of the Fe-C-Mn-S phase diagram, we observe that the δ-Fe solidus and liquidus are represented by planes (assuming the compositions are sufficiently low to adopt the binary approximations of the linear solidus and liquidus), and that the solubility equation defines a cylindrical surface. In Figure 8.12

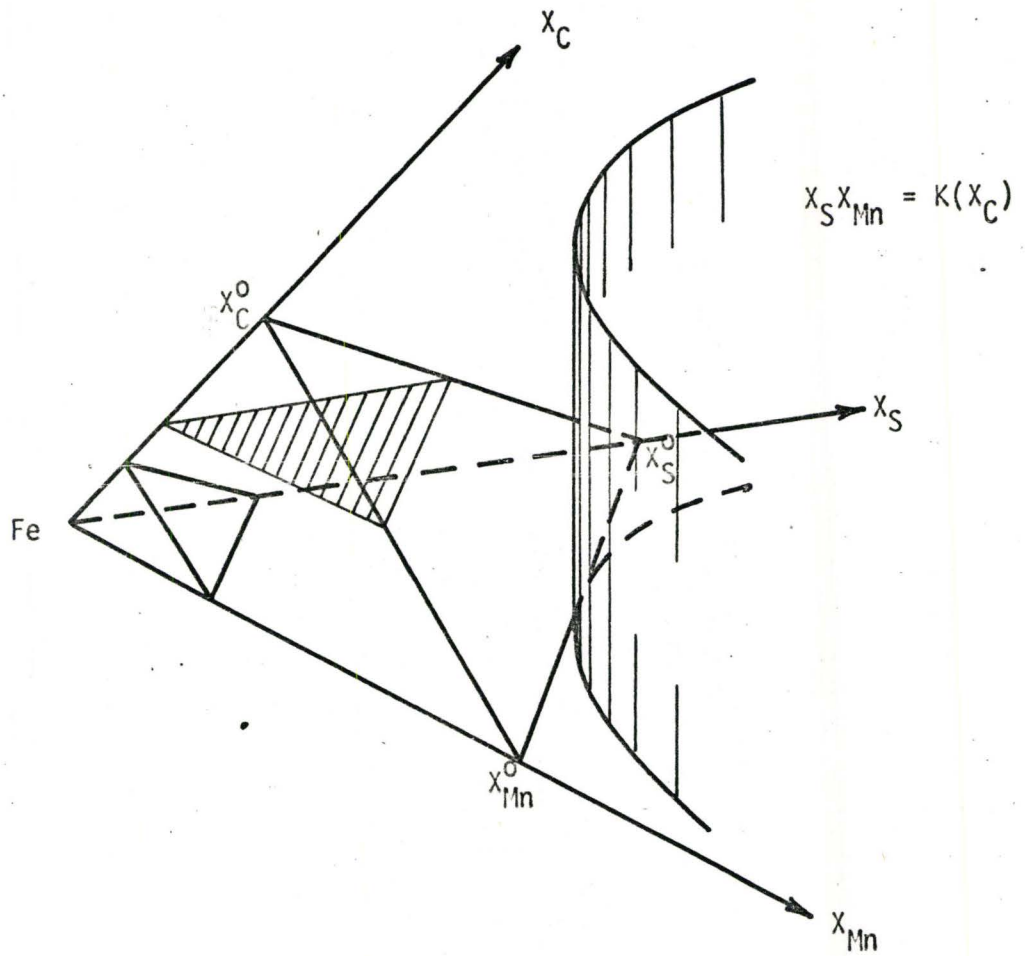

Figure 8.12 A schematic representation of the δ-Fe corner of the Fe-C-Mn-S quaternary system at 1509°C.

we show the solubility curve tangent to the liquidus at $X_C = 0$. To deduce the temperature and composition at which the reaction first occurs in the quaternary at a carbon concentration $< X_C^o$ we describe the liquidus plane as

$$\frac{X_{Mn}}{X_{Mn}^o} + \frac{X_S}{X_S^o} + \frac{X_C}{X_C^o} = 1 \qquad (8\text{-}15)$$

where the X_i^o are the binary Fe-i liquidus compositions of the solutes i. The solubility product surface is described by equation 8-13. Following the procedure of Chapter V we eliminate X_S between equations 8-13 and 8-15 giving

$$X_{Mn}^2 \, (X_S^o \, X_C^o) + X_{Mn} \, (X_{Mn}^o \, X_S^o) \, (X_C - X_C^o) + K = 0 \qquad (8\text{-}16)$$

For tangency of the two surfaces at constant X_C we require a single valued solution of X_{Mn} in equation 8-16. Since this occurs at the temperature T_C, then $X_{Mn} = X_{Mn}^C$, and the solution is

$$X_{Mn}^C = \frac{X_{Mn}^o}{2} \, \frac{(X_C^o - X_C)}{X_C^o} \qquad (8\text{-}17)$$

and similarly

$$X_S^C = \frac{X_S^o}{2} \, \frac{(X_C^o - X_C)}{X_C^o} \qquad (8\text{-}18)$$

We note that when $X_C = 0$, equations 8-17 and 8-18 reduce to the ternary compositions derived in Chapter V. (When comparing, note that the binary

liquidus compositions are written in Chapter V as $X_i^o + a$).

For tangency we also require that the slopes of the two surfaces dX_S/dX_{Mn} at constant X_C, be equal. The slope of the liquidus plane

$$\left.\frac{dX_S}{dX_{Mn}}\right|_{X_C = \text{const.}} = -\frac{X_S^o}{X_{Mn}^o} \tag{8-19}$$

and the slope of the liquidus surface is

$$\left.\frac{dX_S}{dX_{Mn}}\right|_{X_C = \text{const}} = -\frac{K}{X_{Mn}^2} = -\frac{4K}{X_{Mn}^{o2}}\left[\frac{X_C^o}{X_C^o - X_C}\right]^2 \tag{8-20}$$

Equating relations 8-19 and 8-20 gives

$$4K = X_S^o \; X_{Mn}^o \left[\frac{X_C^o - X_C}{X_C^o}\right]^2 \tag{8-21}$$

Again we note that when $X_C = 0$, equation 8-21 reduces to the ternary case.

Of course K, X_S^o, X_{Mn}^o, and X_C^o are functions of temperature, all but X_C^o being previously defined by equations 8-13, 5-32, and 5-33, respectively. The temperature dependence of X_C^o is

$$X_C^o = \frac{T-1535}{L} \tag{8-22}$$

where L is the slope of the liquidus on the Fe-C binary phase diagram. Therefore, at T_C and at constant X_C we have

$$4K_o \, e^{\frac{2Q}{RT_C}} \, e^{-2X_C(\varepsilon_{Mn}^C + \varepsilon_S^C)} = \frac{(T_C - 1535)^2}{MN}\left[\frac{\frac{T_C - 1535}{L} - X_C}{\frac{T_C - 1535}{L}}\right]^2 \tag{8-23}$$

By identifying the left hand side of 8-23 as $F_1(T,X_C)$ and the right hand side as $F_2(T,X_C)$, we can graphically determine T_C as the temperature of intersection of F_1 and F_2 when each is plotted as a function of temperature at constant X_C. For physical solutions T_C must be less than 1535°C, and $X_C \leq X_C^o$. We see from Figure 8.12 that when $X_C > X_C^o$, the Fe is still liquid. The graphical solution is illustrated in Figure 8.13 for various values of X_C up to $X_C = 0.0362$ (0.8 wt.% C). We note that as X_C increases, T_C decreases, a result which one expects intuitively.

To show the effect of carbon additions on X_{Mn}^C we substitute equations 5-33 and 8-22 into 8-17, which yields after simplification

$$X_{Mn}^C = \frac{T_C - 1535 - X_C L}{2N} \qquad (8\text{-}24)$$

Using the values of T_C and X_C from Figure 8.13 we can calculate X_{Mn}^C. The results are plotted in Figure 8.14, and up to $X_C = 0.036$ we see that equation 8-24 can be empirically represented as

$$X_{Mn}^C = 2.45 - 2X_C \qquad (8\text{-}25)$$

The result is that X_{Mn}^C, (and similarly X_S^C), does not change as greatly as qualitative inferences in the literature would imply (see Chapter II). In fact the Mn composition at which δ-Fe first reacts with MnS in a 0.8 wt.%C alloy (the eutectoid Fe-C composition)is only 40% less than the Fe-Mn-S ternary value while T_C has only decreased from 1509° to 1455°C. Thus the tie-line PC for the quaternary Fe-C-Mn-S system remains well to the right of the nominal Mn and S contents found in carbon steels.

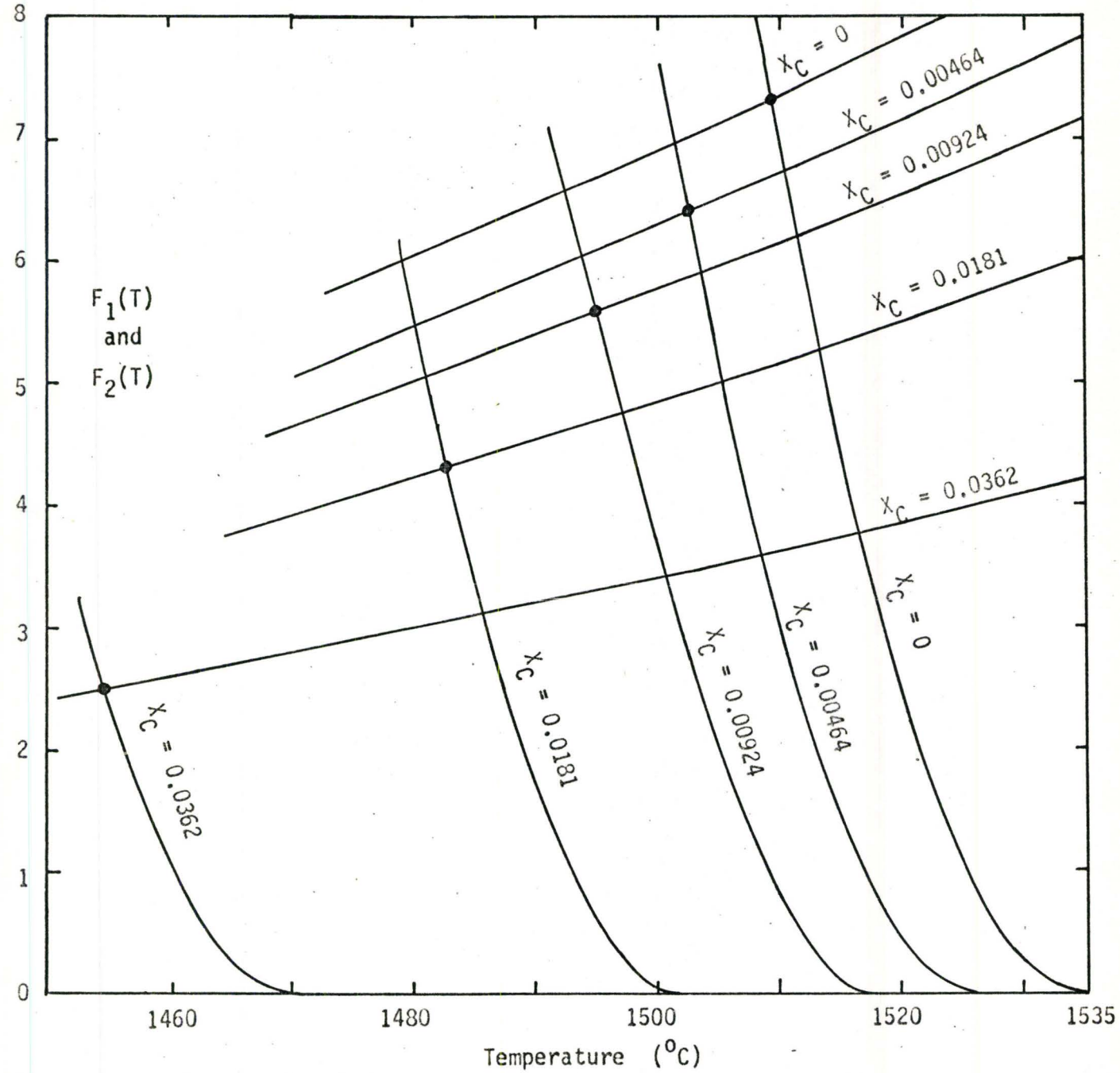

Figure 8.13 The effect of carbon on the upper eutectic, T_C, in the Fe-C-Mn-S system.

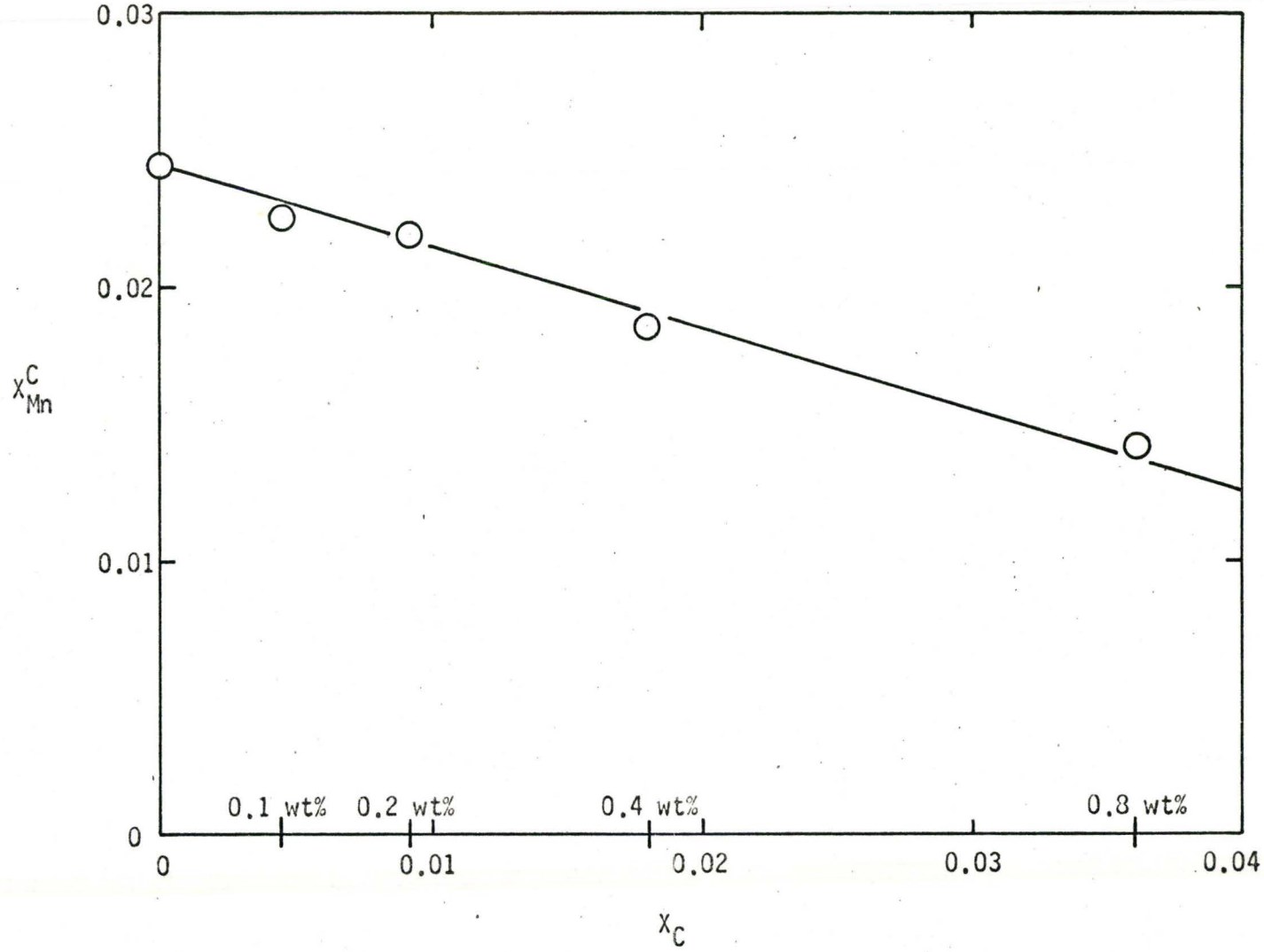

Figure 8.14 The variation of X^C_{Mn} (at T_C) with the carbon content X_C.

Having semi-quantitatively deduced the effect of carbon on the eutectic trough maximum we can return to discussion of the significance of this point in relation to sulfide formation. The results imply that, even though the temperature of point C in Figure 5.17 decreases with increasing carbon content, the composition of point C, and thus the tie-line PC, does not drastically change. This means that the nominal Mn and S compositions of typical low and medium carbon steels is still to the left of the tie-line PC, and consequently these steels will evolve liquid FeS as a high temperature solidification product. This is contrary to the accepted view, first discussed by Wentrup[30], that the amount of Mn added to these steels is such that solid MnS is formed as one of the solidification products. The fact that FeS is seldom observed as a room temperature phase in steels implies that the transformation of the FeS to MnS occurs during the subsequent cooling of the alloy.

Before discussing this transformation we should point out that, although the preceding analysis cannot be strictly applied to high carbon steels (i.e, beyond the limits of the theoretical assumptions and approximations), we believe that the trend of decreasing T_C and (X^C_{Mn}, X^C_S) continues. Thus the tie-line PC would probably approach the nominal Mn and S contents for commercial high carbon steels. Certainly for cast irons, the tie line PC should be well to the left of their nominal compositions indicating that solid MnS will be a direct solidification product.

It should be emphasized that this analysis applies strictly to the quaternary Fe-C-Mn-S system, and does not consider the effects of other solute elements normally found in commercial steels. In particular, oxygen is known to form the very stable oxide, MnO, which in turn, exhibits a

eutectic reaction with MnS at lower temperatures. Oxygen as an impurity has an exceptionally strong effect on the morphology of sulfide precipitates, and undoubtedly has a significant effect on the constitution.

B.2. The Process of FeS Inclusion Formation

The proposition that the nominal Mn and S contents of commercial carbon steels lie to the left of the tie line PC in the Fe-Mn-S and Fe-C-Mn-S systems implies that during solidification the composition of the liquid below T_C tends to follow the eutectic trough between point C and the ternary eutectic near pure FeS at a temperature <988°C. If the cooling rate is slow, as it would be towards the center of a large ingot, then the composition of the liquid will tend to remain in the eutectic trough becoming enriched in S and Fe while displacing Mn to the surrounding solid and building up its concentration there. At the ternary eutectic the remaining liquid is trapped as Fe and S rich inclusions. For fast cooling rates, the composition of the liquid initially enriched with S and Mn lags behind the equilibrium value and becomes supersaturated with respect to all components. The excess Mn and S can then precipitate out as MnS (with a high Fe content), the excess Fe and some of the Mn can precipitate on the quickly advancing δ-Fe front. Again some of the remaining FeS-rich liquid will be trapped in interdendritic sites.

Whether or not the cooling is fast or slow, one of the products will be an Fe and S rich liquid entrapped as inclusions behind the advancing front. As the temperature continues to fall the inclusions become supersaturated with respect to the surrounding iron alloy. This is illustrated in Figure 8.15 in which the inclusion composition is represented by point I in the (δ-Fe + MnS + L_I) three-phase field, and the surrounding alloy has

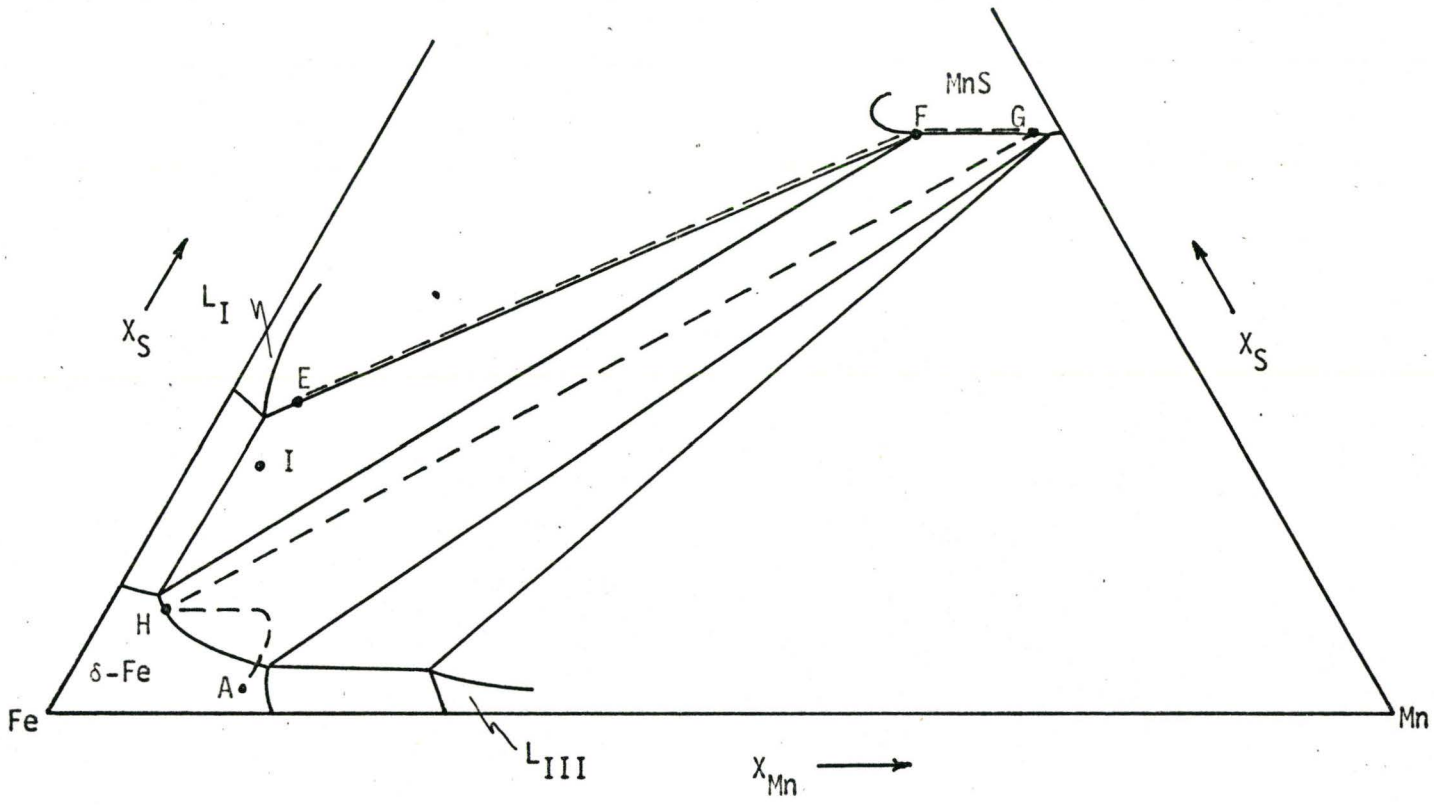

Figure 8.15 Schematic isotherm in the δ-Fe temperature range. An inclusion I surrounded by an alloy A transforms to the inclusion G along EFG and HA.

a nominal composition A. It is at this point that the liquid inclusion begins to transform to the more stable MnS inclusion. For this reason, and due to the prior Mn enrichment in the solid, this transformation occurs very quickly. This is why we invariably observe MnS inclusions in carbon steels at room temperature, and not FeS inclusions.

B.3. Calculation of the Rate of Transformation of an FeS Inclusion to a MnS Inclusion

Referring to Figure 8.15 we see that the Fe has a composition which should be in equilibrium with MnS, and not L_I. Thus Mn from the alloy will diffuse into the liquid inclusion and begin to transform it to MnS. If the inclusion is large enough the excess Fe may precipitate at the Fe/L_I interface as an Fe dendrite tip (the size of the inclusion must be appreciably greater than the characteristic diameter of the dendrite tip). If not, the Fe must diffuse out. In any event the inclusion will revert to a two phase inclusion, L_I + MnS, the mean composition being point E in Figure 8.15. (The former eventuality is sometimes observed as Fe islands or protrusions in MnS inclusions.)

At 1300°C our investigations show that cation diffusion in solid MnS is much faster than Fe or Mn diffusion in γ-Fe and of course this is true for liquid FeS as well. By extrapolation we can infer that the same relative magnitudes exist at δ-iron temperatures. Consequently the rate of transformation will be controlled by the diffusion rate of Mn (or Fe) in δ-Fe.

We therefore have a finite diffusion couple, defined by the inclusion and its surrounding, designated by composition points E and A, and as Mn diffuses into the inclusion, point E moves towards point F which is solid

MnS with dissolved Fe. From point F the MnS reduces its Fe content to G while the alloy content at the iron/inclusion interface remains roughly fixed at point H. This is in agreement with the tie-line directions in the (δ-Fe + MnS) two-phase field. The supersaturation of MnS in δ-Fe is not great enough to cause the internal precipitation which was observed at lower temperatures in the FeS:Fe-Mn diffusion couples. However it can create an iron interface instability if the precipitate is large enough to accommodate it.

To estimate the time necessary for this transformation we assume a spherical inclusion of radius r_o, and calculate the time necessary to supply Mn from an Fe-Mn alloy to the inclusion. Since the inclusion is roughly spherical the Mn is going to be supplied from a surrounding spherical volume of Fe-Mn alloy. The Mn gradient in this volume, starting at r_o and going to greater r, can be determined from the solution of Laplace's equation, $\nabla C^2 = 0$. (This assumes the iron/inclusion interface is stationary with time). The zeroth order solution for the concentration of Mn in the Fe-Mn alloy, C (mass/unit volume), is

$$C = a_1 + a_2/r \qquad (8\text{-}26)$$

For the boundary conditions

$$C = C^{\infty} \quad \text{at } r = \infty \quad \text{and } t = 0$$

$$C = C^{S} \quad \text{at } r = r \quad \text{and } t = t$$

the solution 8-26 becomes

$$C = C^{\infty} + (C^{S} - C^{\infty}) \frac{r_o}{r} \qquad (8\text{-}27)$$

Thus the concentration gradient, dC/dr, is

$$\frac{dC}{dr} = (C^{\infty} - C^{S}) \frac{r_o}{r^2} \qquad (8\text{-}28)$$

Since we are interested in the gradient next to the inclusion, we evaluate dC/dr at r_o, which gives

$$\left.\frac{dC}{dr}\right|_{r = r_o} = \frac{C^{\infty} - C^{S}}{r_o} \qquad (8\text{-}29)$$

The corresponding flux, J (mass/unit area/sec) of Mn diffusing to the inclusion is then

$$J = D \frac{C^{\infty} - C^{S}}{r_o} \qquad (8\text{-}30)$$

where D is the diffusion coefficient for Mn in Fe. The amount of Mn, M, diffusing across the iron/inclusion interface of area A at a time t is

$$M = At\,J$$

$$= (4\pi r_o^{\,2})(t)\, D \frac{(C^{\infty} - C^{S})}{r_o} \qquad (8\text{-}31)$$

This amount of Mn must equal the amount accumulated in the inclusion. As mentioned, the diffusion of Mn in liquid FeS and in solid MnS is considerably faster than in Fe. Consequently the inclusion concentration will always be at equilibrium, (i.e., no perceptible Mn and Fe gradients in the inclusion). Thus the amount of Mn in the inclusion is

$$M = (\text{volume of inclusion}) \times C_{Mn}^{MnS}$$

$$= \left(\frac{4}{3}\ \pi r_o^{\,3}\right) C_{Mn}^{MnS} \qquad (8\text{-}32)$$

where C_{Mn}^{MnS} is the concentration (mass/unit volume) of Mn in the MnS. Equating equations 8-31 and 8-32, and rearranging gives

$$t = \frac{1}{3} \frac{r_o^2}{D} \frac{C_{Mn}^{MnS}}{C^{\infty} - C^{S}} \qquad (8\text{-}33)$$

Consider a 10 micron diameter inclusion of liquid FeS containing no Mn, surrounded by a Fe-1 wt.% Mn alloy. After a time t the FeS has transformed to nearly pure MnS and the iron/inclusion interface compositions have reached the tie-line HG in Figure 8.15. We can further suppose that the Mn content at H is very small (i.e., << 1 wt.% Mn), that the inclusion is pure MnS, and that $D_{Mn}^{\delta\text{-Fe}} \simeq 10^{-7}$ cm^2/sec. Then

$$t = \frac{1}{3} \frac{(5 \times 10^{-4})^2}{10^{-7}} \frac{(63.14)}{(1.0)} \frac{\rho_{MnS}}{\rho_{Fe\text{-}1Mn}} \qquad (8\text{-}34)$$

where $C_i = \rho \times$ wt.% i. Thus

$$t = 53 \frac{\rho_{MnS}}{\rho_{Fe\text{-}1Mn}} \text{ seconds}$$

For $\rho_{MnS}/\rho_{Fe\text{-}1Mn} = 3.99/7.87$, the time required to transform the inclusion of liquid FeS to MnS is 27 seconds.

This analysis has not considered the effect of prior solidification segregation of Mn and so is an over-estimate of the time. Hone has observed in his cellular solidified Fe that, in the presence of carbon, the FeS inclusions are surrounded by an alloy rich in Mn at the cell walls, and that the alloy content towards the center of each cell is Mn depleted. Consequently the subsequent redistribution of Mn is towards homogenization of the alloy as

well as towards the transformation of FeS to MnS. This pile-up of Mn at the Fe/L_I interface means that the sulphide transformation will proceed more quickly because the value of $C^{\infty} - C^{S}$ in equation 8.33 is increased. However homogenization of the Fe cells will partially moderate this increase. It is possible, however, that some liquid inclusions, especially those very rich in sulphur and surrounded by Fe low in Mn, may not begin to transform until lower temperatures. Since $D_{Mn}^{\gamma Fe}$ is $\simeq 10^{-9}$ cm^2/sec, the time for transformation is now extended to 40-50 minutes. However, this time is still well within the cooling time limits normally produced by practice. The elapsed time between pouring, stripping, soaking, and rolling a commercial ingot can be 12 hours or more depending upon the efficiency of the particular mill. Sufficient time is therefore available for the FeS to MnS transformation to occur, and accordingly one rarely observes "hot shortness" effects in steels produced this way.

Continuous casting presents a more serious problem, because the cooling rates are very fast. The high temperature gradients between the cold surface and the hot center of the cast billets lead to exceptionally severe solute segregation. Clark[76] has noted that some presently produced continuously cast billets have high Mn contents at the centre of the billets, whereas the surface regions are deficient in Mn. It is then conceivable, if not likely, that because of the segregation and fast cooling rates the Mn deficient regions will exhibit inclusions of retained FeS, which in the absence of a lengthy soaking process, would retain a liquid film about the grain boundaries at rolling temperatures. This in turn would lead to surface cracking, a flaw which has been observed by Clark in continuously cast products[76].

Our conclusion is that one of the initial solidification products of most carbon steels is an Fe and S rich liquid in the form of inclusions, and not solid MnS as generally believed. However most carbon steels contain sufficient amounts of Mn for the liquid inclusions to very rapidly transform completely to MnS upon cooling through the δ-Fe temperature range. If the cooling rate is very fast, or if there is insufficient Mn in the alloy to transform the liquid inclusion to MnS, then it is possible to have FeS retained as a room temperature phase either as a single phase inclusion of FeS, or a duplex FeS + MnS inclusion.

To illustrate this latter point one is referred to Hone's thesis[64]. While investigating the steady-state solidification of Fe-Mn-S alloys, he observed FeS inclusions behind his rapidly cooled solid/liquid interface in an alloy containing 0.5 wt.% Mn, 0.03 wt.% S, and 0.4 wt.% C. This is to be expected since the nominal composition of this alloy is far to the left of the tie-line PC predicted for 0.4 wt.%C carbon steels. Another experiment by Hone involving the same compositions, but carbon free, should also have produced FeS inclusions, but the oxygen content of his melt lead to the preferential formation of iron and manganese oxides. When Hone increased his Mn contents to 3 wt.% Mn and above, the resultant inclusions were always MnS, again as one would expect from our calculated tie-lines, PC for the Fe-Mn-S and Fe-C-Mn-S systems.

Hone has also shown in a theoretical study that the initial segregation of Mn and S occurring during solidification is such that the Mn content of the remaining liquid increases preferentially. That is the composition of the liquid for the ternary system, increases first in the Mn direction, and then increases in the sulphur direction. Thus it is

possible that some medium to high carbon steels with a nominal composition to the left of PC could exhibit solidification products characteristic of compositions to the right of PC, i.e., the primary crystallization of MnS.

B.4. Inclusion Morphology

We conclude this chapter by presenting a discussion of the morphology of sulphide inclusions which have been observed in some experimental oxygen-free steels (cf. Figures 8.16, 8.17 and 8.18). In Figure 8.16 (due to Clark[34]) we observe the usual globular MnS inclusions with which metallographers are familiar. Also seen are a few MnS inclusions containing islands of Fe which are undoubtedly the result of Fe rejection from the liquid L_I as it transformed to MnS while the alloy cooled through the δ-Fe temperature range. Near the bottom of Figure 8.16 there exists a "star-shaped" MnS inclusion. This is probably the result of instability of the iron/inclusion interface with the consequent rejection of iron from an original globular liquid inclusion.

Figures 8.17 and 8.18 (courtesy of Hone[64]) are examples of the inclusions found behind the solid/liquid interface of his steady state ingots containing 0.5 wt.% Mn, 0.03 wt.% S, and 0.4 wt.% C. As mentioned earlier this nominal alloy composition should produce FeS as a solidification product. In Figure 8.17 we observe a duplex inclusion, FeS/MnS which indicates unequivocally that FeS formed initially and its transformation to MnS was arrested by the rapid cooling characteristic of Hone's experiment. In Figure 8.18, we observe an inclusion which has completely transformed

to MnS. However the partial history at the transformation is recorded as a 'sinusoidal' iron/inclusion interface, which undoubtedly arose from an interfacial instability during the initial stages of the FeS → MnS transformation.

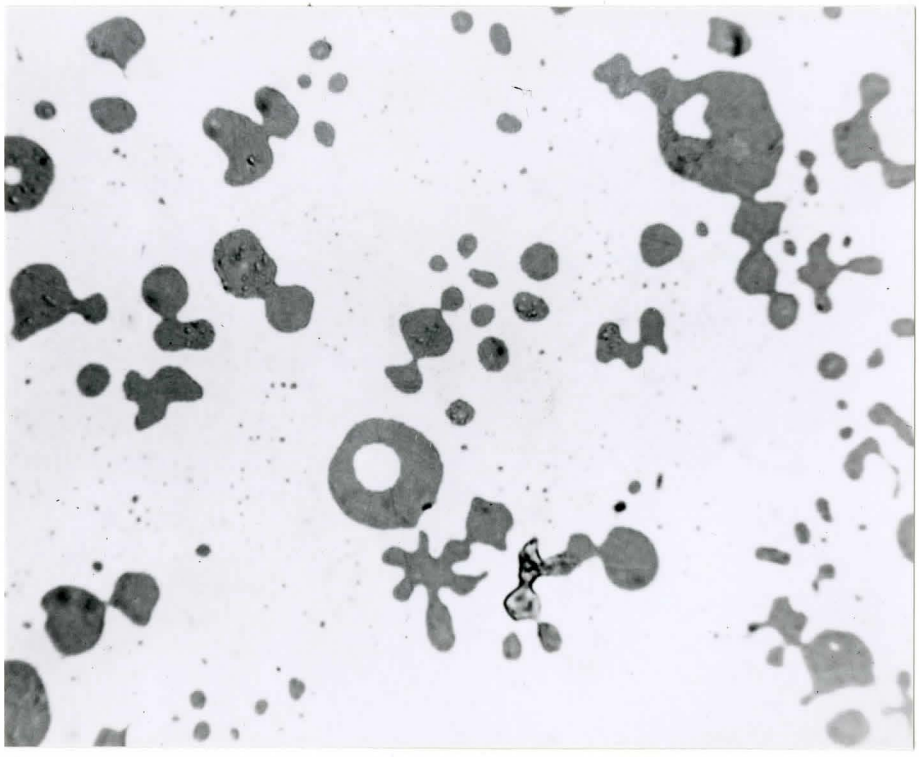

Figure 8.16 MnS inclusions in a Fe-Mn-S steel. (after Clark[34]) X620

Figure 8.17 Duplex MnS/FeS inclusions in a Fe-C-Mn-S steel. (courtesy of Hone[64]) X1000

Figure 8.18 "Sinusoidal" Fe alloy/MnS inclusion interface caused during the FeS to MnS transformation. (courtesy of Hone[64]) X800

CONCLUSIONS

As a result of the investigations carried out on the constitution and kinetics of the system Fe-Mn-S the following conclusions can be presented:

A. The 1300°C isotherm in the system Fe-Mn-S up to 50 at% has been experimentally determined. The compositions of the coexisting phases in the two three-phase fields are

	Fe wt.%	Mn wt.%	S wt.%
γ-Fe	99.9	0.039	0.042
+			
MnS	16.6	47.1	36.3
+			
FeS	67.6	1.0	31.4
γ-Fe	44	56	~0.05
+			
MnS	0.32	63.1	36.6
+			
Mn	38	62	~0.05

The tie-line directions in the (γ-Fe + Mn) two-phase field separating the above three-phase fields have also been experimentally determined. These directions show that nearly the entire γ-Fe composition range is in equilibrium with nearly pure MnS, while the composition range of MnS, from nearly 3.7 wt.% Fe to 16.6 wt.% Fe dissolved in MnS, is in equilibrium with nearly pure γ-Fe. This is demonstrated in Figure 5.2.

B. The MnS and FeS corners of the (γ-Fe + MnS + FeS) three-phase triangle have also been experimentally determined at the temperatures 1190°, 1251°, and 1336°C. Including the 1300°C data, these are

	MnS			FeS		
°C	Fe	Mn	S	Fe	Mn	S
1190	29.8	34.0	36.2	69.1	0.8	30.1
1251	22.5	41.5	36.0	68.5	0.73	30.8
1300	16.6	47.1	36.3	67.6	1.0	31.4
1336	15.4	48.1	36.5	61.1	1.4	37.6

The MnS corner of the three-phase triangle increases in Mn content at a constant value of S as the temperature increases. The FeS corner does not change substantially as the temperature increases.

C. The temperature dependence of Fe diffusion in solid MnS has been experimentally determined using Fe:MnS diffusion couples, and (FeMn)S:MnS diffusion couples over the temperature range 1253° to 1406°C. For the Fe:MnS diffusion couples

$$D_{Fe}^{MnS} = 69.4 \exp(-62{,}000/RT)$$

For the (FeMn)S:MnS diffusion couples

$$D_{Fe}^{MnS} = 0.756 \exp(-53{,}000/RT)$$

For both types of diffusion couples D_{Fe}^{MnS} has been determined for five different diffusion times at 1300°C.

For the Fe:MnS diffusion couples at 1300°C

$$\bar{D}_{Fe}^{MnS} = 3.96 \times 10^{-8} \text{ cm}^2/\text{sec.}$$

For the Fe:MnS diffussion couples at 1300°C

$$D_{Fe}^{MnS} = 2.04 \times 10^{-7} \text{ cm}^2/\text{sec.}$$

The difference between the two values is attributed to a greater cation vacancy concentration in the (FeMn)S:MnS couples (i.e., metal deficit sulphide). The sulphide at the interface region of the Fe:MnS couples is assumed to be close to stoichiometry, therefore exhibiting a smaller cation vacancy concentration.

D. The temperature dependence of Mn diffusion in δ-Fe has been experimentally determined in the temperature range 1446°C to 1494°C as

$$D_{Mn}^{\delta\text{-Fe}} = 0.264 \exp\left(-59{,}500 \frac{\text{cal}}{\text{mole}} /RT\right)$$

E. It has been shown, using the experimental results of the present study, and those of Shibata[15] and Nakao[13] that if one is going to invoke the concept of a pseudo-binary relationship between iron sulphide and manganese sulphide, then one must write the terminal compounds as FeS_X and MnS_X such that the straight line between their compositions on an isotherm coincides with a single tie-line in the (FeS + MnS) two-phase field.

For example, the present FeS:MnS diffusion couple experiments at 1200 and 1300°C (where FeS is liquid) show the diffusion of Fe into the MnS proceeds at rates typical of diffusion in liquids. It was concluded that the above tie-line criterion had been violated. The small sulphur difference in the terminal compositions caused interface instability and the subsequent

penetration of liquid FeS into the MnS.

F. To establish a formula for the solubility of Mn and S in γ-Fe the Wagner dilute solution formalism was applied to the Gibbs-Duhem equations for two phases in equilibrium in a three-component system. The integral of the resultant differential equation, with suitable approximations characteristic of the phase diagram yields the following result for the Fe-Mn-S system

$$X_S^{MnS} \ln X_S - \frac{bX_S^2}{2} + pX_S - CX_S X_{Mn} + g X_{Mn} - \frac{fX_{Mn}^2}{2} + X_{Mn}^{MnS} \ln X_{Mn} = \frac{1}{2} \ln K_o + \frac{Q}{RT}$$

where X_S and X_{Mn} are the mole fractions of Mn and S dissolved in γ-Fe when the γ-Fe is in equilibrium with stoichiometric MnS. The other parameters are functions of the Wagner self- and cross-interaction coefficients, and X_S^{MnS} and X_{Mn}^{MnS}. Q is the constant composition heat of formation of a MnS precipitate in γ-Fe.

Applying the experimental results of Turkdogan et al[9] to this relation the unknown coefficients were determined and an extrapolation from the equation is illustrated in Figure 5.6. When X_{Mn} and X_S are $\ll 1$, this solubility equation reduces to

$$K = X_{Mn} X_S = K_o \, e^{\frac{2Q}{RT}}$$

$$= 0.16 \exp\left(-41720 \frac{\text{cal}}{\text{mole}} \Big/ RT\right)$$

Using this solubility theory it has been shown that the solubility curve of γ-Fe in equilibrium with liquid FeS can be approximated by a

straight line parallel to the Fe-Mn binary at constant temperature. The intersection of this line and the preceding solubility curve at constant temperature determines the γ-Fe corner of the (γ-Fe + MnS + FeS) three-phase triangle.

G. Using the results of the present equilibrium and kinetic investigations, free energy-composition diagrams, the solubility theory, and data culled from the literature the Fe-Mn-S ternary phase diagram (in the form of ternary isotherms) over the temperature range 1200°C to 1600°C (see Figures 8.1 to 8.11) has been consistently described.

H. Using the data of Korber and Oelsen[29], Meyer and Schulte[26], and Sherman and Chipman[32] the temperature dependence of the solubility product defining the solubility of Mn and S in liquid Fe has been calculated.

$$K = 14.08 \exp\left(-40{,}100 \frac{\text{cal}}{\text{mole}} / RT\right)$$

I. Extending the solubility theory to multi-component systems it has been shown that the quaternary effect of carbon on the solubility product defining Mn and S solubilities in liquid Fe is

$$K = X_{Mn}\, X_S = K_o\, e^{\frac{2Q}{RT}}\, e^{-2X_C(\varepsilon^C_{Mn} + \varepsilon^S_{Mn})}$$

$$= 14.08 \exp(-40{,}100/RT) \exp(-19.6\, X_C)$$

J. The temperature T_C and the composition (X^C_{Mn}, X^C_S) at which δ-Fe first

directly reacts with solid MnS has been determined. These are

$$T_C = 1509^oC$$

$$X_{Mn}^C = 2.45 \text{ at\% Mn}$$

$$X_S^C = 0.77 \text{ at\% S}$$

It has also been demonstrated that this reaction is a true pseudo-binary eutectic reaction at T_C, and that the temperature T_C is a maximum in a eutectic trough.

K. It has been shown that the quaternary addition of carbon to the Fe-Mn-S system causes both T_C and (X_{Mn}^C, X_S^C) to decrease with increasing carbon content. The calculations indicate that X_{Mn}^C decreases linearly with increasing carbon content according to

$$X_{Mn}^C = 0.245 - 2\ X_C$$

for X_C up to 0.036 (i.e., 0.8 wt.% C). Above this carbon content we exceed the limits imposed by the theoretical assumptions and approximations.

L. Because the nominal compositions of low and medium carbon steels is less than the terminal Mn and S compositions of the tie-line characterizing the pseudo-binary eutectic reaction between δ-Fe and MnS at T_C for Fe-C-Mn-S alloys containing up to 0.8 wt.%C, it is concluded that the solidification of these carbon steels will always produce a S rich liquid as a high temperature solidification product. In the presence of sufficient Mn, the S rich liquid in the form of inclusions will rapidly (<60 seconds

in δ-Fe) transform to the more stable MnS during the subsequent cooling through the δ-Fe (and possibly, the γ-Fe) temperature range. It is inferred from our kinetic results, and from diffusion data in the literature, that the rate of transformation is controlled by the diffusion of Mn in the iron (either δ-Fe or γ-Fe).

APPENDIX I

THE WAGNER INTERACTION COEFFICIENTS

In a three component system the activity of solute component 1 is given by

$$a_1 = X_1 \gamma_1 \tag{I-1}$$

where X_1 is the mole fraction of component 1, and γ_1 is the activity coefficient. The effect of a second solute component 2 on γ_1 may be determined by expressing $\ln\gamma_1$ as a Taylor Series expansion.

$$\ln \gamma_1 (X_1, X_2) = \ln \gamma_1^o + \frac{X_1 \partial \ln\gamma_1}{\partial X_1} + \frac{X_2 \partial \ln\gamma_1}{\partial X_2} + \frac{X_1^2}{2} \frac{\partial^2 \ln\gamma_1}{\partial X_1^2} + X_1 X_2 \frac{\partial^2 \ln\gamma_1}{\partial X_1 \partial X_2} + \ldots \tag{I-2}$$

where the derivatives are taken for the limiting case of zero concentration of all solutes. At very low concentrations X_1^2 and the product of X_1 and X_2 become vanishingly small and the cross and square terms may be neglected. The functions $\partial \ln\gamma_1 / X_1$ and $\partial \ln\gamma_1 / \partial X_2$ are abbreviated to ε_{11} and ε_{12}, the Wagner self and cross interaction coefficients, respectively.[35] The equation then simplifies to

$$\ln\gamma_1 = \ln\gamma_1^o + X_1 \varepsilon_{11} + X_2 \varepsilon_{12} \tag{I-3}$$

and similarly

$$\ln\gamma_2 = \ln\gamma_2^o + X_1\varepsilon_{21} + X_2\,\varepsilon_{22} \qquad \text{(I-4)}$$

γ_1^o and γ_2^o are the limiting values of the activity coefficients in the pure solvent. It is expected that the ε's will be functions of temperature, but at constant temperature the values derived for the infinitely dilute solution are constant over the concentration range in which Henry's Law is obeyed. The approximations I-3 and I-4 can usually be applied without introducing a large error for moderately dilute solutions.

If the addition of 2 raises or lowers the activity of 1 one would expect that 1 would have a corresponding effect on 2. To show this one recalls that

$$\frac{\partial^2 G}{\partial X_1 \partial X_2} = \frac{\partial \bar{G}_1}{\partial X_2} = \frac{\partial \bar{G}_2}{\partial X_1}$$

It follows that

$$\left(\frac{\partial \ln\gamma_1}{\partial X_2} = \frac{\partial \ln\gamma_2}{\partial X_1}\right)\ X_1 \to 0,\ X_2 \to 0$$

or that

$$\varepsilon_{12} = \varepsilon_{21} \qquad \text{(I-5)}$$

The chemical potential of a component is defined in terms of activity by

$$\mu_i = \mu_i^o + RT\ln a_i$$

$$= \mu_i^o + RT\ln X_i\gamma_i \qquad \text{(I-6)}$$

For component 1, substitution of equation 1-3 into 1-6 gives

$$\mu_1 = \mu_1^o + RT\left[\ln X_1 + \ln\gamma_1^o + X_1\varepsilon_{11} + X_2\,\varepsilon_{12}\right] \qquad \text{(I-7)}$$

and

$$\frac{d\mu_1}{RT} = \frac{dX_1}{X_1} + \varepsilon_{11}dX_1 + \varepsilon_{12}dX_2 \qquad \text{(I-8)}$$

and similarly

$$\frac{d\mu_2}{RT} = \frac{dX_2}{X_2} + \varepsilon_{21}dX_1 + \varepsilon_{22}dX_2 \qquad \text{(I-9)}$$

In the case of the solvent, component 3, it is assumed that if X_1 and X_2 approach zero, then $X_3 \rightarrow 1$ in which case Raoultian ideality is achieved and $\gamma_3 = 1$. Thus $a_3 = X_3$ and

$$\frac{d\mu_3}{RT} = \frac{-dX_1 - dX_2}{1 - X_1 - X_2} \tilde{=} -dX_1 - dX_2 \qquad \text{(I-10)}$$

APPENDIX II

GENERALIZATION OF THE SOLUBILITY EQUATION

The investigation of systems of more than three components becomes somewhat intractable from an experimental point of view. It is therefore of practical interest to examine the general multicomponent solubility theory. The Gibbs-Duhem equations for an n component system in which two phases are in thermodynamic equilibrium under isobaric and isothermal conditions are

$$X_1^I \, \partial\mu_1 + X_2^I \, \partial\mu_2 + X_3^I \, \partial\mu_3 + \ldots + X_n^I \, \partial\mu_n = 0 \qquad \text{(II-1)}$$

$$X_1^N \, \partial\mu_1 + X_2^N \, \partial\mu_2 + X_3^N \, \partial\mu_3 + \ldots + X_n^N \, \partial\mu_n = 0 \qquad \text{(II-2)}$$

Following the same assumptions and procedures described in Chapter III one arrives at a general differential equation which has the same form as that derived for the ternary case. That is

$$\left[\frac{X_1^N}{X_1} + f_1\,(X_1, X_2, \ldots X_{n-1})\right] dX_1 + \left[\frac{X_2^N}{X_2} + f_2(X_1, X_2, \ldots X_{n-1})\right] dX_2 + \ldots$$
$$\ldots + \left[\frac{X_{n-1}^N}{X_{n-1}} + f_{n-1}\,(X_1, X_2, \ldots X_{n-1})\right] dX_{n-1} = 0 \qquad \text{(II-3)}$$

where

$$f_i = \left[-\sum_{j=1}^{n-1} (\varepsilon_{ij} + 1)\, X_j + \sum_{j=1}^{n-1} (\varepsilon_{ij} + 1)\, X_j^N\right] - 1 \qquad \text{(II-4)}$$

Since $\epsilon_{ij} = \epsilon_{ji}$, then equation II-3 is an exact differential equation and may be integrated to give

$$\left[\sum_{i=1}^{n-1} X_i^N \ln X_i\right] + F(X_1, X_2, \ldots X_{n-1}) = \ln K \qquad \text{(II-5)}$$

where $F(X_1, X_2, \ldots X_{n-1})$ is the integrated form of equation II-4 and $\ln K$ is an integration constant. Equation II-5 is then the general multicomponent solubility equation of Phase I in equilibrium with some other phase N. Since F contains linear and quadratic terms of X_i, then one can see that if the solubility of all the solute components in phase I is sufficiently small the ln terms will predominate in equation II-5 and the solubility equation becomes

$$\sum_{i=1}^{n-1} X_i^N \ln X_i = \ln K \qquad \text{(II-6)}$$

By substituting n = 3 into equation II-6 one of course gets an expression identical with equation 3-60 for the ternary case.

If instead of equating equation II-3 to zero, one equates it to $(V^N\, dP/RT)$, then one can produce a generalized equation defining the multicomponent Gibbs-Thompson effect. The conditions for the general case are the same as those outlined in Chapter III for the ternary case. The resultant expression is

$$\left[\sum_{i=1}^{n-1} X_i^N \ln X_i\right] + F(X_1, X_2, \ldots X_{n-1}) = \ln K + \frac{V^N 2\sigma}{RTr} \qquad \text{(II-7)}$$

Similarly one can determine the temperature dependence of ln K by

equating equation II-3 to $-(S^N - S^I)\, dT/RT = -\frac{Q dT}{RT^2}$. In this case the integrated result is

$$\left[\sum_{i=1}^{n-1} X_i^N \ln X_i\right] + F(X_1, X_2 \ldots X_{n-1}) = \ln K = \ln K^o + \frac{Q}{RT} \quad \text{(II-8)}$$

Although experimental studies are usually confined to 3-component systems or less, some researchers have branched to quaternary and quintary systems. For these latter systems the above equations may be of some use.

REFERENCES

1. Kirkaldy, J.S., Brigham, R.J., Domian, H.A., and Ward, R.G., Can. Met. Quart., 2, 1963, 233.

2. Kirkaldy, J.S., Von Destinon-Forstmann, J., and Brigham, R.J., Can. Met. Quart., 1, 1962, 59.

3. Smithells, C.J., Metals Reference Book. Vol. 1, Butterworths (London), 1962, 376.

4. Hansen, M., Constitution of Binary Alloys, McGraw-Hill (New York), 1958.

5. Hume-Rothery, W., and Hellawell, A., Phil. Trans., 249A, 1957, 417.

6. Hume-Rothery, W., and Buckley, R.A., JISI, 202, 1964, 534.

7. Burgmann, W., Urbain, G., and Frohberg, M.G., Memoir. Sci. Rev. Metal. 65, 1968, 567.

8. Rosenqvist, T., and Dunicz, B.L., J. Metals, June 1952, 604.

9. Turkdogan, E.T., Ignatowicz, S., and Pearson, J., JISI, 180, 1955, 349, and Revue de Metal., 52, 1955, 725.

10. Barloga, A.M., Bock, K.R., and Parlee, N., Trans. AIME., 221, 1961, 173.

11. Olander, A., Z. Phys. Chem., 164, 1933, 431.

12. Vogel, V.R., and Hotop, W., Archiv fur das Eisenhuttenwesen, 11, 1937, 41.

13. Nakao, H., M.Sc. Thesis, McMaster University, 1967.

14. Quan, D.T., Compte Rend., 258, 1964, 2045.

15. Shibata, Z., Tech. Repts. Tohoku Imp. Univ., 7, 1928, 279.

16. Rohl, G., JISI, Carn. Schol. Mems., 4, 1912, 18, and Stahl u. Eisen, 33, 1913, 565.

17. Silverman, Morey, and Rossini, Bull. Nat. Research Council (U.S.) 107, 1943.

18. Coughlin, J.P., J. Amer. Chem. Soc., 72, 1950, 5445.

19. Glaser, O., Cent. Mineral. Geol., Abt. A, 1926, 81.

20. Van Vlack, L.H., Chao, H.C., Oberin, F., and Thomassen, L., Trans. ASM 57, 1964, 885.

21. Nornemann, Metallurgie, 5, 1908, 64.

22. Priltz, Zeits. Anorg. Chem. 49, 1903, 328.

23. Friendlich, Metallurgie, 7, 1910, 257.

24. Allen, E.T., Crenshaw, J.L., Johnston, J., and Larsen, E.S., Zeits. Anorg. Chem., 76, 1912, 201.

25. Vogel, V.R., and Baur, H., Archiv fur das Eisenhüttenwesen, 6, 1933, 495.

26. Meyer, V.O., and Schulte, F., Archiv fur das Eisenhüttenwesen, 8, 1934, 187.

27. Wentrup. H., Carn. Schol. Mems., 24, 1935, 103.

28. Korber, V.F., Stahl u. Eisen, 56, 1936, 433.

29. Korber, V.F., and Oelsen, W., Stahl u. Eisen, 56, 1936, 310.

30. Wentrup, H., Techn. Mitteilung Krupp, 5, 1937, 131.

31. Schurmann, V.E., and Zellerfeld, C., Aus Wissenschaft und Praxis des Giessereiwesens, 1955, 51.

32. Sherman, C.W., and Chipman, J., Trans. AIME, 194, 1952, 597.

33. Buzek, Z., Sbornik Ved. Praci Vysoke Skoly Banske Ostrave, Vol. II, (3), 1955, 401.

34. Clark, I., M.Sc. Thesis, McMaster University, 1965.

35. Wagner, C., Thermodynamics of Alloys, Addison-Wesley (London) 1952 , 53.

36. Brown, J.R., JISI, 205, 1967, 154.

37. Hernstein, W.H., Beck, F.H., Fontana, M.G., Trans AIME, 242, 1968, 1049.

38. Kononyuk, I.F., Phys. Met. Metallog., 19, 1965, 159.

39. Wells, C., Mehl, R.F., Trans. AIME, 145, 1941, 315.

40. Angers R., and Claisse, F., Can. Met. Quart., 7, 1968, 73.

41. James, D.W., and Leak, G.M., Phil. Mag., 14, 1966, 701.

42. Fredberg, J., Torndahl, L., and Hillert M., Jernkont. Ann., 153, 1969, 263.

43. Yang, L., Kado, S., and Derge, G., Phys. Chem. Process. Metal, Pt. 1, Interscience (New York) 1961.

44. Rollason, E.C., and Roberts, D.F.T., JISI, 166, 1950, 422.

45. Sims, C.E., and Dahle, F.B., Trans. Amer. Foundrymen's Assoc. 46, 1938, 65.

46. Briggs, C.W., The Metallurgy of Steel Castings, McGraw-Hill (New York), 1946, 147.

47. Lichy, E.J., Duderstadt, G.C., and Samways, N.L., J. Metals, 1965, 769.

48. Kiessling, R., and Westman, C., JISI, 204, 1966, 377.

49. Matsubara, K., Trans. ISIJ, 6, 1966, 139.

50. Tamman, G., Z. Phys. Chem., 85, 1913, 273.

51. Prigogine, I., and Defay, R., Chemical Thermodynamics, Longmans Green, (London), 1952.

52. Rhines, F.N., Phase Diagrams in Metallurgy, McGraw-Hill (New York), 1956.

53. Morris, L., Ph.D. Thesis, McMaster University, 1965.

54. Averin, V., Izv. Akad. Nauk SSSR, Metallurgia i Topliwo, 5, 1961, 3.

55. Chao, H.C., Thomassen, L., and Van Vlack, L.H., Trans. ASM, 57, 1964, 386.

56. Classen, A., Z. Analyt. Chem., 16, 1877, 319.

57. Le Bot, J., and Quan, D.T., Comptes Rendus, Ser.A,B, 262B (1), 1966, 34.

58. Lorenz, R., and Schulz, G., Z. Anorg. Chem., 171, 1928, 261.

59. Dalvi, A., The Electron Probe Microanalyser, Dept. Metal. and Mat. Sci., McMaster University, 1969.

60. Darken, L.S., and Gurry, R.W., Physical Chemistry of Metals, McGraw-Hill (New York), 1953.

61. Roy, P., and Hultgren, R., Trans. AIME, 233, 1965, 1811.

62. Hone, M., Subramanian, S.V., and Purdy, G.R., Can. Met. Quart., 8, 1969, 251.

63. Meijering, J.L., Philips Technical Review, 26 (2), 1965, 33.

64. Hone, M., Ph.D. Thesis, McMaster University, 1970.

65. Delves, R.T., and Lewis, B., J. Phys. Chem. Solids 24 (4), 1963, 549.

66. Morin, F.J., in International Conference on Semiconductor Physics, Prague, Academic Press, 1961, 862.

67. Condon, E.U., and Odishaw, H., Handbook of Physics, 2nd Ed., McGraw-Hill (New York), 1967.

68. Shewmon, P.G., Diffusion in Solids, McGraw-Hill (New York), 1963, 145.

69. Kirkaldy, J.S., and Brown, L.C., Can. Met. Quart. 2, 1963, 89.

70. Harrison, J.D., and Wagner, C., Acta. Met., 7, 1959, 722.

71. Elliott, J.F., and Gleiser, M., Thermochemistry for Steelmaking, Vol. 1, Addison-Wesley (Reading, Mass.), 1960, 248.

72. Jorgensen, C., and Thorngren, I., Thermo Tables for Proc. Metal, Almqvist and Wiksell (Stockholm) 1969, 32.

73. Sherman, C., Elvander, H.I., and Chipman, J., Trans. AIME, 188, 1950, 334.

74. Metals Handbook, 1948 Ed., A.S.M., (Cleveland), 1956, 447.

75. Fuwa, T., and Chipman, J., Trans. AIME, 215, 1959, 708.

76. Clark, I., private communication.